TERAHERTZ NEAR-FIELD COUPLING IN SCANNING TUNNELING MICROSCOPY

by

Peter Hòa Nguyễn

A thesis submitted in partial fulfillment of the requirements for the degree of

Doctor of Philosophy

Department of Physics
University of Alberta

Abstract

Terahertz (THz) optics and scanning probe microscopy (SPM) techniques have gone through several decades of development, enabling numerous research studies and applications related to ultrafast phenomena at the nanoscale. Advancements in THz technology enable physical processes in materials to be identified at precise timescales from nanoseconds down to femtoseconds. Modern scanning tunneling microscopy (STM) systems readily scan surfaces to reveal molecular and atomic structure. Physical phenomena on individual atoms or molecules can be studied at ultrashort timescales simultaneously by combining THz optics and STM to develop a terahertz scanning tunneling microscope (THz-STM), an atomic imaging microscope coupled to ultrafast light pulses. In THz-STM, THz pulses generated by a femtosecond laser source propagate to the STM probe tip, then become focused down to the microscopic volume around the STM tip apex, which drives the tunneling in the sub-nanometer regime. Amidst recent advances in THz-STM techniques where simultaneous atomic spatial resolution and sub-picosecond time resolution has been demonstrated, the nature of the transient bias resulting from the coupling of THz radiation to the STM junction is not completely understood. In order to realize the full potential of THz-STM, there is a need to understand the nature of electromagnetic radiation coupling with the STM system and the sample material being probed.

In this thesis, a detailed investigation is carried out using finite-element method (FEM) simulations with COMSOL Multiphysics, as well as analytical approaches and numerical modeling on the THz-STM. Full scale simulations and modeling are conducted in the far-field regime, the region away from the STM probe at about

a few THz wavelengths and beyond, then focuses on the near-field regime, the gap region between the tip and sample of the STM. The results show several interesting aspects about the tip and sample responding to coupled THz pulses in the near-field regime, which lead to insights for understanding the physical mechanisms in THz-STM operation.

In the THz-STM experiment, the COMSOL simulations visualize the propagation and focusing of a THz pulse to the STM junction and computes a near-field THz electric field existing in the nm-sized gap that is largely enhanced by factors of 10^4 to 10^5 compared to the incident THz electric field. Furthermore, the simulated near-field transients in the STM gap show spectroscopic dependence that resembles THz antenna-wire coupling.

Alternatively, the THz near-field is calculated with electromagnetic models used in scanning near-field optical microscopy (SNOM). The THz field generation, propagation and interaction with the STM geometry is simulated with a discrete dipoles configuration, reproducing similar results as the FEM simulations from COMSOL. A lumped element circuit model that parameterizes the STM junction as RLC circuit elements is also used to calculate the THz near-field voltage, which acts as the bias voltage for the STM junction. The circuit model is linked to a transmission line to simulate pulse propagation and pulse reflections along the tip shaft. Expanded circuit models are also developed for metal-to-metal and the metal-to-semiconductor junctions. Experiments and simulations reveal that subsurface transport of charge carriers driven by large penetrated THz near-fields inside semiconductor samples is needed to account for extreme transient current densities and to also obtain sampled near-field waveforms observed in THz-STM.

Preface

This thesis is an original work by Peter Nguyen. The research conducted for this Thesis was performed from September 2014 to December 2023 at the University of Alberta under the supervision of Professor Frank A. Hegmann. It has led to three collaborative refereed publications. I delivered 7 poster and oral presentations and contributed to 11 conference abstracts at 6 conference events based on the collection of these works. The three refereed publications are listed below, along with their corresponding author contributions. There are manuscripts currently in development for future publications, which will be pursued after this Thesis work is completed, either as a primary or secondary author.

Publications and Manuscripts

[1] **P. H. Nguyen**, C. Rathje, G. J. Hornig, V. Jelic, C. Ropers & F. A. Hegmann. "Coupling terahertz pulses to a scanning tunneling microscope," *Physics in Canada* **71**, 157–160 (2015).

With the guidance of F. Hegmann, I was able to develop and carry out simulations for the THz-STM experiment. F. Hegmann provided the funding for the computational resources and access to the COMSOL Multiphysics software licensed under the CMC server. I performed the electromagnetic simulations, data analysis and composition of the manuscript. C. Rathje, supervised under C. Ropers, and G. J. Hornig assisted in building and running the simulations and developing presentation material for a few conferences listed in the conference presentations section. V. Jelic and F.

Hegmann assisted with the interpretation of the results, contributed to discussions and editing of the manuscript.

[2] V. Jelic, K. Iwaszczuk, **P. H. Nguyen**, C. Rathje, G. J. Hornig, H. M. Sharum, J. R. Hoffman, M. R. Freeman & F. A. Hegmann. "Ultrafast terahertz control of extreme tunnel currents through single atoms on a silicon surface," *Nat. Phys.* **13**, 591–598 (2017).

With guidance from F. Hegmann, V. Jelic designed and built the optical setup, prepared the samples, acquired/analyzed the data, interpreted the results and wrote the manuscript. J. R. Hoffman assisted with construction of the optical setup. I assisted with preliminary measurements, chemical etching of tip probes, testing and collecting data alongside with H. Sharum and G. Hornig. The theoretical modeling was developed by K. Iwaszczuk. M. Freeman, F. Hegmann, K. Iwaszczuk and I assisted with interpretation/analysis of the data and review of the manuscript. Part of the my electromagnetic simulation work as described in chapter 4 was assisted by C. Rathje and G. J. Hornig and also used for main and supplemental figures in the article. V. Jelic and F. Hegmann helped proposed the simulation ideas featured in the article.

[3] Y. Luo, V. Jelic, G. Chen, **P. H. Nguyen**, Y.-J. R. Liu, J. A. M. Calzada, D. J. Mildenberger, and F. A. Hegmann, "Nanoscale terahertz STM imaging of a metal surface", *Phys. Rev. B*, **102** (20), 205417(11), (2020).

Y. Luo was responsible for the experimental work, data acquisition, analysis, interpretation and manuscript composition. V. Jelic, J. A. M. Calzada and D. Mildenberger also carried out the experiments and data acquisition. Y. Luo and I proposed and developed the model and code for the experimental analysis. I alongside with Y.-J. Liu carried out electromagnetic simulations, to assist with complementary analysis and verification. G. Chen contributed to the theoretical modeling. Meetings were regularly held between Y. Luo, V. Jelic, J. A. M. Calzada, F. A Hegmann and I for

discussion, interpretation of results and manuscript composition.

Manuscript in preparation

The work presented in chapters 4 and 5 are currently in a manuscript:

P.H. Nguyen, V. Jelic, Y.-J. Liu, C. Rathje, G.J. Hornig, and F.A. Hegmann. "Simulation of terahertz near-fields in the scanning tunneling microscope junction".

With the guidance of F. Hegmann, I was able to develop and carry out simulations for the THz-STM experiment. F. Hegmann provided the funding for the computational resources and access to the COMSOL Multiphysics software licensed under the CMC server. I performed the electromagnetic simulations, modeling, data analysis and composition of the manuscript. C. Rathje, G. J. Hornig and Y.-J. Liu assisted in building/running the simulations and developing figures. V. Jelic and F. Hegmann provided simulation ideas, assisted with the interpretation of the results, contributed to discussions and editing the manuscript.

Manuscript in preparation

The work presented in chapters 7 and 8 will be developed into another manuscript(s) (to be determined).

V. Jelic, J. A. M. Calzada and Y. Luo carried out the experiments and data acquisition for the experimental content presented in 8. D. J. Mildenberger, assisted with the measurements. V. Jelic, Y. Luo, and I conducted simulations, data analysis and interpretation of results. Several meetings were held to discuss and develop a potential paper.

Conference presentations

Below is the list of first author conference presentations based on the publications listed above and the contents of this Thesis work.

P.H. Nguyen, C. Rathje, G.J. Hornig, V. Jelic, C. Ropers, and F.A. Hegmann.

Poster: "Coupling THz Pulses to a Scanning Tunneling Microscope". Optical Tera-hertz Science & Technology (OTST) Conference, March 2015, San Diego, CA. Dis-tinction: 2nd place prize winner for Best Student Poster Competition

P.H. Nguyen, C. Rathje, G.J. Hornig, V. Jelic, C. Ropers, and F.A. Hegmann. Poster: "Coupling THz Pulses to a Scanning Tunneling Microscope". Alberta Nano Research Symposium, May 2015, Banff, AB.

P.H. Nguyen, C. Rathje, G.J. Hornig, V. Jelic, C. Ropers, and F.A. Hegmann. Poster: "Coupling THz Pulses to a Scanning Tunneling Microscope". Canadian Association of Physicists (CAP) Congress, June 2015, Edmonton, AB. Distinction: Third place winner of the 2015 Best Student Poster Competition.

P.H. Nguyen, C. Rathje, G.J. Hornig, V. Jelic, C. Ropers, and F.A. Hegmann. Oral: "Coupling Picosecond Terahertz Pulses to a Scanning Tunneling Microscope". COMSOL International Conference, October 2015, Boston, MA.

P.H. Nguyen, C. Rathje, G.J. Hornig, V. Jelic, C. Ropers, and F.A. Hegmann. Poster: "Calculating Terahertz Near-fields in the Scanning Tunneling Microscope Junction". CLEO Conference, May 2018, San Jose, CA.

P.H. Nguyen, V. Jelic, Y. Luo, J.A.M. Calzada, Y.-J. Liu, and F.A. Hegmann. Video conference oral: "Modeling the Terahertz Pulse Induced Transient Bias in the STM Junction." International Conference on Infrared Millimeter and Terahertz Waves (IRMMW-THz), October 2020, Buffalo, NY.

"There are far, far better things ahead than any we leave behind."

-C. S. Lewis

This work is dedicated to my big brother, Lương Nguyễn, who paved the road and provided greatly for my academic endeavours, but sadly passed away too soon before we can celebrate this milestone together.

Acknowledgements

Graduate school was a decade long journey full of twists and turns. Early on, I was dealt some good cards such as ample funding and undergraduate research experience. It looked promising for a successful run in grad school. That is completing academic milestones, contribute novel research, then adding the PhD title to my resumé. Little did I expect many personal development challenges that involved a great deal of stress on my physical, mental, emotional and spiritual health. It involved going through years of challenges of battling with mental health struggles, bereavement of family and friends, health problems and financial insecurity. The cards of adversity were drawn from the midpoint all the way to the end of my PhD run. I was impacted by Imposter Syndrome, loss of a family member, depression and anxiety, illnesses and hindrances due to COVID-19, car accident injuries and losses, and difficulty keeping afloat due to funding shortages. Finishing grad school was certainly an epic grind to the finish line met with tons of resistance, that it required some hard extra years to earn this PhD. In the quest to get the degree, it felt like the engine kept on dying or the wheels kept on falling off. It is relieving to finally make it to the end. Though I must admit that my personal development journey that was in parallel with the academic one was the tougher one to battle through. Facing adversities and taking steps to overcome them equipped me with the lessons and tools to deal with challenges as I pursue my next goals. Furthermore, to share them with others who might have to endure a similar journey.

The adversities listed previously have caused much grief during this journey in grad school. They all bombarded me at a time which I did not want to deal with them, but the growth that came from battling them helped build up my character and resilience. After such a long grind to battle my personal demons, I want to strongly emphasize that mental health matters is a key component of personal development and one should seek help when it goes awry. For this long PhD run, there is a countless amount of people to acknowledge who contributed to my journey. Unfortunately, I cannot list everybody but hopefully, there will be opportunities for all of us to encounter so that I can share my gratitude. Firstly, I thank my supervisor Frank Hegmann for being there the whole way for my entire graduate school journey. From guiding me in my Thesis project, completing administrative tasks to keep me in the grad program, helping out with scholarship applications, providing funding, and refining my scholarly works. I am most grateful for the fact that he demonstrated a high level of patience to allow me to pursue my studies beyond the standard degree completion

timelines. I always felt bad for devolving into a student with poor study habits and inconsistencies, resulting in a sluggish progress in my degree during these struggling grind years that followed my PhD candidacy. I am indebted for your patience and all the extra work you did in order to help get me to the finish line.

Secondly, I am thankful for the graduate student colleagues and post-docs that were with me during the academic grind. For my time being part of the Ultrafast Nanotools Lab group, I was part of a positive research environment where the group meshed well and every member contributed to each other's work. Thank you Vedran J., Yang L., David P., Jesus-Alex M., Cameron H., Howe S., Charles J., Nils R., and Mary N. for creating a positive research environment in the lab(s) and even outside during social events and leisure activities. Additionally, I acknowledge international visiting scholars: Christopher R., Krzysztof I. and H useyin A.; and seasonal/internship students: Haille S., Kameron P., Daniel M., Graham H. and Ray L., who made contributions to experiments and/or simulations in this Thesis work. Finally, I want to send my heart out to my soul-helper, who is now my beloved wife and expecting mother, Mrs. Taylor Nguyễn. She entered into my life during the final crucial stretch of the Thesis grind and propelled me to finish my degree by providing loving, mental and emotional support. Furthermore, she dedicated numerous hours to revise this Thesis manuscript and was actively involved in planning the final stages of my program completion. I wish you all the best on your endeavours, whether you are still in the academic grind, or pursuing something else.

Being from east of Canada, I moved out west mainly for grad school without much of a community of relatives or, close friends from the start. Spending time with peers like Trí, Sơn, Kindly, Thông, Huy and Đào, helped refine my fluency in Vietnamese, as well as maintain my heritage. For the friends still out east or abroad: Karol, Henry, Nasit, Oliver and Charles C., I am glad we still stayed in touch online (and rare visits) as I received your ongoing support from afar. In my family, I was the only crazy one among my siblings: Luong, Kim, Vincent, Jason and Melissa, to take school all the way and bury myself in a deep financial hole. Cousin Chính who was like an older brother would often take long inter-province road trips to check up on me. The family had my back and supported my career path all the way. Finally, I have to send my love and gratitude to my parents, Thái and Gái, who provided love, caring support and resources in all the decades of schooling from grade school to grad school.

Lastly, I dedicate this entire work to my older brother, Luong, who was foundational to my life and career, but sadly passed away way too soon before we could celebrate this milestone. He paved the road for me to pursue education to the highest degree. He made sacrifices in his own career to work hard to provide the resources and time for me to carry out my career path. His passing shattered my foundations and brought upon great difficulties during many years of my studies to cope with it. He left behind a lasting legacy which inspires me to finish this work while persevering through all the challenges in this era of my life.

Contents

List of Tables

List of Figures

List of Symbols

Physical Constants

c, c_0	Speed of light in a vacuum inertial system.	$299,792,458\,\text{m/s}$
e	Elementary charge.	$1.60217663 \times 10^{-19}\,\text{C}$
m_e, m_0	Electron mass.	$9.1093837 \times 10^{-31}\,\text{kg}$
k_B	Boltzmann constant.	$1.380649 \times 10^{-23}\,\text{J/K}$
h	Planck's constant.	$6.62607015 \times 10^{-34}\,\text{J} \cdot \text{s}$
$\hbar$	Planck's wave constant.	$1.0545718 \times 10^{-34}\,\text{J} \cdot \text{s}$

Physical Variables

E	Electric field.	V/m
H	Magnetic field.	A/m
V	Voltage.	V
I	Current.	A
R	Resistance.	Ω
C	Capacitance.	F
L	Inductance.	H
J	Current density.	$\text{A}\,\text{m}^{-2}$
Φ	Tunneling barrier.	eV
I_t	Tunneling current.	A

n Carrier density. cm^{-3}

μ Carrier mobility. $\text{cm}^2\,\text{V}^{-1}\text{s}^{-1}$

Other Symbols

ζ Field screening factor.

Abbreviations

AFM Atomic Force Microscope.

CFL Courant–Friedrichs–Levy.

DFT Density functional theory.

EM Electromagnetic.

EO Electro-Optic.

FDG First-derivative Gaussian.

FDTD Finite-difference time-domain.

FEM Finite Element Method.

FF Far-field.

LDOS Local density of states.

NF Near-field.

OPP Optical Pump-Probe.

OPP-THzSTM Optical Pump - THz-STM Probe.

PC Photo-conductivity.

PDE Partial Differential Equation.

RLC Resistor-Inductor-Capacitor.

SDG Second-derivative Gaussian.

SEM Scanning electron microscopy.

SNOM Scanning near-field optical microscopy.

SPM Scanning Probe Microscopy.

SPM Scanning Probe Microscope.

SPPs Surface plasmon polaritons.

SPV Surface photo voltage.

STM Scanning Tunneling Microscope.

STM Scanning Tunneling Microscopy.

STOM Scanning optical tunneling microscopy.

TDS Time Domain Spectroscopy.

TEM Transmission electron microscopy.

TERS Tip-enhanced Raman spectroscopy.

THz Terahertz.

THz-A-SNOM Terahertz Apertureless scanning near-field optical microscopy.

THz-STM Terahertz Scanning Tunneling Microscopy.

THz-STM Terahertz Scanning Tunneling Microscope.

TIP Tip-induced plasmon.

TL Transmission Line.

TLM Transmission-line modeling.

UHV Ultra-high vacuum.

Chapter 1

Introduction

There have been ongoing developments in the world of microscopy to reach the highest attainable spatial resolution in imaging and capture physical events on the shortest timescales. Carrier scattering and trapping times in nanoparticles, electron thermalization times, and coherent structural dynamics all occur on femtosecond to picosecond timescales. Examples of such physical processes in single nanoparticles require novel ultrafast nanoprobe techniques to explore them [4–21]. Modern microscopy instruments such as the Scanning Tunneling Microscope (STM) have made imaging the atomic structure of matter fairly routine. Imaging surfaces on the nanometer scale and beyond with high temporal resolution can be achieved by combining optical techniques with instruments that embody a scanning probe. Towards achieving this goal, table-top optical setups have been combined with microscopes such as the STM [2, 3, 12, 14, 16–18, 20, 22–34] and Atomic Force Microscope (AFM) [5–7, 9, 21, 35–38]. Typically, these microscopes alone are electronic-based, which limits them to resolving events temporally on the microsecond to millisecond timescales. Temporal resolution on the ultrafast timescales can be accomplished by sending extremely short pulses of electromagnetic (EM) radiation to the scanning probe region of the device. About a decade ago, the STM and THz optical techniques were combined to create a terahertz scanning tunneling microscope (THz-STM) with nanoscale-imaging resolution and ultrafast time-capture capabilities [33]. Developments in THz-STM

have progressed over the past decade while emerging challenges make the relatively young field still interesting to pursue with physical phenomena and applications to unravel in condensed matter physics. Furthermore, with recent advancements in THz technologies, THz-STM systems can perform measurements that achieve temporal resolution in the femtosecond timescales [25, 31, 39].

Ultrafast laser technology has evolved over the last few decades. The term "ultrafast" typically refers to timescales on the order of picoseconds or less. Table-top lasers are able to generate pulses with a temporal duration in the femtosecond regime with enough pulse energy squeezed in to result in transient peak powers on the order of gigawatts and terawatts. Ultrafast optical techniques enable exploration of transient dynamics in a wide range of materials with an extremely high temporal resolution, paving new avenues for research and applications such as optical telecommunications, high harmonic generation in gases and solids, femto- and attosecond science, optics-based microscopy, and terahertz technology [40].

Fundamentally, the spatial resolution of laser techniques is determined by the diffraction-limited spot-size of the focused laser beam. Terahertz technology enables the exploration of material properties between the microwave and infrared regions of the Electromagnetic (EM) spectrum. Broadband THz pulses have picosecond (ps) duration and frequency components ranging from 100 GHz to 3 THz or more. THz pulses are capable of probing ultrafast carrier dynamics in materials, but with a diffraction-limited spatial resolution on the order of ~ 1 mm [40, 41]. However, when THz pulses are combined with an extremely sharp tip of a scanning probe microscope (SPM), the electric field of the incident radiation can be localized to the near-field (NF) regime, which is the region of space around the apex end of the tip. The near-field volume is usually scaled with the geometric dimension of the tip, particularly the approximate radius of curvature of the tip apex, which is on the order of 100 to 10000 times smaller than THz wavelengths. This process has enabled THz techniques to be focused down to the micrometer [42, 43], submicrometer [44, 45], nanometer [5,

20, 27, 33, 46], atomic [2, 3, 24], and sub-molecular [22, 27, 47] length scales.

This thesis explores the nature of THz-pulse coupling in the near-field of the THz-STM in order to realize its full potential as an ultrafast microscopy technique for studying physical systems at the nanometer to atomic length-scales. Various materials exhibiting physical phenomena such as carrier transport and structural modifications have been observed with THz-STM by utilizing the high spatial resolution capability of the STM and the ultrafast time resolution of THz pulse spectroscopy [2, 3, 5, 6, 22–27, 33, 39]. Pioneering THz-STM experiments used THz-pulse-induced tunneling currents to image InAs nanodots with simultaneous 2 nm spatial resolution and sub-picosecond temporal resolution under ambient conditions [33]. THz-STM in ultrahigh vacuum has demonstrated that extreme THz-pulse-driven tunneling currents can be localized and controlled through single-atoms [2]. Furthermore, ultrafast dynamics of single molecules have been resolved with the THz-STM operating in a state-selective tunneling regime with single-electron-per-pulse sensitivity [22, 25, 47]. By studying various physical systems in materials and understanding their dynamic behaviour under THz radiation with the THz-STM, the temporal profile of the THz near-field waveform can be sampled [23, 24, 26, 48–51]. THz pulses couple well to the STM junction, which form the THz-NF that would drive the generation of an ultrafast electronic signals measured in THz-STM.

The exact mechanism by which THz radiation forms in the near-field by coupling to the probe tip of the STM is not completely understood. Principles of nano-plasmonics, the study of light and matter interactions in the nano-scale, used to characterize Scanning near-field optical microscopy (SNOM) techniques, can be applied to the THz-STM. Experiments and simulations show that sending THz radiation to an elongated probe tip (i.e. tapered wire) excites surface plasmon polaritons (SPPs), which are electromagnetic surface waves that travel along the wire surface with minimal loss and dispersion [52–55]. Measuring the THz near-field electric-field waveform at the tip apex reveals frequency dependence when comparing the spectrum of the near-

field to the incident THz field due to antenna-like coupling [43, 44, 56, 57]. For metal tip wires, THz electromagnetic fields are enhanced due to the localization of SPPs at the tip apex [55, 58–62]. The local field enhancement in the probing region can influence various interesting phenomena [63] such as field-driven photo-emission [64–71], non-linear current densities [64, 72], localized ionization [73, 74], and the generation of plasmonic hot spots [72, 75–79]. However, more research is needed to better understand these near-field effects.

The contents presented in this thesis aim to contribute to the development of THz-STM by demonstrating a few approaches to simulate and model THz-STM experiments. Numerical and analytical modeling approaches for THz-STM have been reported [80, 81]. Here, we begin with simulations for a macroscopic model of the THz-STM, zoom into the near-field regime and eventually determine the tunneling current as illustrated in Fig. 1.1. Overall, the THz near-field is formed when incident THz pulses couple to the STM structure and undergo a field enhancement transformation. The THz near-field is converted to a transient bias voltage between the tip apex and sample, which drives THz-pulse-induced electron tunneling currents on the picosecond timescale. Due to the sign changes of the pulse's electric field amplitude, the tunneling current direction can alternate. Measurements in the form of electrical signals must arise primarily from near-field activities. Though it cannot be measured directly, finding out how the near-field profile in the STM junction compares with the THz field of the incident pulse will help determine optimal coupling conditions. An extensive amount of simulations, numerical and analytical modeling are required to better understand the electromagnetic coupling to the STM. Accomplishment of such feats benefits the evolution of THz-STM.

This work lays out the process to simulate and model THz coupling and THz-driven tunneling in THz-STM experiments. The process should be described in a sequential manner. That is to begin with a known electric field pulse radiated by a THz emitter, determining the transient bias to the STM junction, then finally calcu-
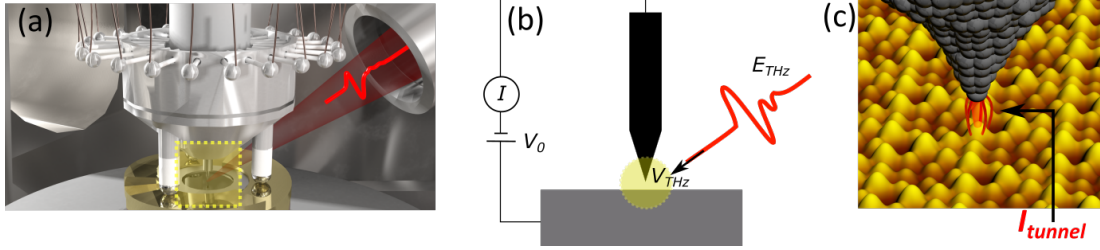
Figure 1.1: (a) 3D drawing of the THz-STM experiment. (b) Modeling schematic for a THz pulse coupling to the tip. (c) The tunneling current is driven by the THz near-field. The highlighted yellow region in (a) is the matter of interest presented in (b), and the same applies for (b) to (c).

lating or fitting the tunneling current. The foundations of THz-STM are described in Chapters 2 and 3. In Chapter 4, the development of a Finite Element Method model of the THz-STM in COMSOL Multiphysics is outlined. Results for simulating the electromagnetic scenario of THz pulses coupling to the STM geometry as well as variants are highlighted and discussed.

An equivalent resistor-inductor-capacitor (RLC) circuit model has been employed in previous works [56, 68] to calculate the THz near-field formed at the end of the tip. The RLC circuit only models the antenna coupling aspects, however an expanded circuit model must be implemented to predict the transient bias inside the STM junction. Chapter 5 goes through analytical models to determine the THz near-field, then reports the methodology and results of using a discrete-dipole model to simulate the THz near-field. Chapter 6 outlines the methodology and results of employing a circuit model to simulate the THz near-field. The circuit model is expanded by implementing transmission lines to simulate pulse propagation. Chapter 7 focuses in on the STM junction region of the circuit by introducing a non-linear conducting element. Interface states and interacting electrons are discussed for the metal-to-metal junction. Modeling a junction consisting of a metal tip and semiconducting sample interface requires additional tunneling parameters due to space-charge effects, penetration of the near-field into the bulk and the Schottky barrier. STM on photo-excited semiconductor materials require additional contributions to the tunnel current

signal due to photo-excitation of the surface creating a surface photo-voltage (SPV). Finally, all of the simulations and models are combined to reproduce fittings to THz-pulse like transients sampled by the THz-STM in Chapter 8.

Chapter 2

Terahertz pulse generation, propagation and detection in the far-field and near-field

In this chapter, schemes of generation, detection, propagation, and focusing of THz pulses are explored. Furthermore, mechanisms of terahertz antennas, guiding systems, and waveguides in tandem with detectors are discussed and modeled. The ability to generate and detect terahertz radiation using tabletop setups is well established [40, 82, 83]. Guiding optics and waveguides lead to dispersion and attenuation effects on propagating THz pulses. The models presented here describe the THz pulse waveforms emitted by THz sources, pulse distortions during propagation, and the signal measured upon detection. Scanning near-field optical microscopy techniques can be expanded in the THz regime, where both high spatial and ultrafast temporal resolution can be obtained. There are three regimes in which the anatomy of the THz pulse needs to be explored, i) the near-field of THz emission around the emitter, ii) the far-field THz emission away from the emitter, and iii) the field generated inside the receiver device upon detection.

2.1 THz Emission

Single cycle THz pulses (e.g. in Fig. 2.1) have a duration of 100 fs to a few ps in which the frequency spectra contains amplitudes ranging from about 0.1 THz to 10

THz. Electromagnetic radiation in the THz regime can be generated using antenna structures similar to radio to microwave frequency antennas, with antenna dimensions on the micron scale [84–87]. An antenna is usually made up of metallic electrodes embedded on a semiconducting material with a band gap that can be photo-excited. Emission of THz pulses from antenna structures is possible when a bias is applied between the electrodes [88, 89]. A THz pulse is depicted in Fig. 2.1, whose waveform resembling a sinusoidal function consists of a main peak that spans a picosecond duration and a spectrum in the terahertz broadband frequency range. Such THz pulses can be generated by a photoconductive antenna with a structure as illustrated in Fig. 2.2. When an ultrafast laser interacts with a photoconducting material, a d.c. polarization is generated, which acts as a source for the THz pulses. The d.c. polarization can have its origin in either a simple flow of free carriers in a photo-conductive gap for semiconductors or from nonlinear optical processes in crystals. The acceleration of photoexcited charges between the antenna electrodes generates a THz pulse. The photo-excitation of carriers, which have excitation lifetimes in the 100 fs to picoseconds range, eventually all recombine thus terminating the THz pulse emission.

2.1.1   THz Antennas

The physical properties of semiconductors allow them to be used in various ways to generate THz fields emitted from their surfaces. Modern integrated circuit techniques have now made possible the precise fabrication of micron-sized dipole structures. When they are driven with sub-picosecond photo-excitation, they can radiate well into the THz regime, as schematically depicted in Fig. 2.2. Photoconductive (PC) antennas have been optimized for high power and directivity that enables terahertz pulse propagation to a target, or detector. Several photoconductive materials have been tested to build antennas: low-temperature grown gallium arsenide (LT-GaAs), semi-insulating gallium arsenide (SI-GaAs), radiation damaged silicon-on-sapphire
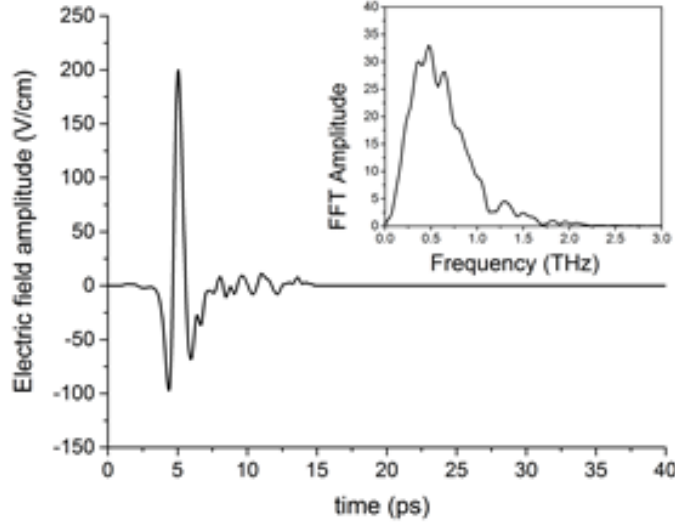
Figure 2.1: Example of a THz pulse generated by a photoconductive antenna that has a main peak width of about 1 ps, oscillations spanning about a 10 ps duration and a broadband frequency range from 0 to 2 THz as shown in the inset.

(RD-SOS), chromium-doped gallium arsenide (Cr-GaAs), indium phosphide (InP), and amorphous silicon (a-Si) [90, 91]. LT-GaAs and RD-SOS are most commonly in use, due to the carrier lifetimes in the sub-picosecond range. For semiconductors at room temperature, the effective carrier mobility ranges from 1000–10000 $\text{cm}^2/\text{V·s}$, in which the carrier transport is mainly dominated by electrons. The mobility ranges from 10–1000 $\text{cm}^2/\text{V·s}$ for hole carriers.[1]

THz emission occurs in semiconductors quite efficiently. When a bias is applied on the electrodes embedded on a semiconductor and the gap region is excited by femtosecond laser pulses, the antenna's conductivity is transiently altered, and THz radiation is generated, as shown in Fig. 2.2. An electron–hole plasma in the PC gap of the emitter is created by the laser pulse excitation. The tight laser focus restricts the spot size of the electron-hole pairs to be smaller than 10 μm, which is much smaller than the wavelength of the radiation. The electrical bias creates an electric field applied on the excited charge carriers to yield a transport photo-current in the material. The photo-generated carriers are accelerated under an electric field and

9

rapidly change in their population density [92].
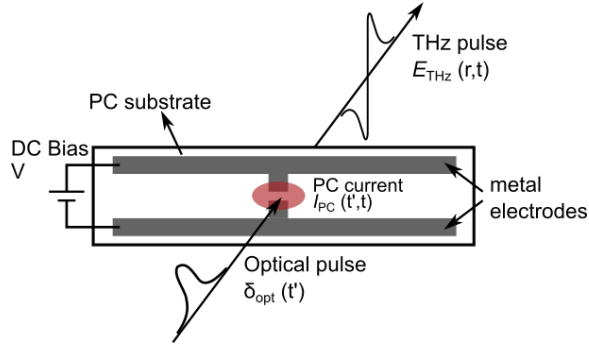
Figure 2.2: Schematic diagram of THz pulse emission with a photoconductive antenna excited by a femtosecond optical laser pulse. The optical pulse creates a photocurrent in the DC-biased gap between the electrodes, which emits THz radiation like a dipole source. (Adapted from [94])

This source is modeled as an electric point dipole located at the dielectric interface between the substrate and the air. In the far-field, the radiated electric field is directly proportional to the first temporal derivative of the photocurrent, $i(t)$, flows through the gap of the emitting antenna. The field amplitude $E(r,t)$ of an antenna with length l_e, observed at long-range (i.e. far-field) observing distance r is given by,

$$E(r,t) = \frac{l_e}{4\pi\epsilon c^2 r} \frac{di(t)}{dt} \sin(\theta),$$ (2.1)

where, θ is the angle between the direction of the photocurrent and the propagation direction (i.e. radial direction in polar coordiates). The waveform of the emitted pulse in the far-field can be predicted based on the current waveform of generation by the antenna. The current depends on the material properties, antenna geometry, biasing conditions and the excitation field. The photocurrent is determined by the profile of the optical excitation pulse and the electronic properties of the carriers in the gap region of the antenna. From equation 2.1, the predicted THz waveform is the derivative of the PC current. Fig. 2.3(a) shows a typical photocurrent current profile and the corresponding THz emission waveform in (b).

---

[1]The mobilities, μ_e/μ_h, for a few semiconductors at room temperature in cm^2/(V·s): Si 1300/500; Ge 3900/1900; GaAs 8800/400; InAs 33,000/460 [93].

Antennas may have various simple structures, such as the "H" dipole, bow-tie and strip-line shape [86, 95]. The dipole antenna should produce a THz waveform as shown in Fig. 2.3(b). Some other complex antenna designs consist of spiral and log-periodic structures [96]. The waveform shape of the emitted THz pulse depends on the antenna design. The waveform profile show geometric signatures, which can be modeled using analytical and numerical methods [86, 95, 97]. The PC current couples to the impedance and transmission line properties of the antenna, this results in the emission of the THz waveform, with resonant features.
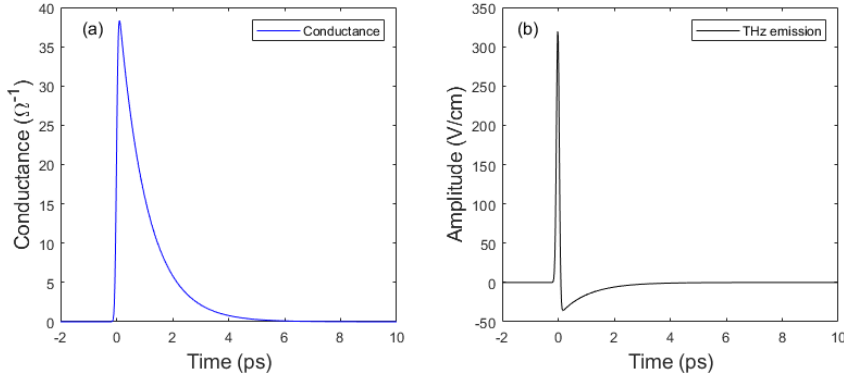
Figure 2.3: (a) Calculated time-dependent conductance function for a THz dipole antenna, which is proportional to the photocurrent. (b) Calculated THz waveform emitted from the antenna due to the generation of the photocurrent. The antenna has a $5 \times 10\,\mu\mathrm{m}^2$ gap area, mobility $\mu = 1000\,\mathrm{cm}^2/\mathrm{V}\cdot\mathrm{s}$, and carrier lifetime $\tau_c = 1$ ps. The optical excitation is a 475 THz center frequency laser pulse with pulse duration $\tau_l = 0.100$ ps, with a 1 W power and 100 MHz rep-rate.

2.1.2 Large-aperture THz antennas

Large-aperture PC antennas can be used for generating high-power THz pulses. The principle mechanism of THz generation is similar to that in a dipole antenna. The radiation source is the current of photoexcited carriers induced by a bias field. For large-aperture antennas, the size of the optically excited area between the electrodes is much greater than the radiated wavelength. The large excitation area enables large-aperture emitters to produce high-power THz pulses. However, high DC bias voltage and amplified femtosecond laser pulses for the excitation are required. Similarly,

saturation properties resulting from carrier-screening effects are also observed in large aperture PC sources [88]. These antennas are capable of producing pulses that are nearly unipolar, as later modeled.

2.2   THz Detection

THz antennas are additionally used as detectors, the physical process is similar to the generation in the emission of the antenna, except that the biasing field is the incoming THz field to be detected. In the absence of a D.C. bias field, photo-carriers are injected by the optical pump pulse in the photo-conductive gap, then the incident THz electric field induces a transient transport photo-current in the gap. The induced photocurrent is proportional to the field amplitude of the incident THz radiation focused on the PC gap. The THz pulse shape is mapped out temporally by measuring the current variation as a function of the time delay, between the THz pulse and the optical excitation pulse. The photo-current density in the receiving antenna is given by the convolution product of the temporal shapes of the optical pump pulse and of impulse response of the detector, respectively. The response characteristics of the detector will considerably reshape the waveform of the incident THz pulse coming from the emitter [97]. In order to get a detection close to the original incident THz pulse, a semiconductor with a fast carrier trapping time ($\tau_c \lesssim 0.5$ ps) is required.

The photo-conductive detector has a time-dependent conductivity response, $g(t)$, driven by the probe laser. The final part of detection process occurs as the incident THz field, $E(t)$, is sampled by the conductivity response. The resultant photo-current as a function of the delay, τ, between the pump laser and the incident THz field, is the experimentally measured quantity in a THz detector. The photo-current excited by one pulse cycle of the incident THz electric field is given by

$$j(\tau) = \frac{1}{T} \int_0^T E(t)\, g(t-\tau)\, dt, \tag{2.2}$$

where T is the repetition time for the laser (note, $1/T$ is equivalent to the repetition

rate, f_{rep}), $g(t)$ is related to the material's conductivity and structure of the detector material, which typically has an impulse temporal profile. Eq. 2.2 is analogous to the $J = \sigma E$ current response for a material with constant conductivity. The response function is usually associated with the transient photo-excited carrier density, $n(t)$. If the carrier lifetime is comparable to the THz pulse duration, the photocurrent response is a convolution between $E_{\text{THz}}(t)$ and the time dependent carrier density after photoexcitation $n(t - \tau)$. Eq. 2.2 for the current density can be expressed as

$$j(t, \tau) = \mu e \int E_{\text{THz}}(t) n(t - \tau) \, dt, \qquad (2.3)$$

where μ is the carrier mobility and e is the elementary charge. The ideal detector should be able to provide exact information about the incident waveform. Different factors influence and limit the detection capabilities, results in reshaping of the signal, owing to the finite bandwidth and sensitivity of the detector. Two important aspects of signal detection are the geometry, where the finite detection area influences the speed and sensitivity; and the carrier dynamics of the material since the detection is based on electron flow in the PC material. Modeling detection becomes more of a challenge if the incident electric field amplitude varies over the spatial extent of the antenna.
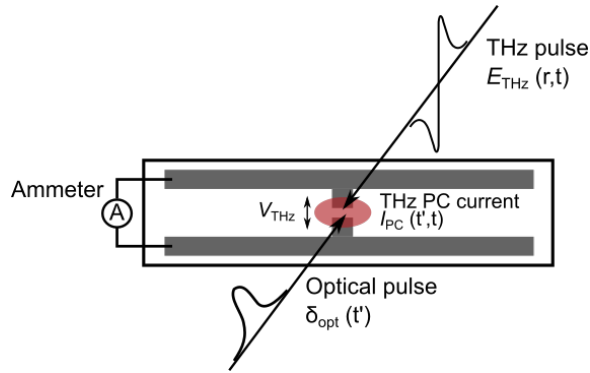
Figure 2.4: Schematic for THz detection with a photoconductive antenna. Photo-carriers are excited in the antenna gap with an optical pulse, however the driving field that forms the bias in the gap is now from the incident THz pulse. The detected signal is a transient photocurrent modulated by the incident THz, which can be measured with an ammeter connected to the device. (Adapted from [94].)

13

2.2.1 Electro-Optic Detection

The THz detection method described previously is also known as photoconductive sampling which requires the photo-excitation of semiconductor material to detect the THz pulse. Non-linear crystals having a non-zero second-order electric susceptibility can be used to sample THz pulse waveforms. A high intensity optical pulse propagating through a transparent medium can excite non-linear processes under specific phase-matching conditions. A non-centrosymmetric crystal has a second-order electric susceptibility, $\chi^{(2)}(\omega)$, which can exhibit a linear electro-optic (EO) effect. The process is known as the Pockel's effect, which is a reciprocal process to optical rectification [98]. Examples of non-linear crystals are ZnTe, LiNbO$_3$ and GaP. Installation of a non-linear crystal requires that it is orientated along a crystallographic direction that maximizes the strength of the EO effect. As the THz pulse and optical pulse co-propagate through the crystal, the electric field of the THz pulse induces a birefringence in the medium that modifies the polarization state of the optical pulse. Chromatic dispersion occurs as the THz pulse propagate through the medium causing distortion to the THz waveform.

The THz pulse shown in Fig. 2.1 is acquired using EO detection using a ZnTe crystal. ZnTe has a large EO coefficient, $\chi^{(2)} = r_{41} = 4\,\text{pm/V}$ as a function of mixed frequencies: optical wavelength of 812 nm and frequency of 1.7 THz. For ZnTe, the EO effect is optimized when both the optical beam and THz pulse are incident onto the crystal along the [110] direction and the polarization of both pulses is parallel to the [1$\bar{1}$0] direction. The detected THz pulse electric field, $E_{\text{THz}}(\tau)$, is given by [94]

$$E_{\text{THz}}(\tau) = \frac{\lambda}{2\pi n_0^3 r_{41} L} \Delta\phi(\tau) \tag{2.4}$$

where $\lambda = 800$ nm is the frequency of the optical sampling pulse, $n_0 = 2.853$ is the refractive index of ZnTe at 800 nm, and $\Delta\phi(\tau)$ is the differential phase retardation that the sampling pulse experiences as it propagates a distance, L, through the crystal. After the sampling pulse has passed through the EO crystal, a quarter-wave-plate and

a Wollaston prism are used to separate the x and y components of its polarization into a pair of balanced photodiode detectors that are connected to a differential amplifier. The differential phase, $\Delta\phi(\tau)$, is given by

$$\Delta\phi = \sin^{-1}\left(\frac{I_y - I_x}{I_y + I_x}\right) \simeq \frac{I_y - I_x}{I_y + I_x} \qquad (2.5)$$

where I_x and I_y are the intensities read by each of the balanced photodiode detectors. There is no THz electric field detected when the detectors are balanced (i.e. $I_x = I_y$). There are reflection losses at the interface of the crystal which has to be considered when calculating the electric field using Eq. 2.4. The refractive index of ZnTe is 3.2 for frequencies around 1 THz at normal incidence, corresponding to an amplitude transmission factor of 0.48 [94].

2.3   Modeling THz emission and detection

THz radiation results from the ultrafast change of the photocurrent, which may arise from two processes: acceleration of photoexcited carriers under an electric field and a rapid change of the carrier density [92]. Models can be prescribed to predict the shape of the THz waveform emitted by a simple THz emitter. The lifetime of the carriers is mainly determined by their trapping time, τ_c, which is the amount of time for carriers to fall from the free state into to mid-gap states. The free-carrier trapping time in mid-gap states is typically much shorter than the recombination time between electrons and holes. Free carriers can screen the electric field, which recovers after electrons and holes recombine over a duration longer than the time scale of the THz pulse. Overall, the recovery process has little effects on the carrier dynamics and THz radiation. The simple Drude-Lorentz model is modified to account for ultrafast changes in the bias field owing to screening effects. From experimental and modeling research, it is evident that the screening process is the key factor in determining the properties of radiated THz pulses [95, 99].

To model the carrier transport, the simple 1D Drude model is used which considers

the interaction between electrons and holes, trapping of carriers in mid-gap states, scattering of carriers and screening effects. The current density is related to the velocity of the free carriers in the THz antenna as

$$j = env_e + epv_h, \tag{2.6}$$

where n is the density of electrons, p is the hole density, v_e is the electron velocity averaged over the carrier distribution and v_h is the hole velocity. Holes, being much slower than electrons, contribute a minor current, so the second term in Eq. 2.6 is often dropped. When free-carriers are created, the population of free electrons and free holes are the same, hence n_f denotes the free carrier density for the model presented in this section [92, 99]. The time dependence of the carrier density where τ_c is the trapping time and $G(t)$ describes the generation of free carriers by the laser pulse is given by

$$\frac{dn_f}{dt} = -\frac{n_f}{\tau_c} + G(t). \tag{2.7}$$

The time dependence of the average velocity is in the Drude model is given by

$$\frac{dv(t)}{dt} = -\frac{v}{\tau_s} + \frac{e}{m^*}E_{\text{loc}}, \tag{2.8}$$

where τ_s is the momentum relaxation time and m^* is the effective mass. The local electric field at position of the carriers, E_{loc} is given by

$$E_{\text{loc}} = E_{\text{bias}} - \frac{P_{sc}}{\eta\epsilon}, \tag{2.9}$$

where η is the geometric factor (typically equal to 3 for an isotropic dielectric material [99]) and ϵ is the dielectric constant of the photoconductive material. The time dependence of the space-charge polarization, P_{sc}, can be represented by

$$\frac{dP_{sc}}{dt} = -\frac{P_{sc}}{\tau_r} + j(t) = -\frac{P_{sc}}{\tau_r} + n_f ev, \tag{2.10}$$

where τ_r is the recombination lifetime. A second order differential equation can be obtained for the carrier velocity by taking the time derivative of Eq. 2.8 and

16

substituting the terms of Eqs. 2.6, 2.9 and 2.10 to yield the following:

$$\frac{d^2v}{dt^2} + \frac{1}{\tau_s}\frac{dv}{dt} + \frac{\omega_p^2 v}{\eta} = -\frac{eP_{sc}}{m^*\eta\epsilon\tau_r},$$

(2.11)

where $\omega_p^2 = n_f e^2/m^*\epsilon$ is the plasma frequency. The radiated electric field is proportional to the carrier acceleration, dv/dt, accordingly. By solving the coupled equations together, this gives full information about the radiated THz pulse and the dynamics of the local field [99]. The Drude model is expected to work well for the THz emitter. Typical densities are 10^{16} to 10^{18} cm^{-3} where carrier recombination works to restore thermal equilibrium.

Assuming carrier transport is one dimensional, functions can be introduced to calculate the THz electric field emitted by an antenna. The dipole moment, p, on the antenna of length w_0 and transport photocurrent, $I_{PC}(t)$, are related according to [94]

$$\frac{dp}{dt} = \int_{-w_0/2}^{w_0/2} I_{PC}\left(z', t\right) dz' = w_0 I_{PC}(t).$$

(2.12)

The time-dependent photocurrent is expressed as the convolution of the optical pulse envelope, $P_{opt}(t)$, and the impulse response of the photocurrent

$$I_{PC}(t) = \int P_{opt}\left(t - t'\right)\left[en(t')v(t')\right] dt'.$$

(2.13)

$P_{opt}(t)$ is the intensity profile of the optical excitation pulse which has a Gaussian shape. $G(t)$ is the Dirac-delta function $\delta(t)$ in Eq. 2.7, which resembles an impulse optical excitation, then the average velocity has the form:

$$v(t) = \begin{cases} \mu_e E_{\text{mol}}\left[1 - e^{-t/\tau_s}\right], & \text{for } t > 0 \\ 0, & \text{for } t < 0, \end{cases}$$

(2.14)

where the electron mobility, equated as $\mu_e = e\tau_s/m^*$. The carrier density is equal to

$$n_c(t) = \begin{cases} e^{-t/\tau_c}, & \text{for } t > 0 \\ 0, & \text{for } t < 0. \end{cases}$$

(2.15)

The dynamics of the screening field from the accelerated charge carriers become a crucial factor to account for the characteristics of the THz pulses from a PC emitter

when the carrier density is high enough to satisfy $\omega_p \tau_s > 0$. By applying the carrier dynamics model the photo-current conductance is calculated in Fig. 2.3(a). The antenna has a $5 \times 10\,\mu m^2$ gap area, mobility $\mu = 1000\,cm^2/V \cdot s$, and carrier lifetime $\tau_c = 1\,ps$. The optical excitation is a 475 THz center frequency laser pulse with pulse duration $\tau_l = 0.100\,ps$, with a 1 W power and 100 MHz rep-rate. The conductance function generally consists of a quick rise-time to the peak, then followed by a decay. The bias field is constant, hence the current is directly proportional to the conductance. The emitted THz pulse results from the calculated PC is shown in Fig. 2.3(b) by taking the derivative.

The emitted THz field, as shown in 2.5(a), is inserted into the model as the local electric field in Eq. 2.9 to generate the THz detection waveform in Fig. 2.5(b). The detected THz pulse is plotted as a function of the time delay between the optical pulse used to excite the detector and the incident THz pulse arriving from the emitter. It was assumed that the same conductance properties of the THz emitter and the same optical excitation pulse are exactly the same for the THz detector. If the detector's conductance is assumed to be the delta function, according to Eq. 2.2, the detected signal should be proportional to the incident THz pulse. A realistic THz pulse is expected to show amplitude ringing features after the main peak as shown in Fig. 2.1. Such features are due to substrate and electrode reflections. A geometric time-dependent response factor $\zeta(t')$ may be incorporated to reproduce a stretched transient due to echoes in the detector antenna [86, 97]. The model presented in this section only accounts for the simple case where the PC is confined in the excitation gap area.

2.4   THz pulse propagation

THz pulses must propagate through media to reach their target, thereby, the dispersion behaviour in free-space and through materials should be known. Table-top setups involve optical techniques used to collect, collimate, and focus the THz radia-
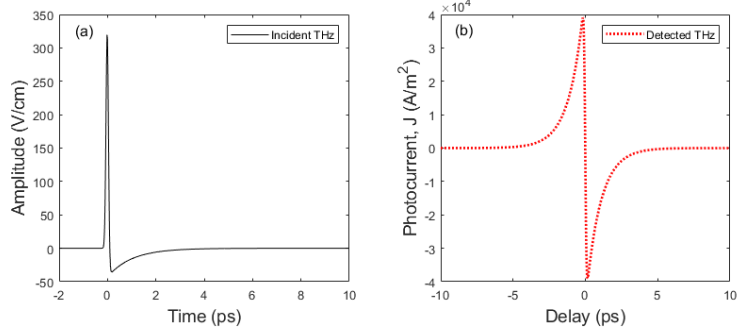
Figure 2.5: (a) Profile of the incident THz pulse incident to the detector. (b) Calculated THz photocurrent in the detector corresponding to the measured THz signal. The calculation assumes the detector is a dipole antenna.

tion emitted by a dipole antenna. Here the spatial dependence of THz emission and propagation through optics components are discussed.

2.4.1 Free-space THz propagation

In free space, the THz antenna can be approximated as a point dipole or a discretized collection of them. If the source current $\mathbf{j}$ on the antenna is known, the dipole moment $\mathbf{p}$ is simply the time integral:

$$\mathbf{p}(t) \propto \int_{-\infty}^{t} \mathbf{j}(t')dt' \tag{2.16}$$

The full form of Eq. 2.1 for the radiated electric field components when considering all components of the dipole moment is given by [56, 61]

$$\mathbf{E}(\mathbf{r},t) = \frac{1}{4\pi\epsilon_0}\left[\hat{\theta}\sin\theta\left(\frac{\mathbf{p}}{r^3} + \frac{\dot{\mathbf{p}}}{c_0 r^2} + \frac{\ddot{\mathbf{p}}}{c_0^2 r}\right) + \hat{\mathbf{r}}\cos\theta\left(\frac{2\mathbf{p}}{r^3} + \frac{2\dot{\mathbf{p}}}{c_0 r^2}\right)\right] \tag{2.17}$$

where c_0 is the speed of light in vacuum, ϵ_0 is the vacuum dielectric permittivity. The electric field radiated by a dipole is the temporal superposition summation of dipole terms and its time derivatives. From Eq. 2.17, two terms can be extracted. In the near-field of the dipole, the electric field is

$$\mathbf{E_{NF}} = \frac{1}{4\pi\epsilon_0}\frac{2\mathbf{p}}{r^3}. \tag{2.18}$$

19
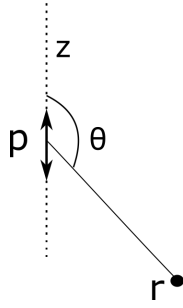
Figure 2.6: The polar-coordinate system used to determine the field component directions radiated by a point-dipole placed at the origin.

In the far-field, the electric field is proportional to the second time derivative of the dipole moment given by

$$\mathbf{E_{FF}} = \frac{1}{4\pi\epsilon_0 c_0^2} \frac{2\mathbf{\ddot{p}}}{r},\qquad(2.19)$$

which is equivalent to Eq. 2.1.

2.4.2 Guiding optics

The three regimes to describe the interaction of light (with wavelength λ) of objects (with dimension scale a) are the components of, i) $\lambda \gg a$, describing small particle scattering, which can be explained by Rayleigh theory, ii) $\lambda \approx a$, known as the mid-wavelength (resonant) scattering regime, which can be approximated by Mie theory [100], and iii) $\lambda \ll a$, the geometric (Ray) optics limit, in which the laws of reflection, refraction and dispersion can be applied.

The radiation pattern of a PC emitter is more complicated than the simple point dipole. The size of the source is much smaller than the THz wavelength, which makes the radiation divergent. In sampling and interferometry experiments, it requires propagating the beam from the emitter through optical paths that are much larger compared with the antenna size. The spatial dependence of the field distribution can be calculated by applying equations for basic optical components, such as lenses or mirrors. However, in the THz regime, the dimension of components ranging from several microns to millimeters is enough to steer away from ray optics and use

formalism in the second regime of mid-wavelength scattering. Components for focusing and guiding pulses can severely alter the pulse shape, since the differential loss from diffraction for high- and low-frequency components are magnified [101–103]. The Fresnel-Kirchoff diffraction integral can be applied to predict the spatial dependence of the electric field radiated by an emitter coupled to a lens [101].

In the far-field, the radiation pattern of the beam appears as a Gaussian-beam profile, the radiated THz field is largest along the optical axis. In detail, there are significant interference fringes that appear at larger angles, that result from the diffraction of the radiation presented by the substrate lens [101]. Low-frequency components that may have been present at the transmitter are lost after the pulse propagates some distance. The power spectrum of the THz pulse on-axis for pulses sampled at different distance from the emitter reveals this aspect. The relation found for the loss of intensity on-axis due to diffraction varies inversely with the square of the frequency. As a result, differential diffraction loss of wide-ranging frequency components can cause severe temporal distortions. Additionally, the phase shift varies with frequency [104].

Gaussian beam optics

Focusing lenses are employed to focus a beam at a target located at a focal distance away. For a fundamental laser beam propagating in the z-axis with a linearly polarized Gaussian field distribution in the beam waist [61].

$$\mathbf{E}(x,y,0) = \mathbf{E_0}\mathrm{e}^{-\frac{x^2+y^2}{w_0^2}} \tag{2.20}$$

Where, $\mathbf{E_0}$ is a maximum amplitude vector with only x and y components, and w_0 is the beam waist radius for the field to reach a $1/e$ amplitude. Thereby, $z = 0$ is located at the beam waist minimum (see illustration in Fig. 2.7). To get the full expression for the Gaussian beam propagation, the Fourier spectrum is calculated in

terms of $k = (k_x, k_y, k_z)$. Where, k_z is the dominating wavevector component,

$$k_z = k\sqrt{1 - \left(k_x^2 + k_y^2\right)/k^2} \approx k - \frac{\left(k_x^2 + k_y^2\right)}{2k} \tag{2.21}$$

The expansion above is known as the paraxial approximation which allows for integration of Fourier integrals to be facilitated. After integrating Eq. 2.20 for the spectrum at $z = 0$, the propagating angular spectrum is obtained using the relation

$$\hat{\mathbf{E}}(k_x, k_y; z) = \hat{\mathbf{E}}(k_x, k_y; 0)\mathrm{e}^{\pm \mathrm{i}k_z z}. \tag{2.22}$$

After another Gaussian integration with respect to k_x and k_y the expression for the Gaussian beam is

$$\mathbf{E}(x, y, z) = \frac{\mathbf{E_0}\mathrm{e}^{\mathrm{i}kz}}{1 + 2\mathrm{i}z/kw_0^2}\mathrm{e}^{-\frac{x^2 + y^2}{w_0^2}\frac{1}{1 + 2\mathrm{i}z/kw_0^2}}. \tag{2.23}$$

The equation above can be reparameterized as $\rho^2 = x^2 + y^2$ and a scaling parameter,

$$z_0 = \frac{kw_0^2}{2} \tag{2.24}$$

which then rewrites it as,

$$\mathbf{E}(\rho, z) = \mathbf{E_0}\frac{w_0}{w(z)}\mathrm{e}^{-\frac{\rho^2}{w(z)^2}}\mathrm{e}^{\mathrm{i}\left[kz - \eta(z) + k\rho^2/2R(z)\right]} \tag{2.25}$$

Where, parameters for the propagating beam radius $w(z)$, wavefront radius $R(z)$ and phase correction $\eta(z)$ are as follows,

$$w(z) = w_0\sqrt{1 + z^2/z_0^2} \tag{2.26}$$

$$R(z) = z(1 + z_0^2/z^2) \tag{2.27}$$

$$\eta(z) = \arctan(z/z_0) \tag{2.28}$$

From the diagram in Fig. 2.7 the hyperbolic wave-fronts enclose an angle of

$$\theta = \frac{2}{kw_0}, \tag{2.29}$$

which is indicated in Fig. 2.7 between the asymptote and the z-axis. Even if a beam has a known profile, propagation effects will cause distortion in the wave-front and

phase over a range. Along the propagation axis ($\rho = 0$), from Eq. 2.26, the beam undergoes a gradual 180° phase shift from $z \to -\infty$ to $z \to +\infty$, which is known as the Gouy phase shift.

Note that the paraxial approximation introduces more error when the focus is tighter or when the beam waist radius becomes comparable with the wavelength λ. Furthermore, it does not fulfill Maxwell's equations. A more accurate description can be achieved by introducing higher-order propagation modes [61].
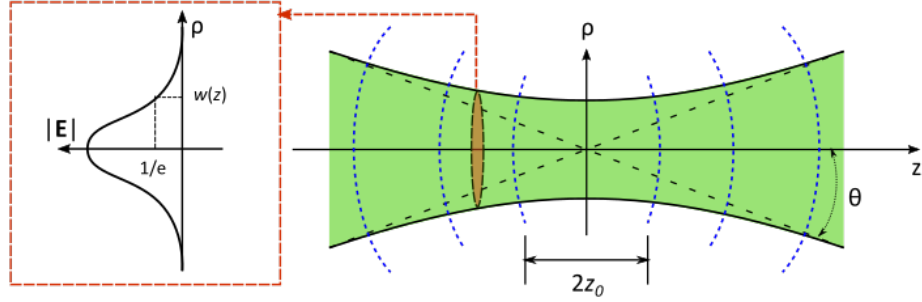
Figure 2.7: Illustration of a Gaussian beam propagating along the z-axis with field distribution in the transverse plane (x,y). The plane-wave fronts where the field is constant are hyperboloids along the z-axis. Adapted from [61].

When a window or aperture with radius a emits a beam with wavelength λ, the Rayleigh range, which describes the beam divergence, is given by

$$z_R = \frac{\pi a^2}{\lambda}.$$ (2.30)

The equation is equivalent to the form in Eq. 2.24. Note that it is the distance of propagation where the beam radius increases from the emitter face to $\sqrt{2}a$, about 1.4 times.

The beam waist diameter, $2w_0$, in terms of input beam parameters is given as

$$2w_0 = \left(\frac{4\lambda}{\pi}\right)\left(\frac{F}{D}\right),$$ (2.31)

23

where F is the focal length of the lens and D is the beam diameter at the lens aperture. The ratio $f\# = F/D$ is known as the photographic f-number of the lens.

2.4.3 Propagation via waveguides

THz pulses can be guided from the emitter to the detector by waveguides. Waveguides can take on several forms such as wires, tubes, dielectric slabs and parallel plates. They are used to propagate the THz pulse radiated by the source at long distances. In addition, it can be used to guide pulses into regions of the experiment that are difficult to reach with optics techniques [52, 105, 106]. For example, a vacuum system may contain a target that cannot be illuminated by the optics setup alone. A solution is to use an external optics system that can focus a pulse into waveguide, which then guides pulses to the target. However distortion and losses often occur in waveguide structures, thus research efforts focus on minimizing them.

Surface plasmon polariton (SPP) modes are formed when a THz beam couples to the waveguide [54, 55, 107, 108]. A coupling feature such as a defect, notch or transmitting device is needed to send a THz waveform into the waveguide due to specific boundary conditions for electromagnetic (EM) modes. Dispersion is one inevitable aspect where pulses become distorted by the waveguide. The observed behavior of a SPP propagating on a wire surface can be understood using Sommerfeld's description of an EM wave propagating along the surface of a cylindrical conductor. This Sommerfeld wire wave is the prominent propagating solution is the axially symmetric TEM wave [107]. Outside the metal, the variation of the radial electric field component is described by a Hankel function of the first kind, $H^{(1)}(\gamma r)$, with γ being the complex propagation constant, r is the radial distance where

$$H^{(1)}(x) \approx -\frac{2i}{\pi x}.$$ (2.32)

Thus, a Sommerfeld wire wave also exhibits $1/r$ decay, within a distance, $r_0 \ll |1/\gamma|$ of the wire surface. The Sommerfeld description can be used to estimate the distance

that the wave extends from the metal surface, for a metal of finite conductivity. The complex constant γ is determined by solving a transcendental equation which results from the boundary conditions at the wire surface. The TEM mode in a coaxial waveguide is radially polarized, and the electric field varies as the inverse of the radial position as

$$E_r = \frac{V}{r\ln\left(\frac{a}{b}\right)}, \tag{2.33}$$

where a and b are the radii of the outer and inner conductors, respectively. Therefore V is a position-independent voltage.

The input and output relationship of the single-mode wave-guide system can be written in the frequency domain as [109]

$$E_{\text{out}}(\omega) = E_{\text{in}}(\omega)TC^2 \exp\left[-j(\beta_z - \beta_0)z\right]\exp\left(-\alpha z/2\right), \tag{2.34}$$

where $E_{\text{out}}(\omega)$ and $E_{\text{in}}(\omega)$ are the frequency spectra of the output and input electric fields, respectively, T is the total transmission coefficient. C is the coupling coefficient at the faces; β_z is the phase constant for the z-axis propagation of the dominant mode in the waveguide, and z is the propagation distance. β_z can be evaluated numerically by determining the dominant waveguide mode characteristic. β_z is experimentally determined using Eq. 2.34, by extracting the phase difference from the ratio of the complex spectra of the output and input pulses. The phase and group velocities can be determined afterwards. The overall coupling which includes reflection from both the entrance and exit faces is expressed as,

$$TC^2 = \frac{4Z_0Z_p(\omega)}{(Z_0 + Z_p(\omega))^2}\left[\int_A (\mathbf{E_{in}} \cdot \mathbf{E_p})dA\right]^2 \tag{2.35}$$

where, $\mathbf{E_{in}}$ and $\mathbf{E_p}$ represent the normalized electric fields of an input Gaussian beam and the dominant waveguide mode, respectively. Z_0 and Z_p correspond to the impedance of free space and the dominant waveguide mode, respectively.

For the general expression in the time domain, the input pulse is expanded into normal modes (i.e. TE$_{mn}$ and TM$_{mn}$; m and n are integer mode descriptors). Each

25

mode has its own waveguide dispersion characteristic and the modes that are allowed to propagate depend on the waveguide geometry. The output signal is a superposition sum of the elementary modes, after they propagate to the end of the waveguide. For a detection of a pulse linearly polarized along the x-axis with a Gaussian profile $E_{in}(x, y)$, the expression of the detected signal in terms of normal modes is given by [53]

$$E_{\text{out}}(\omega, t) = \sum_p A_p X_p t_{\text{out}} \exp\left[i\omega t - \beta_p(\omega)z\right] \exp\left(-\alpha z\right), \qquad (2.36)$$

where the mode overlap integral with the input beam is

$$X_p = \int\int_S \mathbf{E_{tp}} \cdot E_{in}\hat{e}_x dS = \int\int_S E_{p,x} E_{in} dS, \qquad (2.37)$$

and transmission factor t_{out} is,

$$t_{\text{out}} = \frac{2Z_0}{Z_0 + Z_p(\omega)} \qquad (2.38)$$

The integration occurs over the output face S of the waveguide. β_p is the propagation constant corresponding to waveguide mode p, the enumeration index for a TE_{mn} or TM_{mn} modes. If both input and output faces as well as the reflections have to be considered, then the product of X_p and t_{out} is replaced by TC^2 in Eq. 2.35 and calculated for each mode.

Electrical pulses propagate as a guided wave along the transmission line, the electric and magnetic fields are strongly localized at the surface. Fourier analyses of the propagated pulse can be used to characterize the materials. TDS with transmission lines is appropriate for the study of surface excitations and of thin-film substrates and superstrates, as it is possible to obtain long path lengths with small quantities and thicknesses of material [53, 110].

Insights on the modeling of THz waveguide propagation help lead to the development of applications. Some examples of interconnect waveguide technology are THz bandwidth multiplexers, transmitter/receiver lines [108, 111], and integrated interconnect structures with common plates comprising the interconnect layer [109, 112,

113]. Furthermore, studies of THz pulses traveling along tapered waveguides continue to be pursued [114–116]. The ability to focus within the interconnect layer should allow for intense THz pulses to be achieved within the layer and guided wave-based spectroscopy to be performed.

2.5   THz in the near-field

Plasmonics is the study of the electromagnetic radiation coupling to materials. Nano-plasmonics is the field that studies the coupling of light to structures with features on sub-wavelength of optical light (i.e the nano-scale). The diffraction limit is overcome by coupling light to nano-structures or a sharp feature of a larger object such as the apex of a scanning probe tip. The focusing of light at the sharp end of the probe greatly improves the signal contrast due to the field enhancement phenomenon and the spatial confinement of light to the probe's apex dimensions [55, 58, 59]. In order to understand near-field coupling, the key parameters to investigate are the field enhancement factor and its spectroscopic dependence in relation to the materials used and structural configuration of the probe.

2.5.1   Aperture based electromagnetic coupling

When light interacts with materials, it forms electromagnetic modes known as surface plasmons at the interface. SPPs propagate inside or on the interface of a material differently compared to free-space with characteristic propagation constants that are functions of the material property and material geometry. Note that the spatial distribution for the components of electric and magnetic fields may take on several forms depending on the geometry of the configuration. When SPPs are spatially confined, the field is effectively "squeezed" to produce the effect of field enhancement.

The near-field for an aperture setup is established by the transmission of light through a sub-wavelength circular hole in a thin conductive screen forming a localized plasmon [61, 117, 118]. Transmission for an incident light wave with wavelength λ_0

27

through a circular aperture with radius a on a thin perfect conducting screen is given by

$$T \propto \left(\frac{a}{\lambda_0} \right)^4.\tag{2.39}$$

The $T \propto \lambda_0^{-4}$ scaling is consistent with Rayleigh's theory. Surface plasmons are electromagnetic modes formed when light couples to a structure that is generally metallic and have dimensions smaller or comparable to the wavelength. When looking at the transmitted signal through an aperture structure with finite dimensions, it often reveals peaks at particular wavelengths, which cannot be explained by a simple diffraction analysis. The phenomenon can only be explained as transmission mediated by surface plasmons, also known as extraordinary optical transmission of light through sub-wavelength apertures [61, 119–121]. The surface plasmons formed in and around the material is a coupled light-matter system with a unique electromagnetic field profile surrounding the structure. Focusing structures such as apertures have a strong field distribution where the light is channeled. For an array of apertures, light impinging on opaque regions between the apertures can be channeled to the other side via propagating SPPs. The process can be thought as field tunneling mediated via SPPs, which can be further enhanced by strengthening the coupling between the input and exit interfaces [118].

According to Eq. 2.39, it is very difficult for THz to transmit through apertures used in experiments for nanoplasmonic studies. THz would have to be guided into a narrow region as a means by waveguide propagation via SPPs [12, 52, 122, 123]. Microspheres placed in front of subwavelength ($\sim \lambda/50$ and smaller) aperture can amplify the THz transmission since the transmitting THz excites the polarizable sphere and form a dipole where the THz field can be well detected [124, 125]. Furthermore, configurations consisting of an array of nanoslot antennas couple THz quite efficiently [72, 126].

2.5.2   Near-field coupling with a tip probe

In near-field microscopy, the variation of the field on length scales much smaller than the wavelength is studied. Unlike surfaces, a small particle with subwavelength size does not reflect but scatters light. When dealing with a surface larger than the wavelength, each feature along the surface scatters light and interference from all the surface elements produces the reflected field where the differences of all phase components must be considered [119]. The incident THz radiation is scattered by the full geometrical structure of the probe. The main mechanism is scattering, thus important parameters are the polarizability and the susceptibility of a mesoscopic particle/sample. The geometry of the microscopy setup and materials used for the tip and sample, in combination with the nature of the incident radiation, are factors in determining these constitutive parameters. A pure electromagnetic field enhancement effect is one caused by plasmon resonances of rough metal films or particles. An additional enhancement can be caused by charge transfer or bond formation between the sample and the metallic substrate, which can strongly enhance the polarizability [61].

Overall, SNOM is a field where the experiment can truly benefit from advancements on the modeling side [121], but it can be challenging to accurately model the formation of the near-field. There is difficulty understanding how the electromagnetic field is coupled to the probe tip and as well as the additional influence from the structure and constitutive material properties of the sample. In addition, the driving field introduces dynamics on the behavior of excitations in the system being probed, and fitting the measured signals can require a accurate model of the dynamical behavior. Models and numerical studies for the near-field characterization as a function of tip/sample material and geometry have been reported to help understand the measurements of signals in SNOM experiments [58, 60, 62, 127, 128].

A simple way to examine the coupling of radiation to a near-field microscope ge-

ometry is to treat the objects (i.e. tip and sample) as point dipoles. As shown in Fig. 2.8, the entire tip is reduced to the tip apex, represented as a spherical object with radius $\mathbf{a}$ and uniform dielectric constant ϵ_t. The electric dipole moment $\mathbf{p}$ of the sphere induced by a uniform electric field $\mathbf{E_{inc}}$ is

$$\mathbf{p} = 4\pi a^3 \epsilon_0 \left(\frac{\epsilon_t - \epsilon_0}{\epsilon_t + 2\epsilon_0} \right) \mathbf{E_{inc}}. \tag{2.40}$$

The equation can be simplified to the form, $\mathbf{p} = \alpha \mathbf{E_{inc}}$ where

$$\alpha(\omega) = 4\pi a^3 \epsilon_0 \left(\frac{\epsilon_t(\omega) - 1}{\epsilon_t(\omega) + 2} \right), \tag{2.41}$$

is a complex valued polarizability factor for the tip. The scattered field is generally takes form in Eq. 2.17, as well as simplified forms in Eqs. 2.18 and 2.1 when the dipole term is known.

The next step is to consider sample contributions to the near-field where the sample fills the lower half space of $z < 0$ with dielectric value ϵ_s. The tip-sample interaction is approximated by positioning a mirror point dipole inside the sample that can only be polarized indirectly by the tip's field (due to nearfield enhancement), but not directly by the incident field [60], as visualized in Fig. 2.8. The sample dipole is along the same direction as the tip dipole with polarizability β where,

$$\beta(\omega) = \frac{\epsilon_s(\omega) - 1}{\epsilon_s(\omega) + 1} \tag{2.42}$$

is the dielectric surface response of the sample. The phase dependence on α and β is encoded in the complex dielectric functions which vary with frequency. The near-field is a superposition of both the tip apex and image-dipole fields. Solving for the multiple interaction between the tip and sample dipoles yields an effective polarizability for the coupled tip-sample system,

$$\alpha_{\text{eff}} = \frac{\alpha(1 + \beta)}{1 - \alpha\beta / \left(16\pi(a + z)^3 \right)}. \tag{2.43}$$

The effective tip-sample dipole, $\mathbf{p_{eff}} = \alpha_{\text{eff}} \mathbf{E_{inc}}$ can be inserted into Eq. 2.17 to obtain the expression for the scattered field. In an experiment, the scattered field is generally

expressed as,

$$\mathbf{E_{scat}} \propto \alpha_{\text{eff}} \mathbf{E_{inc}}, \tag{2.44}$$

which is measured with reference to the incident field. The resulting amplitude and phase of $\mathbf{E_{scat}}$ is determined by α_{eff}, which is analogous to a response function that transforms $\mathbf{E_{inc}}$. All the internal parameters forming α_{eff} are complex-valued and functions of the optical frequency.
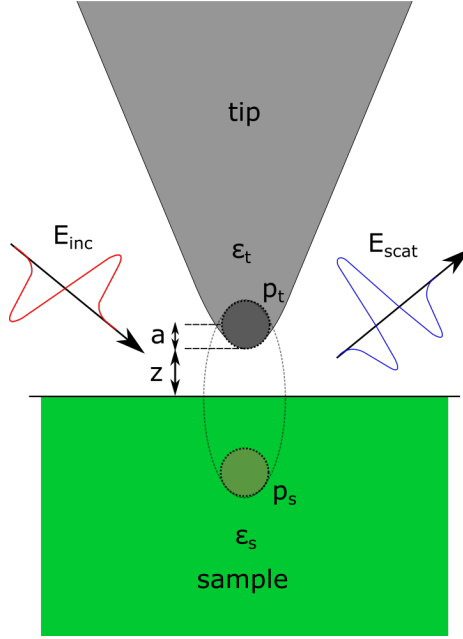
Figure 2.8: Visualization of the model for the near-field tip-sample interaction by the coupled dipole spheres approximation. External radiation, E_{inc}, induces a tip dipole sphere, p_t, located at the tip apex with radius a and distance z from the sample surface. The tip dipole induces a mirror dipole, p_s, in the sample. The scattered radiation, E_{scat}, resulting from tip-sample near-field interaction has phase and amplitude that depends on the local material properties.

According to equations Eqs. 2.41 and 2.43, the signal strength is determined by the tip apex radius, a, and the tip-sample distance z. Usually ϵ_t and z are constant, therefore, any kind of resonances of the sample response in ϵ_s that would cause the signal to vary drastically are of interest. The dipolar formation described above is also known as a tip-induced plasmon, which are localized electromagnetic modes that can be readily excited in the near-field environment [129, 130]. Hence, the

scattering SNOM signal is nano-spectroscopic, which contains information about the local material properties confined to the nano-scale probe dimensions.

Experiments show that the spherical scatterer model needs to be refined as it fails to predict measured field enhancements that are much larger by a few orders of magnitude [45] and does not describe the exact form of the tip-distance dependence [62]. The model does not account for the upper part of the tip, surface plasmons excited on the sample plane, and higher order scattering contributions. A theoretical treatment of a realistic geometry is complicated [120], however some formalism has been developed [127, 131], as they will be applied and noted when doing comparison studies throughout this thesis.

2.5.3 THz Near-field Microscopy

Time-resolved SNOM combines nm scale optical resolution with sub-ps time resolution. Pulsed laser techniques in principle provide the possibility to utilize nonlinear optical techniques like second harmonic generation, hyper-Raman spectroscopy, etc. Such techniques can help to avoid stray light problems in SNOM and can also improve the signal-to-noise ratio. Developments in THz near-field imaging make use of the plasmonics principles discussed. Fig. 2.9 shows a schematic for improving the resolution of THz pulse spectroscopy by implementing a scanning probe. A tip probe should be viewed as a THz receiver. The tip plays two roles, first as a nanodetector and on the other hand, as a nanosource. The interesting aspect is the probed region may be orders of magnitude smaller (10 to 10^5) than the incident THz wavelengths. The field enhancement mechanism makes it possible to resolve THz signals on extremely small length scales, only up to the resolution allowed by the tip sharpness (i.e. radius of the tip).

THz radiation can excite delocalized terahertz surface plasmon polaritons (SPPs) on the surface of a metal with low loss and dispersion (also known as Sommerfeld-Zenneck waves) [53–55]. Field enhancement and subwavelength confinement [58, 59]

occur as THz-SPPs are sharply focused at the tip apex. The THz-SPPs become highly localized at the tip apex, thus charge builds up and create an electromagnetic field density around the apex that is much higher compared to the incident field. The enhanced excitation at the end of the tip enables not only subwavelength resolution, but also the measurement of background-free signals. The tip becomes a "THz lightning-rod" by this charge confinement process.

The description of the near-field in terahertz apertureless scanning near-field optical microscopy (THz-A-SNOM) uses an antenna model, which is slightly different from SNOM as discussed in the previous subsection. An incident THz pulse $\mathbf{E_{THz}}$ excites the dipole moment, p, by driving a local current I_{THz} at the tip apex such that

$$p(t) \propto \int_{-\infty}^{t} I_{\text{THz}}(t')dt'. \tag{2.45}$$

If p is known, then the radiation profile can be determined with Eq. 2.17. In the near-field, the electric field falls off rapidly as $1/r^3$ where r is the distance from the center of the tip apex sphere. I_{THz} is the response to $\mathbf{E_{THz}}$ according to Eq. 2.2. Alternatively, the response function can be modeled as a simple electronic network [43, 44, 56, 57] consisting of a radiation resistance, R, a capacitor C, and an inductance L, all in series. In the frequency domain, the complex transfer function expression for the incident THz electric field inducing a tip current is given by

$$I_{\text{THz}}(\omega) \propto \frac{E_{\text{THz}}}{(R + i\omega L + (i\omega C)^{-1})}. \tag{2.46}$$

In the time domain, a few coupling regimes can be described by setting limits to the circuit parameters. In the low frequency limit, $\omega L \longrightarrow 0$ while R and C are large, $I_{\text{THz}}(t) \propto E_{\text{THz}}(t)/R$. $E_{\text{THz}}(t)$ acts as the driving voltage. The relation using these circuit parameters is Ohmic-like and describes the resistive coupling regime [56]. In the capacitive coupling limit where the R and L parameters are small, which applies to smaller antenna configurations, the capacitive term dominates. The THz current is proportional to $i\omega E_{\text{THz}}(\omega)$, which describes the capacitive coupling regime. Thus

the near-field, which is proportional to the dipole moment, is obtained by the time integral of $E_{\mathrm{THz}}(t)$.

According to Eq. 2.45, the near-field signal is proportional to the time integral of $E_{\mathrm{THz}}(t)$. This is the case where the inverse of ωC term dominates as $\omega \longrightarrow 0$. Lower frequencies are favored by the antenna coupling. As the frequency drops, the current generated by the incident THz radiation increases.

In the THz-A-SNOM picture (now referred to THz-SNOM for simplicity) as shown in Fig. 2.9, THz pulses are incident on a metal tip having an apex of subwavelength dimensions, which is held close to a sample. Near-field information from the region of the tip apex can be extracted by measuring the light that is scattered into the far field [44] or by placing a detector directly below the tip [42, 43, 56]. Both measurement methods measure the THz electric field amplitude instead of intensity. All the mentioned THz-A-SNOM experiments report the measured temporal profile of the near-field signal to be very different from the incident THz pulses. Furthermore, there is a reduction of THz near-field bandwidth compared to the bandwidth of the incident THz pulses. These observations are caused by the antenna properties of the metal tips used in the A-SNOM experiment [24, 43, 56]. This will be analyzed in more detail in chapter 6.

2.5.4 THz Scanning Tunneling Microscopy

The THz-STM is an advanced form of the THz-SNOM, where the scanning probe relies on the tunneling mechanism for its current signal. THz pulses couple to the tip-sample configuration in the STM then activates the tunneling junction, as illustrated in Fig. 2.10. The first demonstration of the THz-STM was carried out in experiments under ambient conditions [4, 33]. The instrument's development has progressed into ultra-high vacuum (UHV) [2, 132]. The main purpose of the THz-optics setup is to direct a THz pulse generated by a photo-conductive switch to the STM tip which sits in a UHV chamber. THz pulses created outside the STM instrument
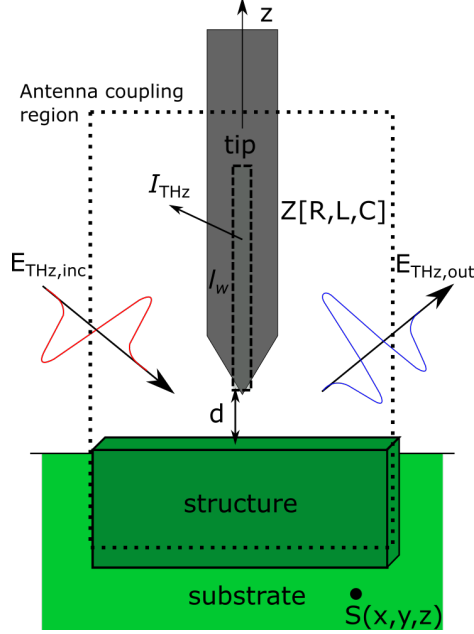
Figure 2.9: Antenna model for the tip wire interacting with the sample in the near-field. Incident THz radiation entering the near-field region experience an impedance (parameterized by R, L, and C) by antenna-coupling with the tip and sample. The incident THz field induces a current in the wire, which creates local THz field that can be measured in the far-field or detected inside the sample as signal, S.

enter into the chamber by way of a custom built window port that is aimed directly at the tip, details of the optics setup can be found in [133]. In a UHV environment, THz-STM has successfully demonstrated the imaging of a Si(111) surface with sub-nanometer resolution, in conjunction with measuring THz-induced tunneling current in subpicosecond time scales [2, 132].

THz-STM is an example of a scanning near-field optical microscope, therefore discussions and models describe the nature of THz-SNOM experiments [44, 56, 131] can be prescribed to this technique. Nano-plasmonic and antenna coupling mechanisms used to describe SNOM are necessary for determining the near-field in THz-STM. The near-field is focused in the region surrounding tip apex. Typically, measured THz signals in THz-SNOM are spatially resolved based on the tip apex dimensions. For example, the tip sharpness, which is quantified by the radius of curvature. Other factors influence the sensitivity for imaging such as sample's geometric and dielectric
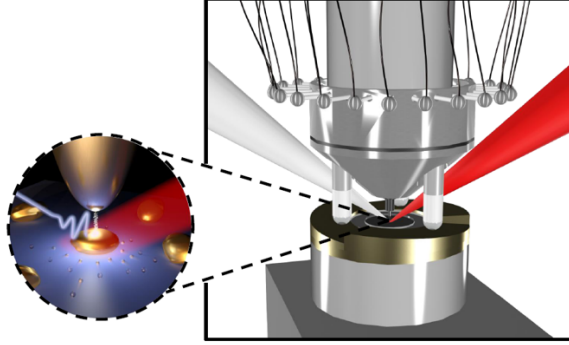
Figure 2.10: Combining THz optics with STM to form an ultrafast microscope. The tunneling current signal measured by the STM is modulated by THz pulses (white beam) produced by an external optical setup. Additionally, optical pulses (red beam) may be sent to the STM to create an optical pump-THz probe instrument. The zoomed in portion depicts the tunneling junction formed by the tip and sample.[1]

properties.

Current measurements obtained from THz-STM is unique in the sense that the THz near-field is driving the quantum mechanical tunneling of the STM junction. The tunneling current is generally expressed as,

$$I \propto \exp\left(-2z\kappa\right) \tag{2.47}$$

where, z is the distance between the tip and sample and κ is coefficient related to the transmission probability, which will later be discussed in depth in Chapter 3. The tip height relative to the sample is extremely sensitive to surface corrugations on the order of Angstrom (Å) length scales. Thus, coupling THz pulses to the STM junction allows for the spatial resolution to be improved towards atomic resolution via quantum tunneling between the tip apex and sample.

2.5.5   Achievements in THz-STM

This section demonstrates the most relevant literature in the THz-STM field to date. THz-STM is still a relatively young field, but more THz research groups around the world are establishing THz-STM research programs [12, 13, 29]. Highlights of time-resolved STM are summarized in Table 2.1, THz scanning near-field microscopy in

---

[1]Graphics used in a conference presentation that featured the THz-STM based on the article [2].

Table 2.2 and THz-STM in Table 2.3. Developments are ongoing in these active research fields to improve their spatial and time resolution capabilities.

Table 2.1: Table summarizing the highlights of STM where dynamical changes of the surface being studied are also tracked temporally. The final two entries are optical pump-probe (OPP) techniques coupled to the STM.

Reference	Topic	Highlights
van Houselt, Zandvliet, 2010 [134]	Review: Time-resolved STM	Summarizes experiments that demonstrate the manipulation of single atoms and tracking the changes in ms time-scales.
Loth et al., 2010 [14]	Electronic voltage-pulse pump-probe STM	Measured spin relaxation times of Fe-Cu dimers that vary between 50 and 250 ns.
Saunus et al., 2013 [135]	120 ps time resolution STM	Autocorrelation signals of fast pump-probe voltage pulses measured while obtaining atomic images on HOPG.
Rashidi et al., 2016 [30]	Time-resolved STM	Applied voltage pulses on a H:Si dangling bond to measure tunneling transport lifetimes of ns durations.
Feldstein, 1996 [136]	Fs Optical Spectroscopy and SPM	Measured optical pump-probe STM signal with 1 μm spatial and 0.05 ps temporal resolution on Ag film.
Yoshida et al., 2014 [20]	Ultrafast OPP STM	Ultrafast (0.1 ps res.) detection of spin precession in nm-sized AlGaAs quantum wells.

Table 2.2: Table summarizing highlights of THz-SNOM experiments where THz spectroscopy is combined with apertureless near-field microscopy. The progression of the entries chronologically highlights the improvement of both the temporal resolution (from ps to 10 fs) and spatial resolution (from µm to 10 nm).

Reference(s)	Topic	Highlights
van der Valk and Planken, 2002 [42]	EO THz detection using metal tip	Sub THz wavelength (1 µm) spatial detection of a THz beam spot size in the near-field of a metal tip.
Wang et al., 2004 [56]	Apertureless THz NF microscopy	Measured near-field and scattered far-field THz signals from a tip probe that demonstrated antenna effects.
Cho et al., 2005 [57] Kersting et al, 2005 [45]	Apertureless THz NF microscopy	THz pulses combined with tip to image of gold gratings on Si with sub-µm spatial resolution.
Eisele et al., 2014 [6]	THz spectroscopy and AFM	THz pulses coupled to an AFM tip used to image and probe optically excited InAs nanowires (10 nm scale) within sub-cycle field resolution (0.01 ps).
Huber et al., 2017 [7]	OPP and AFM	Probed the fs response of a plasmon-polariton-phonon excitation using MIR pump-THz probe spectroscopy combined with AFM imaging on a 110 nm thick black phosphorus heterostructure.
Klarskov et al., 2017 [35]	Laser THz emission microscopy	Excited AFM tip and sample with IR beam to image a gold nanorod with 20 nm resolution using THz emissions coming from the underlying doped InAs substrate.
Mooshammer et al., 2018 [36]	OPP and AFM	Probed local dielectric response of a topological insulator with 10 nm resolution using MIR pulses to illuminate an AFM tip.

Table 2.3: Table chronologically summarizing the developments and highlights of THz-STM.

Reference(s)	Topic	Highlights
Cocker et al., 2013 [33]	Novel THz-STM technique	Pioneered coupling THz-pulses to the STM to achieve simultaneous nm and sub-ps resolution. Demonstrated time-dependent imaging on Au islands on HOPG and InAs nanodot samples.
Cocker et al., 2016 [47]	THz-STM on single molecule	Imaged and probed the switching of molecular states of a single pentacene molecule within the sub-cycle of a THz pulse (0.1 ps).
Yoshioka et al., 2016, [34]	THz manipulation of STM	Coherently driven tunneling electrons with tip-enhanced THz fields whose waveform is shaped by a carrier-envelope phase. Measured extreme tunneling current rectification of $\sim 10^5$ electrons per pulse.
Jelic et al., 2017 [2]	THz-STM on single atoms	Demonstrated atomic spatial and sub-ps temporal resolution on the Si(111)-(7×7) surface in UHV. Extreme transient tunneling current densities of $10^{11} \mathrm{A\,cm^{-2}}$ in the tunneling junction.
Yoshioka et al., 2018 [48]	THz manipulation of STM	Sub-ps time resolved and phase tuning of the THz-biased tunneling. Found phase-differences between THz FF and NF transients for various tip shapes.
Yoshida et al., 2019 [49]	Visualization of THz NF in STM	Photoelectrons on a tip are spatially and temporally mapped with a time-of-flight spectrometer while measuring photoelectron current reaching the sample to yield THz NF waveforms.
Jelic et al., 2019 [133][2]	OPP-THz-STM on GaAs	Optical pump-THz probe STM measurements on photo-excited GaAs yielded tunneling transients that depends on the photo-conductivity transport dynamics driven by the THz NF.
Peller et al., 2020 [22, 23]	THz-STM of molecular switch	Use THz NF pulses to physically rotate a McPc molecule forming an ultrafast molecular switch. Used the switch system to probe the NF-THz transient bias acting as a gate voltage.
Continued on next page		

Table 2.3 – continued from previous page

Reference(s)	Topic	Highlights
Müller et al., 2020 [24, 26]	THz NF detection in STM	Applied high broadband THz pulses to the STM and sampled the THz NF in the STM junction with tunneling currents of single electrons. The tunneling current transient reflects an antenna functional response.
Luo et al, 2020 [3]	THz-STM of metal surfaces	Resolved the THz-STM signal over a single-atom metal step edge (0.3 nm). Expanded the STM-tunneling model to account for areal tunneling for a 3D tip geometry for better accuracy.
Ammerman et al., 2021 [28]	THz-STM on graphene	Demonstrated THz driven STM on graphene nano-ribbons where various localized wavefunctions are spatially mapped with atomic resolution. Varying the THz field amplitude or tip-sample distance varies the accessible range of LDOS features that can be probed.
Yoshida et al., 2021 [27]	THz-STM of carrier motion	Time-resolved imaging of a C_{60} multilayer structure showing the ultrafast motion of optically excited photoelectrons throughout various regions of the sample.
Abdo et al., 2021 [25]	THz source for THz-STM	Developed THz source that emits THz pulse trains with variable repetition rates to vary the THz bias amplitude, creating tunnel currents varying from < 1 to 1000 electrons per pulse.
Ammerman et al., 2022 [80]	THz-STM algorithm	Proposed algorithm for determining STM IV and LDOS probed by THz-STM which can reasonably map the THz incident field to THz tunneling current between the tip and metal, semiconductor or molecular samples.
Garg and Kern, 2020 [137] Garg et al., 2022 [31]	Ultrafast STM on molecules	Molecular orbital imaging of HOMO and LUMO states of PTCDA molecules on Au(111) with the STM coupled to ultrashort laser pulses of duration < 6 fs.
Continued on next page		

Table 2.3 – continued from previous page

Reference(s)	Topic	Highlights
Sabanés et al., 2022 [26]	Ultrafast STM photocurrents	THz-STM on an optically excited tip over a Ag(111) sample to probe non-thermal currents from the strong enhanced THz-field in the junction and hot electrons from photocurrents. The THz near-field experiences phase changes from arising photocurrents.
Arashida et al., 2022 [39]	Mid-IR STM	Coupled mid-IR pulses with THz to the STM and probed non-equilibrium dynamics on $MoTe_2$ surface with temporal resolution of 30 fs.
Chen, Shi and Ho, 2022 [32]	Continuous-Wave THz-STM	Rectification spectroscopy with continuous-wave THz radiation on junction consisting of tip and single molecules. THz-induced bias modulation is sinusoidal and the current signal indicates a molecular switching response.
Iwaya et al., 2023 [51]	OPP-STM on GaAs(110)	Measurement of tunneling current on n-type LT-GaAs(110) surface and the SPV from the illuminated I-V. OPP tunneling currents reveal both short and long carrier life-times in the sample.
This work[3]	THz near-field in STM	Determining the THz NF response and transient bias of the STM junction via simulations and modeling. Fitting of measured THz-STM tunneling currents and transients with modeled parameters.

---

[2]Topic located in chapters 7 and 8 of thesis, which is combined with this thesis is to develop potential manuscripts

[3]Manuscripts based on the content within this thesis are to be determined. This thesis will be completed before the manuscripts are written.

Literature focused only on theoretical, numerical and analytical modeling approaches for THz-STM were recently published [80, 81]. Portions of the experimental literature listed in table 2.3 were also dedicated to the theoretical aspects. However, there is still much need for developing the theoretical foundations of THz-STM, much of which are borrowed from SNOM theory. For example, further work is required to calculate the near-field that accounts for: (i) the antenna properties of the metal tip, (ii) excitation and propagation of SPPs excited on metallic surfaces, and (iii) the tip-sample interaction. Such information can be revealed when the simulation or the model embodies as much of the entire microscope geometry. Simulation work described in Chapter 4 for the THz-STM geometry seeks to accomplish these goals. Furthermore, involvement of the tunneling junction adds to the complexity. Much of the STM tunneling theory is developed for static biasing conditions. In the case where THz radiation becomes the driving field, time-dependent transport in the tunneling junction is activated, thus a dynamic tunneling theory is necessary.

STM and SNOM were separate disciplines due to the challenges that arise when combining optics with the STM system. SNOM was used to study plasmonic systems in the nano-scale regime where optics setups are combined with simpler scanning systems such as the AFM that operate in ambient conditions. Early techniques of light coupling were done with microwaves [138, 139] and wave guide structures. Usually, thermal heating of the tip due to optical pulses will cause tip expansion [140] and modification (e.g. bond breaking) on the sample surface. The STM junction is drastically changed under illumination with optical pulses where thermal effects such as tip expansion may occur. THz pulses provide a good range to combine with the STM due to their ultrafast duration (which is not attainable with microwaves) and their low energy (meV) cannot cause tip and surface morphology.

The only matter of concern is the field strength of THz pulses going into the junction. It is ideal to work with low field amplitudes and have the measurement electronics capable of detecting tiny perturbations as the input field strength varies.

However the coupling efficiency for THz pulses to a wire was measured and simulated to be less than 1% (0.4%) [54, 133, 141]. Also the performance of the external optics setup can vary day to day, so tuning the input electric field strength is not as simple as adjusting a knob. Secondly, if the STM environment is modified such as with a tip change, the optics will couple to a new geometry. Even though the field profile can be probed externally using detection systems like EO sampling, there is always a degree of uncertainty for the radiation profile that actually couples to the STM junction. High field amplitudes implies a large bias across the junction. High amplitude THz pulses can induce non-linear effects such as field emission and structural damage [74, 133]. Later on in this thesis, THz fields existing inside the sample play a significant role in driving transport that contribute to large tunneling currents for THz-STM on semiconductor samples. The THz-STM technique sets up a multi-faceted discipline that takes into consideration all the matters and issues that occur in the STM and SNOM research fields.

2.6 Chapter summary

This chapter discussed the foundations of THz science and near-field microscopy necessary for understanding THz-STM from THz generation all the way to coupling THz with the STM. The mechanisms and formalisms for generating a photo-current, free-space and wave-guide propagation of THz radiation, generation of plasmons in materials, and the focusing of fields in near-field microscopy are all useful for understanding the variables that constitute a measurement in a THz-STM experiment. As THz-STM is proven to be a multidisciplinary field, these concepts should help with the design of future experiments and applications. These principles are used to guide the design of THz-STM simulations and modeling, as presented later on.

Chapter 3

Scanning Tunneling Microscopy

Tunneling phenomena are fundamental in several scientific fields, predominantly for condensed matter physics, with scanning tunneling microscopy (STM). Sharp metal tips can be used as probes in near-contact proximity to a sample surface to probe condensed matter systems as a means of the tunneling process. In this configuration, electrons have finite probabilities of existing in either the tip or sample, even with the insulating gap between them. Thus, there is a transmission probability of the electron going from the tip to the sample, or vice-versa, which leads to concept of a tunneling current.

The STM obtains images of surfaces at the atomic level using the principle of quantum mechanical tunneling [142, 143]. In Fig. 3.1, when an atomically sharp needle-like metallic tip is brought close to a conducting sample, but not in contact, electrons can tunnel through the gap between the tip and sample. Applying a voltage between the tip and sample results in a net tunnel current that is exponentially dependent on the tip-sample separation, which is in the range of 5-10 Å.

Under stable UHV conditions, the STM is capable of imaging surfaces with atomic spatial resolution. For example, images of atoms on a silicon surface can be obtained, as shown in Fig. 3.2. The STM equipment is a sensitive instrument since the image contrast is influenced by a number of components. This includes the sequential succession of scanning motion controls, mechanical stability, tip sharpness, sample
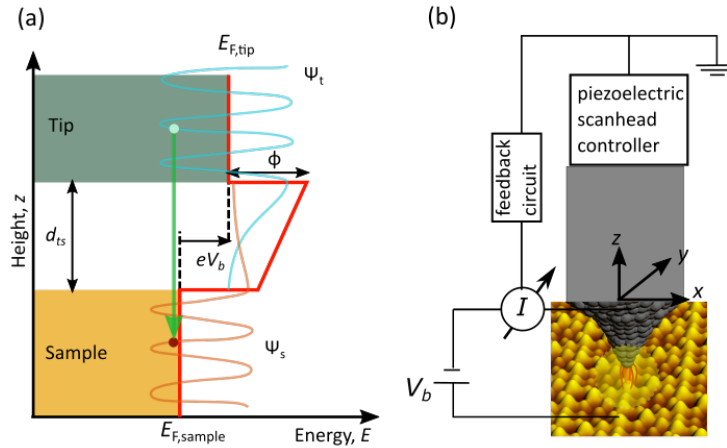
Figure 3.1: Principles of the STM illustrated showing the (a) tunnelling process between the tip and sample across a vacuum barrier of d and energy height ϕ. The electron's wavefunction decays from the tip region into vacuum to the sample region. The direction of tunnelling depends on the applied bias voltage. (b) Schematic circuit diagram of the STM. Adapted from [144]

cleanliness and surface roughness [142, 143]. These conditions also set and control the junction environment into where light couples, therefore, these factors greatly influence the imaging contrast of THz-STM.
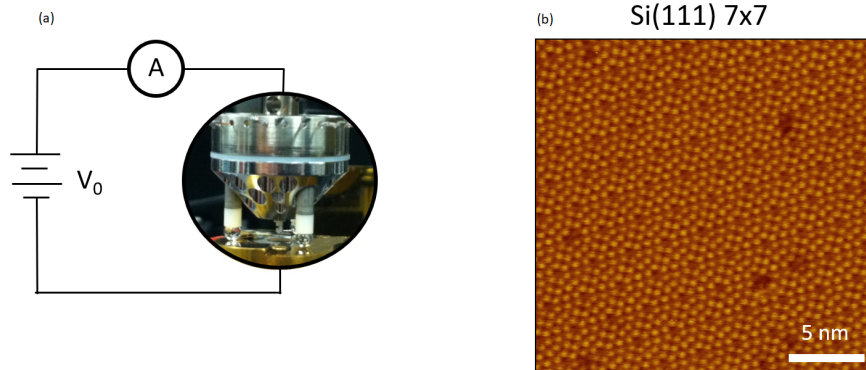
Figure 3.2: (a) Circuit schematic for the STM containing the STM scan head that houses the tip and sitting above the mounting puck that holds the sample. A d.c. bias, V_b, is applied to the sample and a tunneling current is measured by a preamplifier system. (b) Image of the Si(111) surface obtained using the STM. The sample bias is positive relative to the tip.

3.1   1D tunneling model

The tunnel current carries with it information about the local electronic wave-function of both the tip and the sample. The concept of a wave-function is familiar for single atoms and molecules, however, for bulk crystals, the STM probes the electronic local density of states (LDOS). The tunnel current is proportional to the electron transmission through a 1D square barrier potential with a height ϕ_0 relative to the Fermi level ϵ_F (Fig. 3.1(a)). The probability of an electron tunneling across the barrier is determined by solving the 1D time-independent Schroödinger equation:

$$[\phi_0 - E]\,\psi(z) = \frac{\hbar^2}{2m}\frac{d^2}{dx^2}\psi(z), \tag{3.1}$$

where the wavefunction, ψ, is solved in regions to the left, right and inside the potential barrier, ϕ_0, as a function of position z, m is the electron mass, E is the energy relative to E_F, $\hbar$ is the reduced Planck's constant. One can perform a textbook derivation by solving Eq. 3.1 for the wavefunction in the regions inside and around the barrier and match wavefunction amplitudes using boundary conditions. The transmission probability for the electron wavefunction tunneling through the barrier is approximated by [143]

$$T \approx \left(\frac{4k\kappa}{k^2 + \kappa^2}\right)e^{-2\kappa z_0}, \tag{3.2}$$

where the wavenumber of the incident and transmitted electrons at energy E is $k = \sqrt{2mE}/\hbar$, z_0 is the spatial barrier width, and the wavefunction's $1/e$ amplitude decay constant κ is given by

$$\kappa = \sqrt{2m(\phi_0 - E)}/\hbar. \tag{3.3}$$

The transmission probability for 1D tunneling in Eq. 3.2 yields the experimental tunneling current as

$$I = I_0\exp\left(-2(z - z_0)\kappa\right), \tag{3.4}$$

where z is the tip distance from the sample and I_0 is a setpoint current, a constant tunnel current obtained at the initial tip-sample separation z_0 by setting a feedback

47

loop control. The current demonstrates the exponential decay dependence of the tunnel current on increasing tip-sample separation z. The STM probe measures a current that is sensitive to z, thereby, even surface corrugation variation on the order of Å's can be traced according to Eq. 3.4. Hence, the origin of the high spatial resolution down to the atomic scale.

3.2   Scanning Tunneling Spectroscopy

The STM junction can be characterized by single point measurements on a sample. The *I-V* characteristic shown in Fig. 3.3(a) is a single point measurement obtained by fixing the tip's position and varying the relative bias voltage between the tip and sample. For the STM system used in this work, the d.c. bias, V_b is applied on the sample. When $V_b > 0$, the sample is positively biased, thus the tunneling current describes electrons going from the tip to the sample. When $V_b < 0$, the sample is at a negative bias relative to the tip and tunneling current direction is reversed. The applied bias shifts the tip's energy range $E_{\mathrm{F,tip}} = E_{\mathrm{F,tip}} + eV$ relative to the sample, which allows electrons from the tip to tunnel through the barrier to occupy available energy states in the sample. Therefore, the *I-V* characteristic sweeps through the LDOS for the tip and sample. The *I-V* curve alone does not directly reveal the local DOS structure.

The differential conductance obtained by $\mathrm{d}I/\mathrm{d}V$ has to be normalized by the *I-V* to plot out the LDOS spectrum as shown in Fig. 3.3(b).

The *I-z* characteristic shown in Fig. 3.4 is obtained by fixing the bias voltage but varying the tip height. The tunnel current dependence as a function of z is expected to follow the relation in Eq. 3.4. The slope of $\ln(I)$ is used to experimentally extract the barrier height.

$$\phi_{\exp} = \frac{\hbar^2 \kappa^2}{2m} = \frac{\hbar^2}{8m} \left(\frac{\mathrm{d}\ln(I/I_0)}{\mathrm{d}z} \right)^2 \tag{3.5}$$

Though the STM exhibits impressive spatial resolution, the interpretation of data
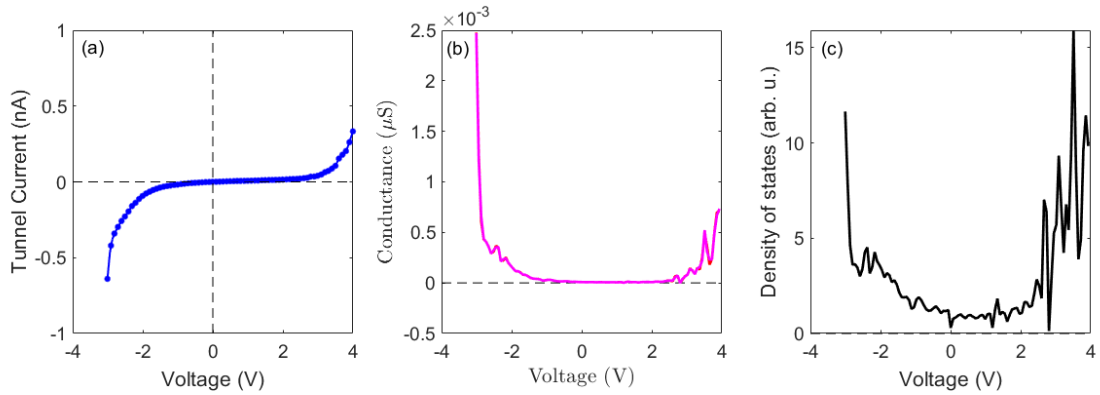
Figure 3.3: (a) Experimentally measured I-V curve of the STM. (b) Corresponding differential conductance (dI/dV) and (c) density of states plot. STM measurements were obtained using a tungsten tip was used on a Si(111) surface at room temperature. $I_0 = 20$ pA.
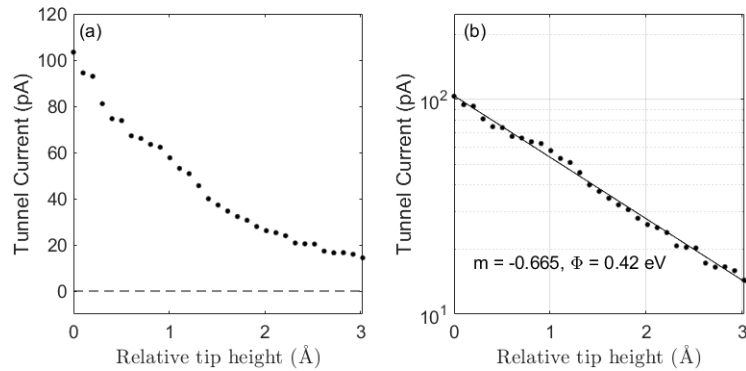
Figure 3.4: (a) Experimentally measured I-z curve where plotting the same curve in a semi-log plot shown in (b) can be used to determine the tunneling barrier height. STM measurements were obtained using a tungsten tip was used on a Si(111) surface at room temperature. $I_0 = 20$ pA.

49

requires extensive analysis and modeling. STM is a field that has existed for several decades and models to interpret STM signals still continue to develop and be refined. Theoretical models discussed here are strictly one-dimensional in order to explore the behaviour of the tunnel current as a function of tip-sample separation

3.3   Bardeen's tunneling model

Bardeen's formalism describes the general tunneling mechanism in STM for all possible materials and interfaces [142]. It incorporates all spatial dimensions to solve the time-independent Schrödinger equation for the tip and sample regions separately, then eventually combines the two to approximate the tunneling probability between two superconductors separated by an insulating layer. Even though the formalism is used for superconductors, it may be applied to the STM [142] to arrive at the tunnel current in its most general form,

$$I = \frac{4\pi e}{\hbar} \sum_{i,f} |M_{fi}|^2 \delta(E_F - E_i), \tag{3.6}$$

where E_i and E_f are the initial and final energy of the electron, respectively, $|M_{fi}|^2$ is the tunneling probability for each transition $(i \to f)$ given by

$$M_{fi} = \frac{\hbar^2}{2m} \int_S \left[\psi_i(\mathbf{r}) \nabla \psi_f^*(\mathbf{r}) - \psi_f^*(\mathbf{r}) \nabla \psi_i(\mathbf{r}) \right] \cdot d\mathbf{S}, \tag{3.7}$$

where ψ_i and ψ_f are the wavefunctions of the tip and sample, respectively. The integration is performed over the surface, S, lying within the barrier region. The Bardeen tunneling model can be approximated as an integral over the bias range in one-dimension. Instead of using wavefunctions, density of states for the tip, ρ_t, and sample, ρ_s, are replaced to give the tunneling current expression:

$$I = \frac{4\pi e}{\hbar} \int_0^{eV} \rho_t(E - eV)\rho_s(E) \, T(\phi_t, \phi_s, E, V, z) \, dE, \tag{3.8}$$

where ϕ_t, ϕ_s are the tip and sample barrier heights, respectively. Fig. 3.5 illustrates the parameters involved in calculating the tunnel current using density of states functions for the tip and sample where the voltage corresponds to the difference of the tip's

Fermi level relative to the sample's. The $|M_{fi}|^2$ element is converted to a transmission factor given as

$$T(\phi_t, \phi_s, E, V, z) = \xi \cdot \bar{\phi} \cdot \exp\left(-2z\sqrt{\frac{2m}{\hbar^2}\bar{\phi}}\right), \tag{3.9}$$

where $\xi = 2[\hbar A \psi_i(0)\psi_f(z)]^2/m$, A is the tunneling area, and $\bar{\phi}$ is the average barrier height given by

$$\bar{\phi}(\phi_t, \phi_s, E, V) = \left(\frac{\phi_t + \phi_s \pm e|V|}{2}\right) \mp |E|. \tag{3.10}$$
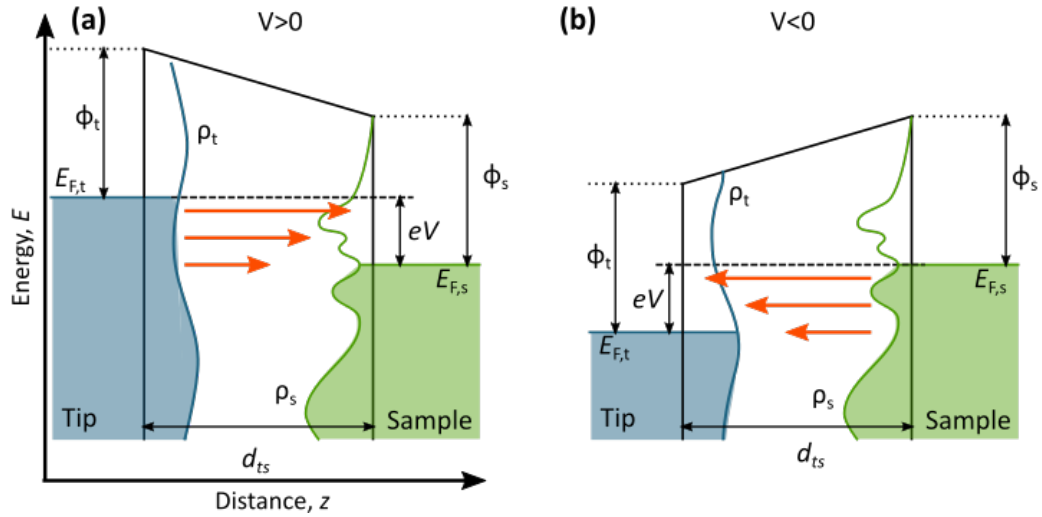
Figure 3.5: Tunneling diagram illustrating the parameters involved in calculating the tunnel current at (a) positive tip bias $V > 0$ and (b) negative tip bias, $V < 0$, relative to the sample. The density of states for the tip, ρ_t, and sample, ρ_s, both take on a generalized form as illustrated by the drawn curves. (Adapted from [143].)

3.4 Simmons model

The Simmons model [145, 146] is one particular case of the Bardeen model, where the current density is derived for the case of two planar metal electrodes separated by a nm-scale insulator in the gap. The tunnel current is given as

$$I = \frac{meA}{2\pi^2\hbar^3}\left[eV\int_0^{E_F - eV} T(E)dE + \int_{E_F}^{E_F - eV} (E_F - E)T(E)dE\right], \tag{3.11}$$

where A is the spatial area of the tunnel current, V is the applied voltage, and the tunneling transmission probability is given as

$$T(E) = \exp\left(-\frac{2\sqrt{2m}}{\hbar} \int_{z_1}^{z_2} \sqrt{E_F - E + \phi(x)} \, dx\right), \qquad (3.12)$$

where $\phi(x)$ is the barrier height as a function of position in the gap x, and z_1, z_2 are the positions where the barrier height crosses E_F. The I-V curve and corresponding differential conductance in Fig. 3.6 are calculated using the Simmons model, which assumes zero temperature and constant density of states over all energy. T can be approximated by replacing $\phi(x)$ with the average barrier height given in Eq. 3.10.
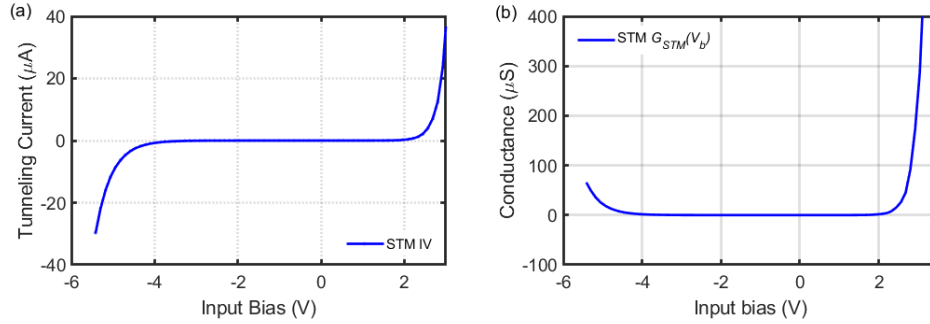
Figure 3.6: (a) Calculated I-V curve using the Simmons model. (b) Calculated conductance curve from the derivative of the I-V in (a). The tip-sample distance is 1 nm, $\Phi_t = \Phi_s = 4$eV and $I_0 = 20$ pA.

If the density of states is flat for both the tip and sample, the Bardeen model agrees with the Simmons model. As the voltage increases, there is a gradual transition from the tunneling regime to the field emission regime (10 to 100 V) and finally to the space-charge limited regime (100 V to 1000 V) [147–149].

3.4.1 Trapezoidal barrier

Calculating the barrier height is non-trivial, however, there are reasonable approximations that can be used when the tunneling scenario obeys the assumptions previously declared. Assuming a trapezoidal geometry for the potential barrier, integrals can be modified to area approximations. The integral for the transmission probability in Eq.

3.12 is approximated as

$$T(E) \approx \exp\left(-\frac{2\beta\delta\sqrt{2m}}{\hbar}\sqrt{E_F - E + \bar{\phi}}\right),$$ (3.13)

where $\bar{\phi}$ is the average barrier-height given by

$$\bar{\phi}(\phi_t, \phi_s, V, z) = \frac{1}{\delta}\int_{z_1}^{z_2}\phi(x, \phi_t, \phi_s, V, z)\,dx,$$ (3.14)

where ϕ_t is the barrier height of the tip (determined by the material work function), ϕ_s is the barrier height of the sample, z is the tip-sample separation, β is a correction factor (close to unity) and $\delta = z_2 - z_1$ is the effective barrier width. For the standard trapezoidal shape, $z_1 = 0$ and $z_2 = z$, which leads to the following expression for the barrier height,

$$\phi(x, \phi_t, \phi_s, V, z) = \begin{cases} \phi_t + \frac{x}{z}(\phi_s - \phi_t - e|V|)\,, V \geq 0 \\ \phi_t + \frac{x}{z}(\phi_s - \phi_t + e|V|)\,, V < 0 \end{cases}$$ (3.15)

and the effective barrier-width as

$$\delta(\phi_t, \phi_s, V, z) = \begin{cases} z\,, -\phi_t < eV < \phi_s \\ \frac{z\phi_t}{\phi_t - \phi_s + e|V|}\,, \phi_s \leq eV \\ \frac{z\phi_s}{\phi_s - \phi_t + e|V|}\,, eV \leq -\phi_t. \end{cases}$$ (3.16)

The average barrier-height can finally be determined by placing Eq. 3.15 and Eq. 3.16 into Eq. 3.14 to obtain

$$\bar{\phi}(\phi_t, \phi_s, V) = \begin{cases} (\phi_t + \phi_s - e|V|)/2\,, -\phi_t < eV < \phi_s \\ \phi_t/2\,, \phi_s \leq eV \\ \phi_s/2\,, eV \leq -\phi_t. \end{cases}$$ (3.17)

The general expression for the correction factor, β, is given as

$$\beta(\phi_t, \phi_s, V) = \begin{cases} 1 - \frac{1}{8\delta}\int_{z_1}^{z_2}\left(\frac{\phi(x)}{\bar{\phi}} - 1\right)^2 dx & , V \geq 0 \\ 1 - \frac{1}{8\delta}\int_{z_1}^{z_2}\left(\frac{\phi(x) - e|V|}{\bar{\phi} - e|V|} - 1\right)^2 dx & , V < 0. \end{cases}$$ (3.18)

Inserting for ϕ using Eq. 3.15 leads to a quadruplet of cases,

$$\beta(\phi_t, \phi_s, V) = \begin{cases} 1 - \frac{1}{24}\left(\frac{e|V| - \phi_s + \phi_t}{e|V| - \phi_s - \phi_t}\right)^2\,, 0 \leq eV < \phi_s \\ 1 - \frac{1}{24}\left(\frac{e|V| + \phi_s - \phi_t}{e|V| - \phi_s - \phi_t}\right)^2\,, -\phi_t < eV < 0 \\ \frac{23}{24}\,, \phi_s \leq eV \\ \frac{23}{24}\,, eV \leq -\phi_t. \end{cases}$$ (3.19)

Hence, $23/24 \leq \beta \leq 1$. The final steps to determine the tunneling current by inserting the approximation of $T(E)$ in Eq. 3.13 into Eq. 3.11 yields,

$$I = \frac{\pm eA}{\hbar(2\pi\beta\delta)^2} \left[\bar{\phi} \cdot \exp\left(-\frac{2\beta\delta\sqrt{2m}}{\hbar}\sqrt{\bar{\phi}}\right) \right.$$
$$\left. - (\bar{\phi} + e|V|) \cdot \exp\left(-\frac{2\beta\delta\sqrt{2m}}{\hbar}\sqrt{\bar{\phi} + e|V|}\right) \right], \quad (3.20)$$

where A is the tunnel junction contact area. The $+$ case applies to a positive bias ($V > 0$) and $-$ case is for negative bias ($V < 0$). Several terms were dropped to obtain the expression above assuming that the $\sqrt{\bar{\phi} + e|V|}$ is the most dominant one while terms with $\sqrt{\bar{\phi} + E_F}$, $\sqrt{\bar{\phi} + E_F - E}$, and higher reciprocal orders, $1/\alpha^2, 1/\alpha^3, \ldots$, of prefactor $\alpha = 2\beta\delta\sqrt{2m}/\hbar$ were ignored (see [145, 146] for details).

A plot of the trapezoidal barrier is shown in Fig. 3.7 (blue curve), which is naturally formed when the tip and sample materials have different work functions. Note that there is no bias applied between the tip and sample. When both materials are held to zero potential, the potential barrier in the gap region is forced to tilt, thus creating the trapezoidal shape. If the tip and sample materials have the same work functions, a bias must be applied between them in order to create the trapezoidal potential (later shown in Fig. 3.8).

The Simmons model can be applied to generate I-V curves and conductance curves shown in Fig. 3.6. The bias range sweeps over the density of states at various energy levels of the tip and sample. Due the assignment of constant density of states for both ρ_t and ρ_s in the model, the I-V characteristic is monotonic in the bias direction (i.e. strictly grows for $V > 0$ and decreases for $V < 0$).

As for the more general case, with the Bardeen model, arbitrary functions ρ_t and ρ_s can be inserted into the tunneling calculation to produce interesting I-V curves that fluctuate along a bias direction. Though the degree of difficulty increases to determine the tunneling current, the Bardeen formalism can be applied to model the tunneling in the general metal-insulator-metal [150–152], interband interfaces in

54
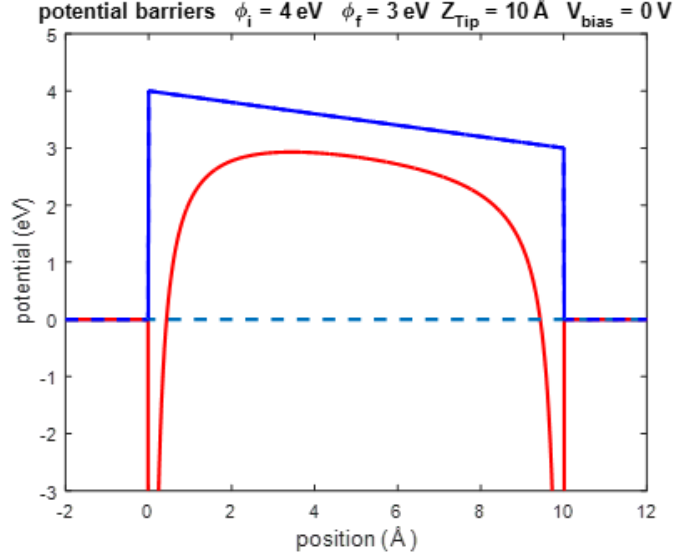
Figure 3.7: Trapezoidal potential barrier (blue) when the tip and sample have different barrier heights with a 1 nm separation. Modification of the trapezoidal barrier by introducing the image potential (red). There is no applied d.c. bias. (Credit: K. Iwaszczuk[1])

metals [153], metal-insulator-semiconductor [147, 154–156], molecular interfaces [157] and superconductor [158] scenarios.

3.4.2   Image potential barrier

The barrier height ϕ is a dynamic parameter that depends on the junction geometry and materials. Once ϕ is known, the tunneling profile can essentially be predicted. Various studies have been done to come up with a formalism and expression for ϕ [145, 148]. A 1D form for ϕ to be discussed is the image potential.

By considering an image charge formed from the interaction of the tip with the sample, it forms a Coulomb potential that reduces the effect of the applied field. Thus, the overall barrier height deviates from trapezoidal barrier height, $\phi_{\text{trapz}}(x, \phi_t, \phi_s, V, z)$ from Eq. 3.15, by an amount given by

$$\phi_{\text{img}}(x, z) = -\frac{e^2}{8\pi\epsilon_0}\left[\frac{1}{2x} + \sum_{n=1}^{\infty}\left(\frac{nz}{(nz)^2 - x^2} - \frac{1}{nz}\right)\right], \tag{3.21}$$

---

[1]Figure produced by tunneling current model code developed by K. Iwaszczuk.

where ϵ_0 is the permittivity of free space. This expression is equivalent to [148]

$$\phi_{\text{img}}(x, z) = -\frac{e^2}{16\pi\epsilon_0 z}\left[2\psi(1) - \psi\left(\frac{x}{z}\right) - \psi\left(1 - \frac{x}{z}\right)\right],\tag{3.22}$$

where $\psi(x)$ is the digamma function given by,

$$\psi(x) = \frac{d}{dx}\ln(\Gamma(x)) \approx \ln x - \frac{1}{2x}.\tag{3.23}$$

Using the approximation for $\psi(x)$, Eqs. 3.21 and 3.22 can be approximated as

$$\phi_{\text{img}}(x, z) \approx -\frac{1.15e^2\ln 2}{16\pi\epsilon_0}\left[\frac{z}{x(z-x)}\right].\tag{3.24}$$

The effective barrier width, $\delta = z_2 - z_1$, is determined by calculating the two positive roots (in x) in the summation of barrier terms,

$$\phi_{\text{trapz}}(x, \phi_t, \phi_s, V, z) + \phi_{\text{img}}(x, z) = \begin{cases} 0 & , V \geq 0 \\ e|V| & , V < 0. \end{cases}\tag{3.25}$$

Fig. 3.7 (red curve) shows a plot of the image potential barrier at zero bias, but on a STM junction with different work functions for the tip and sample at a 1 nm separation. The applied modifications lowers the effective potential by curving the potential edges of the trapezoidal barrier. Fig. 3.8 shows how the barrier tilts when a bias is applied between the tip and sample, with the tip and sample separation 10 nm apart for the purpose of comparison with the trapezoidal barrier. At further separation, the image-potential becomes less pronounced and the potential barrier plot resembles the trapezoidal shape.

There are more detailed models that take into account the effects when a large population of electrons are tunneling. The space-charge effect describes the modification of the potential landscape experienced by a tunneling electron due to the presence a temporary build-up of charges. This is also known as the Coulomb-Blockade effect [149, 159–163]. The situation applies usually for tunneling electron current densities of 10^2 to 10^{10} A/cm^2 in the junction. It opens up another regime that has to be treated differently than the cases of standard tunneling and field emission [148, 163, 164].

---

[2]Figures produced by tunneling current model code developed by K. Iwaszczuk
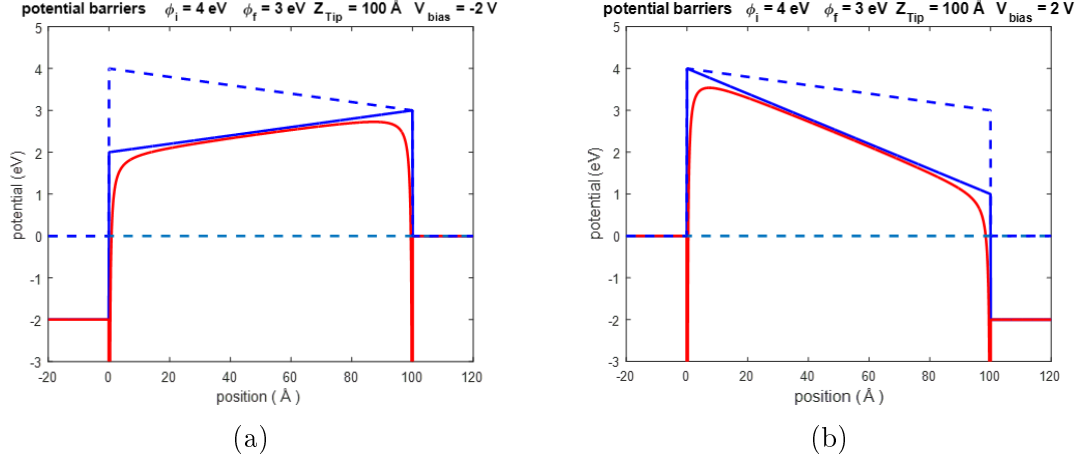
Figure 3.8: Modification of the trapezoidal barrier by introducing the image potential. Application of a voltage or bias field tilts the shape of the barrier across the gap. Plots are shown when the tip is biased at (a) -2 V and (b) $+2$ V. (Credit: K. Iwaszczuk[2])

3.4.3 Area tunneling Simmons model

The Simmons model combined with the image potential as described in the previous sections can reasonably determine the tunneling current in the bias range of -3 V to 3 V for a metal-metal tunneling junction. At larger biases, the tunneling current must factor in the DOS functions of the tip and sample and current contributions beyond the tip apex. Fig. 3.9(a) shows the energy diagram for smaller bias of 2 V and (b) for a large bias of 10 V for the metal-metal interface. The model is expanded to support a geometry of a hemispherical tip apex tunneling with a planar metal surface [3], as shown in Fig. 3.9(c). In this case, the area parameter, A, for the case of planar tunneling does not apply. Instead Eq. 3.20 rather becomes a unit current density, J. The total tunneling current is calculated by integrating over the curved surface area of the tip apex tunneling above a flat plane, expressed by

$$I = \int \int_A J(z(x,y), \bar{\phi}(x,y)) \, dxdy. \tag{3.26}$$

The tunneling is assumed to be a vertical line path, where one point on the tip apex can only form a tunneling barrier with one point on the sample surface. Thus, the tip height, z, and barrier width, ϕ, vary with lateral coordinates x and y. The z_1 and

57

z_2 limits are modified for each tip apex coordinate. For a flat sample plane $z_1 = 0$ and $z_2 = z(x, y)$ where $z(x, y)$ is the vertical distance between a point on the tip apex and the sample plane at fixed lateral position (x, y). Here we have a parameterized equation where the current density term is computed from the Simmons model tunneling using the tip to sample distance and the image potential barrier at each (x, y) coordinate.

The cumulative tunneling method successfully models the tunneling over metal step edges [3], in which the tip is exposed to an atomic step change in the sample topography. Fig. 3.9(d) shows the modeled DOS of Cu(111) in the STM.

The current density given by the Bardeen model with the image potential is given by

$$J(z) = \frac{4\pi e}{\hbar} \int_0^{eV_b} \rho_{\text{tip}}(\epsilon - eV_b)\rho_{\text{samp}}(\epsilon)T(\epsilon, z)d\epsilon, \qquad (3.27)$$

where V_b is the total bias voltage on the sample, which is the sum of the steady-state bias voltage, $V_{\text{d.c.}}$, and the transient ultrafast bias voltage induced by THz pulses, V_{THz}. The sample DOS ρ_{samp}, is modeled with piece-wise elementary functions that generally fits Cu(111) data. The potential barrier ϕ is calculated using the image potential as discussed in the previous sections, which is eventually plugged into the transmission factor T.

The area tunneling model can also be applied to metal-to-semiconductor tunneling, as outlined in [165]. Here, it maps out the potential barrier landscape in the vicinity of tip and calculate the near-field voltage around the tip and inside the sample using Poisson's equation for the steady-state. The transient case will be presented in Chapters 7 and 8.

3.5 THz-STM tunneling

Formalism for tunneling under a transient bias is described in this section. Instead of applying a constant bias, V, it now uses a transient voltage, $V(t)$, to sweep the
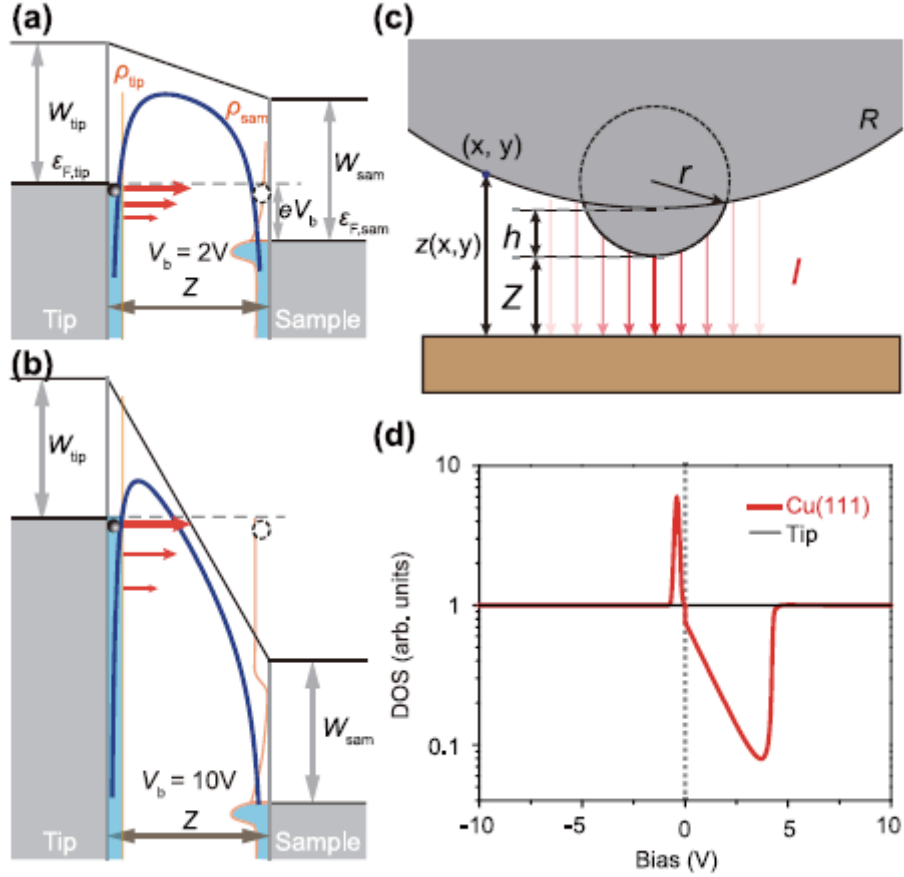
Figure 3.9: Expanding the tunneling model by using a 3D tip apex geometry. Tunneling using Simmon's model is accumulated for all points of tunneling between the tip apex surface and the sample surface. The potential-energy landscape of the tunnel junction at (a) low and (b) high positive bias voltages V_b. W is the work function (in place of Φ for this research work), ϵ_F is the Fermi level, ρ_{tip} is the DOS function for the tip and ρ_{sam} is the DOS for the sample. The image potential barrier is taken into account as outlined by the blue curves. (c) Cross-section of the 3D-tunnel junction where the STM tip is constructed as two attached spheres of radii r for the tip apex and R for the macroscopic tip with relative offset h. (d) The DOS of the tip and Cu(111) sample used in the simulation. (Adapted from [3].)

tunneling junction, as illustrated in Fig. 3.10. *I-V* curves and differential conductance
for the THz-STM case can be generated, as shown in Fig. 3.11.
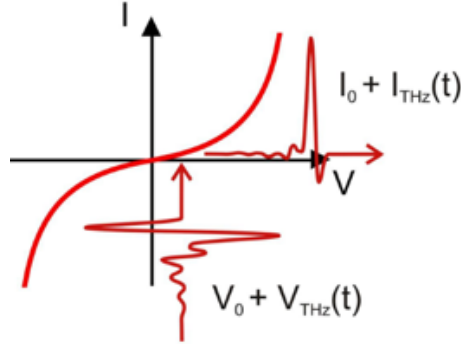
Figure 3.10: Schematic for Sweeping the tunneling junction *I-V* with a THz transient
bias. The d.c. bias added to THz electric field coupling to the STM junction translates
to a transient bias. The current obtained from the *I-V* curve is also a transient. Due
to the non-linearity of the *I-V* of the junction, the current is rectified (i.e. integral of
current waveform is non-zero), thus a net THz current is measurable (Adapted from
[133, 141]).

I-V curves for STM junctions are generally asymmetric as experimentally measured
in Fig. 3.3 and calculated in Fig. 3.6. The shape of the *I-V* curves is dependent
on the tip and sample used due to the difference of the density of states profiles
in each material. The plots show that more tunneling current can be obtained at
negative biases. Furthermore, sweeping the STM junction with a transient bias is
waveform dependent. The net current per THz pulse cycle is obtained by integrating
the *I-V* sweep using the full waveform, which implies that both positive and negative
amplitude regions of the pulse waveform contribute the net current. By using a large
THz amplitude of 6V, the negative part of the pulse cycle drives a large negative
current by having the negative of the pulse sweep the negative region of the *I-V*. The
positive current generated by the positive amplitudes of the pulse cycle cannot match
the negative current, hence the net current is negative. This results in a negative
current amplification when a large amplitude THz transient is introduced to the STM
junction as shown in Fig. 3.10. When pulses of small amplitudes are used for the
THz-*I-V* sweep, there is no current rectification. The sweeping ends up being focused

in the linear region of the *I-V* at the zero crossing. This is confirmed experimentally by conducting THz-STM experiments using small amplitude THz pulses where zero THz current rectification were measured. Ideally, unipolar pulses have to be used in order to better obtain the current rectification for a pulse with amplitudes at mainly one polarity.
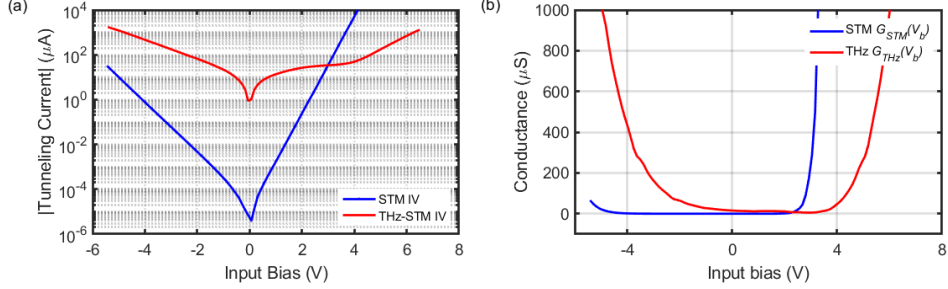
Figure 3.11: (a) Modification of the STM I-V (blue) with the added THz transient pulse (red). The incident THz pulse waveform in Fig. 2.1 is scaled to a peak voltage of 6 V to generate the THz contribution to the tunneling current and added to the d.c. bias in the I-V calculation. (b) The corresponding THz conductance curve.[3]

In the equations for tunneling current listed previously, it replaces the constant bias *V*, with a transient voltage, *V*(t), that takes on the same form as a THz pulse (see Fig. 3.12(a)). Essentially, the tunneling calculations are done for each point in time using a new value of *V*. By sweeping the voltage pulse along the calculated *I-V* curve, a tunneling current waveform is obtained (see Fig. 3.12(b)). If the voltage amplitude is large enough to enter the non-linear onset of the *I-V*, the tunneling current waveform should have net d.c. component when integrated (see Fig. 3.12(c)). The final value of the integral is the net charge, which directly gives the number of rectified electrons during the transient's duration.

The THz transient bias does not necessarily assume a single cycle waveform as for the case in Fig. 3.12. When geometric factors are considered such as THz pulse reflection pulses propagating along the tip wire shaft, the THz transient bias pulse shown in Fig. 3.13(a) is produced. The tunneling current waveform in Fig. 3.13(b) does not appear to differ much from Fig. 3.12(b), however the net rectification changed from
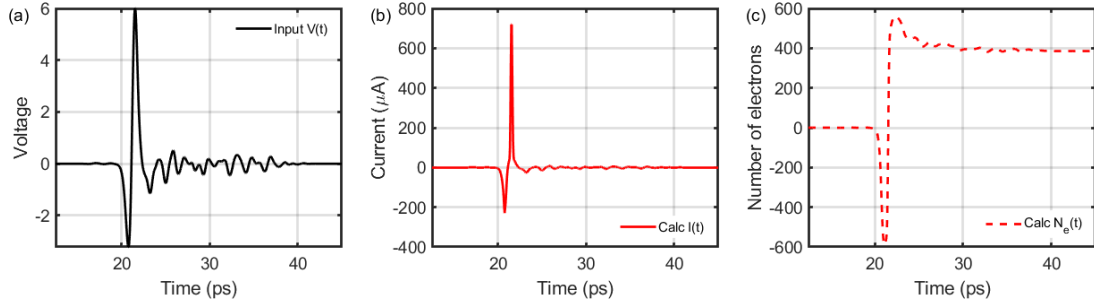
Figure 3.12: (a) The input transient voltage waveform taking the form of a THz pulse shown in Fig. 2.1 with peak amplitude of 6 V. (b) Tunneling current waveform from sweeping the I-V curve. (c) The net number of electrons is obtained by integrating the current waveform over a single cycle of the input THz pulse.

400 electrons in 3.12(c) to 325 electrons in Fig. 3.13(c). Chapters 7 and 8 will show that at larger THz amplitudes or if the THz transient waveform shape is significantly distorted, the rectified tunneling current would be affected.
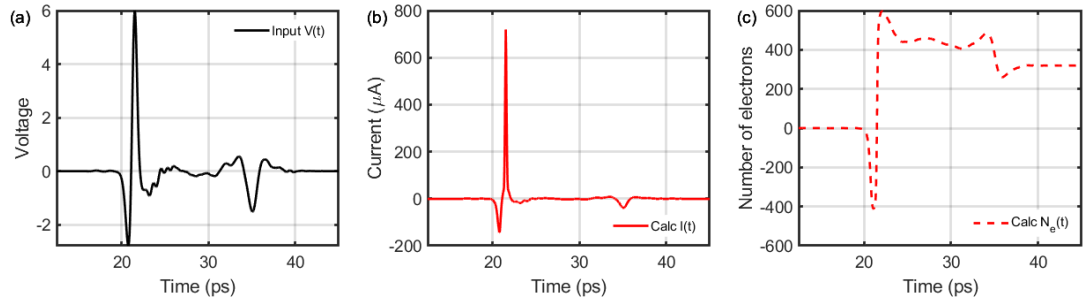
Figure 3.13: (a) The input transient voltage waveform taking the form of a THz pulse with a trailing reflection pulse feature. (b) Tunneling current waveform from sweeping the I-V curve. (c) The net number of electrons is obtained by integrating the current waveform over a single cycle of the input THz pulse is modified.

With the tunneling current models presented in this chapter, the tunneling at an instant in time does not depend on any past instances. In Chapters 7 and 8, the presence of transient charges existing in the junction actually influences tunneling in the present and future times. In general, tunneling will be calculated as a convoluted response between the transient bias and the junction conductance.

---

[3]A version of this figure was featured in [2].

3.6   Chapter Summary

The foundations of STM were discussed using formalisms to quantify quantum mechanical tunneling through a potential barrier that exists in the region between the tip and sample. The barrier height can take on several forms depending on the models or approximations used. With the effective barrier height determined, the calculation for tunneling current follows through. The equations for calculating the tunneling current are expanded to support a transient bias that takes on the form of a THz pulse, which sets up the basis for modeling THz-STM.

Chapter 4

Finite Element Simulations for the Coupling of THz Pulses to the STM

Simulations are useful for optimizing the design of the scanning components used in near-field microscopy [58, 166]. Conical tip tapers are commonly employed in these methods because of their ability to focus electromagnetic fields to the tip apex [167, 168]. There has been near-field simulations done for the tip structure, particularly for other applications such as tip-enhanced Raman spectroscopy (TERS) [167, 169–173], AFM [173], scanning electron microscopy (SEM) [174] and for the STM [175, 176]. The finite-difference time-domain (FDTD) method [166, 168, 169, 172, 177] was commonly used in simulating near-field plasmonics since it was computationally feasible[1]. However, it truly limits the simulation domain to a volume that is on the order of a few wavelengths of the excitation radiation. For example, if the tip apex radius of the probe is on the order of 10 nm, the simulation domain dimension using FDTD methods can only be on the order of a few µm's.

The finite element method (FEM) divides the simulation domain into triangular mesh divisions (tetrahedral for 3D) where the size of the mesh unit can change dynamically depending on the domain boundaries [177, 178]. The regions with a higher density of meshing will require more computational resources to solve for physical quantities, but will make a better approximation of the solution. For microscopy

---

[1]FDTD uses a uniform grid meshing in a coordinate system.

applications, especially THz-STM, the FEM is more practical to employ since the simulation domain can be several orders of magnitude larger than the wavelength (i.e. 1 to 10 mm). The mesh size can strategically vary so that the far-field regions have large mesh sizes while the near-field region will have a very fine mesh structure [179, 180]. In microscopy simulations, the FEM algorithm would smoothly transition a very fine mesh structure in the tip near-field to a coarser one at the outer regions, as already demonstrated by [78, 167, 181]. Therefore, for THz-STM, where the excitation wavelength is about 300 μm at 1 THz, a nearly full scale model of the STM of several mm can be created using the FEM method. The actual STM device is much larger, thus particular components of the setup can be placed in the simulation volume. In STM, the probing tip is a few mm in length and the sample can be a few mm wide and 100s of μm thick. Although THz radiation may propagate on the scale of cm to m to get to the STM junction, far-field optics is assumed where the original waveform emitted by a THz source should be the same waveform incident to the STM. Therefore, the propagation region contains the background radiation, which is assumed to have the same profile as the known field measured in the far-field as shown in Figure 2.1. While FDTD simulators are readily available and can be built by an individual researcher, high-level FEM simulators that include 3D model construction are usually provided in commercial software package. This Thesis employs COMSOL Multiphysics© software to create simulations of the THz-STM experiment.

4.1   COMSOL Multiphysics

COMSOL Multiphysics© [182] is a powerful tool for FEM electromagnetic simulations of complex structures that have has no analytical solutions. It is appropriate to employ the software to simulate the the electromagnetic coupling of THz pulses to the STM. A typical sequence using COMSOL is to first build the geometry, define material properties, set up physics boundary conditions, generate the mesh, run the simulation and then analyze the generated output. The remainder of this chapter

goes through the details to setup a THz-STM simulation and to analyze simulated solution data.

4.1.1 Electromagnetism for the Finite Element Method

The Wave-Optics module in COMSOL is employed to formulate and numerically solve the differential form of Maxwell's equations where boundary conditions are defined at material interfaces [182]. Magnetic and electric fields can be solved by first computing the vector potential $\boldsymbol{A}$, using the equation:

$$\nabla \times \mu_r^{-1} \left(\nabla \times \mathbf{A} \right) + \mu_0 \sigma \frac{\partial \mathbf{A}}{\partial t} + \mu_0 \sigma \frac{\partial}{\partial t} \left(\epsilon_0 \epsilon_r \frac{\partial \mathbf{A}}{\partial t} \right) = 0, \tag{4.1}$$

where μ_0 is the magnetic permeability and ϵ_0 is the electric permittivity of free space, μ_r is the material's relative permeability, ϵ_r is the material's relative electric permittivity and σ is the material's conductivity. All material properties are assumed to be isotropic. This is a form of Ampere's law in Maxwell's equations where the electromagnetic field components can be numerically solved for spatially and temporally [182, 183].[2]

The model is only focused on the space embodying the tip and sample, as depicted in Figure 4.1, which is illuminated by a THz pulse similar to the one shown in Figure 2.1. To simulate a free-space THz pulse propagating from the port window to the tip-sample junction, the Electromagnetic Waves, Transient interface, a package under the Wave-Optics branch [183], is implemented to first solve a time-domain wave equation for the magnetic vector potential, and then map out the time dependent electric field values.

4.1.2 Simulation Assumptions

Explicit methods (known as time-crawling) calculate the state of a system at a later time from the state of the system at the current time, while implicit meth-

---

[2]The manual does not specify the name of a specific gauge in for solving $\mathbf{A}$. It is quoted in the Wave Optics Module manual [183]: "using the gauge for which the scalar electric potential vanishes".

ods find a solution by solving an equation involving both the current state of the system and the later one. In a 1D case, for an electromagnetic simulation to have numerical stability and convergence, the mesh size and time-step must satisfy the Courant–Friedrichs–Levy (CFL) condition [184, 185]:

$$C = \frac{c\Delta t}{\Delta x} \leq C_{\max} \tag{4.2}$$

where C is a dimensionless parameter, c is the speed of light, Δt is the time-step and Δx is the mesh size. C_{max} is usually equal to 1 for explicit methods (implying that small time steps should be used) and can be very large for implicit methods depending on the algorithm and type of problem. In the 3D case, Eq. 4.2 is a summation of three C components, one for each direction, which still have to satisfy the inequality. Based on Eq. 4.1 where the net sum of all space and time components must equal zero, the solver is implicit by nature. The COMSOL Multiphysics software utilizes advanced algorithms to take short-cuts when it is appropriate to help eliminate redundancy [182, 183]. The case of simulating THz-STM allows for $C_{\max}$ to be set reasonably high and short-cuts to be taken by the solver. This is beneficial, especially for the detailed mesh regions in the near-field where the electromagnetic radiation within a single time-step would essentially span the entire near-field region and would not change too much spatially.

It is important that simulations have to undergo several trials where the mesh size and time-step vary to test for numerical stability of the solution. If the same solution is outputted over a range of tested Δt and Δx, we can be confident in the simulation stability.

4.2 THz-STM simulation setup

4.2.1 Geometry

The COMSOL model shown in Figure 4.1 is built to closely resemble a real THz-STM experiment. The simulation geometry consists of an exposed 2 mm long tapered

tungsten wire with a shaft diameter of 0.25 mm and full cone angle of 32°, resting above the sample at a separation distance, d_{ts}. THz pulses enter the STM chamber at a default angle of incidence, $\alpha = 35°$, which is close to the angle used in our THz-STM experimental setup [132]. Table 4.1 lists all geometric parameters used to build the model. The experimentally measured THz pulse using EO detection (see Chapter 2), as shown in Figure 2.1, is expected to be the waveform seen at the location of the STM junction after several mm of propagation. In order to produce this effect, the integral of the EO waveform is inputted into the simulation as a pulsed-waveform function with peak value of 2.0×10^4 V/m and excited at the port window. The THz emitter generates a THz pulse that evolves into the EO THz pulse in the far-field due to propagation effects from a dipole emitter source. THz pulses generated at the port window propagate towards the tip-sample junction. After 4 mm of propagation, the pulse profile has a 1 picosecond pulse duration, spectral power peaked at 0.5 THz, resulting electric field peak amplitude of 1.8×10^4 V/m due to dispersion losses, and a spatial Gaussian beam width of about 2.2 mm as typically measured by EO sampling experiments.

In the real experiment the dipole THz emitter is located on an optics bench setup outside of the STM. The THz beam is focused into a custom-built STM chamber port window that contains a focusing lens. The simulation geometry and boundary condition setup attempt to mimic the port window to get a THz beam of constant width towards the STM junction. Representing the port window as a disk source using a Gaussian spatial profile for the THz beam, the beam waist diameter is obtained using Eq. 2.31 where the inputted dimensional parameters corresponds to the actual STM chamber window port for focusing THz beams. The lens inserted into the port window has a focal length of 54 mm and diameter of 18.5 mm. Using the lens' dimensions and 600 μm wavelength for a THz beam that peaks at 0.5 THz gives a beam waist diameter as 2.2 mm. The spatial beam profile with regards to the simulation geometry is shown in Fig. 4.2.
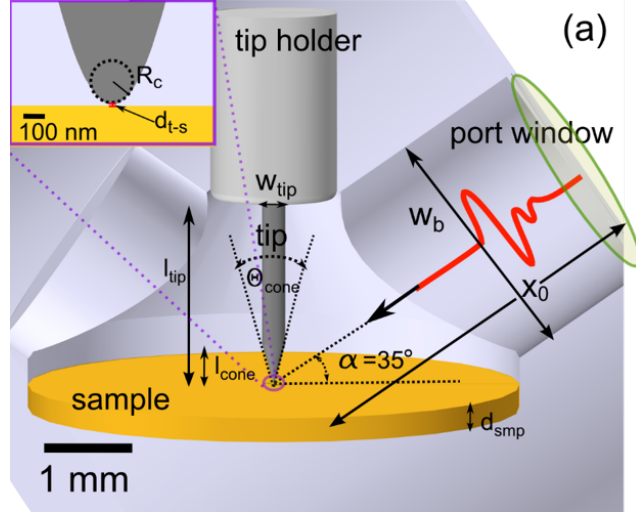
Figure 4.1: The representative COMSOL geometry of the THz-STM which consists of only the tip held by a tip holder, sample, and port window incident to the sample at 35°. Physical dimensions of the geometric entities in the model are best to set scale with the actual experiment. The inset shows a zoomed image of the STM junction where the tip apex has radius of curvature R_c and is separated from the sample by gap distance d_{ts}.

Table 4.1: Table containing the dimensional parameter values corresponding to the geometry in Figure 4.1.

Description	Symbol	Value
Tip shaft diameter	w_{tip}	0.25 mm
Full tip length	l_{tip}	2.0 mm
Full taper height	l_{cone}	0.45 mm
Full taper cone angle	$2\theta_{\text{cone}}$	32°
Apex radius of curvature	R_c	15 to 100 nm
Sample thickness	d_{samp}	0.25 mm
Sample diameter	w_{samp}	5.3 mm
Tip-sample distance	d_{ts}	10 to 100 nm
Effective beam diameter (1/e width)	$w_b = 2w_0$	2.2 mm
Port angle relative to sample plane	α	35°
Distance from port to STM	x_0	4.0 mm
Full port window diameter	W	8.0 mm
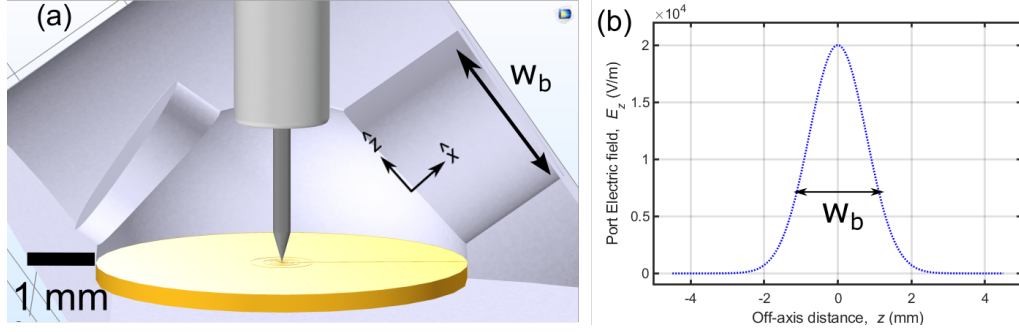
Figure 4.2: (a) Diagram showing the geometric parameters and coordinates of the simulation port window. The entire port window spans 9 mm in diameter. The inner tube shows the region where most of the beam amplitude is contained, in which the meshing structure is more detailed. (b) Plot of the spatial profile of the port beam having a Gaussian structure with 1/e beam width of $w_b = 2.2$ mm. The port width is wide enough to compensate for the decaying amplitude tails which helps minimize the beam cut-off.

In this chapter, simulations were conducted using the initial condition based on the waveform of the port pulse excitation applied to the window. In earlier versions of the simulation, propagation effects were not known so the EO waveform was inputted at the port window and assumed to be the same waveform that would appear as the incident field at the STM junction. However, it was discovered that the port window behaves like a disk dipole where the electric field of the emitted pulse at the source evolves into its derivative (i.e. its far-field form) after propagating to the STM junction location. Subsequent simulations corrected the far-field propagation effects by using the integral of the EO pulse as the source pulse for the port window. Therefore, the correct pulse that appears at the STM junction location should be the EO pulse.

For the sake of distinguishing old versions of the simulation from the newer simulations with regards to the port waveform input, figure captions in this chapter will be noted with "first generation" for the older simulations. The first generation simulations do not account for the propagation effects and excites the EO THz pulse at the port window. Otherwise, figures that do not have any special notes are assumed to have the port pulse corrections applied by exciting the integral of the EO THz

pulse at the port window, which would eventually evolve to the proper EO THz pulse at the location of the STM junction. More details for the port pulse dependence are discussed later in subsection 4.4.4.

4.2.2 Variables

The COMSOL solver obtains the magnetic and electric fields by first computing the vector potential $\mathbf{A}(\mathbf{r}, t)$ as a function of spatial coordinate, $\mathbf{r}$, and time. $\mathbf{A}(\mathbf{r}, t)$ can be converted to the corresponding electric, $\mathbf{E}(\mathbf{r}, t)$, and magnetic field, $\mathbf{H}(\mathbf{r}, t)$, components. The Cartesian field components can be thought as "raw" quantities outputted by the solver. Variables are defined to transform simulated quantities into meaningful forms. For this setup, the propagation direction for incident THz pulses is along the true x-axis. Figure 4.1 shows the x-z plane of the simulation model tilted at 35° counter-clockwise so that the tip appears vertical. The angle of incidence between the propagation axis and sample plane is set at α, thus the STM geometry must rotate relative to the Cartesian axes in the x-z plane. To measure the field components perpendicular and longitudinal to the tip shaft axis, the x-z field components generated in COMSOL have to be transformed with the following rotation operation:

$$
\begin{pmatrix} E_\perp^{\text{tip}} \\ E_\parallel^{\text{tip}} \end{pmatrix} = \begin{pmatrix} \cos(\alpha) & -\sin(\alpha) \\ \sin(\alpha) & \cos(\alpha) \end{pmatrix} \begin{pmatrix} E_x^{\text{sol}} \\ E_z^{\text{sol}} \end{pmatrix}
\tag{4.3}
$$

where $E_\perp^{\text{tip}}$, $E_\parallel^{\text{tip}}$ are the perpendicular and parallel components relative to the tip axis, which are transformations of E_x^{sol} and E_z^{sol}, the Cartesian x-z components generated by the solver. Rotated field components obtained by applying the transformation in Eq. 4.3 is an example where the user must manually set up the definitions before the start of the simulation. The Wave Optics Module also has built-in EM variables such as current density, energy density, polarization fields, etc. that can be acquired during or after the simulation run.

Table 4.2: Variables that can be extracted from raw simulation output. Variables without an equation are equal to simulation values generated by the solver.

Description	Symbol	Equation
Electric field components	E_x, E_y, E_z	E_x^{sol}, E_y^{sol}, E_z^{sol}
Magnetic field components	H_x, H_y, H_z	H_x^{sol}, H_y^{sol}, H_z^{sol}
E-field parallel to tip	$E_\parallel^{\text{tip}}$	$E_x^{\text{sol}}\sin(\alpha) + E_z^{\text{sol}}\cos(\alpha)$
E-field perpendicular to tip	$E_\perp^{\text{tip}}$	$E_x^{\text{sol}}\cos(\alpha) - E_z^{\text{sol}}\sin(\alpha)$
Gap voltage	V_{gap}	$\int_0^d E_\parallel^{\text{tip}}(z_\parallel)\,dz_\parallel$
Sample reflection field ($\perp$ component)	$E_{k,\perp}^{\text{ref}}$	$E_x^{\text{sol}}\cos(\pi - 2\alpha) + E_z^{\text{sol}}\sin(\pi - 2\alpha)$
Current density	J_x, J_y, J_z	J_x^{sol}, J_y^{sol}, J_z^{sol}

4.2.3 Materials

The next step is to assign material properties of the domains dividing up the simulation geometry. Material properties fundamentally change how Eq. 4.1 is solved by setting up boundary conditions. The constitutive parameters for each material are the conductivity, dielectric and magnetic permeability constants. The conductivity parameter, σ, is calculated using the Drude model for complex conductivity ($\tilde{\sigma} = \sigma_1 + i\sigma_2$):

$$
\begin{aligned}
\tilde{\sigma} &= \frac{\sigma_{\text{d.c.}}}{1 - i\omega\tau} \\
&= \frac{\sigma_{\text{d.c.}}}{1 + (\omega\tau)^2} + i\frac{\sigma_{\text{d.c.}}\omega\tau}{1 + (\omega\tau)^2}
\end{aligned}
\tag{4.4}
$$

where $\sigma(\omega = 0) = \sigma_{\text{d.c.}}$ is material's d.c. conductivity at zero frequency, $\omega = 2\pi f$ with f being the peak frequency (0.5 THz), and τ is the electron scattering time. Table 4.3 summarizes material constants that could possibly be assigned to each entity of the STM geometry. Tungsten (W) is normally assigned to the tip and steel to the tip holder. The sample can vary from standard metals such as gold, doped semiconductors and dielectrics. The background dielectric, ϵ_b, is usually assigned to the sample while the magnetic permeability of all materials is typically set to 1.

The electron scattering time is obtained from measured electron mobility versus

doping data [186] via the formula:

$$\tau = \frac{m_{\text{eff}}\mu_e}{e},\qquad(4.5)$$

where m_{eff} is the effective electron mass and μ_e is the electron mobility.

Table 4.3: Table of values of conductivity constants used for the materials in the simulation. The values correspond to the peak frequency of 0.5 THz.

Material	$\sigma_{\textbf{DC}}$ [S/μm]	τ (fs)	$\sigma_{\textbf{f=0.5}\text{THz}}$ [S/μm]
Air/Vacuum	0	—	0
W	17.9	10	$17.9 + i0.6$
Au	41.0	30	$40.6 + i3.8$
Steel	1.4	20	$1.4 + i0.1$
n-Si 10^{19}cm^{-3}	0.019	65	$(18.1 + i3.7) \times 10^{-2}$
n-Si 10^{18}cm^{-3}	0.0045	150	$(3.72 + i1.75) \times 10^{-3}$
n-Si 10^{17}cm^{-3}	0.0012	500	$(4.52 + i5.68) \times 10^{-4}$
n-Si 10^{16}cm^{-3}	0.00019	720	$(3.09 + i7.02) \times 10^{-5}$
Dielectric Si	0	—	0

The material parameters are restricted to be constant even though the simulation is in the time domain. By plotting the conductivity in Fig. 4.3, one can see that over the range of 0 to 1 THz, the conductivity of standard metals does not vary too much. The same goes for highly-doped semiconductors in the low broad-band range as seen in Fig. 4.4. Thus it is safe to assign constant parameters for the materials used in this simulation when dealing with low THz input frequencies. From 4.3, the material parameters at low THz frequencies do not even deviate much from their corresponding d.c.

The conductivity variations for doped semiconductors as shown in Fig. 4.4 do become a concern when frequency components in the 0.5 to 10 THz range are simulated. The functional dependence for conductivity would be inserted in frequency domain simulations. However in time domain simulations, the fixed complex conductivity
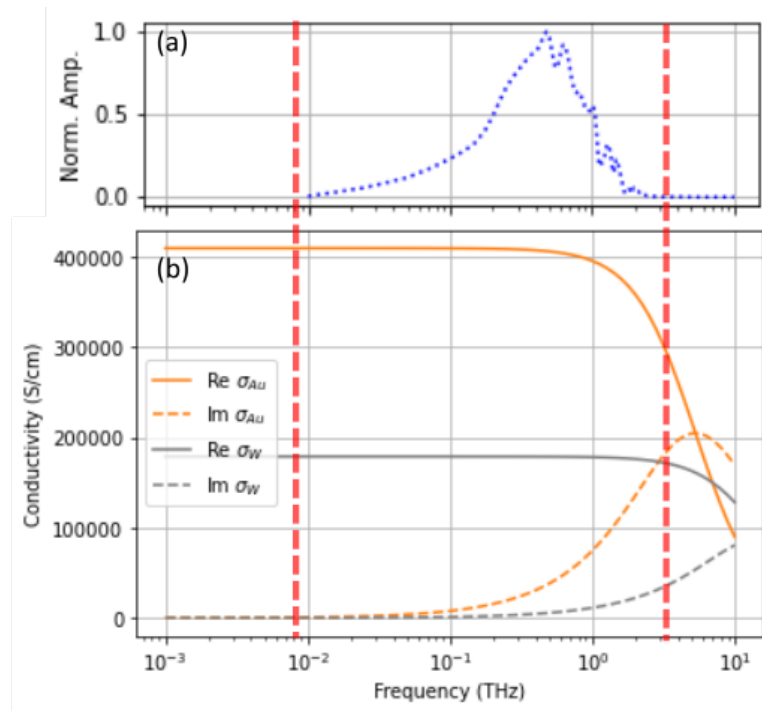
Figure 4.3: (a) Frequency spectrum of a typical THz pulse used for THz-STM experiments showing a broadband range of 0.01 to 3 THz. (b) Plot of the THz conductivity for standard metals, Au and W. The highlighted region between the vertical red dashes outlines the regime of the experimental THz pulse broadband. The simulation specs are set to work within the same broadband range.

value in Table 4.3 corresponding to 0.5 THz must be used in the entire simulation run. The dropping tail of the real part of the conductivity spectra and the increase of the imaginary component at higher frequencies imply that the numerical accuracy for the material's response to high frequency components of the incident THz pulse is compromised. For example, the ringing oscillations that follow the main pulse of the THz waveform would have drove the lower conductivity components of the material. Regardless, according to Fig. 4.3(a), the field amplitude of higher frequency components greater than 1 THz should be low enough to justify using a single value of conductivity for all time-domain simulations. There are algorithms to convert frequency dependent conductivity to transient conductivity or vice-versa as done for the data-analysis of experiments where THz transient conductivity is measured [83, 187–189]. Unfortunately, COMSOL does not have the algorithm built into their software. It would require a separate project to create a custom module that couples with the rest of the simulation.

The simulation parameters are set to cater to the THz broadband of about 0 to 3 THz. The physics of THz coupling can be properly simulated and visualized for spatial and temporal details corresponding to 3 THz frequency components and below. A different design would need to be considered to effectively simulate the THz coupling for higher THz frequencies.

4.2.4   Mesh

FEM uses an algorithm to dynamically mesh the geometry according to the set boundaries. The mesh structure is shown in Fig. 4.5. Usually, a defined material region would consist of one domain. However due to the nature of the problem, in order to properly simulate THz-STM experiments in full detail, the meshing geometry must be divided up into the far-field and near-field. That means that the same material may be composed of several mesh regions. Using the auto-mesh algorithm would create one or a few mesh elements for the near-field region. The solution outputted
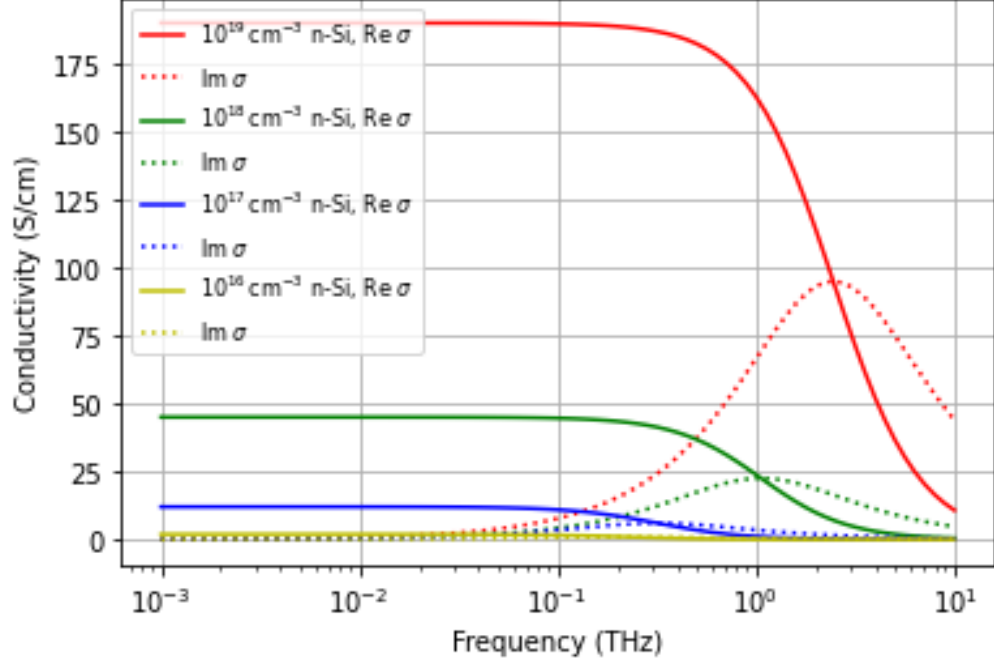
Figure 4.4: Conductivity plots within the experimental THz broadband range for n-doped Si at various doping levels ranging from 10^{16}cm^{-3} to 10^{19}cm^{-3} at room temperature.

by the solver is numerically stable in a standard mesh. However, it can miss some of the rich physics in the detailed near-field regime, that is the STM gap region.

Fig. 4.5(a-d) shows how the vacuum region, tip and sample are divided up into sub-domains. The meshing dimension varies from about 100 μm in the far-field propagation regions (Fig. 4.5(a)) to 1 nm in the STM gap region (Fig. 4.5(d)). For this particular setup, using the values from Table 4.1, the mesh sizes around the tip apex must be a fraction of the tip-sample distance ($d_{ts}/5 \sim 2$ nm) according to the C parameter in Eq. 4.2, while the outer domain mesh sizes are a fraction of the THz wavelength corresponding to peak of the spectrum at 0.5 THz ($\lambda_{THz}/5 \sim 120\mu$m). That is a mesh size difference of 5 orders of magnitude between the far-and-near-field regions. The meshing algorithm fails to accomplish the mesh structure for sub-nanometer tip–sample separation as used in STM experiments while maintaining the same dimensions for the rest of the geometry. $d_{ts} = 10$ nm is the smallest distance

that can be properly meshed in the junction region. The COMSOL software was not capable of creating a proper mesh grid that spans more than 6 orders of magnitude in mesh element sizes within a simulation[3]. The main interest is to simulate the EM coupling of THz, so by performing the same simulation over a range of distances, any discovered trends can be used to extrapolate for the case of small distances below 10 nm (to be later discussed in the upcoming sections).
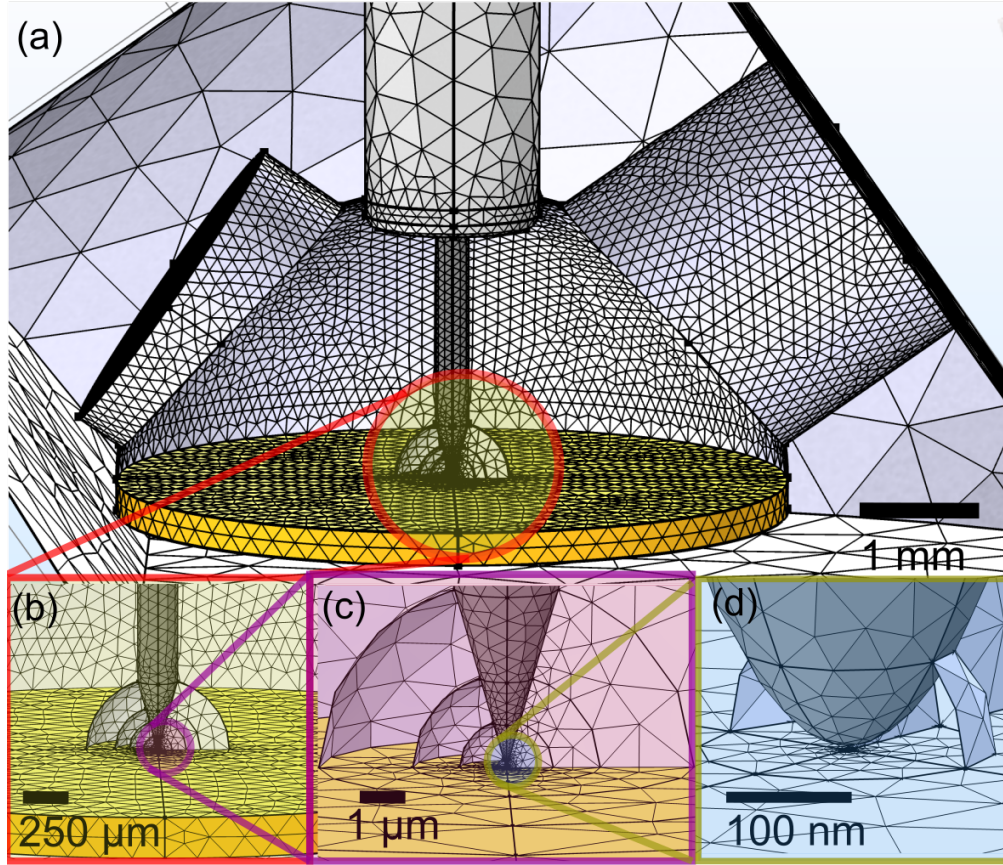
Figure 4.5: (a) The COMSOL THz-STM model is meshed using the finite element modeling (FEM) technique. The free-space propagation regions surrounding the tip have mesh size 100 μm (i.e. ($\lambda/5$)). The outermost zones where negligible amounts of field exists contains mesh sizes as large as 500 μm. (b, c) The mesh element sizes decrease in the regions surrounding the conical taper. The space around the tip is divided into circular mesh zones to enable a smooth meshing transition from the outermost to inner zones. (d) The innermost zone is the 10 nm tip-sample gap region consisting mesh elements of 2 nm size (i.e ($d_{ts}/5$)).

According to Eq. 4.2, the C parameter can range from 0.01 in the far-field to 10^4 in

the near-field based on the range of possible meshing length scales. The background incident field should be constant within a $(15\,\mu\text{m})^3$ volume at any given time-step. For the low C regime, which is in the far-field where the mesh size is 100 μm, solving for the propagation of THz would proceed explicitly similar to FDTD. In the high C regime, the solver must adapt to perform EM computations in the narrow near-field regions and output solutions for every NF mesh coordinate while respecting the boundary constraints set by the material properties. Thus, for numerical stability, C_{max} for this type of simulation must be really large to tolerate the mesh reduction by 5 orders of magnitude.

4.2.5 Processing simulation data

The time-step increment usually used in the setup is $\Delta t = 0.05$ ps, which divides a 40 ps simulated time window into 801 time-steps. According to the time-step the distance traveled by a light wave is 15 μm (i.e. $c_0 \Delta t$), which divides a 1 THz wave (300 μm) into 20 elements. When the simulation is complete, each mesh unit contains a temporal array of solved field component quantities. EM field components can be extracted at any point within the simulation space. Fig. 4.6(a) shows how point probes are placed at the port, below the tip apex as well as several other locations of interest. Fig. 4.6(b) plots the E_z^{tip} component waveform extracted at the marked locations. Line-cuts and volume cuts of the simulation data are also useful post-processing steps to analyze interesting regions. Unlike real measurement devices, all probes are "theoretical" detectors that measure the simulated electromagnetic quantities at their assigned positions and do not have any influence on the physics simulations.

Table 4.4 summarizes the probing locations in Fig. 4.6, symbolic references used in figures for this chapter, and the typical field quantities of interest that are probed

---

[3]Attempts were made to create a geometry with a tip-sample separation of less than 10 nm. The usual consequence is that the tip and sample end up being in contact (i.e. no gap) after the mesh generation, which is not the desired simulation setup.
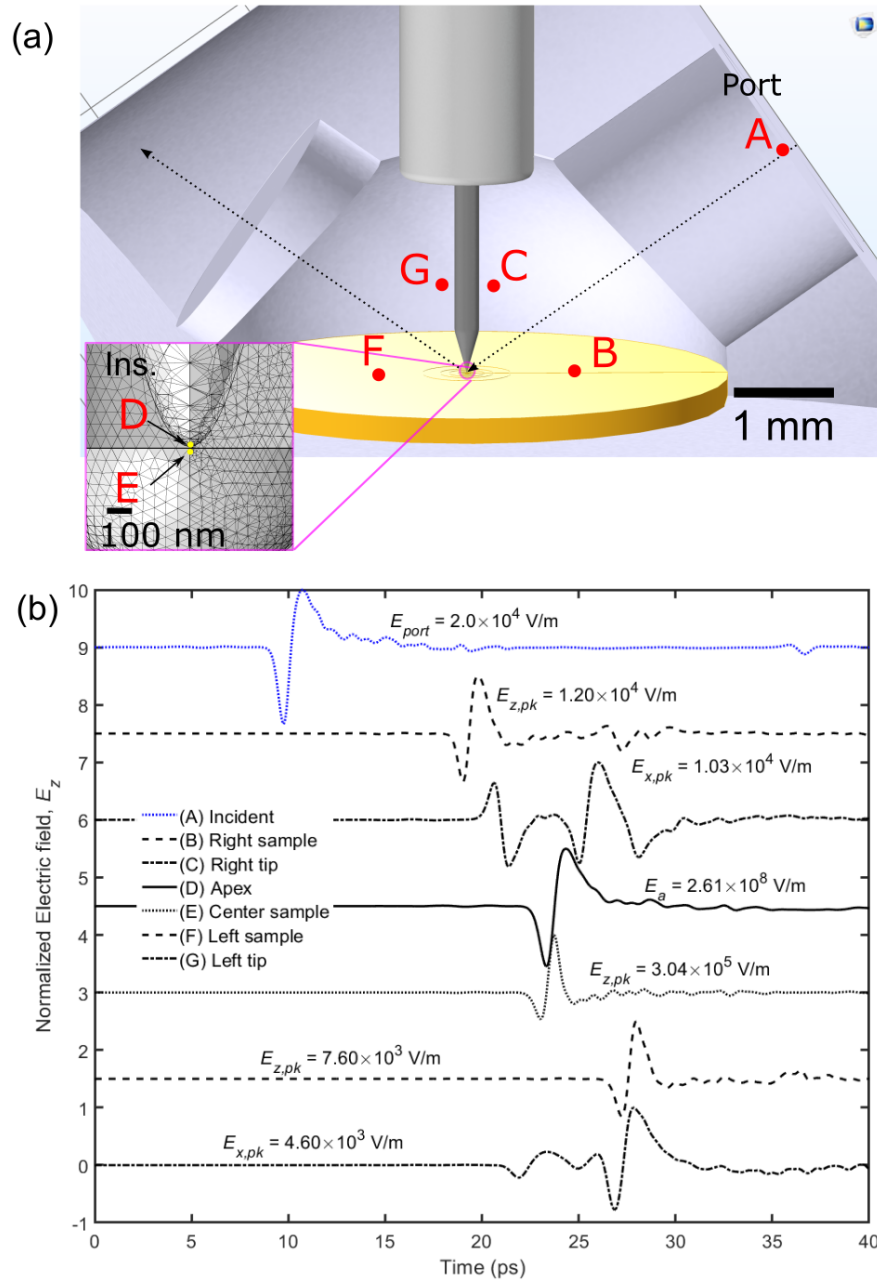
Figure 4.6: (a) Field measurement probes are placed at locations A to G as shown in the mesh figure. The probes can measure the components of electric and magnetic fields, as well as other various electromagnetic quantities. (b) In a time-dependent study which runs from 0 to 40 ps, all probes collect electric field measurements at their positions. The z-component of electric field, E_z is shown for all probes. Probes C and G, measure the perpendicular component, E_x, of the electric field that travels along the tip shaft. Peak field amplitudes are annotated.

at the locations. COMSOL allows all possible computationally generated quantities in the Electromagnetics and Wave Optics modules such as electric field components, magnetic field components, current densities, polarization fields and energy density, to be outputted in simulated data files. For the majority of this chapter, the only quantities of interest are the electric field waveforms.

Table 4.4: Table describing probing locations and variables of interest corresponding to the location markers at 4.6.

Location	Description	Symbol	Probed fields
Fig. 2.1	E.O. Measurement[4]	E_{EO}, E_0	$E(t)$
A	Port window	E_{port}	$E_z(t)$
B	Right side of sample	$E_{\mathrm{samp,R}}$	$E_\parallel^{\mathrm{tip}}(t)$
C	Right side of tip	$E_{\mathrm{tip,R}}$	$E_\perp^{\mathrm{tip}}(t)$
D	Incident field at the junction[5]	E_{inc}	$E_z(t)$
D	Tip apex near-field	E_{apex}, E_A	$E_\parallel^{\mathrm{tip}}(t), E_\perp^{\mathrm{tip}}(t)$
E	Near-field above sample surface	$E_{\mathrm{samp}}^+, E_S^+$	$E_\parallel^{\mathrm{tip}}(t), E_\perp^{\mathrm{tip}}(t)$
E	Near-field below sample surface	$E_{\mathrm{samp}}^-, E_S^-$	$E_\parallel^{\mathrm{tip}}(t), E_\perp^{\mathrm{tip}}(t)$
D - E	Gap voltage line-cut	V_{gap}	$V_{\mathrm{gap}}(t)$
F	Left side of sample	$E_{\mathrm{samp,L}}$	$E_\parallel^{\mathrm{tip}}(t)$
G	Left side of tip	$E_{\mathrm{tip,L}}$	$E_\perp^{\mathrm{tip}}(t)$

In Table 4.4, the locations not shown in Fig. 4.6 are the electro-optic (EO) measurement and the tip apex position in free-space. The experimental optics setup to measure the EO THz pulse treats the detector as a far-field receiver that detects the propagated waveform in far-field away from the THz source. It is important to run the THz-STM simulation without any objects present (i.e. no tip and sample) to obtain the pulse waveform after propagating away from the port window to a distance in the far-field. The field measured at the far-field position in free-space simulations, E_{inc}, should match the EO pulse. It will be shown later that E_{inc} from simulation and

E_{EO} from experimental measurement are equivalent, hence either pulse can be used as the incident pulse in waveform and frequency spectra analyses. There are subtle phase differences between a simulated E_{inc} versus a real detection of E_{EO} using a THz detector due to the environment in which THz pulses have to propagate. In the simulation, the propagation distance is several millimeters. For the external THz optics setup, the THz pulses emitted by a source have to travel meters while being guided by optics apparatus (i.e. mirrors and lenses) before they reach the detector. For the remainder of the figures in this chapter, E_{inc} and E_0 notations are interchanged. This also applies to the Fourier amplitudes, A_{inc} and A_0.

Numerical stability has been verified by using finer mesh sizes and a smaller time-step of $\Delta t = 0.025$ ps, thus halving the CFL number. The same waveforms in Fig. 4.6(b) are basically traced out by reducing the mesh and/or time-step size with waveform amplitudes that have been observed to differ by about 5% or less.

4.3 Pulse Propagation and Coupling

4.3.1 Free-space propagation

Wave optics behaviour is shown in the simulation for a freely propagating THz pulse. The pulse front deviates away from a plane wave the farther the pulse travels away from the port window as shown in Fig. 4.7. The pulse wave-front front resemble the hyperboloid surfaces discussed for Gaussian beam optics. The waveforms and corresponding spectra at various distances away from the port window are plotted in Fig. 4.8.

The field evolution from the near-field to the far-field can be quantified by plotting the product of the propagation distance with the peak field amplitude as shown in Fig. 4.9. The electric field depends on $1/r$ far from the source. Thus, when the product reaches a constant, the pulse has propagated into the far-field regime. In Fig. 4.9,

---

[4]Electro-optic measurements are not part of the simulation. The external optics for THz generation and detection is located outside of the STM chamber.

[5]Only for the case of free-space simulations where no objects are present.
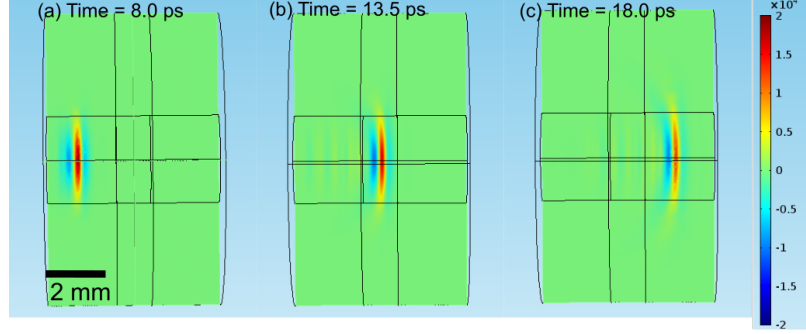
Figure 4.7: Snapshots of the THz pulse propagation in free-space animation at propagation times: (a) 8 ps showing the pulse exiting the port; (b) 13.5 ps where the pulse reaches the middle and (c) 18 ps as the pulse exits the simulation volume. Note the port window is on the left-hand side in these simulations and uses the same port window dimensions as the THz-STM setup (see Table 4.1).

the curve plateau occurs at about 4.5 mm of propagation. Therefore, beyond 4.5 mm, the radiation is in the far-field. Determining the near-field and mid-field regime requires calculating a fidelity factor, which is a form of the overlap integral between the waveform at a particular position and one of components of the source dipole term ($p, \dot{p}, \ddot{p}$ from Eq. 2.17). The end of the near-field (or beginning of the mid-field) is where the waveform begins to resemble $\dot{p}$ (i.e. overlap increases with $\dot{p}$). The end of the mid-field is where the propagated pulse begins to resemble $\ddot{p}$.

The Rayleigh range calculated using Eq. 2.30 yields about 2 mm, corresponding to a $\lambda = 600\,\mu\text{m}$ (0.5 THz) beam emitted out of a window with a 2 mm radius. In Fig. 4.8, after 2 mm, the THz pulse emerging out of the port evolves into its first derivative shape and maintains the waveform shape all the way towards the end of the simulation. The shape of the pulse in the far-field of the source should reflect the first derivative of the source current. The pulse measured near the port should appear like the source current waveform as verified by the first simulated waveform in Fig. 4.8(b). The pulses simulated at 3 mm and beyond already reflect the first derivative of the source current according to Fig. 4.8. Beyond the Rayleigh range, the THz pulse enters the far-field regime. This is depicted in Fig. 4.9 where the product of the pulse peak amplitude and propagation distance plateaus at 4.5 mm and beyond.
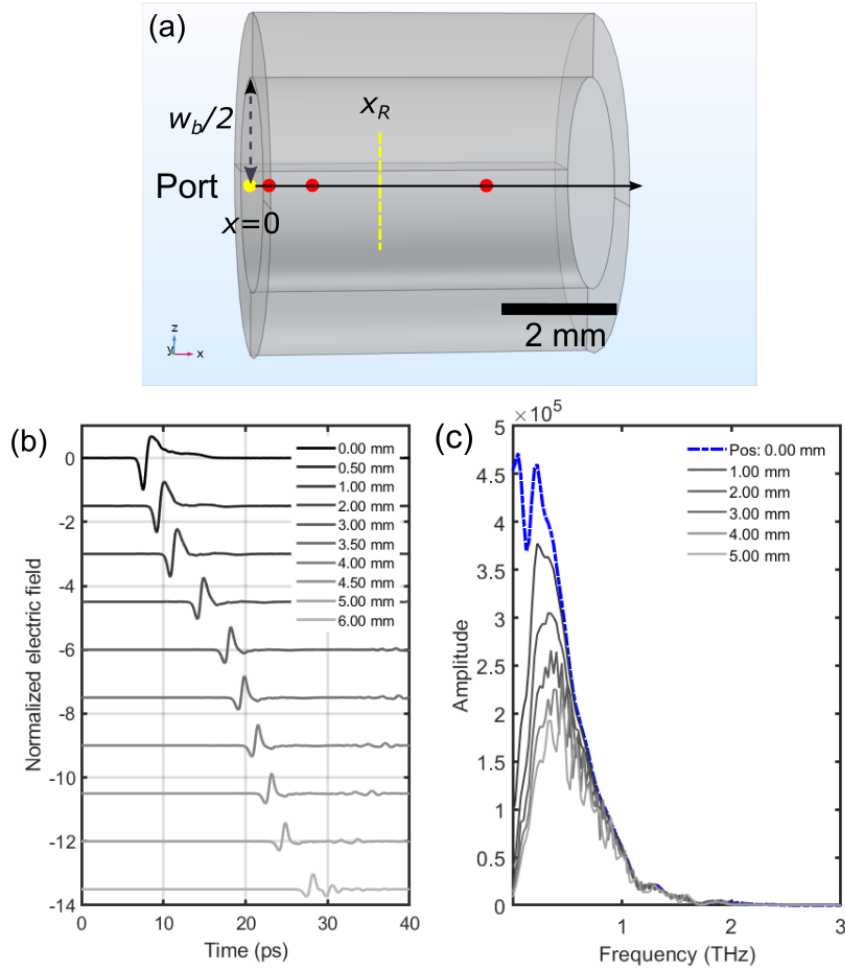
Figure 4.8: (a) A free-space tube geometry used to propagate an inputted THz pulse at the port window located at $x = 0$ mm. The red dots indicate critical regions for the transition of near-field to mid-field to far-field. Blue squares indicate the probing locations for the simulated waveforms. Waveforms are normalized with respect to the absolute maximum pulse peak in the series (i.e. waveform at $x = 0$) to depict the amplitude drop versus propagation distance and vertically shifted for distinction. (b) Waveforms collected at various distances away from the port window and (c) their corresponding frequency spectra.
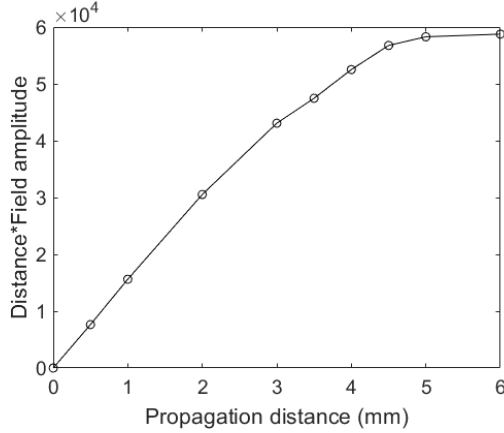
Figure 4.9: Plot of the propagation distance and peak amplitude product vs propagation distance to determine the critical far-field distance. The plateau occurs around 5 mm of propagation.

According to Eq. 2.1 or 2.19, the electric field is entirely in the far-field regime when the product of the field amplitude with distance, r, yields a constant.

Waveforms and spectra for a planar pulse-front are shown in Fig. 4.10. The waveforms are collected off the propagation axis along the $+z$-axis. Away from the propagation axis or at increasing z, the peak of the spectrum shifts to lower frequencies. Fig. 4.11 plots the time delay for the peak of the off-axis pulse to get to propagation distance x relative to the on-axis pulse. Note that the time delays for the pulse peak would be zero if the pulses are extracted along a hyperbolic arc, as shown in Fig. 4.11 (inset). The propagation dispersion is important in THz-STM since different sections of the tip wire would receive a transformed version of the incident THz pulse in the unfocused beam regions.

4.3.2 Far-field visualization

A completed simulation contains computed EM field components for every mesh co-ordinate at every time-step. This allows for the evolution of EM coupling to the STM to be animated. Fig. 4.12 are animation snapshots for the electric field components relative to the tip axis, E_x^{tip} and E_z^{tip}, in the xz-plane at several time stamps. In Fig. 4.12(a-b), the pulse leaves the port with polarization aligned in the xz-plane
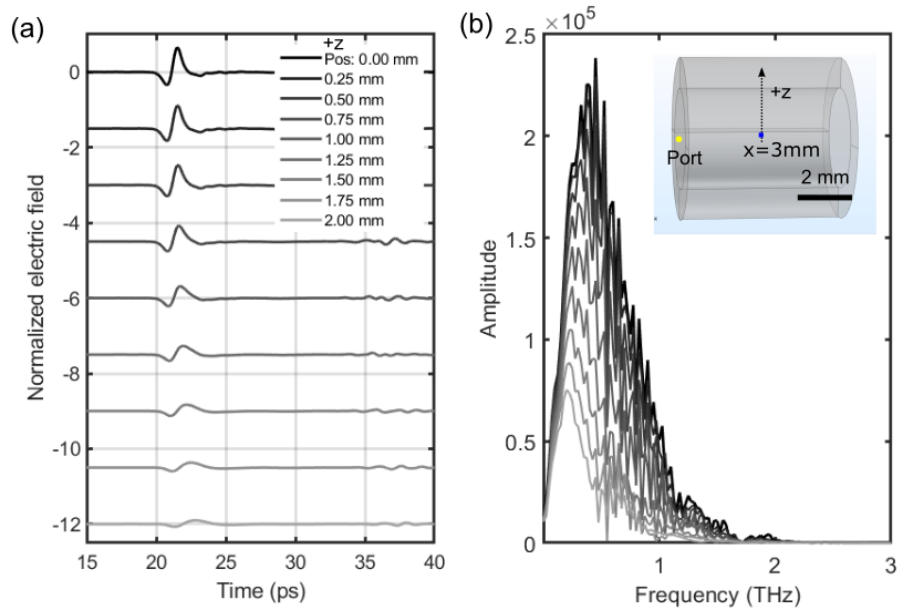
Figure 4.10: (a) Waveforms are collected off the propagation axis along the $+z$-axis at $x = 3$ mm (shown in the inset in (b)) and (b) their corresponding frequency spectra. The peak shifts to lower frequencies away from the focus. Waveforms are normalized to the peak of the $z = 0$ mm pulse where the amplitude is maximum and vertically shifted for separation.
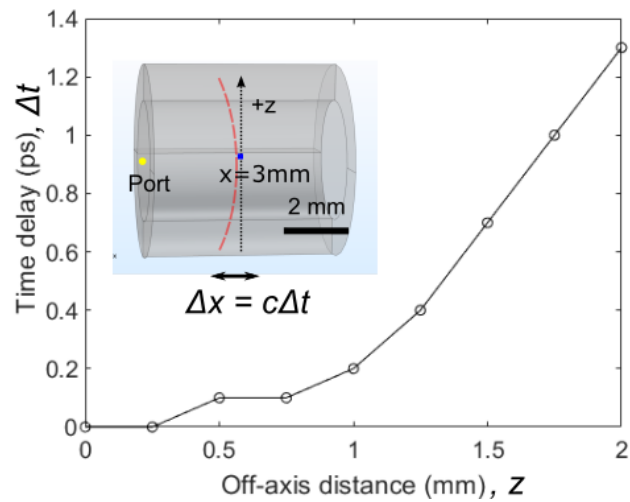
Figure 4.11: Plot of the time delay, Δt, of the pulse peak arrival versus the off-axis distance along the $+z$-direction at $x = 3$ mm. The inset shows a hyperbolic arc where the wavefront has the same phase at 3 mm away from the port window.

85

and propagates towards the tip-sample at an incident angle of 35°. In Fig. 4.12(c), the x-component of the incident field couples to the tip-shaft, which excites a surface wave that propagates towards the STM junction in the –z-direction. In Fig. 4.12(d), as the incident pulse approaches the STM junction, the z-component of the incident field couples to the sample's surface, which excites a surface wave that propagates towards the STM junction in the –x-direction. The overall electric field measured at the tip apex is the superposition of the incident pulse, the sample and tip-shaft surface waves, and scattered fields.

4.3.3 Near-field visualization

Fig. 4.13 zooms into the near-field at the pulse peak arrival time at the junction, $t = t_p$. Fig. 4.13(a,b) displays the NF frame at the peak time. Although the sample used for this is simulation is n-Si that has a high conductivity, the snapshots show that there is an electric field that penetrates below the sample surface. Simulations suggest that the NF region around the tip apex must include not only the gap but also the region below the sample surface. Field penetration is only present in simulations for the transient case. When a constant bias is applied to the tip, field penetration is absent as depicted in Fig. 4.13(c). This demonstration for the existence of the near-field inside the semiconductor sample was important for interpreting the THz-field driven transport observed in THz-STM measurements of Si(111) [2].

Spatial characterization of the near-field consists of extracting electric field profiles by doing line-cuts along the x and z-directions at the peak-field time, t_p. In Fig. 4.14(a), the E_x and E_z components are plotted along x show that the full-width-half-maximum (FWHM) of the E_z peak is 0.18 μm, which is less than the twice the radius of curvature of the tip apex, $2R = 200$ nm. Fig. 4.14(b) shows the electric field line-cut of E_z in the z-direction. Crossing the sample interface, the electric field drops two orders of magnitude and decays further. In the d.c. case where the tip is statically biased at 3 V relative to the sample, no field penetration was simulated
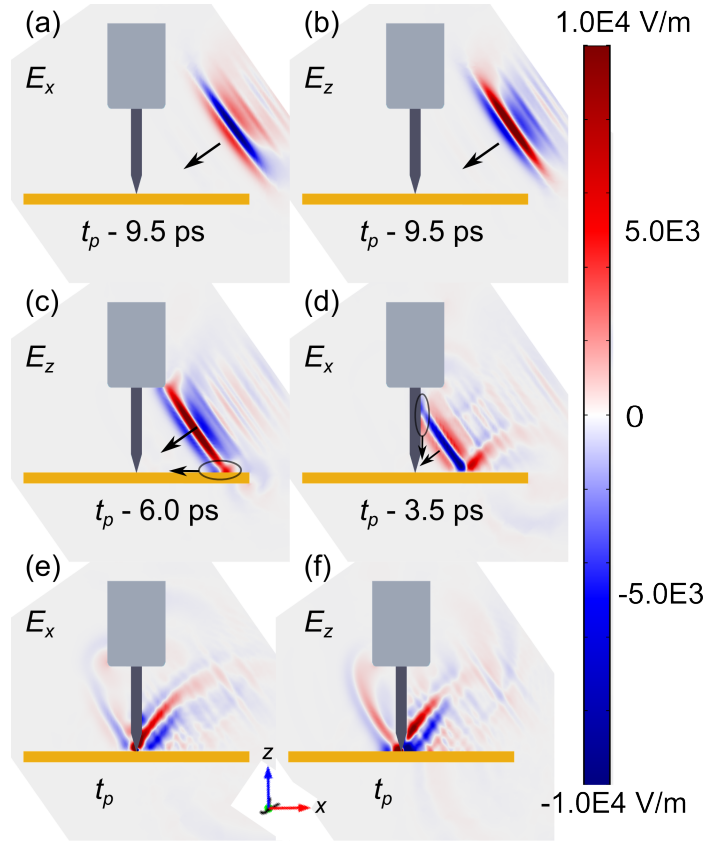
Figure 4.12: Temporal snapshots of the simulated far-field showing (a) the x and (b) z-components of the THz pulse excited at the port and propagating towards the STM junction. (c) As the incident pulse approaches the junction, the z-component of the field excites a surface plasmon polariton (SPP) that propagates along the sample's surface, and (d) then, the x-component of the field, E_x excites a SPP that propagates along the tip shaft. The (e) x and (f) z-components of the field, when the pulse reaches the junction. The time shown is relative to the pulse's peak arrival at the tip apex, t_p. A complicated scattered radiation pattern is depicted in the far-field. The incident field is vertically polarized at linear polarization angle $\beta = 0$ at the port window with peak amplitude of 2.0×10^4 V/m., propagating at an angle of incidence of $\alpha = 35°$ relative to the sample. The sample used was 10^{19} cm^{-3} n-doped Si. Note that the sequence of plots are placed in order of chronology where the components shown help illustrate the coupling of the incident THz pulse to either the tip or sample. (Results from the first generation of simulations.)

$t = t_p$ Steady-State (DC)

(a) (b) (c)

E_x E_z E_z

1.4 μm x 1.4 μm

1.0E5 V/m

0

-1.0E5
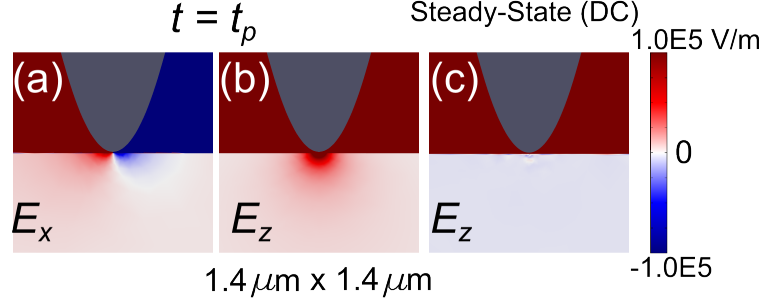
Figure 4.13: Snapshots zoomed in at the junction in at time t_p when the main peak of the incident THz pulse arrives, showing the (a) x and (b) z-components of the nearfield. In the 10^{19}cm^{-3} n-doped Si sample, small amounts of field penetrate below the sample surface. (c) In a DC simulation, no field exists below the sample surface. (Results from the first generation of simulations.)

(Fig. 4.13(c)).
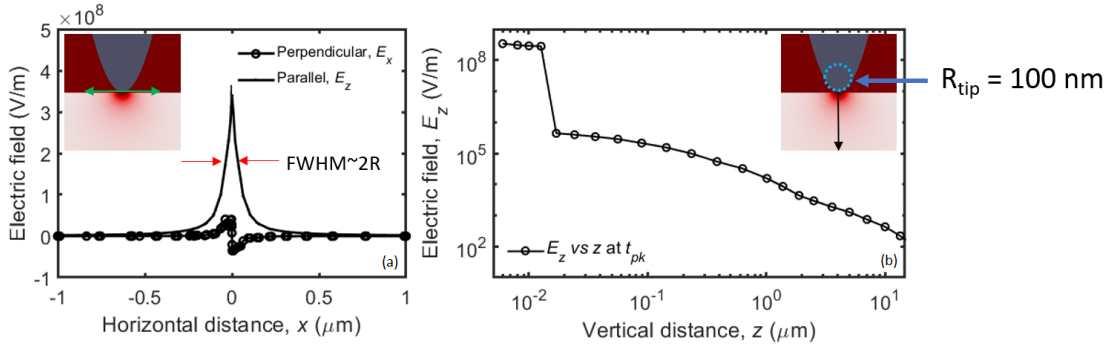
Figure 4.14: (a) Lateral field profiles of field components Ex and Ez obtained at $t = t_p$ and $z = 1$ nm below the apex. The full-width-half-maximum (FWHM) of E_x is $0.18\,\mu$m, which is approximately the tip apex's diameter $2R = 0.20\,\mu$m. (b) The vertical profile of E_z along the center $x = 0\,\mu$m at $t = t_p$. (Results from the first generation of simulations.)

The field decay in the sample shown in Fig. 4.14(b) shows a $1/z$ dependence beyond 1 μm. The near-field forms around the tip apex which has a spatial dependence that follows the dipole model in Eq. 2.17. A few microns away is already considered far-field considering the dipole size for a 100 nm radius tip, which resolves the $1/z$ dependence in Fig. 4.14(b) at 1 μm and beyond. Closer to the sample surface, which is close to the tip apex, the other near-field terms with $1/z^2$ and $1/z^3$ dependence are still contributing to the net electric field, thus resulting in a slower decay at

sub-micron distances.

4.3.4   Probed waveforms

In THz-STM simulations, the desired THz pulse depicted in Fig. 2.1 is required to target the tip-sample in order to match closely with the actual experiments. Day-to-day measurements of the THz field using EO sampling typically yields the same waveform, hence it is assumed that THz pulses of the same profile are sent into the STM. A source current transient, $j_0(t)$ is applied at the port, which radiates the incident electric field, $E_0(t)$, towards the STM junction. $j_0(t)$ is set to be proportional to the integral of the EO-measured pulse. The electric field amplitude of the far-field radiation is expected to be the proportional to the first time derivative of $j_0(t)$, which returns back the EO-measured pulse profile. A simulation was conducted where the STM geometry is absent to measure the uncoupled far-field pulse. As the pulse propagates, the waveform changes shape as it travels further away from the port. The simulated far-field pulse, $E_{inc}(t)$, probed several mm away from the port is shown in Fig. 4.15(a) (blue dash), is verified to be nearly the same as the measured E_O pulse. At further distances, the pulse maintains the same shape. There are small waveform differences due to propagation dispersion. Therefore, the pulse that is incident to the STM junction is an evolved pulse with amplitude $E_{inc}(t) \propto dj_0(t)/dt$.

Using a source current to generate an electric field with peak of $E_{0,pk} = 2.0 \times 10^4$ V/m, the incident field decays to a peak amplitude of $E_{inc,pk} = 1.4 \times 10^4$ V/m when it reaches the STM junction. The simulated near-field waveform at the tip apex in Fig. 4.15(b) (black line) has a different waveform shape compared to the incident pulse. The apex pulse has a peak field amplitude, $E_{a,pk}$, that is about 10^4 times greater than the incident field. The probed field at the apex peaks at 3.2×10^8 V/m, corresponding to a field enhancement of 2.3×10^4. The apex pulse waveform consists of a broadened main peak followed by a series of reflection pulses whose origin is the excitation of THz-SPPs that propagate along the tip shaft and reflect off the tip holder boundary.
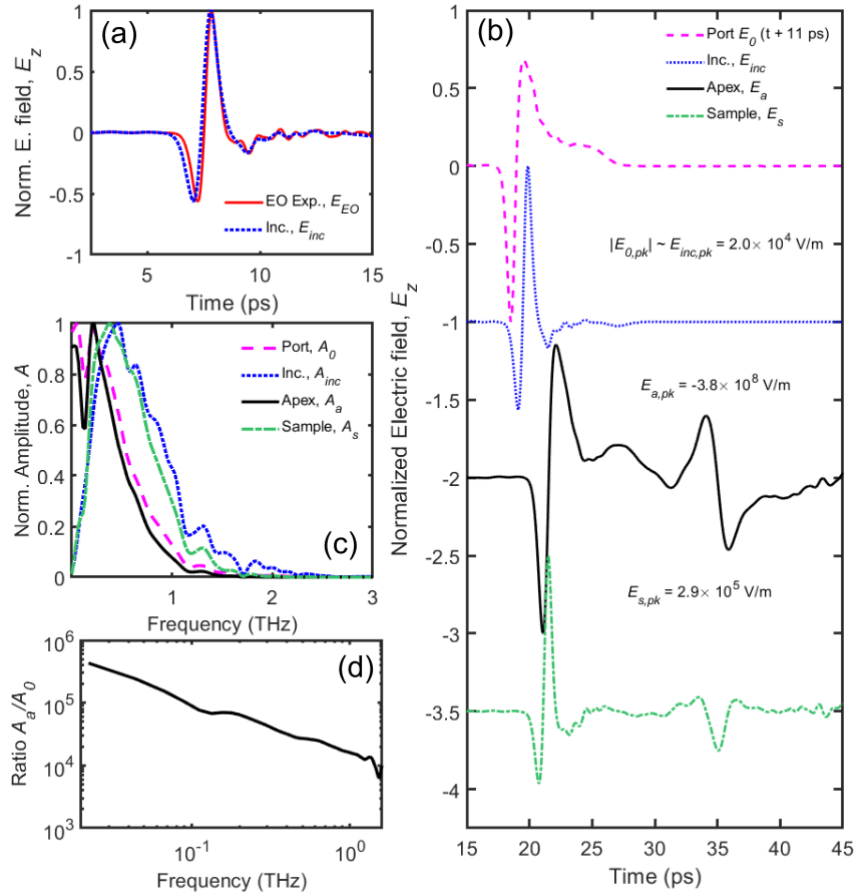
Figure 4.15: Probed waveforms for the STM geometry: (a) The simulated incident pulse in the far-field propagating 4 mm from the port window (blue dash) compared with an experimentally measured pulse using electro-optic (EO) sampling (red line). (b) The port pulse (magenta) is plotted with the peak shifted forward by 11 ps for alignment purposes. The incident pulse is repeated from (a). The THz near-field pulse probed at the tip apex (black), and 2 nm below the sample surface (green) plotted with the simulated incident pulse (blue dash). The pulses are normalized to their peak amplitude. Their actual peak amplitudes of the apex pulse and the incident pulse are annotated. All pulses are shifted vertically for separation. (c) Corresponding frequency spectra for the near-field pulses with normalized amplitudes. The experimental EO spectrum (blue) is shown for reference. (d) The amplitude of the apex near-field spectrum divided by the amplitude of the incident spectrum which gives the field enhancement factor as a function of frequency. The curve follows a $1/f$ trend.

90

As previously observed, field penetration occurs within the sample. The electric field existing below the sample showed a peak value of 3.2×10^5 V/m, 3 orders of magnitude lower than that in the gap. The near-field consists of both the field in the gap and the field below the sample surface. The electric field waveform probed 2 nm below the sample surface is shown in Fig. 4.15(b) (green line), which is strikingly different compared to the near-field in the STM gap. The waveform of the electric field existing in the sample has roughly the same shape as the incident pulse.

The normalized frequency spectrum of each simulated pulse is plotted with the spectrum of the incident pulse in Fig. 4.15(c). The peak of the EO spectrum (red) and the incident spectrum (blue) occur at 0.45 THz. The sample spectrum (green) overlaps with the incident spectrum. The spectrum for the apex (black) is shifted towards lower frequencies (0.2 to 0.4 THz). The frequency spectrum of the apex pulse is referenced with the spectrum of the incident pulse in Fig. 4.15(d), which is the frequency dependent field enhancement factor. The field enhancement decreases as $1/f$ in the frequency range of 0.25 THz to 2 THz, then decays further in the noise regime.

The presentation of the spectral dependence of the THz near-field amplitude such as the example presented in Fig. 4.15(d) will be recurring throughout this chapter and in the later chapters. The intent is to highlight THz antenna coupling as previously discussed in section 2.5.3 and schematically shown in Fig. 2.9. The mapping of THz incident fields to near-field via antenna coupling is a neat feature that can be extracted from these full-scale electromagnetic simulations. In general, the simulations only embodies a time window ranging from 40 to 100 ps since they generate solutions of electromagnetic quantities only in the THz regime. The smallest frequency that can be resolved from these simulations is simply $1/T_{\text{sim}}$ where T_{sim} is the total simulation time, which works out to 0.01 to 0.025 THz.

Figs. 4.15(c) and (d) only shows the spectral behaviour from 10^{-2} to 3 THz which is in the higher frequency regimes. It appears that there is a d.c. component at

zero frequency from the plots. However this is simply a simulation artifact where the lower frequencies cannot be resolved. To go beyond the scope, one can pursue these simulations in the frequency domain or excite infrared and microwave pulses at the port window. This allows for the frequency dependence to be mapped out in a wider range of the electromagnetic spectrum. According to Eq. 2.46, the transfer function plot over a wider range of the electromagnetic spectrum will show an amplitude rise to the resonant frequency (determined by $f_0 = 1/(2\pi\sqrt{LC})$) and then drop off afterwards. These simulations, which focus in the THz range, only show the $1/\omega$ drop-off portion of the spectrum. The spectroscopic behaviour of the near-field amplitude dependence on frequency will be discussed further using RLC and transfer function analyses in Chapter 6.

4.4   Geometry Variations

One crucial aspect for the THz-STM simulations is the ability to set degrees of freedom. Geometric parameters are allowed to be defined as variables for the purpose of conducting parameter sweeps where one or more dimensions can be varied and the others are fixed. The purpose of parameter sweeps is to optimize the structure design and conditions for THz pulses to couple to the STM. Some figures in this section belong to an older generation of simulations where the EO THz pulse is used for the port window.

The inset illustrations in Fig. 4.16(a), (c) and (d) depict how geometric parameters such as the tip-sample separation, d_{ts}, the angle of incidence of the incident pulse's propagation vector relative to the sample surface, α, and the angle of the linear polarization of the incident pulse relative to the tip axis, β, can all be varied to create unique simulation cases. Parameter sweeps were carried out using $E_0 = 2.0 \times 10^4$ V/m for the incident pulse. A metal sample (i.e., gold) was used.

The parameter sweeps performed using this COMSOL model of the THz-STM only focuses on the THz regime spanning 0 to about 3 THz (i.e. the bandwidth of
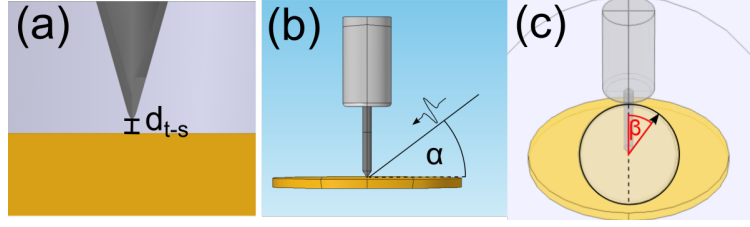
Figure 4.16: Variations of the simulation can be created by performing parameter sweeps of (a) tip-sample distance, d_{t-s}, (b) angle of incidence from the sample plane, α and (c) linear polarization of the radiation exiting the port window.

the incident THz pulse). The coupling is frequency dependent in general. Different configurations for the experimental apparatus may cater to or be optimized for certain frequencies. The summaries that will be presented for the geometric parameter sweep simulations are only descriptive for the 0 to 3 THz range, which does not necessarily imply that reported geometric coupling behaviour is universal for other frequency ranges.

4.4.1   Field enhancement versus distance

The tip-sample separation, d_{ts}, is increased beyond 10 nm to simulate the field enhancement as a function of distance. E_z^{tip} is measured at the tip apex and above the sample surface to obtain the field enhancement factors as a function of distance in Fig. 4.17(a). The field enhancement drops approximately by a factor of 10 for a factor of 10 increase in the tip-sample distance for distances, $d_{ts} \leq 1\,\mu\text{m}$. The field enhancement factor is obtained from ratio of the peak electric fields:

$$F = \frac{E_{\text{apex,pk.}}}{E_{\text{inc,pk.}}}, \tag{4.6}$$

where $E_{\text{inc,pk.}}$ is the peak of the electric field incident to the STM junction which must be obtained from a free-space simulation with no objects present, and $E_{\text{apex,pk.}}$ is the peak of the near-field around the tip apex obtained from the THz-STM simulation. From Fig. 4.15 the incident and apex waveforms differ in shape where the apex field resembles the integral of the incident pulse. The peak of the pulse occurs at different times where the max of the incident pulse is an inflection point for the apex pulse.

93
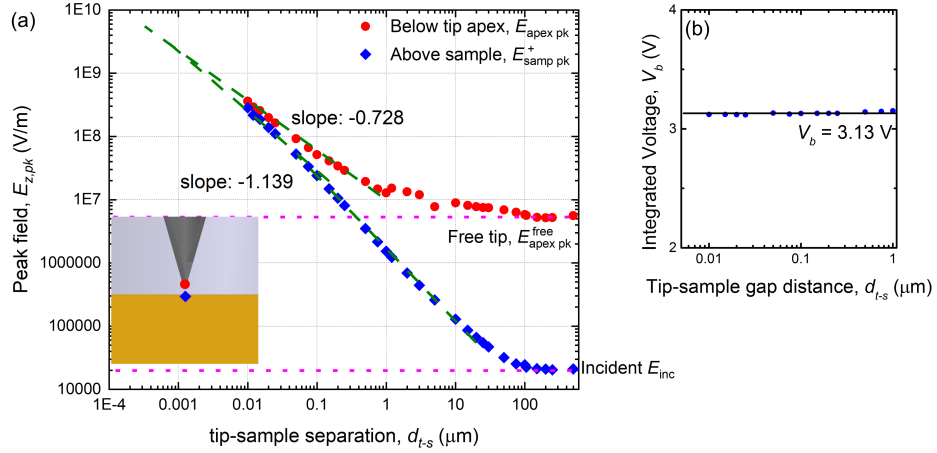
Figure 4.17: (a) Field enhancement factor versus tip-sample separation measured below the tip apex (red circles) and above the sample surface (blue diamonds) as depicted in inset. The field generally grows by a factor of 10 for every decrease of separation by factor of 10. The slopes of the linear region in the log-log plot are annotated. (b) The probing locations for the near-fields are below the tip apex and above the sample surface. The near-field bias voltage obtained by integrating the z-component of the electric field over the gap distance. The bias stays nearly constant for $d_{ts} \leq 1\mu m$. The gap integration is carried out at the peak field time, t_0, for several tip-sample separations d_{ts}. The simulations used a tungsten tip with a 100 nm apex radius and cone-shaped taper with a 32° cone angle on a gold sample. (Results from first generation of simulations.)

94

It was already stated that for a 10 nm gap, the enhancement factor is 2.3×10^4. Fig. 4.17(a) shows the electric field probed at the extremities of the gap (i.e. below tip apex and above sample surface), which allows the natural field enhancement by either structures to be known by the asymptotic behaviour at large distances. In the limit where the tip-sample distance is large, the field values plateau to a constant. Beyond 100 μm, the field measured at the tip apex approaches a constant value corresponding to a field enhancement of 280, which is the free tip's natural field enhancement due to the tip's sharpness. At the sample's surface, the field enhancement approaches 1, indicating that the incident field propagates along sample's surface without interacting with the tip. Fig. 4.18(a) displays various waveforms at the same probing location where the simulation geometry is a free sample (Fig. 4.18(b)) or a free tip (Fig. 4.18(c)). The enhanced field at the apex for the STM geometry differ drastically compared to the waveforms for the free-tip and free sample. It is further seen in the frequency spectra plot in Fig. 4.18(d).

The slopes of the linear regions in the log-log plot shown in Fig. 4.17(a) were determined for the enhanced field plots versus tip-sample separation distance to be -0.728 at the tip apex and -1.139 below the sample surface. If the field was plotted for a probe placed in the middle of the gap, the slope should be about -1. The slope of -1 directly translates to a $1/d$ dependence for the electric field strength versus distance. At small tip-sample separations, the electric field inside the gap should be uniform similar to that of a parallel plate capacitor. The field strays from the gap by fringing due to the tip shape, hence the plots do not visualize a perfect $1/d$ dependence.

The voltage at which the tip is biased relative to the sample can be calculated by integrating E_z^t across the gap. Although the field penetrates to some depth within the sample, the magnitude of the field also drops 3 orders of magnitude when crossing the sample interface. Integrating E_z^t beyond the sample surface only increases the voltage negligibly. The peak gap voltage plotted in Fig. 4.17 stays nearly constant for $d_{ts} \leq 1\mu$m. Similar results for constant voltage over a small tip-sample separation

were experimentally found and theoretically fitted for the AFM case [190]. Using the results in Fig. 4.17(a) and (c), the peak of the incident field can be used to estimate the gap voltage, which leads to the product approximation:

$$V_b = F(d_{ts}) \times E_0 \times d_{ts} \tag{4.7}$$

A gap voltage of 3.13 V corresponds to the enhanced peak incident field of $E_0 = 2.0 \times 10^4$ V/m in a 10 nm gap. The average field enhancement factor, F below the tip apex is about 1.6×10^4. The STM geometry capacitance can be simulated by applying a 1 V d.c. bias on the tip and letting the sample be grounded. Fig. 4.19 plots the capacitance versus tip-sample distance. Similar to the behavior of gap bias, up to about 1 μm, the capacitance is constant with distance, then decreases monotonically with increasing distance. Capacitance computations for the STM geometry were carried out using COMSOL to reveal that the tip wire alone produces half the capacitance compared to the combination of the tip and tip-holder. In THz-STM operation, the tip-holder does not get illuminated since the spot-size of the focused THz beam is about 2 mm. The capacitance dependence on the illumination conditions upon the tip structure suggest that the EM fields around the tip and sample is governed by a partial capacitance.

When the tip-sample distance is much smaller compared to the overall dimensions of the tip geometry (i.e. $d \ll l_{\text{cone}}$), the voltage (or integrated electric field) in the gap stays constant. Fig. 4.19 shows the simulated capacitance versus the tip-sample distance for a tip with dimensions much larger than the sweeping range of gap distances. The capacitance does not show much of a distance dependence up to 1 μm, but drops slightly afterwards. Therefore, the overall capacitance is determined by the full tip structure instead of focused just at the tip apex. Using the $Q = CV$ relation, for a certain amount of charge that becomes focused at the tip apex upon THz illumination, the capacitance stays constant for the voltage between the tip and sample to remain constant regardless of the gap distance.
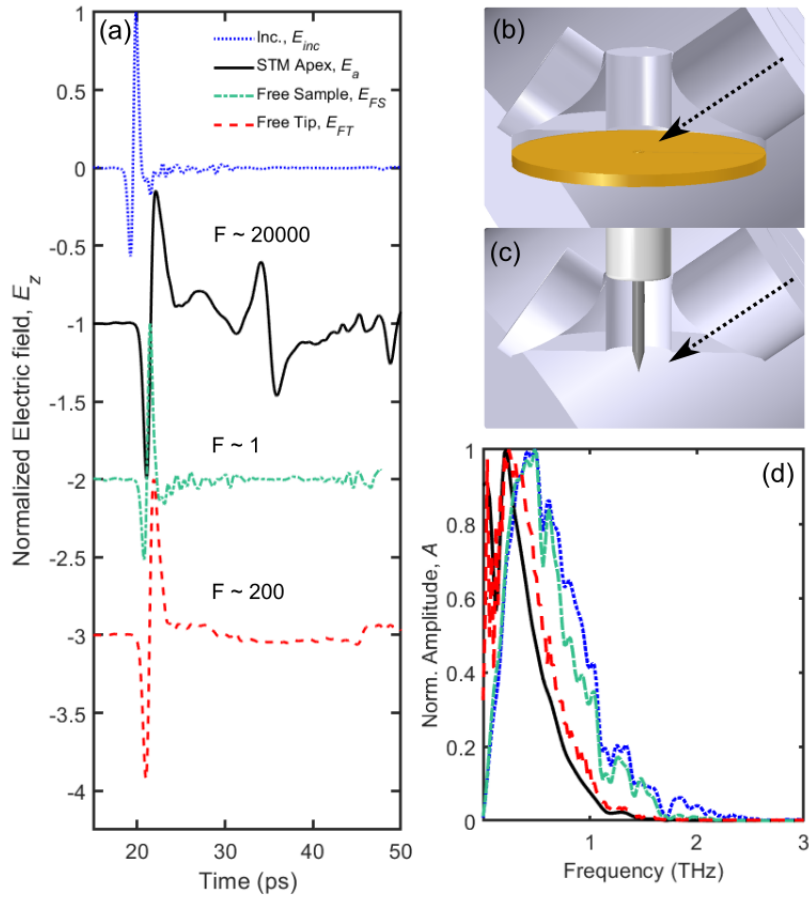
Figure 4.18: (a) Waveforms plotted for the incident field (blue dash), tip apex enhanced field in a full STM geometry (black line), at the surface of the sample with no tip present (teal), and at the tip apex with no sample present (red dash). (b) The free sample geometry. The field is probed at where the tip apex would have been. (c) The free tip geometry. (d) Corresponding frequency spectra using the same legend as in (a).
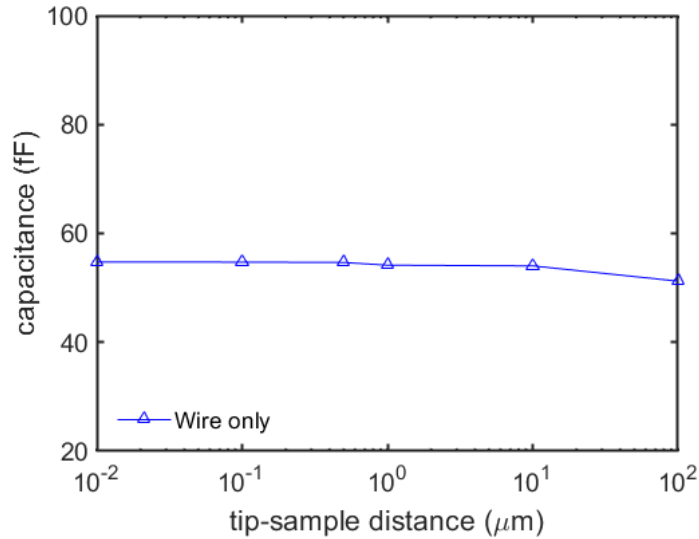
Figure 4.19: Plot of the simulated capacitance vs the tip-sample distance for the tip wire. The capacitance remains constant for up to about 10 μm. Tip apex radius is 100 nm with a cone taper length of 0.5 mm.

4.4.2 Field enhancement versus angle of incidence

Fig. 4.20 plots both the field enhancement factor and the bias voltage obtained from field integration in Eq. 4.7 as functions of the angle of incidence in the xz-plane, α. In the actual THz-STM experiment, the port window guides the THz to the STM junction at 35°. Although 35° is not the optimum angle according to the simulations, its field enhancement value of 1.7×10^4 at $\alpha = 35°$, does not differ too much from the maximum value of 1.8×10^4 at 55°. Angles of incidence around 10° to 30° relative to the tip axis (corresponding to $\alpha = 60°$ to 80°) are optimal for coupling 0.5 to 1 THz field components [105, 106]. The simulations reported $\alpha = 45°$ to 60° maximize the field enhancement. This is consistent with the theoretical studies showing that the enhanced radiation peaks around 55° to 60° since the tip-sample system functions as an antenna with a radiation pattern that peaks at those angles [191]. At low α the incident THz beam gets clipped by the large outer volumes of the sample. Similarly, the lower field enhancement at 60° to 80° is likely due to the cut-off caused by the tip holder.
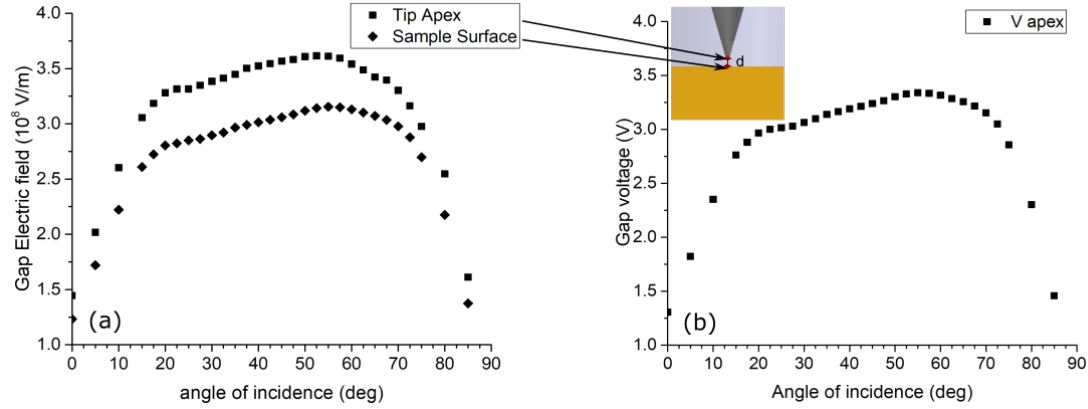
Figure 4.20: The peak near-field amplitude dependence on the angle of incidence, α, of the propagation direction of the incoming pulse relative to the sample. The angle where the near-field sees a maximum is around 55°. (Results from first generation of simulations.)

An additional trace shown in Fig. 4.21(blue) of the enhanced electric field versus α was done for a tip without a tip holder. At large α, the tip holder was becoming an obstacle, so it was removed to allow the incident THz pulses to couple to the STM. At $\alpha = 67.5°$, there are two values for enhanced fields for the case with no tip holder and with an extended tip shaft so the total length covers the tip-holder. The α sweep at larger angles beyond 67.5° continue for the long tip-shaft geometry. The field enhancement is improved for large angles of incidence without the tip holder blocking the propagation of incident THz pulses.

Varying the angle of incidence changes the ratio of field component that can be excited either on the tip or sample surface, which forms SPPs that propagate towards the junction. Little field enhancement should be expected for extreme angles around $\alpha = 0°$ and 90° since these configurations do not provide an optimal coupling condition to form SPPs. Sharp features located on the STM tip such as the tip apex, the taper/shaft edge and the rim at the top of the tip/tip-holder, assist in the formation of SPPs. The optimal angles depict the configurations where center of the THz beam directly targets the tip apex and taper with minimal clipping by other obstacles.
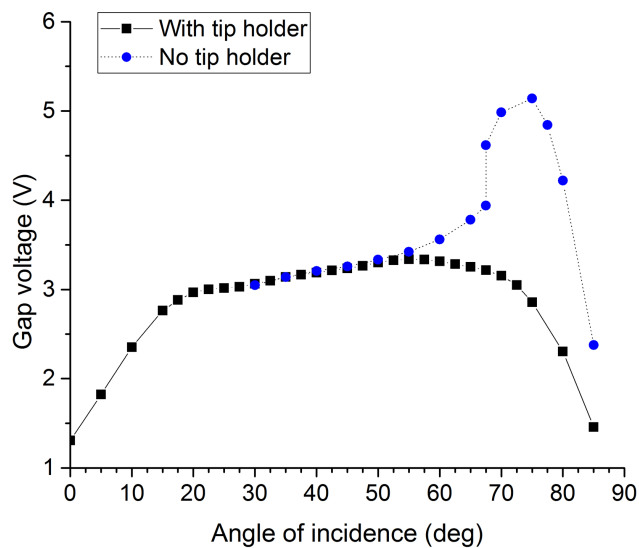
Figure 4.21: The peak near-field amplitude dependence on the angle of incidence, α, of the propagation direction of the incoming pulse relative to the sample. The angle where the near-field sees a maximum is around 55°. In the series with no tip holder, it was replaced by wire, making the entire tip length 4 mm. At $\alpha = 67.5°$, the simulation was done for both 4 mm long wire and then shortened to 2 mm wire, which explains the presence two data points. For the remainder of the no tip-holder case, the 2 mm wire was used for the α sweep beyond 67.5° to allow for the THz pulse to propagate a consistent distance compared to the lower angle sweeps. (Results from first generation of simulations.)

4.4.3 Field enhancement versus polarization

Various linear polarization angles in the yz-plane, β, are tested from the p-polarized (0° and 180°) to the s-polarized (90°) orientation of the incident field relative to the tip-shaft. Sweeping the β angle yielded expected field enhancements which vary as the cosine of β, as fitted in 4.22a. At cross-polarization (90°), the field enhancement is nullified. The results of sweeping β are consistent with dipole antenna-coupling, where the incident field is required to be polarized along the tip axis to measure a near-field signal that stands out from the background. Furthermore, the polarity of the near-field pulse is the same as the incident pulse. Therefore, the direction of the terahertz-driven signals in the STM junction can be controlled by the incident polarity [2, 33]. Fig. 4.22b illustrates how vertically polarized ($\beta = 0°$ or $\beta = 180°$) pulses can couple strongly to form induced tip-sample dipoles along the vertical axis. A horizontally polarized ($\beta = 90°$) pulse is unable to couple to the tip-sample configuration.

(a)   (b)
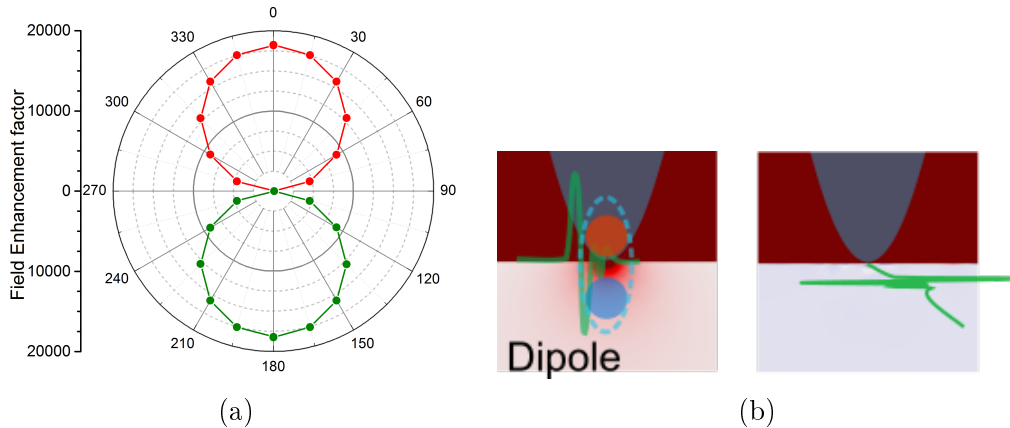
Figure 4.22: (a) By changing the linear polarization of the THz input pulse relative to the tip, the electric field at the near field vanishes when $\beta = 90°$, which is the case of cross-polarization. The field is only maximum when the incident polarization is parallel to the tip. (b) Coupling visualized when the polarization of the incident pulse is parallel or perpendicular to the tip. A dipole can only be formed when the polarization has a vertical component. (Results from first generation of simulations.)

The situation is different when pulses of optical frequencies are used. The tip apex is essentially a polarizable sphere with radius R on the order of 10 to 100 nm. A nano-plasmonic mode consisting of the tip apex combined with the optical wavelength

of light on the same order of dimensions as R can be excited. Thus redoing the β sweep simulations for near-infrared optical frequencies ($\sim$ 800 nm) will not show much drastic change in the field enhancement for horizontally or vertically polarized light. The sinusoidal relation of field enhancement versus polarization depicted in Fig. 4.22 applies strongly to THz frequencies where the wavelength of light is on the same order of dimensions as the tip (i.e. μm to mm). The polarization dependence as simulated is experimentally observed in THz-STM and signals cannot be detected using horizontally polarized incident THz pulses [2]. The THz near-field can only form according to antenna coupling conditions described here and well supported by the results of these simulations where α and β are varied.

4.4.4 Variation of the port pulse

The THz pulse waveform generated at the port window is actually defined by a current source on the window boundary. The THz current transient generated at the window emits an electric field that becomes its first derivative form after propagating away from the window and enters the far-field regime. In order to obtain a standard THz pulse that one would typically measure from experiments (e.g. in Fig. 2.1) to be simulated in the far-field, one must excite the port window with a waveform equal to the integral of THz pulse. The port should emit a THz pulse that would eventually evolve from integral shape near the port to the THz pulse shape at the far-field. In real experiments, the STM components may be located cm's or meters away from the THz source. Simulations cannot be created where the port window is too far from the STM target due to computational resource limitations. We must assume that the THz pulse observed in the far-field of the emitter is the same pulse that is incident to the STM junction. It was already discussed that the far-field regime for THz pulses is already reached after 4 mm of propagation. The simulation was designed so that the STM components are placed at least 4 mm away from the port window.

Previously, it was not known from older generations of COMSOL simulations that

the THz pulse at the port window would quickly evolve into its derivative form after a few mm's of propagation. Fig. 4.23 shows the case when the port window is excited with a current pulse with the same profile as the THz pulse in Fig. 2.1. The propagation of a THz pulse emitted by this window is simulated in free space without any of the STM components in place. Fig. 4.24 shows that the port pulse evolve into its derivative form in the far-field, which we eventually realized, was not the desired THz pulse that was intended for THz-STM simulations.
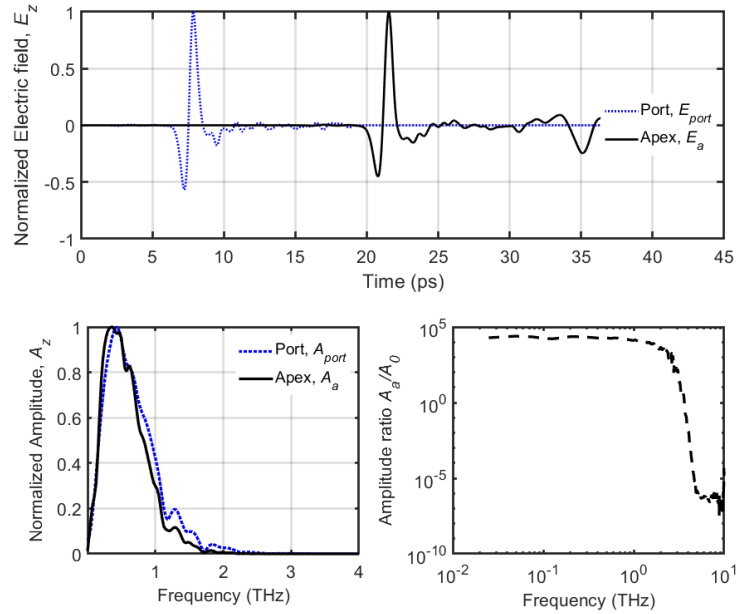
Figure 4.23: (a) The port pulse and apex pulse waveforms. (b) Corresponding frequency spectra. (c) Computing the field enhancement amplitude ratio yields unity for the majority of the spectrum. (Results from first generation of simulations.)

The consequences of assuming the port window pulse being the same as the pulse incident to the STM target may cause one to use the port pulse in analysis instead of the incident pulse. One can see the difference in the field enhancement ratio versus frequency plots in figs. 4.23(c) and 4.24(c) when the incorrect pulse is used. THz antenna coupling is expected filter out the high frequency components of the input and enhance the low frequency amplitudes. Fig. 4.24(c) shows the proper relation.

In the first generation of simulations, the desired THz pulse, as measured experi-
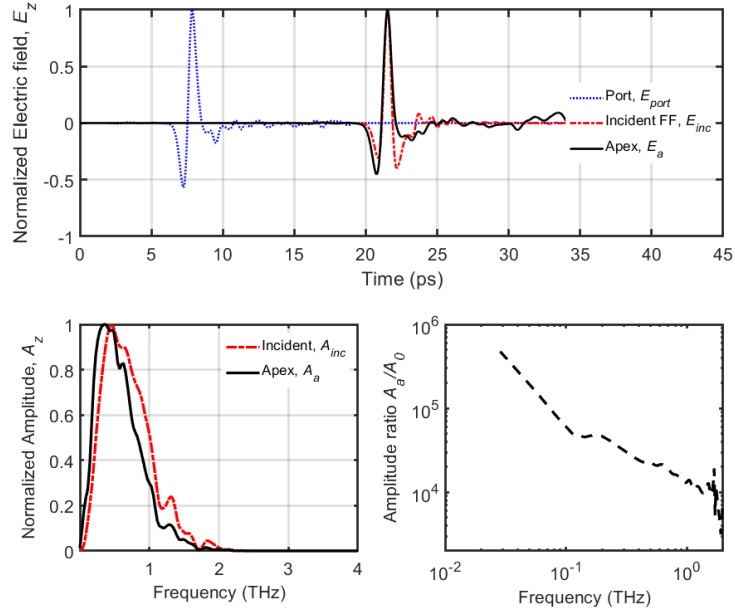
Figure 4.24: (a) The incident pulse obtained from free space propagation simulation without the presence of the tip and tip apex pulse waveforms. (b) Corresponding frequency spectra. (c) Computing the field enhancement amplitude ratio yields a high frequency cut-off spectrum. (Results from first generation of simulations.)

mentally using EO sampling, was inputted directly into the simulation port. However, the analysis is corrected by using the incident far-field pulse in Fig. 4.24(a) when doing pulse or spectrum referencing calculations. Fig. 4.25 shows the corrected series of steps in conducting the second generation of THz-STM simulations in COMSOL. The port window is excited with the integral of the desired input THz pulse. After propagating into the far-field to reach the STM target, the THz electric field would resemble the desired THz pulse that agrees with EO sampling. Finally, the STM geometry can respond to the incident THz pulse and generate a near-field response. The full analysis of the apex waveform with respect to the incident pulse is summarized in Fig. 4.15.

The parameter sweeps of tip-sample distance, angle of incidence, and linear polarization angle in the previous sections were part of the old generation of simulations. The simulations were redone using the new generation method for port excitation
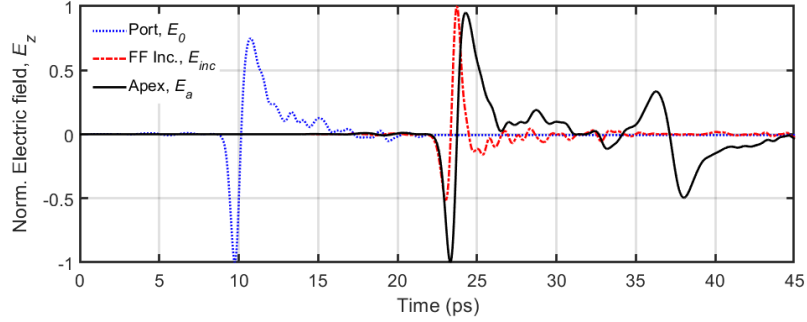
Figure 4.25: Plots of the port, incident far-field and tip apex waveforms where the port input is the integral of the desired THz pulse. Every other simulation not labeled as "first generation" have adapted to this standard for inputting THz pulses into a THz-STM simulation.

only for a few values of the parameter sweep. Fig. 4.26 shows that redoing the distance parameter sweep did not change too much compared to the old generation of simulations. The distance dependence of both data-sets nearly overlap. Redoing a few simulation runs for the angle parameter sweeps yielded a similar result, but would be redundant to create new plots for. The antenna coupling behaviour of the tip is maintained by yielding a high frequency cut-off and low frequency field enhancement response to the incident THz field. The field enhancement versus distance stayed relatively consistent regardless of the port pulse being used. The near-field voltage by integrating the electric field across the gap changed from 3.13 V per 200 V/cm of incident field to 2.85 V by switching to the new generation method of port excitation.

4.5 Material Variations

Another kind of parameter sweep study is to vary the materials used to build the geometry. For all simulations conducted here, tungsten is only used for the tip material. The sample material can vary from standard metals to doped semiconductors. The sample's complex dielectric permittivity influences the near-field coupling [192]. Table 4.3 displays the material constants for the various kinds of materials tested. Near-field snapshots at the peak time are acquired for various samples ranging from

---

[6]Unable to find the filler data points in between for the old-generation series.
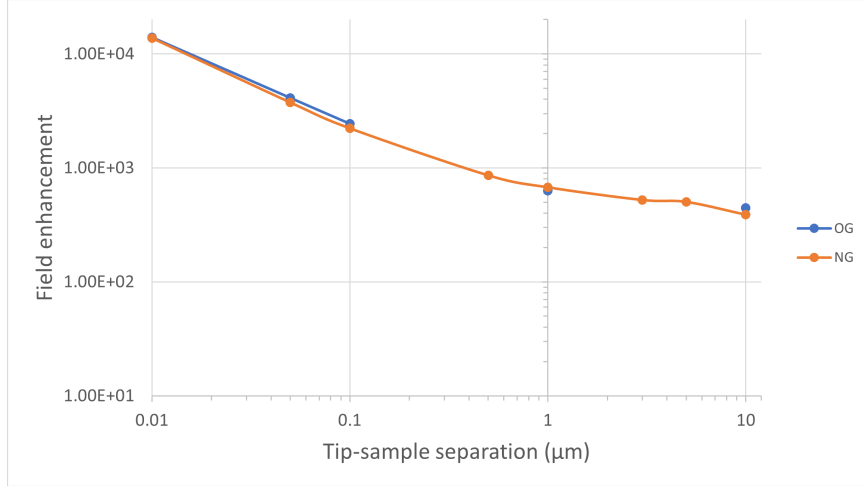
Figure 4.26: Plot of field enhancement vs tip-sample distance using simulated data in old generation and new generation simulations where the inputted port pulse varied between the original THz pulse and its integral.[6]

gold to n-doped Si of varying carrier concentrations and displayed in Fig. 4.27. The colour bar is fixed for all plots to emphasize the penetration field. (a-e) shows that the higher the conductivity of the sample, the smaller the distance that the near-field is allowed to penetrate below the sample surface. If the simulation is done for the steady-state (i.e. applying a constant voltage between the tip and sample) to reproduce the same peak field in the gap, one can see that there is no penetration field just like in the Au case (Fig. 4.27(a,f)). Field penetration of a semiconductor is a phenomenon that only occurs when the coupled field is transient. In the simulation, the charge carriers in the sample must respond to the transient background field. If the moving carriers cannot effectively screen the incident field, then the near-field is able to penetrate several nm deep into the bulk regions of the sample.

The near-field is mostly contained inside the gap between the tip and the sample. However, the semiconductor material allows nearfield THz pulses to form within the sample. Fig. 4.28 shows the waveform variations from the tip and various depths within the sample. The field in the gap resembles the port pulse. The waveforms inside the tip and sample materials differ in shape. The peak of the pulse occurs at slightly different times. For the field in the gap, the peak occurs at 21.5 ps which is
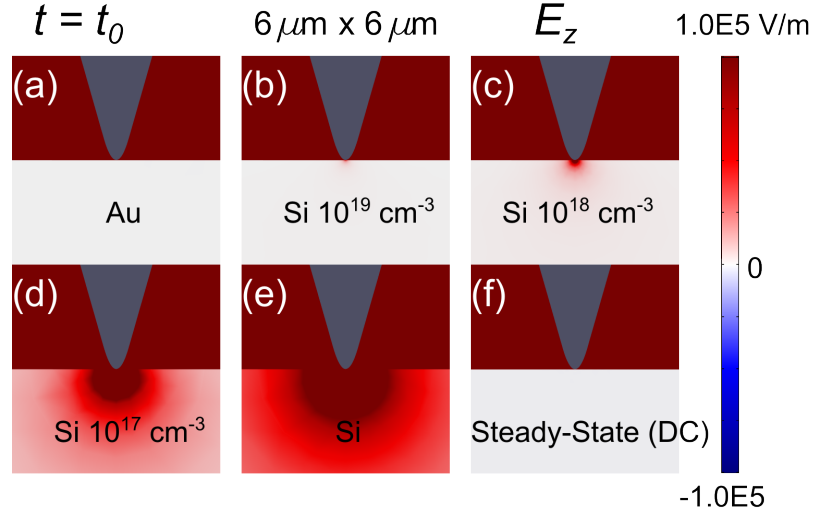
Figure 4.27: (a-e) Visualizations of the THz near-field for several samples ranging from Au to doped Si of a few doping concentrations to undoped Si. (f) Shows the near-field in the d.c. case using a conducting sample (i.e. Au or doped Si). The colour bar scale is saturated to show the extent of the penetrated near-field inside the sample.

a node for the field inside the sample. The peak of the sample occurs at 21.2 ps.

Fig. 4.29(a) shows the vertical profile of the z-component of electric field in at two THz peak times corresponding to where the field peaks in the gap, 21.5 ps, or in the sample at 21.2 ps. The d.c. case is shown in Fig. 4.29(b). A constant d.c. bias equal to 3.13 V to match with the peak electric field voltage of a THz pulse results in a slightly larger field in the gap, but a small constant steady-state field in the sample bulk as a function of z. The THz field decays over 8 orders of magnitude in the bulk of the semiconductor sample within a depth of 100 μm. The classical skin depth at 1 THz for gold is 80 nm, 3 μm for 10^{19} cm^{-3} doped Si and increases further for lower dopings. The near-field interaction volume is much increased for the semiconductor samples.

Vertical, z-linecuts, are done for n-doped Si in Fig. 4.14(b), have been extracted for various sample materials plotted in Fig. 4.30. Note that the exact same geometric dimensions are maintained while the sample material is varied. In standard metals like gold, the field essentially vanishes as soon as it crosses into the bulk of the sample. In
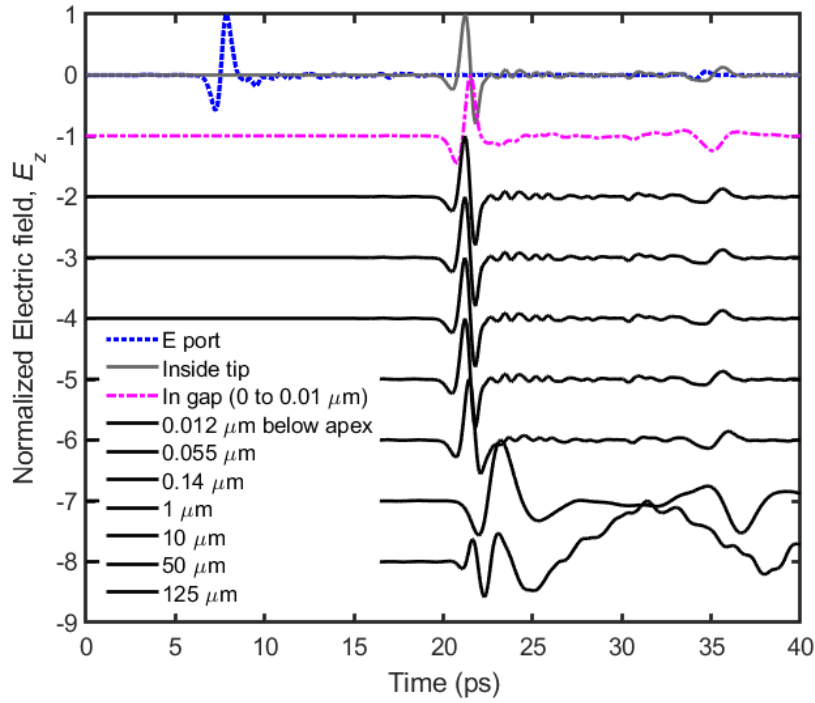
Figure 4.28: Waveforms for E_z taken at various depths along the z axis, and fixated at $x = 0$ μm, below the tip apex. The port THz pulse is located at the top left. The top middle waveform is the inside the tip. The second waveform from the top is inside the gap. The black waveforms are plotted at increasing depth below the sample surface. The legend shows the z distances below the surface. The waveforms are normalized to unity and shifted for separation. Note: These results belong to an old generation of simulations. (Results from first generation of simulations.)
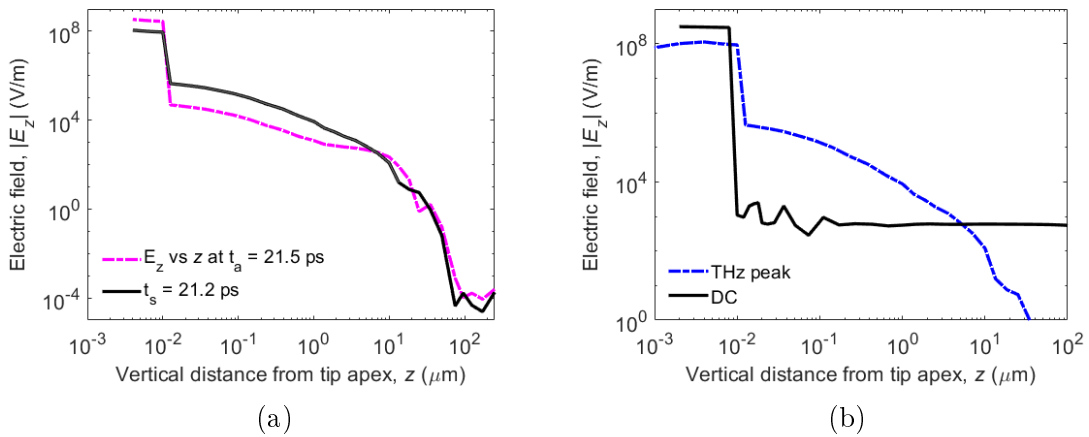
Figure 4.29: (a) Vertical profiles of E_z at different times in the THz pulse bias simulation for 10^{19}cm^{-3} doped Si. (b) Vertical profile in the d.c. case. (Results from first generation of simulations.)

the doped Si case, there is a significant amount of penetrated field nanometers within the bulk regions where the field drop is only 1 to 2 orders of magnitude.
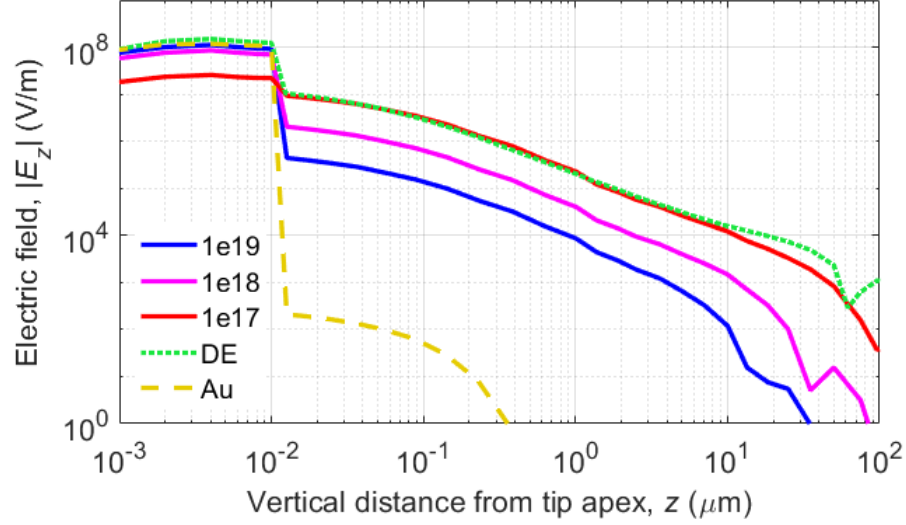
Figure 4.30: The vertical profile of the E_z component along the center $x = 0$ μm occurring at the peak time, $t = t_p$, for various semiconductor samples with varying doping concentrations, dielectric (DE) Si and for gold (Au). (Results from first generation of simulations.)

4.6 Field Penetration

This section continues from the Material sweep studies to further explore the field penetration process. Field penetration in a semiconductor occurs when the incident field is transient. In the simulation, the charge carriers in the sample must respond to the transient background field. If the moving carriers cannot effectively screen the incident field, then the nearfield could develop deep into the bulk regions of the sample. The sample material undergoes a slight modification by introducing a surface conductivity layer, which has units of S/□. The bulk n-Si region maintains the same conductivity value summarized in Table 4.3. Due to the nature of the FEM, the surface must actually be a thin volume of of a few nm thick for the sake of meshing.

A surface conductivity can mocked by assigning a slab conductivity equal to:

$$\sigma_{\text{slab}} = \frac{\sigma_{\text{surf}}}{d_{\text{slab}}} \tag{4.8}$$

where σ_{slab} is the slab conductivity, σ_{surf} is the desired surface conductivity and d_{slab} is the slab thickness. The bulk region of the n-doped Si sample has a conductivity of 20,000 Sm^{-1}, while the surface layer was approximated as a 10 nm slab with a conductivity of 500 Sm^{-1} (The product forms a 5 µS$\square^{-1}$ interface[193]). Thus σ_{surf} is another parameter that can be varied in material sweep studies.

A schematic of the simulation geometry in the tunnel junction region is shown in Fig. 4.31(a). The spatial profile of the vertical component of the steady-state electric field, $[E_{d.c.}]_z$, is shown in Fig. 4.31(b), while the spatial profile of the peak THz electric field within the silicon sample is shown in Fig. 4.31(c) for the vertical field component, $[E_{\text{THz}}]_z$, and in Fig. 4.31(d) for the horizontal field component, $[E_{\text{THz}}]_x$. In the steady-state, the metallic-like surface screens the d.c. field from the silicon bulk. However, due to the relatively low conductivity [193, 194] and low carrier density of the metallic-like Si(111)-(7×7) surface, the THz electric field is not effectively screened by the surface and is able to penetrate several microns into the bulk.

Vertical profiles (i.e. z-line cuts) are plotted in Fig. 4.32 using bulk n-doped 10^{19} cm^{-3} Si, then variations where 10 nm layers of 5 µS$\square^{-1}$ sheet conductivity, Au film and dielectric slab are applied. The simulated nearfield exists in three interfaces as shown by the field amplitude discontinuities in the plots. With the top layers being less conducting, larger fields of about 1 to 2 orders of magnitude lower than the gap field, can exist in the interface before decaying in the bulk.

The material variation and field penetration simulations show that the nearfield has both temporal and spatial complexities. Interactions between the tip and sample play a significant role in altering the environment in which the nearfield forms. When the incident field is time-dependent and ultrafast as for the case of THz pulses, the
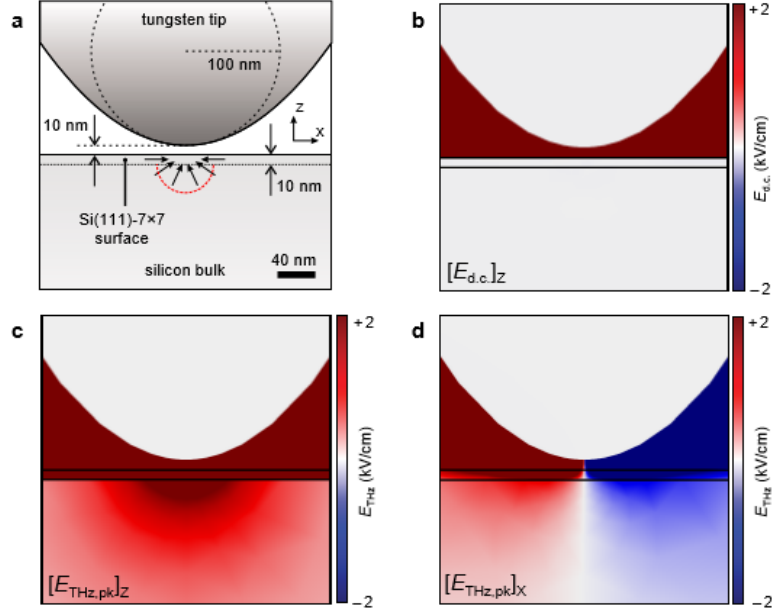
Figure 4.31: Electric field spatial profiles obtained from COMSOL simulations. The bulk region of the n-doped Si sample has a conductivity of 20,000 Sm^{-1}, while the surface layer was approximated as a 10 nm slab with a conductivity of 500 Sm^{-1} (The product forms a 5μS$\square^{-1}$ interface). (a) Simulated geometry with a tip-sample separation of 10 nm and tip radius of curvature of 100 nm. (b) Simulated spatial profile of the vertical component of the steady-state electric field with $V_{d.c.} = 1V$ applied to the sample. The d.c. electric field does not penetrate significantly into the bulk under steady state. (c), (d) Simulated spatial profile of the THz electric field for the vertical component (c) and horizontal component (d), at the time when the THz undergoes maximum enhancement in the junction. The colour map range was chosen to emphasize the terahertz electric field penetration into the bulk (the electric field in the gap is saturated dark red/blue). The peak field amplitude of the incident THz field is 200 V/cm. The electric field obtained from the simulation is enhanced by a factor of 28 in the slab region. (Adapted from [2, 133].)
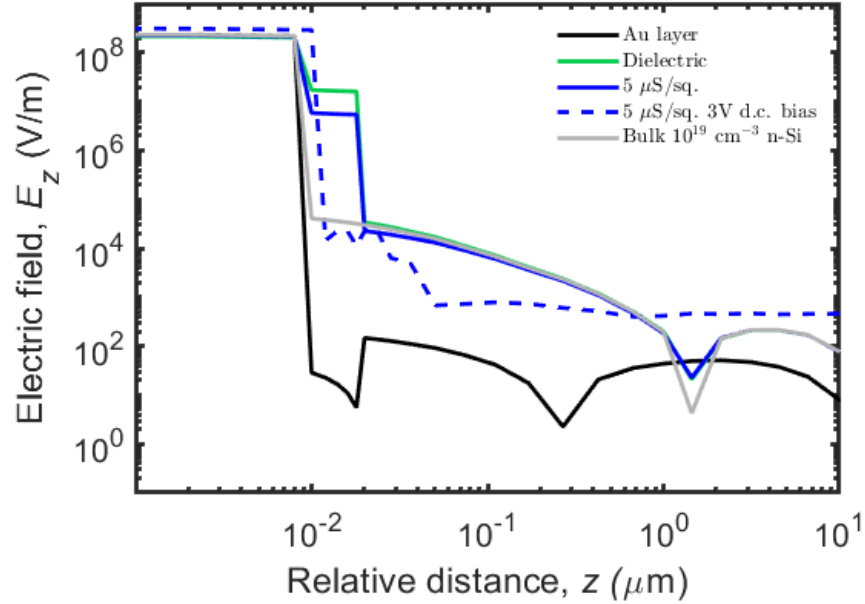
Figure 4.32: The vertical profile of E_z amplitude along the center $x = 0$ μm at $t = t_p$ for bulk high doped silicon (10^{19}cm^{-3}) topped with a sheet conductivity layer varying from Au, dielectric Si and 5μS$\square^{-1}$. The plots show the field decay through the interfaces. The d.c. case and pure bulk case are plotted for comparison.

finite response of the sample based on material properties results in decaying nearfield profile within the bulk.

Simulation of the penetrated near-field its extent into the bulk of the sample is essential for understanding the transport behaviour in semiconductors. The simulations can explain that the large currents observed with THz-STM on Si(111) come from field-driven conduction in the bulk of the sample [2]. The near-field interaction with the semiconductor sample encompasses a significant volume ($\sim$ μm^3) in the bulk. Fig. 4.31(a) shows that a hemisphere with a 100 nm radius in the bulk can provide significant conduction from thousands of carriers where there is sufficient amount of penetrated near-field to accelerate the carriers towards the tip.

4.7   Long-wire Geometry

To further study the antenna-like coupling of THz pulses to the metal wire, a long-wire (LW) geometry, as shown in Fig. 4.33, is used to avoid reflection pulses from the tip holder and obtain a cleaner near-field output. The geometry is similar to Fig. 4.1, except the tip holder is removed and replaced by an extended tip shaft. Table 4.5 summarizes the dimensions for the long-wire configuration. Figs. 4.34 and 4.35 summarize the simulated near-field waveform obtained at the tip apex in comparison with the incident pulse. The LW pulse (black dash) only shows the integral waveform as expected from antenna coupling.
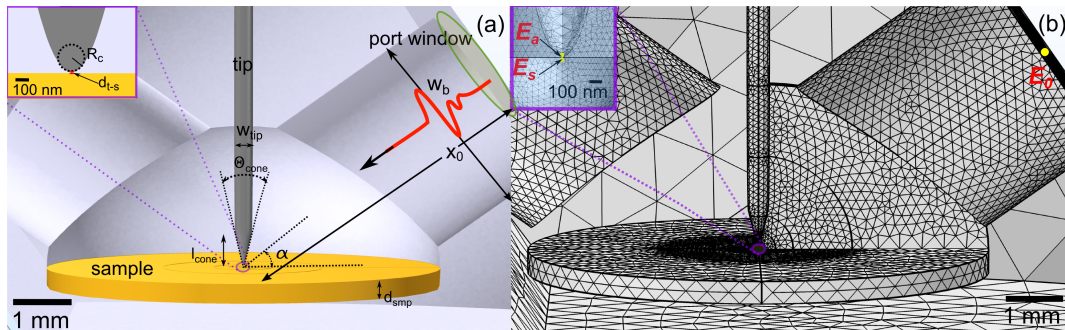
Figure 4.33: (a) Geometry for a long wire tip built in COMSOL (b) The meshing structure is similar to the normal geometry in Fig. 4.5. The hemi-spherical mesh zones are displayed as a cross-sectional plane to the right of the tip to show the reduction of the mesh size approaching the STM gap. The inset shows the mesh zone in the near-field regime.

In Fig. 4.35, the nearfield waveforms produced by the normal STM geometry and the long wire simulations are compared with each other. The key contrast between the two simulations are the reflection pulses in both the waveforms produced at the tip apex and below the sample surface.

Fig. 4.36 plots the capacitance when an effective tip length is biased at height l_b. The plot shows the simulated capacitance if the tip is only a nano-sphere, to a full taper, then towards a long-wire tip. The THz beam that illuminates the tip has a Gaussian 1/e beam width of about 2 mm. A fraction of the incident field strength is concentrated around the tip taper regions.
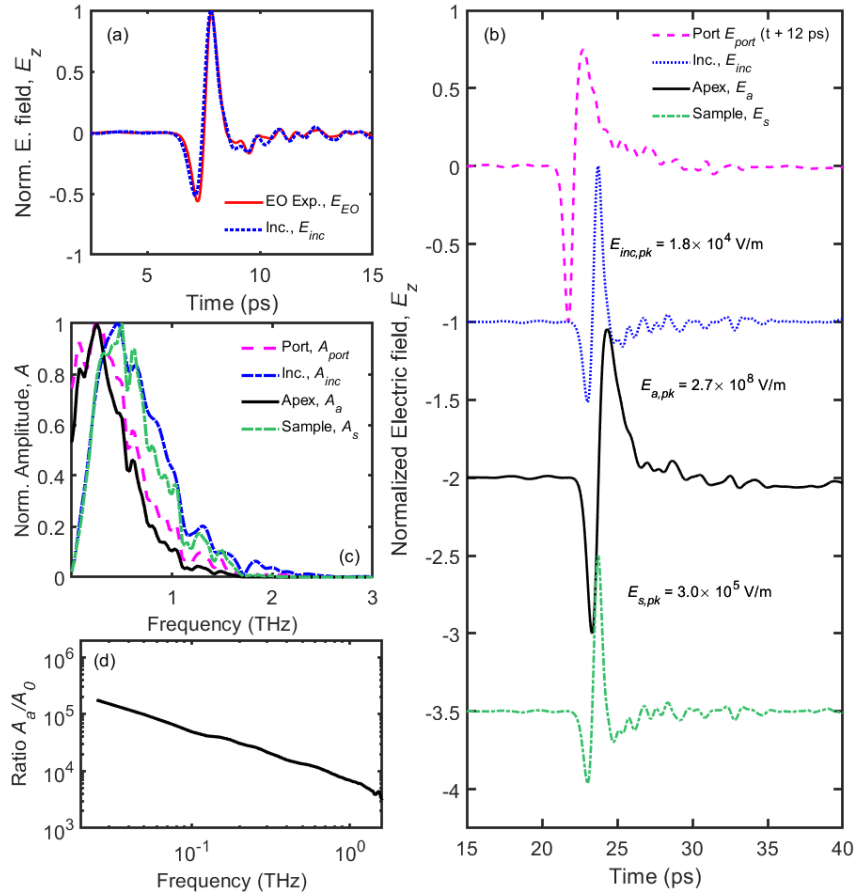
Figure 4.34: Probed waveforms for the Long-wire STM geometry. (a) The simulated incident pulse in the far-field propagating 4 mm from the port window (blue dash) compared with an experimentally measured pulse using electro-optic (EO) sampling (red line). (b) The port pulse (magenta) is plotted with time shifted forward for alignment purposes. The incident pulse is repeated from (a). The THz near-field pulse probed at the tip apex (black), and 2 nm below the sample surface (green) plotted with the simulated incident pulse (blue dash). The pulses are normalized to their peak amplitude. Their actual peak amplitudes of the apex pulse and the incident pulse are annotated. All pulses are shifted vertically for separation. (c) Corresponding frequency spectra for the near-field pulses with normalized amplitudes. The experimental EO spectrum (blue) is shown for reference. (d) The amplitude of the apex near-field spectrum divided by the amplitude of the incident spectrum which gives the field enhancement factor as a function of frequency.

Figure 4.35: Comparing the simulated near-field for the tip geometry with the tip holder and long wire geometry. From the top of the plot are the port pulse, incident pulse, nearfield pulse at the tip apex in the normal STM and long wire geometry simulation, and the nearfield pulse below the sample surface overlapped for each simulation.

Table 4.5: Table containing the dimensional parameter values corresponding to the geometry in Figure 4.33.

Description	Symbol	Value
Tip shaft diameter	w_{tip}	0.25 mm
Full tip length	l_{tip}	2.0 mm
Full taper height	l_{cone}	0.5 mm
Full taper cone angle	$2\theta_{\text{cone}}$	28°
Apex radius of curvature	R_c	15 to 100 nm
Sample thickness	d_{samp}	0.25 mm
Sample diameter	w_{samp}	5.3 mm
Tip-sample distance	d_{ts}	10 to 100 nm
1/e beam width	w_b	2.2 mm
Port angle relative to sample plane	α	35°
Distance from port to STM	x_0	4.0 mm
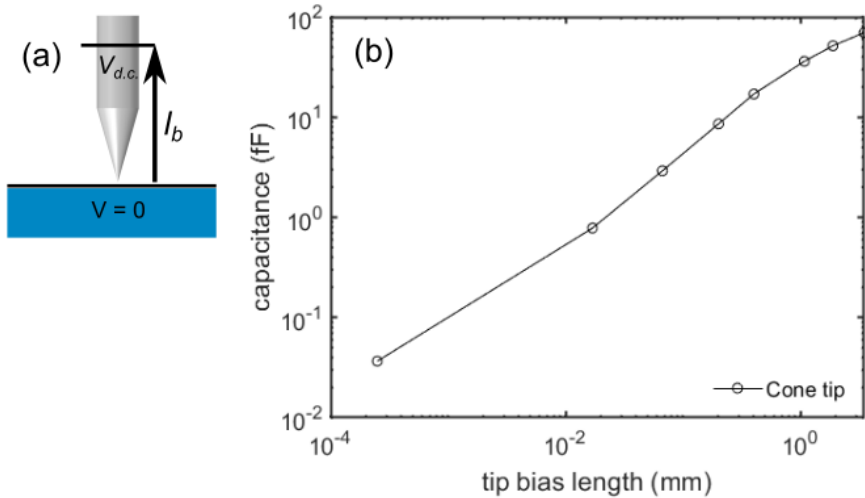
Figure 4.36: (a) Diagram labeling the bias length where only part of the tip is biased up to a height l_b. (b) Simulated tip capacitance versus the tip bias length.

116

Using a modified geometry such as the long wire setup helps isolate the main nearfield pulse produced by the field enhancement from the tip and sample. It makes analysis simplified to not have to consider secondary effects such as the reflection pulse. As seen in Figs. 4.34(c) and (d), the Fourier analysis is facilitated by the simplified geometry. When comparing the field enhancement factor versus frequency for a full STM tip that includes the tip holder in Fig. 4.15(d) with that of the long wire geometry in Fig. 4.34(d), there is a slightly stronger field enhancement using the full STM tip geometry.

4.8 Tip Shape Variations

Similar to how different antenna structures exhibit varying THz radiation profiles, the tip acting as a THz receiver, generates a THz near-field profile that varies with the structure. In this section, simulations are conducted for when the tip taper shape, apex shape and taper length vary.

4.8.1 Tip taper shape

Tips used in STM experiments can be imaged by a simple bench microscope to check their shape. However the sharpness is only visible in the micron scale. Advanced techniques such as scanning electron microscopy (SEM) and transmission electron microscopy (TEM) can reveal the tip structure in the nano-scale. Fig. 4.37(a)-(c) shows the common tip taper structures produced by standard tip-etching methods: conical, cusp and hyperbolic. During the etching process, one cannot control which tip shape will be produced in the end. However, Pt-Ir tips usually produce the hyperbolic taper. The simulation models attempt to reproduce the common tip taper structures dimension-wise, but maintaining the rotational symmetry. The tip apex base, which is a circular arc of radius R_c, remains the same regardless of the taper structure used. Fig. 4.37(d) summarizes the simulated near-field waveforms and the spectroscopic dependence in (e),(f). The conical taper has two variations, that is

117

the basic cone shape and a smoothed edge version to mimic the SEM image. The long-wire variation shown in Fig. 4.38 produces near-field waveforms without the trailing reflection pulses. The near-field THz profile have features resembling the THz emission profiles outputted by I-shape and bowtie shaped THz antennas [86, 95], which provides insight on how the tapered geometry shape the near-field.
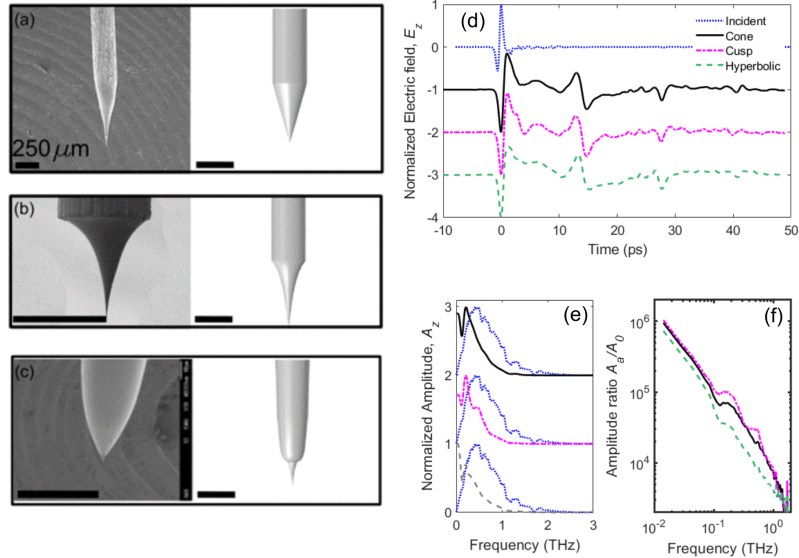
Figure 4.37: Typical tip tapers measured by a scanning electron micrograph (SEM) have a sharp cone tip (a), cusp shape (b) or hyperbolic shape (c). The taper shapes are created in COMSOL. The black bar width is equal to the tip shaft diameter of 250 μm. The simulated radius of curvature at the apex is around 50 nm. (d) Apex pulses measured for the tip shapes with their corresponding frequency spectra (e) and frequency dependent field enhancement factors (f).

The spectral plots for the STM tip presented in Figs. 4.37(e) and (f) and long wire tips in Figs. 4.37(b) and (c) demonstrate the $1/f$ dependence of the near-field amplitude for all tip shapes. There are noticeable peaks and dips in the field enhancement versus frequency plots in the range of 0.1 to 1 THz for all tip shapes. The taper region of the tip acts like a partial cavity and provide opportunities for particular THz wavelengths to establish resonance. THz frequencies that couple nicely to tip features are amplified. The propagating coupled THz fields around the STM structure ends up being enhanced in the near-field at the tip apex. Full-scale THz-
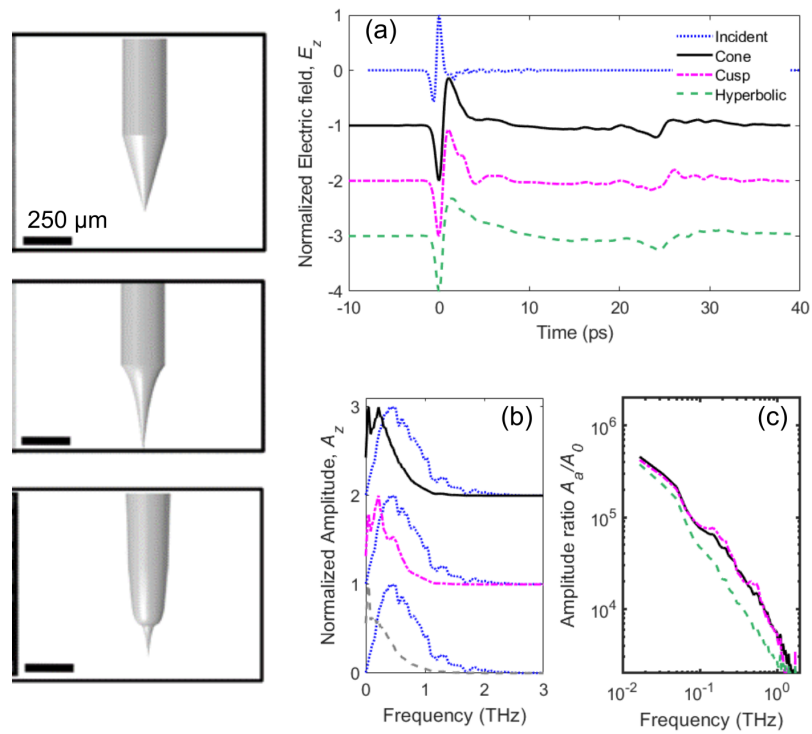
Figure 4.38: (a) Pulses around the tip apex using the long wire geometry and varying the tip tapers according to the shapes in 4.37. (b) Corresponding spectra for the varied tip tapers long wire geometry. (c) Corresponding frequency dependent field enhancement factors.

STM simulations demonstrate that the near-field formation encompasses the entire structure and accounts for details such as the shape of the tip used in THz-STM experiments.
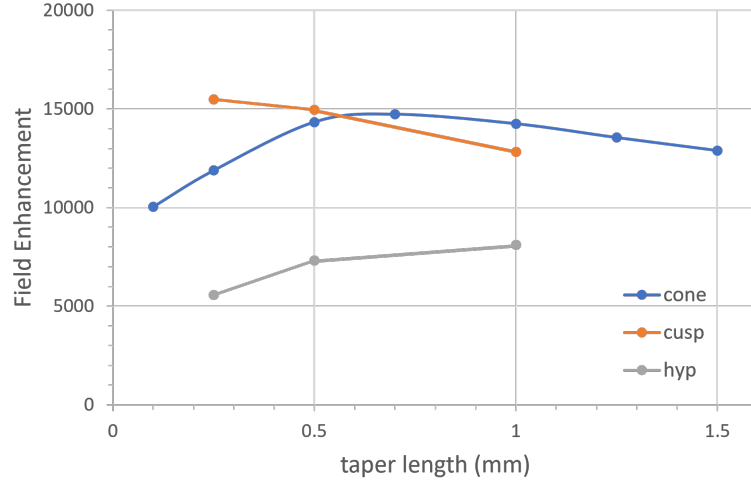
Figure 4.39: Field enhancement at the apex versus tip taper length for various tip shapes. A full data set is only available for the cone series. The other tip shapes only had simulations for 3 taper lengths completed for.

The field enhancement differs according to the tip shapes. Fig. 4.39 shows the variation in how the different tip shapes focus the near-field around the tip apex. Conical tapers ranging from 500 µm to 700 µm show an optimal field enhancement. Shorter cusp tapers tend to focus the near-field better. Hyperbolic tip shapes enhance the near-field at a factor of 3 lower compared to the cone and cusp shapes. The taper region combined with the sample surface forms a partial cavity where incident THz pulse radiation could become partially trapped[128]. In frequency dependent simulations, THz standing waves form along the taper edges [37]. If the dimension of the taper edge matches with the coupling wavelength of the incident THz pulse, a resonance condition can be met to increase the overall field enhancement [37, 128]. This is confirmed by field enhancement factors simulated for the conical tapers ranging from 500 µm to 700 µm where the length of the taper edge matches with the peak wavelengths of the input THz pulse (i.e. 600 µm). The cusp tapers tend to favor the

coupling of a half THz wavelength as the shorter cusp lengths form a closed cavity that prefer to support a half cycle of a THz standing wave. The tip apex and the cusp edge form the node points.

4.8.2 Tip taper length

The taper length l_c for a long-wire cone tip is varied in a parameter sweep simulation. Fig. 4.40 shows the progression of the apex waveforms (and corresponding spectra) for a short taper of 100 µm towards a long taper of 1.5 mm. The broadening increases with l_c. Fig. 4.41 shows a selected sample of the waveforms and spectra for a short (250µm), medium (500µm) and long (1 mm) cone taper with the free-tip (500µm) for comparison. Every spectrum shows a peak at about 0.1 THz and a main peak at about 0.3 THz.

Fig. 4.42 shows the simulation for the long-wire cusp taper geometry with varying taper heights. The cusp taper shows the broadening with increasing l_c more clearly than a cone taper. The 250 µm cusp tip peaks around 0.35 THz while the 500 µm and 1 mm tapers both peak at around 0.3 THz. The free-tip (500 µm) does not show the 0.1 THz peak, but still has a main peak at around 0.3 THz.
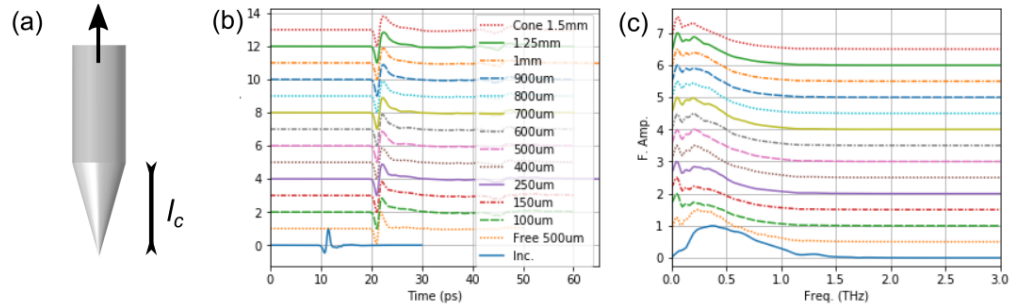
Figure 4.40: (a) The diagram labels the cone taper length sweeping parameter. The tip shaft extends to the top of the simulation boundary. (b) Full display of the near-field pulses simulated for the cone tip long wire geometry where the taper height is varied. (c) Corresponding spectra for the cusp tip long wire geometry with varied taper height. The incident pulse and spectrum is shown for reference.

The hyperbolic taper geometry consists of two free parameters: the taper height

l_c up to where the tip diameter reaches about 90% of the full tip-shaft diameter and the height l_a at where the cusping inflection point occurs. Fig. 4.43 summarizes the waveforms at varying l_c and l_a fixed to $l_a = 25\,\mu\mathrm{m}$. The waveform shape appears the same for all l_c, suggesting that l_a might need to be varied instead in a future parameter sweep study.
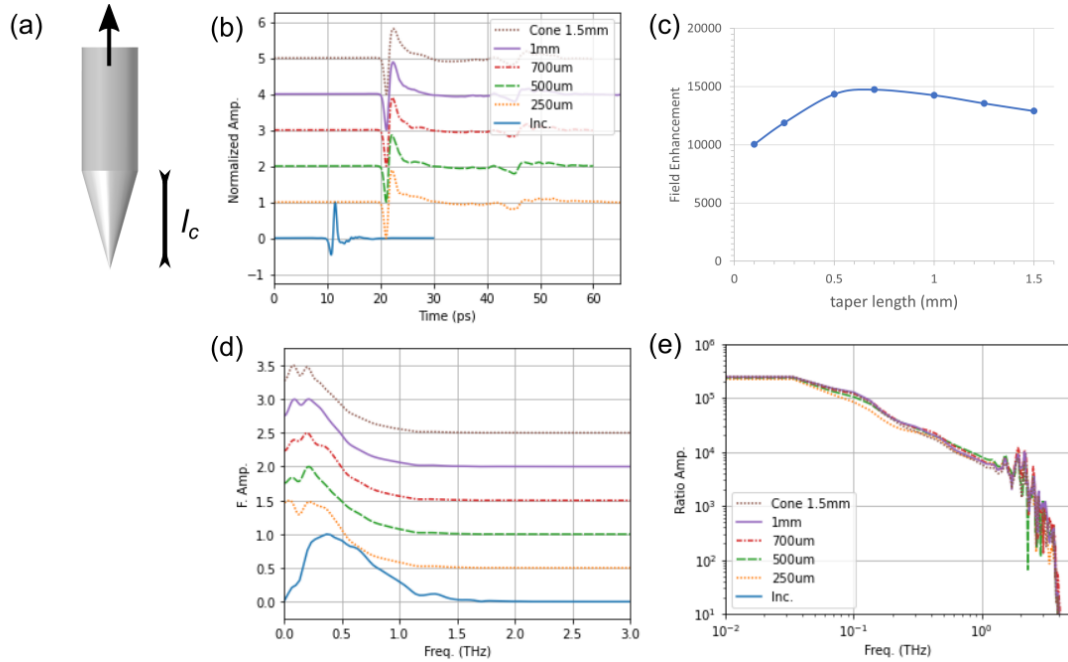
Figure 4.41: (a) The diagram labels the cone taper length sweeping parameter. The tip shaft extends to the top of the simulation boundary. (b) Selected near-field pulses simulated for the cone tip long wire geometry where the taper height is varied. The free tip is also shown. (c) Corresponding spectra for the cusp tip long wire geometry with varied taper height. The incident pulse and spectrum is shown for reference.

The simulated capacitance of each tip shape is plotted in Fig. 4.44 versus the bias length of the wire. The hyperbolic taper's capacitance grows the fastest because the taper radius bulges out to about most of the tip-shaft radius much earlier (height of 200 µm) compared to the other tapers. The capacitance mainly due to the taper section is can be interpolated to where bias length equals the taper height $l_c = 500\,\mu\mathrm{m}$ in Fig. 4.44. They are found to be equal to about 25 fF, 20 fF and 30 fF for the cone, cusp and hyperbolic tapers, respectively.
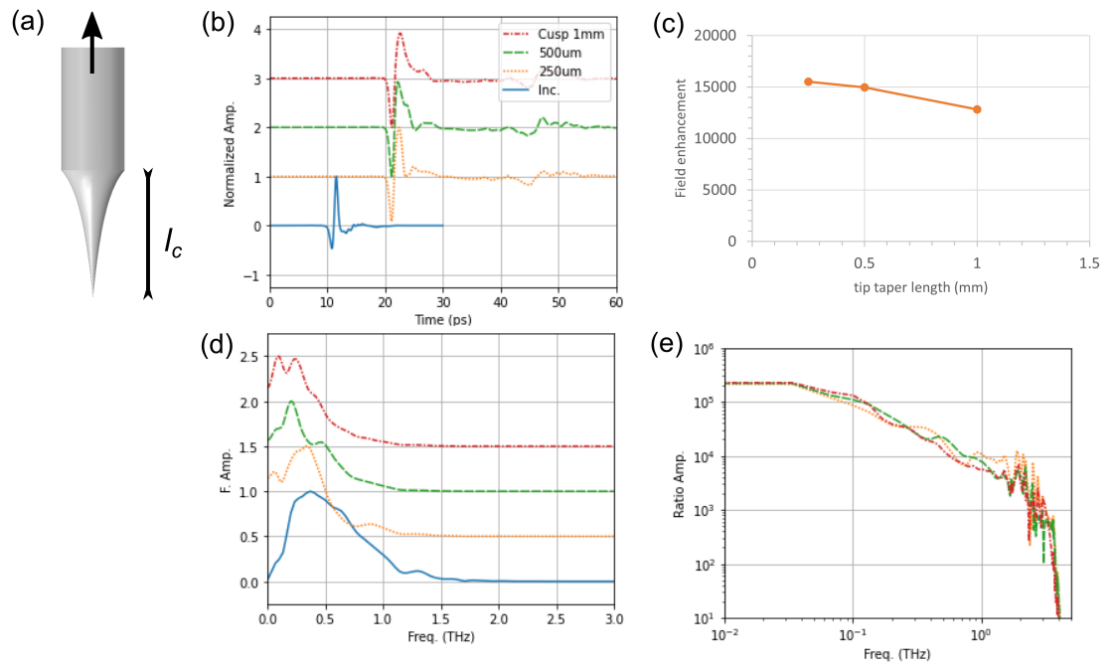
Figure 4.42: (a) The diagram labels the cusp taper length sweeping parameter. The tip shaft extends to the top of the simulation boundary. (b) Selected near-field pulses simulated for the cusp tip long wire geometry where the taper height is varied. The free tip is also shown. (c) Corresponding spectra for the cusp tip long wire geometry with varied taper height. The incident pulse and spectrum is shown for reference.
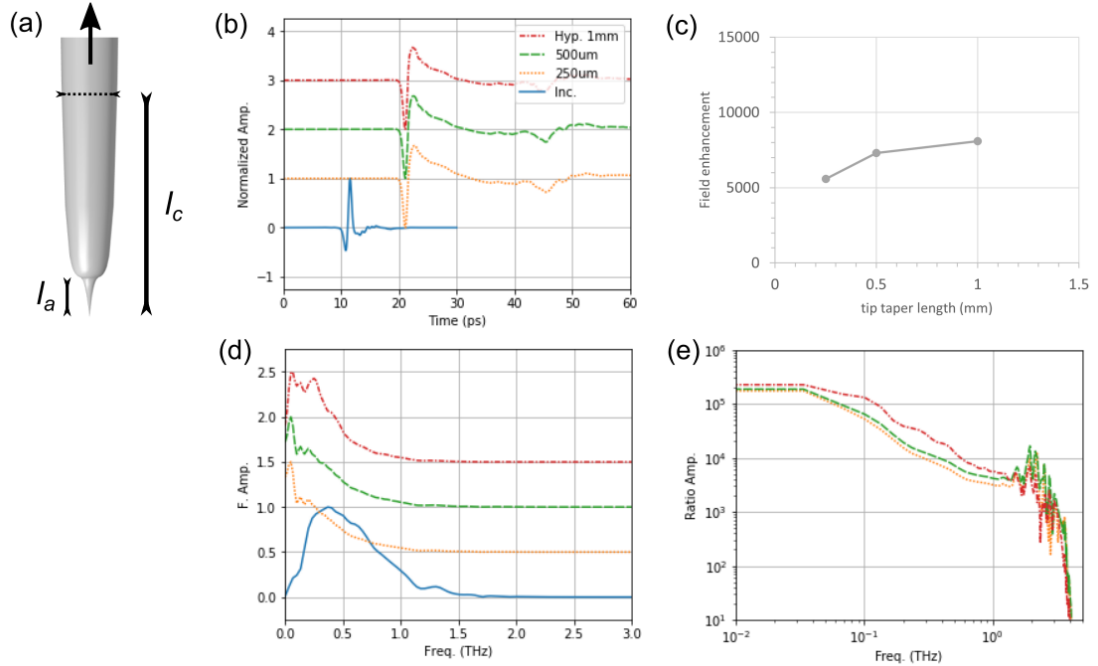
Figure 4.43: (a) The diagram labels the hyperbolic taper length l_c and the height of the inflection point l_a as sweeping parameters. The tip shaft extends to the top of the simulation boundary. (b) Selected near-field pulses simulated for the hyperbolic tip long wire geometry where the taper height is varied. (c) Corresponding spectra for the cusp tip long wire geometry with varied taper height. The incident pulse and spectrum is shown for reference. The cusp inflection point $l_a = 25\,\mu\text{m}$ for all plots.
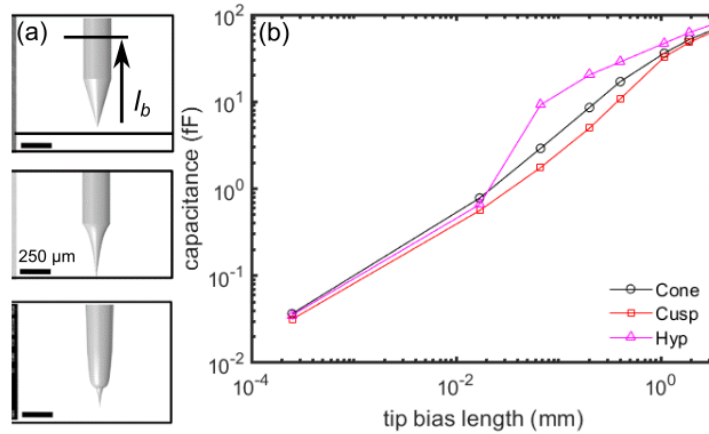
Figure 4.44: (a) Tip shapes used in simulation for the capacitance. The fractional length of the tip from the apex indicates the fraction of the tip surface that is biased relative to the sample. Intent is to find the capacitance where part of the tip is illuminated by an external field. (b) Simulated capacitance values for each tip shape where the taper height is 500 μm.

4.8.3   Tip apex radius of curvature

The tip sharpness (i.e. apex radius R_c) influences the field enhancement around the tip apex [58, 76, 166]. The semiconductor sample in the simulation is semi-transparent to the incident field. Waveforms are obtained at various depths within the sample as shown in fig. 4.45. Beyond 10 μm, the waveforms become noisy due to interference via internal sample reflections. Fig. 4.46 plots the electric field vertical profiles at peak times corresponding to the waveform either in the gap or inside the sample. In Fig. 4.45, the in gap waveform differs from all the others peaking at 21.5 ps, 0.3 ps after the peak of the field inside the sample, which occurs at 21.2 ps. Therefore, careful consideration of the timing must be taken when extracting field profiles. If we are interested in the field plot in the gap, then use t_a, the peak of the field around the tip apex. Then use t_s, the peak of the field inside the sample, for getting the penetrated peak field distribution. Note that t_s is also the peak time of the free-space propagation of the incident field in the case where there is no tip or sample. The waveforms of the penetration field correspond to transmitted incident fields.
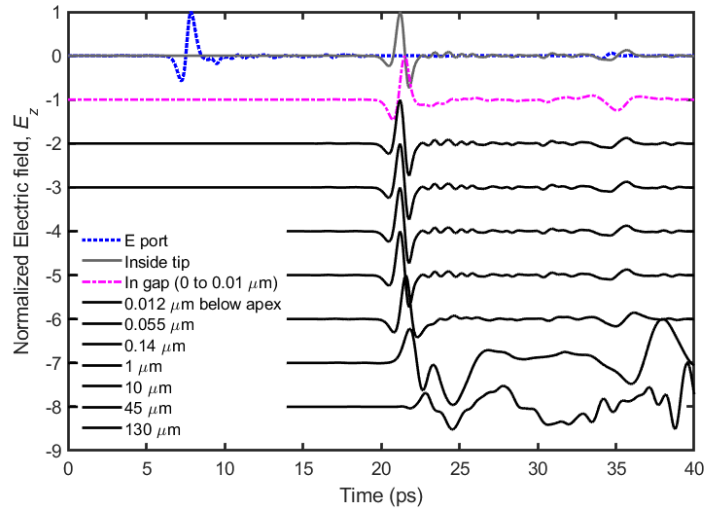
Figure 4.45: Penetration field waveforms at various depths inside the semiconductor sample for a 100 nm radius tip apex.

Variations of the simulation are done for R_c ranging from 10 nm to 500 nm. Fig.
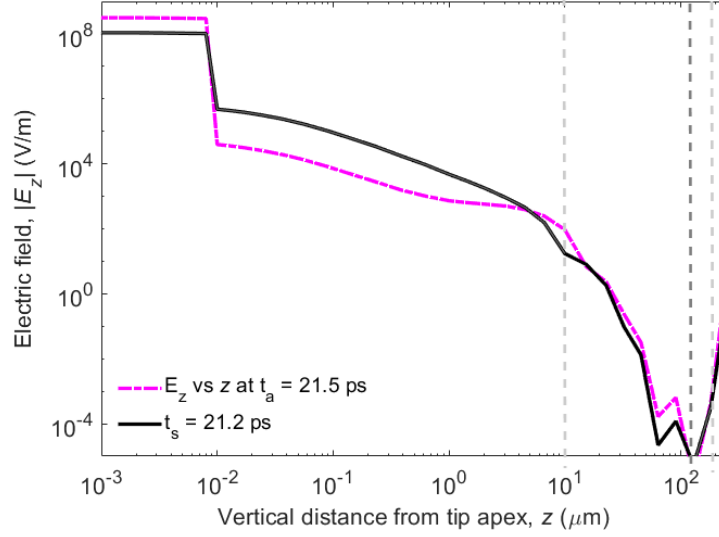
Figure 4.46: Plot of the magnitude of the z-component for the penetration field versus depth inside the semiconductor sample at different peak times: t_a, where the peak of the apex field occurs and t_s, where the peak of the field inside the sample occurs. Peak times are separated by 0.3 ps and produce different results for the vertical field profiles. Dashed lines indicate where the field changes sign within the sample. All plots use a 10 nm gap distance.

4.47 shows the near-field spatial distribution and summarizes the field enhancement. The field enhancement increases as the tip radius is reduced as shown in Fig. 4.47(a). In (b), the horizontal profile of the electric field around the tip apex are plotted for selected tip radii. Both the sharpness of the peak and amplitude increase with decreasing tip radius. Peak shapes do not vary much until the tip apex radius goes beyond 100 nm. The FWHM of each lateral profile was measured to be smaller than the diameter of the tip apex. For example, the FWHM corresponding to the profile for the 100 nm radius tip is about 150 nm. Overall, the larger the tip, the wider the spread of the near-field while lowering the field enhancement.

The side inset images in Fig. 4.47 for the large tip apex radii show how the enhanced field spans over a large volume in the penetration region. Vertical profiles plotted in Figs. 4.47(c) and (d) show the decay depth of the enhanced fields as a function of tip radius. A sharp tip produces a vertical profile where the field decays rapidly into the bulk. According to these linear plots, well after 1 μm, the field
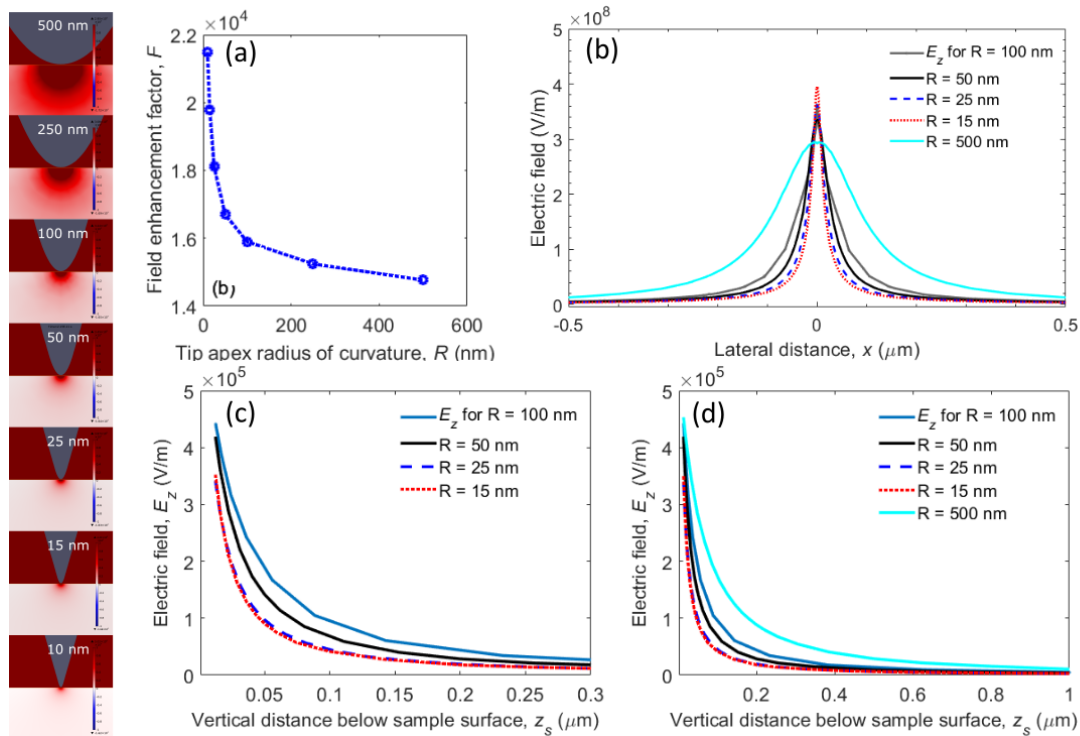
Figure 4.47: Side insets: The tip sharpness is studied by varying the radius of curvature of the apex. The tip-sample separation is 10 nm. The colour-bar visualizations are set to the same field magnitude scale to illustrate the extent of the enhanced penetration field into the semiconductor sample as influenced by the size of the tip apex. (a) The field enhancement as a function of tip apex radius of curvature plot shows that the electric field in the tip-sample gap grows as the tip gets sharper. (b) Lateral profiles (i.e. versus x) for the z-component of the electric field below the tip apex in the gap region occurring at the peak field time. (c) Vertical profile for the z-component of the electric field within the sample extracted at the penetration peak field time. (d) Vertical profiles shown over 1 μm range.

effectively drops to zero. A larger tip radius makes the field decay slower within the bulk due to the large near-field interaction volume between the tip and sample.

4.8.4 Unique tip geometries

Unique geometries such as grooved tip shaft, grated shaft, multi-cusp tapers [133, 166, 195] are simulated. Note that the sample geometry can also be varied by introducing step features [3], nano-spheres, nano-islands, etc. and by creating sample regions where the material parameters vary (e.g. doping and defect regions [133]).

Fig. 4.48 shows a simulation where grooves are placed on the tip shaft to excite THz surface plasmons. Each groove represent excitation regions for a tip plasmon. The nearfield shows an enhanced main pulse followed by a series of pulse trains from the tip shaft reflection.
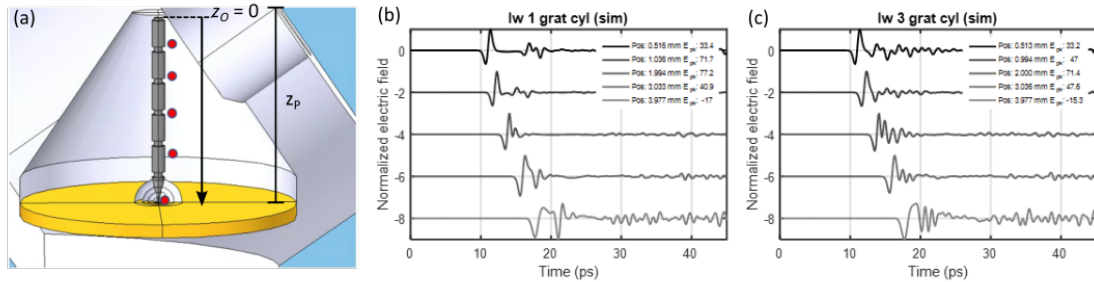
Figure 4.48: (a) Grated tip shaft created in COMSOL. The tip length is 4 mm. The grating is 100 μm wide and 50 μm deep with the first position at 0.5 mm from the top of the tip. Additional gratings are placed 0.6 mm below the previous one until the end of the tip. The red dots indicate the locations where simulated waveforms are probed. (b) Waveforms collected along the tip starting from the top for a single grating positioned at 0.5 mm. (c). Waveforms collected along the tip starting from the top for a triple grating tip.

Fig. 4.49 shows one of the tip tapers that can be chemically etched featuring several cusps. The COMSOL geometry mimics the actual tip and the nearfield pulse has a main pulse composed of a few peaks. There are several reflection pulses that follow.
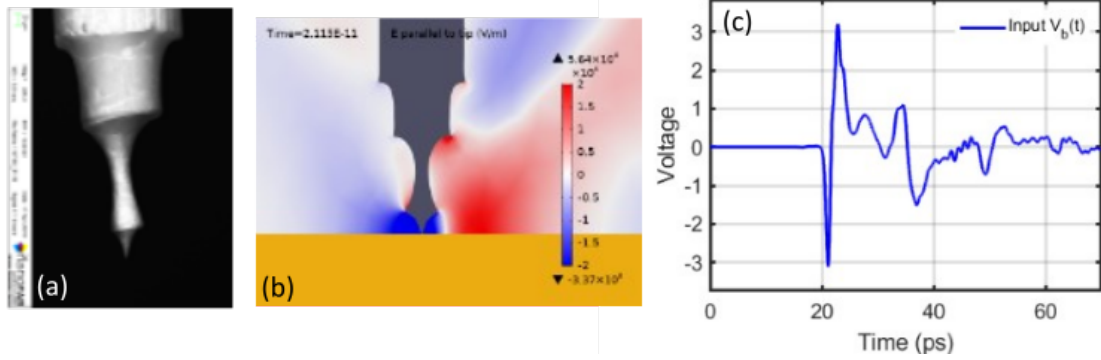
Figure 4.49: (a) SEM image of a multi-cusp taper tip. (b) Image of the tip created in COMSOL, however the geometry is rotationally symmetric unlike the real tip with slanted cusp edges. (c) Simulated apex waveform showing that the main peak is the superposition of multiple peaks.

4.9   Multi-probe THz-STM

A multiprobe STM is a sophisticated setup which allows for techniques such as four-point-probe spectroscopy to be accomplished simultaneously with imaging. Coupling THz to the multiprobe STM is an interesting case to simulate. The β angle parameter sweep was done for the single tip showing that vertically polarized THz pulses couples efficiently with the STM tip. In a multi-tip setup, all the tips have to be configured at an angle to probe a single region. Sending in a THz beam linearly polarized relative to one tip should make the tip "THz-active".

A double tip STM model shown in Fig. 4.50a is developed in COMSOL. The meshing structure shown in Fig. 4.50b is the same as the previous models for the single tip. There are 4 angular degrees of freedom in this simulation: α the angle of incidence between the THz propagation axis and sample plane; β the linear polarization angle for the port window relative; ϕ_i the angle between the tip shaft axis and sample plane with i being a label index for a tip; and ψ the spread angle between the two tip shaft axes.

A double cusp-tip simulation is carried out using $\alpha = 35°$ and $\beta = \phi = \psi = 45°$, where tip 1 set to be "THz-active". To avoid tip collision and maintain good mesh

(a)   (b)
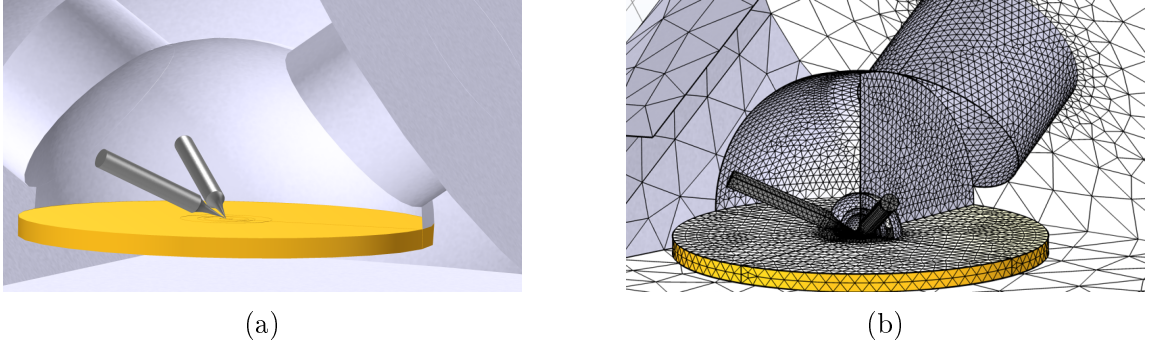
Figure 4.50: (a) Double tip geometry. Parameters are as follows: Long tip length: 4 mm; Angles: $\alpha = 35°$, $\phi = 45°$, $\psi = 45°$. THz Polarization: $\beta = +45°$. Distances: $d_{t-s} = 125nm, d_{t-t} = 200nm$. (b) Corresponding mesh for the double tip geometry.

order, a large tip-sample distance of 125 nm and tip-tip separation of 200 nm is used. The distance dependence studies have already shown that the near-field in terms of the gap voltage is maintained for gap distances of up to 1 µm. Fig. 4.51 plots the simulated near-field waveform obtained at each tip's apex. Tip 1 being THz active shows an enhanced THz pulse while Tip 2 shows a waveform generated by reflections with half the amplitude.
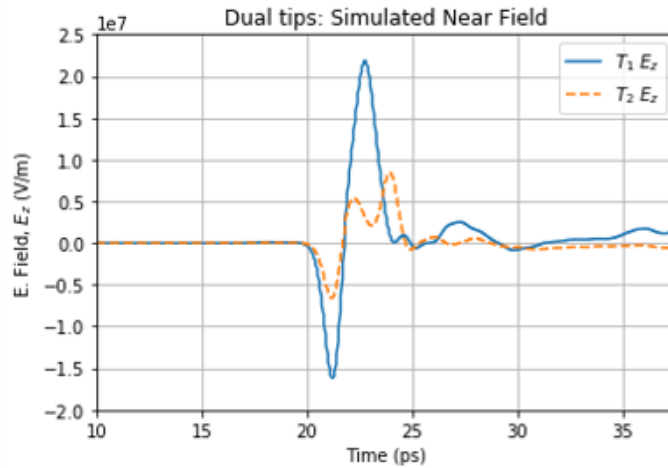
Figure 4.51: Contrast of the near-field between the two tips when the incident polarization is in line with the longitudinal axis of tip 1 ($\beta = +45°$).

In the future, the multi-probe THz-STM simulation will house up to four tips. The mesh design using circular mesh zones is quite robust with plenty of computation resources available to execute multi-probe simulations. The optics aspect should

contain at least two port windows. One for the THz and another for an optical frequencies or a second THz port. The various kinds of THz tip-plasmon modes and the structure of the nearfield still have to be studied deeply with the two tip design. In future simulations, many interesting modes will be simulated with four tips.

4.10 Chapter Summary

The COMSOL Multiphysics software was employed to solve the electromagnetics of THz pulses coupling to the STM geometry. The steps of a Finite Element Method model of the THz-STM in COMSOL have been described from constructing the geometry, meshing, assigning boundary conditions accounting for material properties and extracting data from the simulation data set. The data set contains the solved electromagnetic field components in space and time. Due to the meshing strategy, the electric fields in the far-field and near-field of the STM gap can be probed. The far-field visualization of the EM simulation in COMSOL illustrates THz pulse propagation, coupling and scattering to the STM geometry. In the near-field, the electric field is enhanced by large factors of 10^2 to 10^4 depending on the gap distance. The electric near-field waveform in the gap region differs from the incident pulse, consistently showing a broadened main pulse followed by reflection pulses. The next key result is the simulation of field penetration. The conducting interface on the sample surface cannot screen the fast transient of the coupled fields, so a small enhanced form of the incident field exists below the sample surface. Lastly, the spectrum of the near-field amplitude follows a $1/f$ dependence, which implies that THz pulses interact with the STM tip via antenna coupling. The full-scale simulation of the THz antenna coupling establish that the entire geometry of the STM configuration and tip shape play a crucial role in the formation of the near-field inside the STM junction.

Geometry variations were performed as simulation parameter sweeps. The tip-sample distance dependence show larger field enhancements at smaller distances, but a constant gap voltage. Varying the angle of incidence and polarization angle show

that the field enhancement is optimal when the field component of the incident radiation is mostly along the axis of the tip shaft. Sample material dependence was studied to investigate the field penetration versus sample conductivity and dielectric values. Various tip shapes were simulated which consist of adjusting the tip dimensions (length, taper length, apex radius) and building various taper geometries to imitate realistic tips used in STM experiments. Lastly, the multi-probe STM geometry is simulated to show the prospects of a THz-STM system where one or more tips may be coupled to THz. The simulation results presented in this chapter are used to understand THz-STM observations and may suggest effective experimental designs for efficient THz/optical radiation coupling.

Chapter 5

Modeling the THz Near-field with Electrodynamics

5.1 Near-field Plasmonics

Electromagnetic radiation coupling to a conical tip structure is a deeply researched physics problem that does not have full analytical solutions [118]. Often, approximations and assumptions have to be set to simplify the problem. For example, reducing the dimensional length scale of the geometry to be on the same order with parameters such as the wavelength of the coupled light wave or tip-sample distance. The near-field plasmonics picture only considers reducing the tip down to geometry that scales with the light wavelength. Often, such experiments are conducted with infrared and visible light, so that the problem deals with length scales on the order of 100 nm.

This chapter summarizes published works in the field of near-field microscopy that attempts to model the electromagnetic (EM) scenario where light couples to a simple tip probe [60, 62, 127, 167, 196, 197]. The electrodynamic effects on charge carriers under the influence of the near-field are described. The second half of the chapter summarizes analytical and approximate solutions in the literature as well as simulations using a first order discrete dipole model in attempt to reproduce basic radiation and scattering scenarios.

5.1.1 Maxwell's Constitutive Relations

The formalism for near-field optics starts with Maxwell's equations of electromagnetism [61, 118]:

$$\nabla \cdot \mathbf{E}(\mathbf{r}, t) = \frac{\rho(\mathbf{r}, t)}{\epsilon_0}, \tag{5.1}$$

$$\nabla \cdot \mathbf{B}(\mathbf{r}, t) = 0, \tag{5.2}$$

$$\nabla \times \mathbf{E}(\mathbf{r}, t) = -\frac{\partial \mathbf{B}(\mathbf{r}, t)}{\partial t}, \tag{5.3}$$

$$\nabla \times \mathbf{B}(\mathbf{r}, t) = \mu_0 \left(\epsilon_0 \frac{\partial \mathbf{E}(\mathbf{r}, t)}{\partial t} + \mathbf{j}(\mathbf{r}, t) \right). \tag{5.4}$$

where $\mathbf{E}$ denotes the electric field, $\mathbf{B}$ the magnetic field, ρ the charge density which is the sum of free and bounded charges (i.e. $\rho = \rho_f + \rho_b$), ϵ_0 is the free-space permittivity constant, μ_0 is the free-space permeability and $\mathbf{j}$ is the current density. The field quantities can be related to the fields inside a medium associated with bound charges and currents: $\mathbf{D}$, the electric displacement field and $\mathbf{H}$, the magnetizing field. The fields in matter are linked to the polarization $\mathbf{P}$ and magnetization $\mathbf{M}$ fields inside a medium by the following expressions:

$$\mathbf{D} = \epsilon_0 \mathbf{E} + \mathbf{P} = \epsilon_0 \epsilon_r \mathbf{E} = \epsilon \mathbf{E}, \tag{5.5}$$

$$\mathbf{H} = \mu_0^{-1} \mathbf{B} - \mathbf{M}, \tag{5.6}$$

$$\mathbf{P} = \epsilon_0 \chi_e \mathbf{E}, \tag{5.7}$$

$$\mathbf{M} = \chi_m \mathbf{H}. \tag{5.8}$$

where χ_e is the electric susceptibility and χ_m is the magnetic susceptibility. The dielectric constant, ϵ, is the product of the relative dielectric constant of the material, $\epsilon_r = 1 + \chi_e$, and ϵ_0. The final constitutive relation is the internal current density $\mathbf{j}$ and electric field $\mathbf{E}$, defined as

$$\mathbf{j} = \sigma \mathbf{E}, \tag{5.9}$$

where σ is the electrical conductivity of the medium and is a function of space.

With an ansatz for the field of $\exp(-i\omega t)$ time-dependence, Maxwell's equations in the absence of any external source charges and currents read,

$$\nabla \cdot \epsilon(\mathbf{r}, \omega)\mathbf{E}(\mathbf{r}, \omega) = 0 \tag{5.10}$$

$$\nabla \cdot \mathbf{B}(\mathbf{r}, \omega) = 0 \tag{5.11}$$

$$\nabla \times \mathbf{E}(\mathbf{r}, \omega) = i\omega\mathbf{B}(\mathbf{r}, \omega) \tag{5.12}$$

$$\nabla \times \mathbf{B}(\mathbf{r}, \omega) = -i\omega\mu_0\epsilon_0\mathbf{E}(\mathbf{r}, \omega). \tag{5.13}$$

This set of equations uses a macroscopic approach where the response of matter to an excitation EM field is described by the dielectric function $\epsilon(\mathbf{r}, \omega)$. The materials used in the simulations and models are assumed to be non-magnetic, thus the magnetic permeability is equal to μ_0 everywhere. The scatterer's size is usually large enough so that one would model the response of a large number of atoms to an external electric field using a global property.

5.1.2 Surface Plasmons

Now we consider EM propagation which is useful for time and frequency domain analyses of the system we attempt to model.

Maxwell's Wave Equations

The general form of wave equations can be obtained by substituting fields $\mathbf{D}$ and $\mathbf{B}$ in Maxwell's curl equations. The expression is derived as

$$\nabla \times \nabla \times \mathbf{E} + \frac{1}{c_0^2}\frac{\partial^2 \mathbf{E}}{\partial t^2} = -\mu_0\frac{\partial}{\partial t}\left(\mathbf{j} + \frac{\partial \mathbf{P}}{\partial t} + \nabla \times \mathbf{M}\right), \tag{5.14}$$

$$\nabla \times \nabla \times \mathbf{H} + \frac{1}{c_0^2}\frac{\partial^2 \mathbf{H}}{\partial t^2} = \nabla \times \mathbf{j} + \nabla \times \frac{\partial \mathbf{P}}{\partial t} + \mu_0\frac{\partial \mathbf{P}}{\partial t}. \tag{5.15}$$

where the constant c_0 is substituted for $(\epsilon_0\mu_0)^{-1/2}$ and known as the vacuum speed of light.

In the absence of net charge and free current densities, the fundamental wave equation of the electric field in space where dielectric media may be present is given

135

as

$$\nabla^2 \mathbf{E} - \frac{\epsilon_r}{c_0^2} \frac{\partial^2 \mathbf{E}}{\partial t^2} = 0. \tag{5.16}$$

Inside the medium with refractive index n, the dielectric constant is $\epsilon_r = n^2$. The coefficient in front of the second time derivative term of Eq. 5.16 can be expressed in terms of the phase velocity inside the medium, v:

$$\frac{\epsilon}{c_0^2} = \frac{n^2}{c_0^2} = \frac{1}{v^2}. \tag{5.17}$$

Using the continuous wave time-dependence for electric field, $\mathbf{E}(\mathbf{r}, t) = \mathbf{E}(\mathbf{r})e^{-i\omega t}$, the wave equation becomes the *Helmholtz equation*,

$$\nabla^2 \mathbf{E} + k_0^2 \epsilon_r \mathbf{E} = 0 \tag{5.18}$$

where $k_0 = \omega/c_0$ is the wave-vector of the propagating wave in vacuum.

Electromagnetic Surface Modes

Surface plasmon polaritons (SPPs) can bind EM fields to the interface between a dielectric and a conductor. On typical metals, SPPs evolve into grazing incidence light fields as the frequency drops. The field pattern observed along the interface indicates that there is an oscillating spatial charge distribution in the metal. The parameter that describes highly confined surface excitations due to light field in the dielectric propagating along the interface with the same phase velocity of the unbound radiation, is the complex metal's permittivity where there is a large negative real part and a positive imaginary component [61]. The field amplitude is an evanescent decay perpendicular to the interface in either direction. Highly-doped semiconductors can also support the formation of SPPs.

The next step is to perform a boundary condition analysis to derive the equation for an EM wave propagating along a single interface consisting of two media with dielectric values ϵ_1 and ϵ_2 as shown in Fig. 5.1.
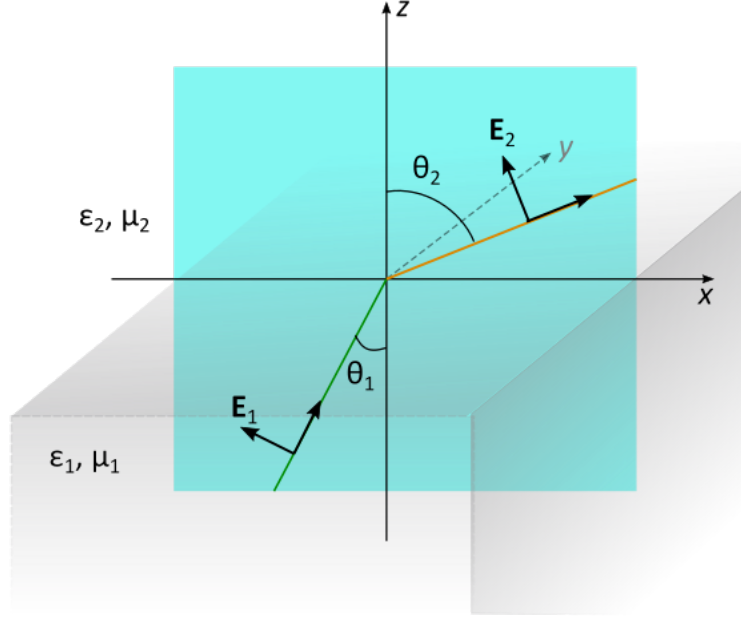
Figure 5.1: Interface between two media with given constitutive parameters, ϵ, μ. The interface is located at $z = 0$ in a Cartesian coordinate system. Adapted from [61, 118].

Consider only p-polarized waves in both half-spaces as no solutions exist for the case of s-polarization. The plane waves in half spaces 1 and 2 can be written as

$$\mathbf{E_{inc}} = \begin{pmatrix} E_{n,x} \\ 0 \\ E_{n,z} \end{pmatrix} e^{ik_x x - i\omega t} e^{ik_{n,z} z}, \quad n = 1, 2. \tag{5.19}$$

The wavevector component has the following relation:

$$k_x^2 + k_{n,z}^2 = \epsilon_n k^2, \quad n = 1, 2, \tag{5.20}$$

where ϵ_n is the dielectric constant in the medium, $k = 2\pi/\lambda$ and λ is the wavelength of the incident light. The displacement fields in both half-spaces must satisfy $\nabla \cdot \mathbf{D} = 0$ for being source free, so

$$k_x E_{n,x} + k_{n,z} E_{n,z} = 0, \quad n = 1, 2, \tag{5.21}$$

which allows the field in Eq. 5.19 to be rewritten in terms of the k vectors as

$$\mathbf{E_{inc}} = E_{n,x} \begin{pmatrix} 1 \\ 0 \\ -k_x/k_{n,z} \end{pmatrix} e^{ik_x x - i\omega t} e^{ik_{n,z} z}, \quad n = 1, 2. \tag{5.22}$$

The fields at the interface are solved using boundary conditions where the parallel component of $\mathbf{E}$ and perpendicular component of $\mathbf{D}$ are continuous. Plugging in the index values for n, another set of equations are given as

$$E_{1,x} - E_{2,x} = 0 \tag{5.23}$$

$$\epsilon_1 E_{1,z} - \epsilon_2 E_{2,z} = 0. \tag{5.24}$$

Putting in indices for Eqs. 5.21 and combining with Eqs. 5.23 form a system of equations to solve for four unknown field components. Cases where the determinant of the system vanish, implying the existence of a solution, occur for $k_x = 0$ (i.e. a static excitation), or for

$$\epsilon_1 k_{2,z} - \epsilon_2 k_{1,z} = 0. \tag{5.25}$$

Combining Eq. 5.20 with Eq. 5.25 leads to a function for the excitation's angular frequency, ω versus the wavevector, known as the dispersion relation. The wavevector in the propagation direction is

$$k_x^2 = \frac{\epsilon_1 \epsilon_2}{\epsilon_1 + \epsilon_2} k^2 = \frac{\epsilon_1 \epsilon_2}{\epsilon_1 + \epsilon_2} \frac{\omega^2}{c^2}. \tag{5.26}$$

The normal component of the wavevector in either medium is

$$k_{n,z}^2 = \frac{\epsilon_n^2}{\epsilon_1 + \epsilon_2} \frac{\omega^2}{c^2}, \quad n = 1, 2. \tag{5.27}$$

A real k_x is required to have a propagating interface mode. Considering the real component of the complex dielectric functions is dominant such that the imaginary component can be neglected, then the sum and product of the dielectric functions in Eq. 5.26 must be either both positive or both negative. Looking at the exponential term for z in Eq. 5.19, a bound solution occurs when the normal component of

138

the wavevector is purely imaginary so that the field decays exponentially with z in both media. Thus the sum of the denominator must be negative in Eq. 5.27. The conditions for an interface mode are given by:

$$\epsilon_1(\omega) \cdot \epsilon_2(\omega) < 0, \tag{5.28}$$

$$\epsilon_1(\omega) + \epsilon_2(\omega) < 0. \tag{5.29}$$

One of the dielectric functions must be negative whose magnitude must be larger than the other to avoid the case of zero denominator. In general, considering imaginary components of the dielectric function would make k_x complex, which leads to a damped propagation in the x direction. The physical cause for damping is by ohmic losses of the electrons participating in the SPP, resulting in heating of the metal.

Typical metals such as gold and silver have a large negative real component and a small imaginary component for their dielectric constant. Dielectric materials such as glass or air have real positive values for their dielectric constant. Propagating modes at the metal-dielectric interface can be supported according to the discussion above. Given an interface where the metal has a complex dielectric value

$$\epsilon_1 = \epsilon_1' + i\epsilon_1'', \tag{5.30}$$

and the dielectric medium, ϵ_2, is real and positive, the wavelength of the SPP is approximated as

$$\lambda_{\text{SPP}} = \frac{2\pi}{\text{Re}(k_x)} \simeq \sqrt{\frac{\epsilon_1' + \epsilon_2}{\epsilon_1' \epsilon_2}} \lambda. \tag{5.31}$$

Decay lengths scale as $1/k$. The decay length of the normal component of electric field is much smaller in the metal (order of 10 nm) than in the dielectric (order of 100 - 1000 nm).

The physical reason for the increased momentum of the SPP is the strong coupling between light and surface charges. The light field has to "drag" the electrons along the metal surface, which means that the light of any frequency in free space does not always excite the SPP on the planar interface. Excitation of a SPP by light is only

achievable when the wavevector component of the exciting light is increased over its free-space value.

At THz frequencies, the complex permittivity of metals is $|\epsilon| \simeq 10^5$, leading to negligible field penetration into the conductor and highly delocalized fields, known as Sommerfeld waves [107]. Propagation of THz SPPs on metal surfaces have been measured experimentally, supporting the highly delocalized nature of these EM modes. Measurements and simulations show that single metal wires specifically support radial TEM modes [52, 108, 198]. The THz waveform at the input of the waveguide remains relatively undistorted all the way to the end of the waveguide, demonstrating a low group velocity dispersion.

5.1.3 Localized Surface Plasmons

Consider the focusing and confinement of free propagating radiation as light interacts with nanoscale matter. Localized surface plasmons are non-propagating excitations of the conduction electrons of metallic nanostructures coupled to the EM field. The amount of confinement significantly decrease for frequencies below the metallic plasma frequency (See Ch. 2, section 2.3 and Ch. 4, section 4.2.3) due to the decrease in propagation constant $\beta_{\mathrm{prop}} \simeq k_0 n$. Standard metals or highly doped semiconductors can support well-confined SPPs only at visible and near-infrared frequencies.

The simple case to analyze is a uniform polarizable sphere as shown in Fig. 5.2.

The curved surface of the nanostructure exerts an effective restoring force of the driven electrons, which leads to a resonant condition where field amplification occur both inside and outside the particle in the near-field regime. Even a large structure can support a surface plasmon if it contains a small roughness feature that could act as an excitation center.

A Laplace equation analysis can be used to solve for the electric potential and field around the spherical particle [61, 118]. The particle has spherical radius of a and volume dielectric function $\epsilon_1(\omega)$ surrounded by a medium with dielectric constant of
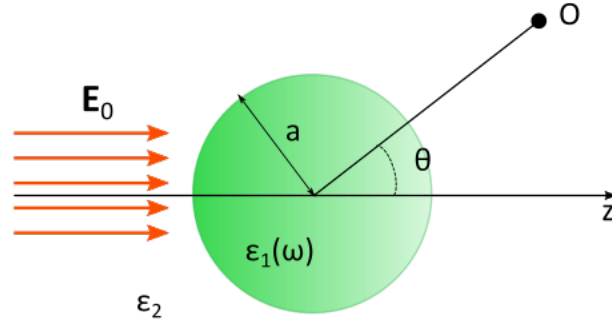
Figure 5.2: Dielectric sphere of uniform polarization placed into a background field polarized in the z-direction. Adapted from [118]

.

ϵ_2. The potential outside the sphere is

$$\Phi_{\text{out}} = -E_0 r \cos\theta + \frac{\mathbf{p} \cdot \mathbf{r}}{4\pi\epsilon_0\epsilon_2 r^3}, \tag{5.32}$$

where the dipole moment of the sphere is

$$\mathbf{p} = 4\pi\epsilon_0\epsilon_2 a^3 \frac{\epsilon_1 - \epsilon_2}{\epsilon_1 + 2\epsilon_2} \mathbf{E_0}. \tag{5.33}$$

Using the definition of $\mathbf{p} = \epsilon_0\epsilon_2\alpha\mathbf{E_0}$, we arrive back at the complex polarizability factor of

$$\alpha = 4\pi a^3 \frac{\epsilon_1 - \epsilon_2}{\epsilon_1 + 2\epsilon_2}. \tag{5.34}$$

The electric field outside the sphere is evaluated by taking $\mathbf{E} = -\nabla\Phi$ of Eq. 5.32. Along the radial direction the field is evaluated as

$$\mathbf{E}(r) = \left(E_0 \cos\theta + \frac{\epsilon_1 - \epsilon_2}{\epsilon_1 + 2\epsilon_2} \frac{2a^3}{r^3} E_0 \cos\theta \right) \hat{r}. \tag{5.35}$$

The near-field contains the strong $1/r^3$ dependence (analogous to the field emitted by a point dipole at close range), which is a useful concept when using nano-probes to exhibit a strong field to a nearby target. However the challenge is getting the target close enough to the probe as the field vanishes very quickly with distance.

141

The charge and field distribution for a spherical particle is visualized in Fig. 5.3(a). Unlike in Fig. 5.2, here the background field is polarized in the vertical direction.

5.1.4   Imaging localized SPPs

The intensity enhancement near the interface due to the excitation of surface plasmons is an important parameter in NF applications. It can be obtained by evaluating the ratio of the incoming intensity and the intensity surfacing the metal interface [199].

We can employ Scanning optical tunneling microscopy (STOM) theory to generalize a model for the effective polarizability [119, 120, 200]. The concept of a polariton is used to describe the dispersion observations. Polaritons are the polarization waves of a crystal which are excited by incident light. They are EM eigenmodes of condensed matter [200]. Modeling the polariton allows one to identify the conditions of existence of evanescent EM eigenmodes bound to the surface and to other interfaces.

Losses in the plasmon's propagation can be directly derived from the metal's bulk dielectric function. Fields associated with surface plasmons penetrate into the metal by more than 10 nm. The metallic thickness within the skin depth is responsive to the incident field. Charges within the skin depth layer are driven by the field, thus forming a charge density fluctuation along the surface of the metallic surface. The SPP embodies the charge density and the field lines at the interface of a metal plane, as depicted in Fig. 5.3(b). A similar mechanism applies for a metal tip as shown in Fig. 5.3(c). The SPPs are initiated along the tip shaft, then propagate towards the end of the tip where the charge density becomes confined at the tip taper and eventually get focused at the apex. The mechanism for field enhancement due to SPPs is due to the localized charge density at the tip apex, which increases with tip sharpness, thus the field lines get highly concentrated. The near-field resulting from the localization of SPPs becomes orders of magnitude greater than the incident field used to excite the SPP.
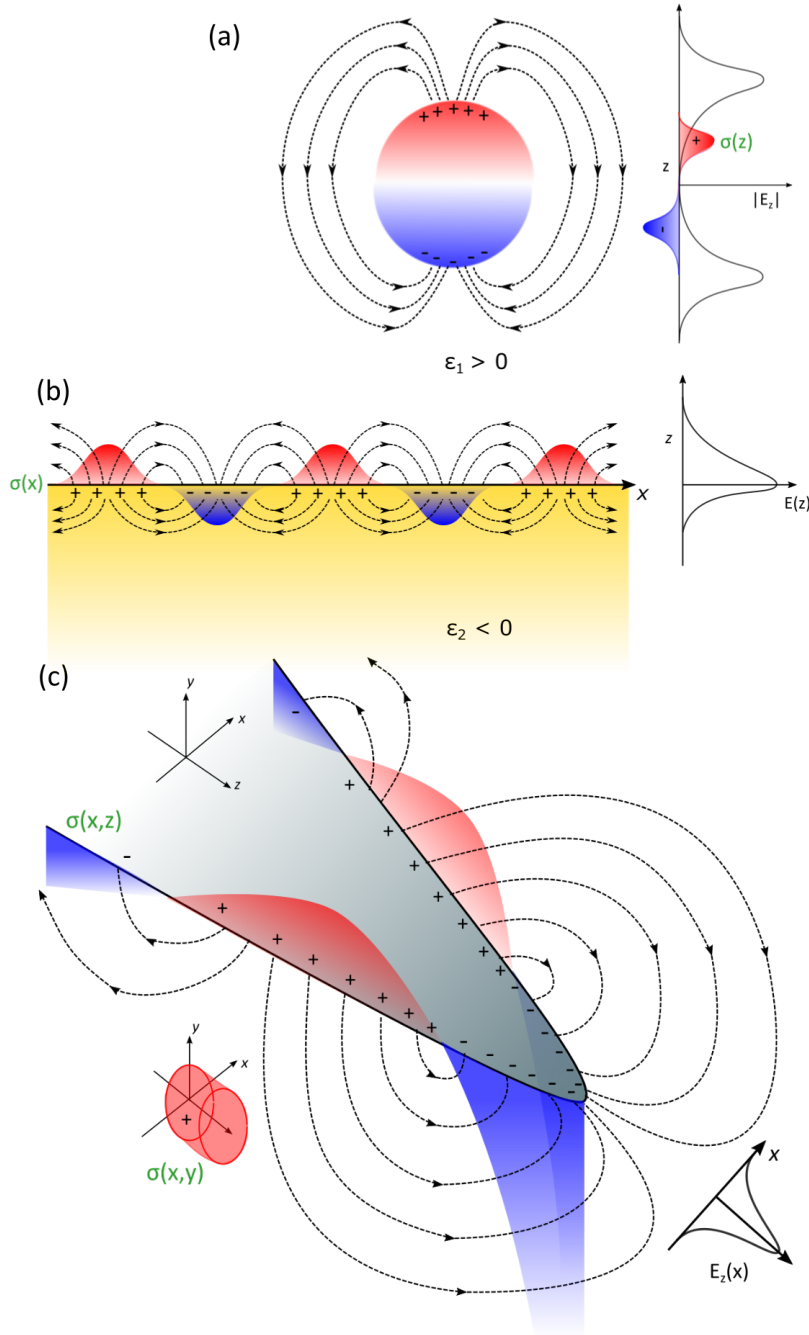
Figure 5.3: (a) Sphere dipole visualization with corresponding plots for the charge density and strength of electric field corresponding to the density of the field lines around the poles. (b) SPPs along an infinite planar interface with oscillating charge density inside the metal. The side plot shows the electric field strength along z at the image's cut-off location. (c) SPPs for a tip structure where the charge density and field lines converge at the tip apex. The corresponding charge density plot is shown before the tip apex indicating the positive lobe. The magnitude of the electric field is plotted for the tip apex. Note that the presence of surface current on the tip allows tangential field components to exist inside the metal. Hence the field lines do not necessarily have to be exactly perpendicular to the surface.

143

Figure 5.4: (a) Spheroid dipole dimensional parameters. (b) Schematic showing how the field and scattering by a spheroid can be calculated by approximating charges at various points. The tip-sample distance is d, radius of the base of the ellipsoid is R, major axis radius is L and the focal distance is F. Adapted from [127].

5.1.5 Finite-dipole approximation

The signal is a quantity with an overall amplitude and phase with a complex prefactor that couples to the incident field that can be determined using material parameters. In the frequency domain, the signal is the product of the coupling factor and the Fourier transform of the incident field.

Instead of using the sphere model summarized in Ch. 2 section 2.5.2, a better model approximates the tip as an spheroid as shown in Fig. 5.4a. The finite dipole is elongated so that the image dipole is also a spheroid.

The complex scattering factor for the specific geometry shown in Fig. 5.4(a) (see illustration of dimension parameters) is evaluated by integrating the field in the z direction, which yields [127]

$$\alpha_{\text{eff}} = R^2 L \frac{\frac{2L}{R} + \ln\frac{R}{4eL}}{\ln\frac{4L}{e^2}} \left(2 + \frac{\beta(g - \frac{R+d}{L})\ln\frac{4L}{4d+3R}}{\ln\frac{4L}{R} - \beta \left(g - \frac{3R+4d}{4L}\right)\ln\frac{2L}{2d+R}} \right). \tag{5.36}$$

where d is the tip-sample distance, g is a charge fraction of the effective integration region over the entire charge (See Fig. 5.4(b) and [127]), and β is the near-field interaction between the probe and the sample given by Eq. 2.42. The equation above only accounts for the geometric dimensions of the spheroid dipole. Analytical models for α_{eff} applied in SNOM can become highly complicated with more terms to factor

144

in when we attempt to model the near-field interaction for a full-scale geometry. Furthermore, the polarization factors, α and β, are functions of frequency, which encodes for phase dependence. However, when applying the model for materials with a highly variable response at a particular frequency range, the extent of the dipole interaction between the tip and sample must be adjusted. Eventually, numerical methods will have to be employed when the geometry grows in complexity, which was already demonstrated in Ch. 4 and later to be shown in the next section of this chapter.

5.1.6 Finite-dipole antenna model

Another approximation is summarized by approximating the tip as a line current with varying strength along its length [131]. The dipole moment is related to the current according to

$$p(z_0, t) = dz_0 \int_{-\infty}^{t} I(z_0, t')dt' = G(t)I(z_0)dz_0, \tag{5.37}$$

where all the time dependence is separated out into the term $G(t)$ and the spatial dependence is in $I(z_0)$.

Setting relative dielectric $\epsilon_r = \epsilon/\epsilon_0$, the electric field of the vertical antenna observed at location $\mathbf{r} = (x, y, z)$, where $r^2 = x^2 + y^2$, is given by the expression

$$E_z = -\frac{2G(t)}{4\pi\epsilon_0(1 + \epsilon_r)} \int_a^b \left(\frac{I(z_0)r^2}{(r^2 + (z - z_0)^2)^{5/2}} - \frac{2I(z_0)(z - z_0)^2}{(r^2 + (z - z_0)^2)^{5/2}} \right) dz_0. \tag{5.38}$$

where z_0 are the z coordinates contained in the wire antenna, a and b are the endpoints of the antenna along the z-axis. For an antenna with a triangular current distribution that peak at position $z = a + (b - a)/2$ with value I_0, the integration in Eq. 5.38 evaluates as

$$E_z = \frac{2I_0 G(t)}{4\pi\epsilon_0(1 + \epsilon_r)} \left(\frac{1}{R_a} + \frac{1}{R_b} - \frac{2}{R} \right), (z \leq 0), \tag{5.39}$$

where the observer must be positioned below the antenna along the z-axis (i.e. $z \leq 0$). The R values are defined in Fig. 5.5.

We now have various forms of expressions for the near-field radiated by the tip-sample system. The system is also selective on the frequency components that would get enhanced due to the material properties and coupling geometry.
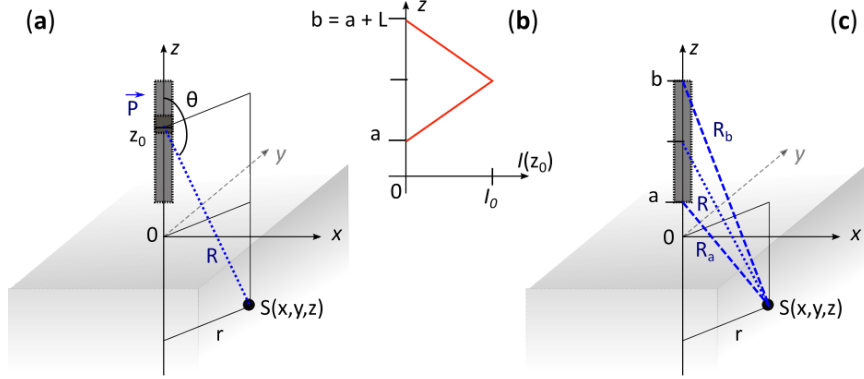
Figure 5.5: (a) Wire dipole is approximated as a current distribution. A unit dipole relative to the observation point. (b) The current distribution is triangular across the length of the wire. (c) The signal is the integrated electric field due to the dipole current along the wire.

5.1.7   Field-Enhancement

Large fields can be generated in optical cavities via the generation of confined surface plasmons. Resonance conditions in metallic nanostructures can be met to optimize the field enhancement at specific frequencies. The main mechanism is the establishment of constructively interfering standing waves in the cavity. Ideally, near-perfect conductors minimize field leakage. Field enhancement is also a natural phenomenon in antenna theory. It occurs because an antenna concentrates electromagnetic energy into a tight space thereby generating a zone of high energy density. For THz frequencies, the losses are quite low since THz radiation does not penetrate far into metals (i.e. $< 1\mu$m). The field enhancement in a gap formed by two metallic planes can be approximated as the ratio of the incident wavelength of the plane wave and the size of the gap:

$$FE = \frac{\lambda_{\text{inc}}}{d_{\text{gap}}}. \tag{5.40}$$

146

In SNOM, the tip-sample cavity geometry generally consists of a curved metallic surface with a parameter representing the curvature (i.e. tip apex radius) on one side and a metallic plane on the other side. Modeling of the enhanced field around the tip apex where geometry and material dependence are considered [58, 201] shows the field enhancement factor is more like power dependence,

$$FE = \left(\frac{\lambda_{\mathrm{inc}}}{d_{\mathrm{gap}}}\right)^\delta \tag{5.41}$$

where δ is a power exponent parameter which can vary from less than or greater than 1. Some resonance conditions can produce stronger field enhancements at certain frequencies to boost the exponent value. This power dependence was simulated in the field enhancement versus distance using COMSOL and summarized in Fig. 4.17(a). The slopes determined by fitting the log-log plot provides an estimate for the δ parameter.

5.2   Near-field Dynamics

The large field enhancement consequently leads to various field-driven processes that will be discussed in this section. Many unseen processes occur when matter interacts with the near-field of the probe. It is possible to deduce the near-field quantities by observing the behaviour of particles driven by the field. A sample can be used as a detector to measure charge carrier signals localized in the near-field regime.

5.2.1   Field-driven processes around the tip apex

Strong-field interactions of light with atoms and nanostructures can be described by both quantum-mechanical and classical concepts. Examples of strong-field phenomena in the near-field of sharp tips are field emission, quiver motion, nonlinear photoemission and hot electron plasmon generation [66–68, 70, 79]. THz pulses alone can be used to induce electron emission from nanostructures via a nonlinear process [66, 69, 74]. More interestingly, near-field dynamics is studied generating hot electrons by

exciting the nanotip with an optical pulse, then sending in a THz pulse to accelerate the electrons [67, 68, 70, 79]. In this case both field-driven tunneling electrons and hot electrons under the THz field potential can be studied. The ponderomotive potential created by the driving field around a nanostructure such as a tip is given by

$$U = \frac{e^2 E^2}{4 m \omega^2} \tag{5.42}$$

where E is the magnitude of the electric field, e is the elementary charge, m is the electron's mass and ω is the optical driving frequency. The characteristic tunneling frequency where electrons escape out of the tip into vacuum with the assistance of the electric field is given by

$$\omega_K = \frac{eE}{\sqrt{2m\Phi}}, \tag{5.43}$$

where Φ is the workfunction of the metal in vacuum. The inverse of Eq. 5.43 is related to the time needed for an electron to acquire a ponderomotive energy equal to the ionization potential, Φ. The Keldysh parameter is the ratio of the driving frequency ω and tunneling frequency ω_K, $\gamma = \omega/\omega_K$. When $\gamma \gg 1$, the driving field has a high photon energy and electrons are emitted from the tip with the assistance of photons, thus termed as the multiphoton regime. When $\gamma \ll 1$, which typically occurs for THz fields, the ionization is driven by large field amplitude, which describes the field-emission regime. Therefore an optical excitation of the tip versus a THz excitation can produce different ratios and drive the emission of electrons. Photoinduced electron emission from sharp metal tips require high kilovolt bias voltages which is a deterrent for nanoimaging [202, 203].

5.2.2 Field-driven processes below sample surface

When the sample is not a perfect conductor, the signal will vary with the sample material properties, whether it is measured in the far-field or in the near-field (i.e. the sample is used as a probe). If the signal is measured in the far-field, the scattering parameters have to be determined. There is a formation of net dipole which

includes the body of charges created within the sample. The field mapping inside the sample has its own coupling parameters. The spatial amplitude can be determined by boundary conditions for the various possible polarizations and angle of incidences. The phase is determined by calculating the full complex scattering parameter.

The field inside the semiconductor below the sample surface following field enhancement in the gap is given by

$$E_{\text{THz}}(\omega) = \frac{E_{\text{THz}}^{\text{gap}}}{\epsilon_{\text{samp.}}(\omega)}, \tag{5.44}$$

where $E_{\text{THz}}^{\text{gap}}$ is the field inside the gap determined from Eq. 4.6 and the dielectric constant $\epsilon_{\text{samp.}}$, is for the semiconductor as a function of frequency. From the simulations in chapter 4 and using the peak THz fields generated from the experimental optics setup, the field in the gap is calculated to peak at 10 MV/cm. Using the dielectric constant for n-doped Si which ranges from 10-100 at THz frequencies, corresponding to $10^{15} - 10^{19} \, \text{cm}^{-3}$ doping, the peak THz field in the sample bulk ranges from 1 to 0.01 MV/cm, respectively. From the simulation plots in Fig. 4.30, the decaying field values inside the bulk of variously doped Si samples matches with the expected ranges of low and high doping concentration.

5.2.3 Electron dynamics in the THz nearfield

The nearfield influences carrier motion inside the tip, gap and sample. A simple model for the electron's ballistic motion can be described by the following. Given that the only force influencing free electrons is from the THz nearfield, the electron's ballistic acceleration is

$$a = \frac{eE_{\text{THz,NF}}}{m_e}, \tag{5.45}$$

where $E_{\text{THz, NF}}$ is the local THz field in the nearfield region driving the electron motion, e is the elementary charge and m_e is the electron's mass. The acceleration stops when the electron scatters within a time constant τ. The electron gains peak velocity,

$$v = a \cdot \tau. \tag{5.46}$$

Thus, the corresponding peak kinetic energy is

$$E_K = \tfrac{1}{2}\, m_e v^2 = e^2 E_{\text{THz,NF}}^2 \tau^2 / 2 m_e, \tag{5.47}$$

and average distance traveled within the time constant is

$$\Delta z = \tfrac{1}{2}\, a\tau^2 = \tfrac{1}{2}\, e E_{\text{THz,NF}} \tau^2 / m_e. \tag{5.48}$$

The model is applied for n-doped Si where the electron scattering time constants range from 1 to 0.01 ps in $10^{15} - 10^{19}\,\text{cm}^{-3}$ doped materials, respectively. The mean-free-paths range from 10^3 nm in lowly doped Si and 1 nm in highly doped Si. The model is quite simplistic assuming the THz field to be constant, when usually the THz field peak occurs within hundreds of femtoseconds. Electrons usually escape regions of high fields in times less than the scattering time.

When combined with Monte-Carlo simulations, the probability of electrons to reach the tip starting at the sample's surface or bulk, can be computed. In this simulation setup, electrons have to crawl towards the sample surface by undergoing acceleration driven by THz nearfield that penetrated into the bulk while being impeded by scattering events. The Drude model uses the scattering times parameterized by the material's doping. For impact ionization scattering, the electron crossing an energy threshold scatters entirely and loses all energy. According to the simplified model, for each scattering event, the electron gains thermal energy $\frac{1}{2}k_B T$. After accumulating sufficient energy, the electrons can thermalize and enter vacuum.

5.3 Discrete-Dipoles Model

Here we model the pulse propagation from near-field to far-field from a THz source using array of point dipoles. Similar work using discretized dipoles was done in [127, 181].

Fundamental radiation unit emitted by a point dipole is given by the previously

mentioned equation 2.17, in polar coordinates

$$\mathbf{E}(\mathbf{r}, t) = \frac{1}{4\pi\epsilon_0} \left[\hat{\theta} \sin\theta \left(\frac{\mathbf{p}}{r^3} + \frac{\dot{\mathbf{p}}}{c_0 r^2} + \frac{\ddot{\mathbf{p}}}{c_0^2 r} \right) + \hat{\mathbf{r}} \cos\theta \left(\frac{2\mathbf{p}}{r^3} + \frac{2\dot{\mathbf{p}}}{c_0 r^2} \right) \right]. \tag{5.49}$$

The dipole waveform can be any arbitrary function of time, usually in the form of a pulse. For the simulations in this section, the fundamental dipole waveform is a Gaussian pulse, where the first-derivative Gaussian (FDG) and second-derivative Gaussian (SDG) components are plotted in Fig. 5.6.
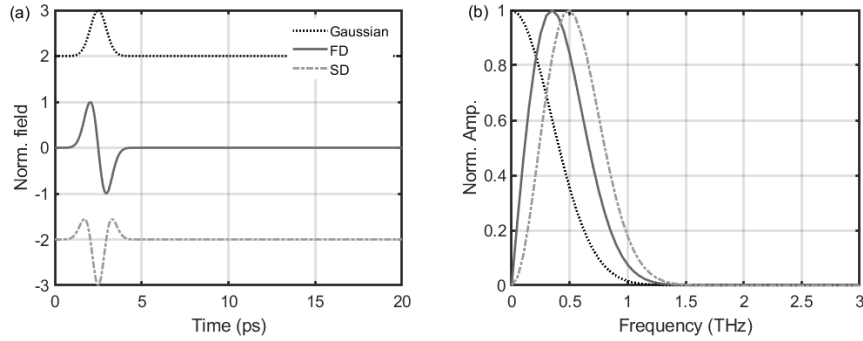
Figure 5.6: Dipole moment waveform for a unit dipole using Gaussian function forms. The elementary dipole moment term, $\mathbf{p}(t)$ is set as a Gaussian pulse. The first derivative (FD), $\dot{\mathbf{p}}(t)$, and second derivative (SD), $\ddot{\mathbf{p}}(t)$, dipole terms are the corresponding first and second order Gaussian derivatives, respectively.

A dipole configuration is defined for the source that generates the incident electric field radiation. Simple geometries can be a linear array configuration shown in Fig. 5.7a or a 2D disk configuration of many unit dipoles shown in Fig. 5.7b.

Next, an observation point is set in space to measure the radiated electric field by the source configuration. The distance from a source dipole unit to the observation point located at $\mathbf{r_O}$ is d_{PO}. The distance from the source's center to the observation point is generalized as d_{SO}. Fig. 5.8(a) shows how an observer measures the electric field components of the source's radiation, $\mathbf{E}^{\text{inc}}(\mathbf{r_S O}, t)$. The observed electric field is given as a summation:

$$\mathbf{E}^{\text{inc}}(\mathbf{r}, t) = \sum_{S}^{p} \mathbf{E_p}(\mathbf{r_{pO}}, t - t_{pO}) \tag{5.50}$$

151

(a)   (b)
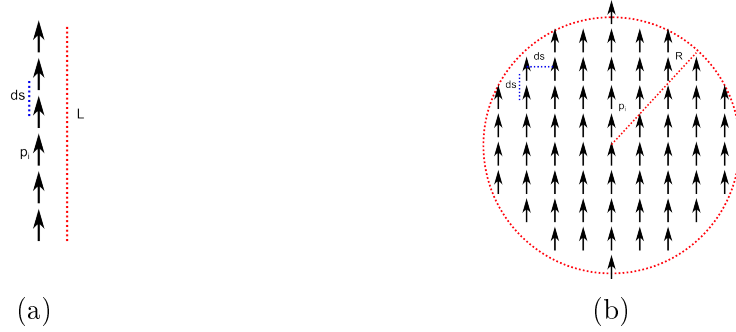
Figure 5.7: (a) Line dipole configuration by stacking unit dipole moments in a linear array with spacing ds. The total number of unit dipoles is the configuration length L divided by ds. (b) Disk dipole configuration. In reality, the dipoles are stacked so that the number of dipoles decrease by 2 units on the next level until it thins out at the top. The spacing ds is the same for horizontal and vertical directions. The estimated disk radius is R.

where dipole unit $\mathbf{p}$ is part of the configuration S, the relative distance $\mathbf{r_{pO}}$ is $\mathbf{r_O} - \mathbf{r_p}$, and the time delay t_{pO} is the duration for light radiation to go from the dipole unit to the observer. In free-space $t_{pO} = d_{pO}/c_0$ where c_0 is the speed of light in vacuum.

To calculate scattering by another object, we define a scattering dipole configuration located at some distance away from the source, as shown in Fig. 5.8(a). The scatterer reacts to the incident field radiated by the source. A dipole within a configuration may be given a coupling strength factor which is related to the geometric or material's response to external radiation. Note that when a complex value is introduced, then there will be a phase for the dipole response. The distance from a source dipole unit to a scattering dipole unit is d_{SC}. The incident field radiated by the source and received by a scattering dipole unit is the excitation field, $\mathbf{E^{exc}}(\mathbf{r_S}C, t)$. The scattered field measured by the observer is $\mathbf{E^{scat}}(\mathbf{r_O}, t)$ given by the expression:

$$\mathbf{E^{scat}_C}(\mathbf{r_C}, t) = \alpha^{scat}_C \sum_S^p \mathbf{E^{inc}_p}(\mathbf{r_{pC}}, t - t_{pC}) \tag{5.51}$$

where C is a scattering dipole configuration, p is a dipole unit within S, α^{scat}_C is a complex scattering coefficient that responds to the excitation field and the time delay is from a source dipole to a scattering dipole, $t_{pC} = d_{pC}/c_0$.

Each dipole in the scatterer configuration receives a unique input electric field
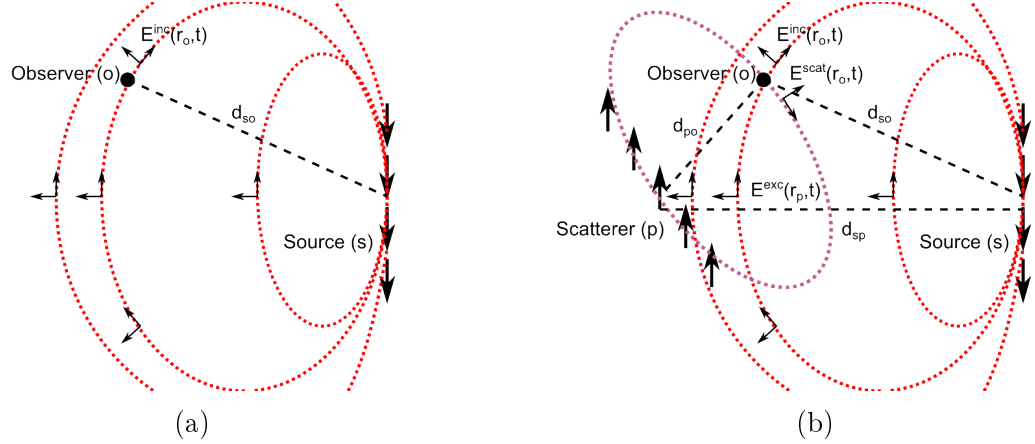
Figure 5.8: (a) Observing the radiated field from a source configuration, S. The observer at position $\mathbf{r_O}$ is located at a distance d_{SO} from the source and measures the radiated electric field $\mathbf{E}(\mathbf{r_S O}, t)$. (b) Schematic for an observer measuring both the radiated and scattered fields. The distance from a source dipole unit to a scattering dipole unit is d_{SC}. The incident field radiated by the source and received by a scattering dipole unit is the excitation field, $\mathbf{E^{exc}}(\mathbf{r_S C}, t)$. The additional scattered field component measured by the observer is $\mathbf{E^{scat}}(\mathbf{r_O}, t)$.

from the source due to position dependence and the time delay for the incident pulse to excite the scattering dipole. The distance between the scattering dipoles to the observer also varies, so the observer sees a time-delayed superposition of fields radiated by all scattering dipoles. Fig. 5.8(b) visualizes the time-delayed superposition of radiated and scattered fields from each contributing point dipole in the simulation.

The electric field is calculated using equation 5.49, which yields the angular and radial component of electric field. These components must be converted to Cartesian components before field superposition can be applied. Fig. 5.9 shows how the polar components, $\hat{r}$ and $\hat{\theta}$, can be converted to the Cartesian x and z components.

Next, we apply time-delayed field superposition to obtain the total field measured by the observer for all components. The summation is performed for all contributing dipoles, given as:

$$\mathbf{E^{tot}}(\mathbf{r_O}, t) = \sum_{S}^{p} \mathbf{E_p^{inc}}(\mathbf{r_{pO}}, t - t_{pO}) + \sum_{C}^{p} \mathbf{E_p^{scat}}(\mathbf{r_{pO}}, t - (t_{Sp} + t_{pO})), \qquad (5.52)$$

where the time delays considered are from the source to the observer, the source to the scatterer, and the scatterer to the observer. Note that the scattering coefficient,
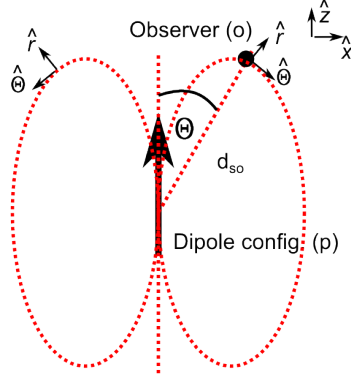
Figure 5.9: The angular and radial field components in angular coordinates, which can be converted to the Cartesian x and z components using simple trigonometric ratios. The relative angle, ϕ, between the $\hat{r}$ - $\hat{\theta}$ axes to the x - z axes must be known for different observer positions along θ.

α_p^{scat}, for a scattering dipole is already contained in $\mathbf{E_p^{scat}}$ as mentioned in Eq. 5.51.

5.3.1 Disk source emitter

Fig. 5.10 (a) depicts the geometry used for a disk source emitter. The tube end at $x = 0$ is a disk dipole configuration, as modeled in Fig. 5.7b. In COMSOL, the boundary is defined as a planar current source where the input dipole waveform is the unit Gaussian pulse as shown in Fig. 5.6.

The radiated electric field from a disk source can be simulated using the discrete dipoles configuration in Fig. 5.7. The THz pulse emission and propagation from a disk current source in Fig. 5.7(b) can be compared to the port window THz emission and free-space propagation in the COMSOL geometry, as shown in Fig. 5.10. Fig. 5.11 shows the electric field waveforms measured from the center of the disk source along the propagation axis at various distances. The waveforms in both simulations are shown to be very similar. It can also be seen that close to the source, the waveform looks like the first derivative Gaussian, then evolves to the second derivative Gaussian as the pulse propagates further away.
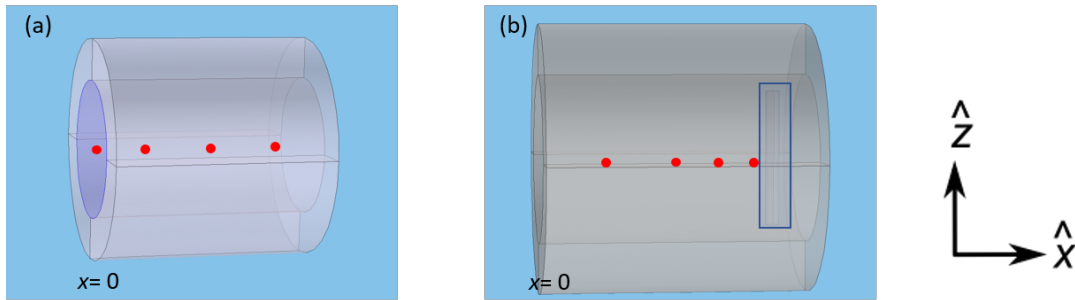
Figure 5.10: (a) Geometry for a disk source emitter used in both calculations and COMSOL simulations. The tube diameter is 5 mm and 6 mm in length. The red dots indicate observer positions at 0.1, 0.5, 1, 2, 3 mm from the source along the propagation axis. The other end of the tube is set as a reflective boundary for the disk source and disk scatterer simulation in subsection 5.3.3. (b) Geometry for a disk source emitter or wire scatterer (highlighted by the shaded box) placed at about 5.5 mm away from the source. The observation positions are located at 0.1, 0.5, 1, 2, 3 mm from the center of the scatterer along the propagation axis.
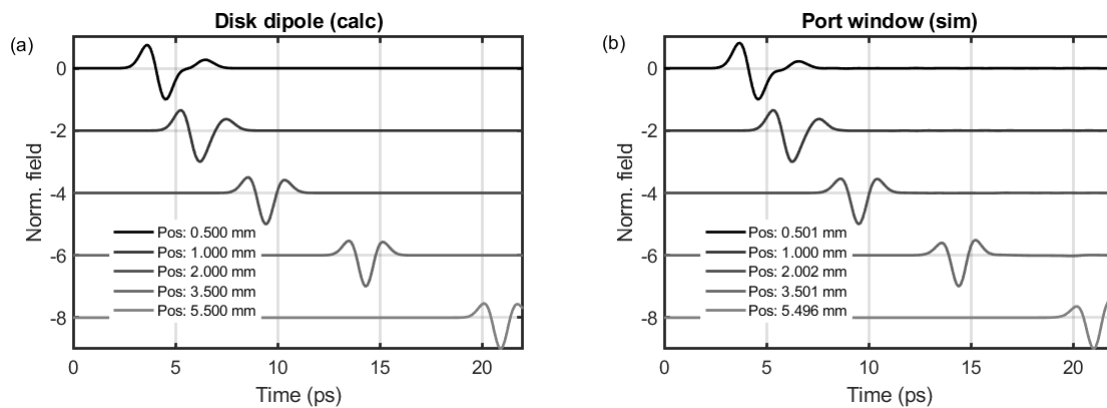
Figure 5.11: The disk dipole configuration in Figure 5.7b is used to simulate a THz pulse coming out a port window. The propagating pulse is probed at several distances away from the port window. A single cycle Gaussian pulse is excited at the port with a spatial Gaussian beam amplitude profile such that the dipoles closer to the edge of the disk have weaker radiation strength. The discrete dipoles simulations in (a) are compared with COMSOL simulations in (b) at observation distances of 0.5 (top), 1.0, 2.0, 3.0, 5.5 (bottom) mm along the propagation axis. All waveforms are normalized to 1 with the peak amplitude displayed in the legend.

5.3.2   Disk source, wire scatterer

The next scenario is to input objects that respond to the radiated source field. A scatterer reacts to the incident radiation and re-radiates electric field in the form of dipole radiation by the same rules as the source. A scatterer is also a configuration of unit dipoles, however, the dipole is excited by coupling with the incident field. The coupling term is defined by the complex coefficient α^{scat} which depends on the material properties and geometry of the scatterer.

In the COMSOL simulation, a 2 mm long and 0.25 mm diameter cylindrical metal wire scatterer is placed 4 mm away from the disk source emitter used in the previous subsection as shown in Fig. 5.10(b). The wire is modeled as a linear array of unit dipoles along the z-direction as shown in Fig. 5.7 placed 4 mm away from a disk source emitter in the same configuration as Fig. 5.10(b). Simulated waveforms for a Gaussian pulse emitted from the disk source scattering with a simple wire are shown in Fig. 5.12 at 0.2, 1.0, 2.0 and 3.0 mm away from the wire along the propagation axis. The simulated waveforms using the discrete dipoles model is compared with COMSOL where a cylindrical tungsten wire was used. The scattered field is only plotted for this case by subtracting out the incident background field, as the background field would likely dominate in the waveform trace. Results are strikingly similar where the scattered field waveform mostly resembles the second derivative Gaussian. The metal wire simply reflects the incoming far-field radiation from the source.

5.3.3   Disk source, disk scatterer

Scatterers can take various shapes and material forms. A disk scatterer is implemented to test the model and compare it against COMSOL simulations. The geometry is shown in Fig. 5.10(a) where the source is port window emitter at $x = 0$ of the tube. The tube has a 5 mm diameter and 6 mm length. In COMSOL, the other end of the tube is set to a perfectly reflective boundary, making it a disk scatterer. For the discretized dipoles simulation, the dipole configuration consist at the source end
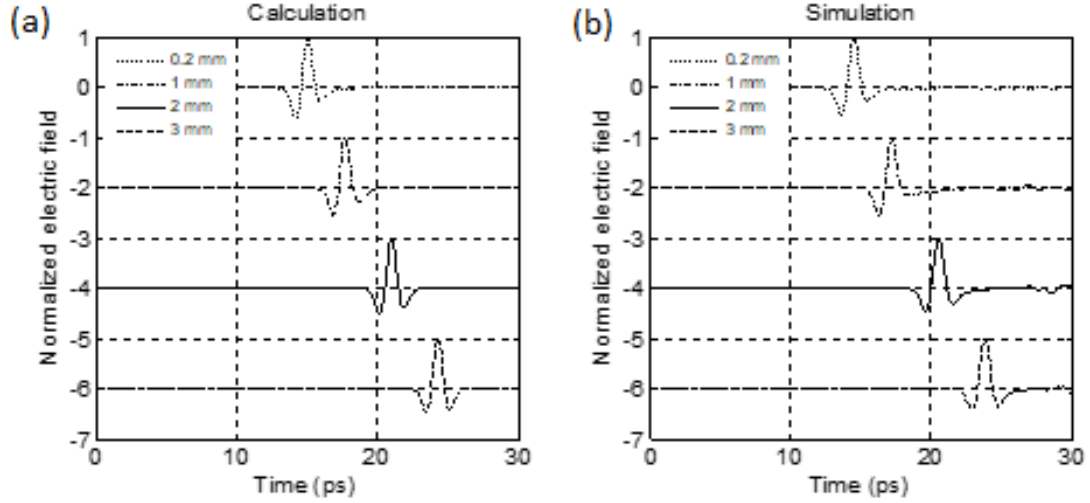
Figure 5.12: (a) Discrete dipoles modeling and (b) COMSOL simulations for the wire object scattering configuration. The scattered electric field is measured at 0.2, 1.0, 2.0, and 3.0 mm from the wire along the propagation axis. The background incident field has been subtracted out.

and the scattering end are exactly identical having a diameter of 5 mm and placed 6 mm apart. The source's field strength follows a Gaussian spatial profile as shown in Fig. 4.2 for both simulations. In this setup, the source disk emits THz pulses along the propagation axis (i.e. x-axis) at normal incidence to the scattering disk.

Simulated waveforms for the disk scatterer are plotted in Fig. 5.13. The ordering of the plots is for increasing distances away from the scatterer. In the plots, one can see that since the entire simulation is contained to the same propagation tube, there is a progression of the incident pulse propagating towards the scattering end of the tube, then the reflective boundary at the end caused the waveform to be overlapped by the reflection pulse. The background incident radiation was kept to show the separation of the incident and reflective scattering pulses. In the COMSOL simulation, the 5th waveform observed at 5 mm away from the scattering end (or 1 mm away from the port) shows a secondary reflection. In the discrete-dipoles model, the source emitter is "transparent" and was not set to be a secondary scattering source.

The general configuration is to simulate scattering at an oblique angle of incidence. The source emitter is positioned away from the disk scatterer where the incident
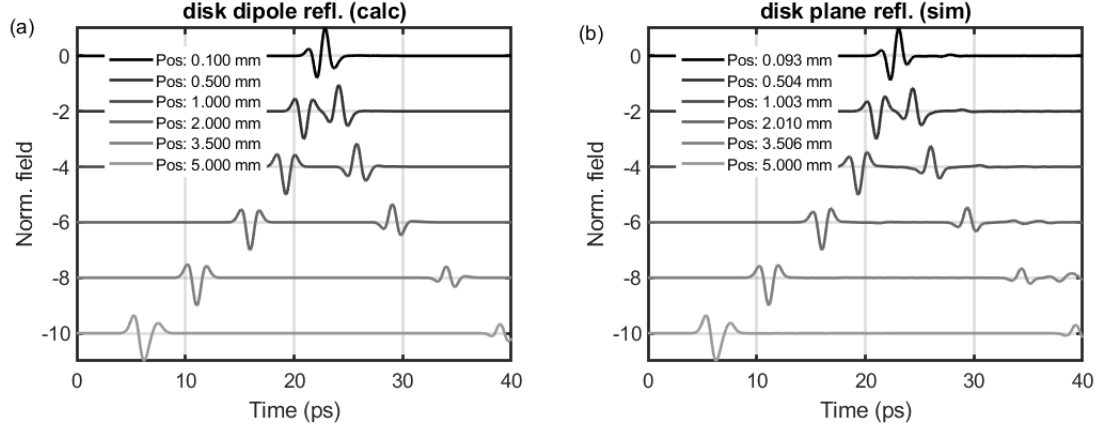
Figure 5.13: Disk source and disk scatterer configuration. The distance indicated is away from the scatterer, top waveform being the closest at 0.1 mm and the bottom waveform being the farthest at 3.5 mm. Waveforms obtained using the discrete dipoles model (left) and COMSOL (right) simulations. The background incident field is included to show the propagating radiation from the source superimposed with the scattered radiation from the tube end. The first 15 ps was cut out to focus on the scattering progression, which would have shown the propagation of the incident field from close to the source.

propagation axis crosses the scattering disk plane at angle α as shown in Fig. 5.14. Other propagation paths to measure scattered pulses are the "mirror" reflection, surface plane, and surface normal propagation axes. The electric field components can be measured normal to the propagation k vectors.

The simulated waveforms along the incident propagation axis is shown in Fig. 5.15 where the waveforms evolve to a SDG as the pulse propagates further away from the source. The waveforms along the reflection propagation axis is shown in Fig. 5.16. The reflected far-field trends towards an evolution to the third-derivative Gaussian. In COMSOL, the sample disk acts as a total reflector such that the incident SDG pulse bounces off it and continues along the reflection axis.

Simulated waveforms along the sample surface is plotted in Fig. 5.17. Waveforms along the sample normal that combines the incident and scattered fields are plotted in Fig. 5.18. The model and COMSOL simulations agree quite well in the observed field components for these regions of space.

The calculations do not account for the fact that the incident propagation disperses
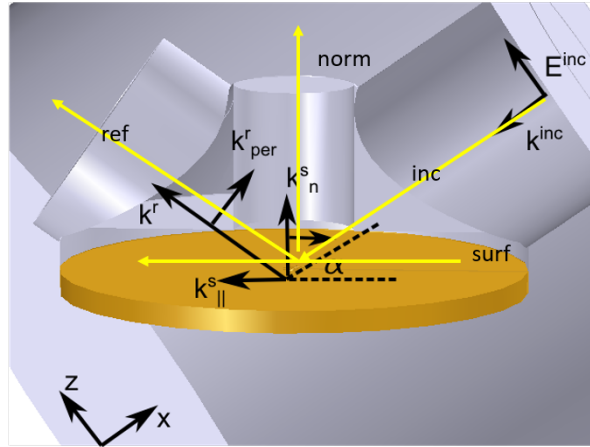
Figure 5.14: Disk source and disk scatterer configuration at an oblique angle of incidence visualized using COMSOL. α is the angle of incidence between the propagation axis and the sample surface. The port is shown on the right. The bright green lines trace out the propagation paths of interest where "inc" is the incident, "ref" is the reflection, "surf" is the sample surface, and "norm" is the sample normal reflection, propagation axes. Various $\boldsymbol{k}$ components are labeled.
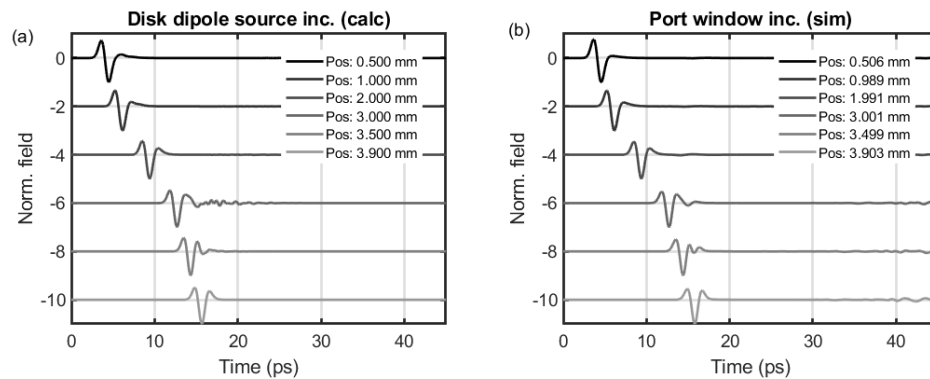
Figure 5.15: Waveforms simulated for the disk scatterer configuration using (a) the discrete dipoles model and (b) COMSOL at various distances from the source along the incident propagation axis.
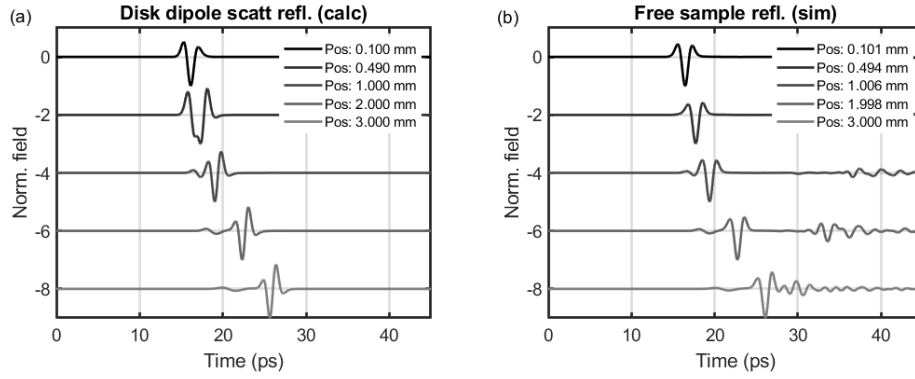
Figure 5.16: Waveforms simulated for the disk scatterer configuration using (a) the discrete dipoles model and (b) COMSOL at various distances from the source along the sample reflection propagation axis.
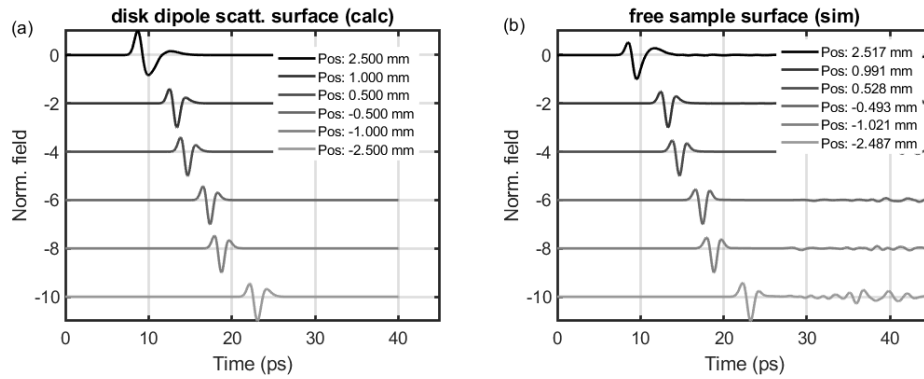
Figure 5.17: Waveforms simulated for the disk scatterer configuration using (a) the discrete dipoles model and (b) COMSOL at various distances from the source along the sample surface propagation axis.

as it propagates farther from the source. The pulse front curves due to free-space propagation dispersion. One can see that in the waveforms where the background field and the scattered field are nearly separated, the calculated waveform shows a slight time delay compared to the COMSOL simulated waveforms. The second and third waveforms in Figs. 5.18 and 5.16 show the separation of the background field and the scattered field, however the calculation and simulations would have matched more closely by adjusting the time delays if dispersion was accounted for in the model.
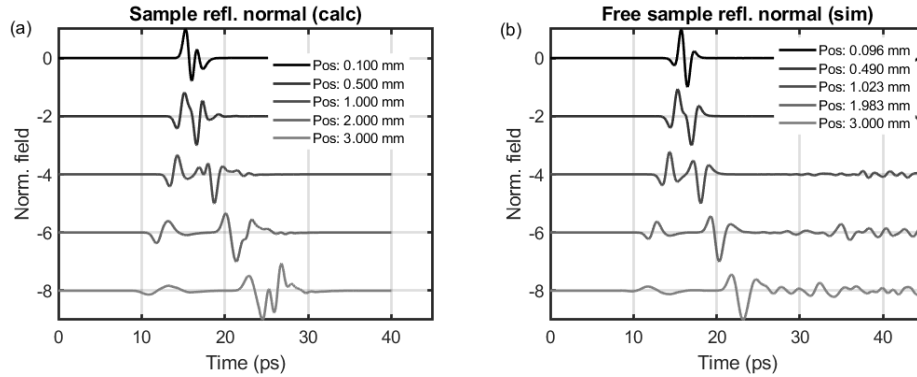
Figure 5.18: Waveforms simulated for the disk scatterer configuration using (a) the discrete dipoles model and (b) COMSOL at various distances from the source along the sample normal propagation axis. The background field from the radiated source is included to depict the source and scattering field superpositions.

5.3.4   Disk source, wire and disk scatterer

The ultimate goal of the discrete dipoles model is to reproduce the field propagation and scattering for the case of the THz-STM experiment. The first attempt is to model the tip scattering alone whose geometry is depicted in Fig. 5.19. The conical taper structure of the tip localizes incident electric field towards the apex. Thus a tip can be modeled as a linear dipole array with a z-dependence where dipole strength at the end of the wire is increased to mimic strong near-field response at the tip apex. The α^{scat} coefficients are larger in magnitude around the end of the wire compared to at the tip shaft. The equations for α using either expressions in Eqs. 2.43 or 5.36 can be used to evaluate the dipole coefficient as a function of tip-sample distance. Note that

the coefficients do not contain a phase-dependence. The tapered section of the tip provides a modified pathway for propagating pulses as well as sharp coupling regions for pulse interference.
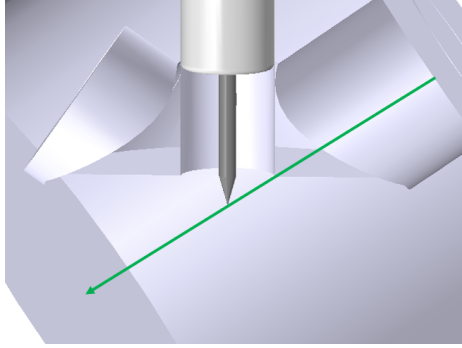
Figure 5.19: The tip scatterer geometry in COMSOL. In the discrete dipoles simulation, the tip is modeled as a line configuration where the dipole strength is strongest at the tip apex end. In COMSOL, the tip is a cylindrical rod and a conical taper. The propagation axis crosses the tip axis at the angle, 90 degrees minus α.

The near-field scattering response of the tip is plotted in Fig. 5.20 along the z-direction at various distances away from the tip apex, where the background incident field is subtracted out. The waveforms at 0.0 and 1.0 µm resemble a first derivative Gaussian, which is the near-field response. The scattered waveform evolves to a SDG farther away from the tip apex. The far-field radiation from the source takes the form of the SDG, which induces a proportional dipole-current response. Therefore, the tip apex source dipole term is the integral and is observed as the dominating $1/r^3$ near-field term. In the COMSOL simulation, the near-field waveform does not strictly follow a FDG, but rather shows a tail-peak and an after pulse about 5 ps after. The COMSOL simulation shows "real"-tip coupling effects where pulse-propagation along the tip shaft and taper shapes are accounted for. Modeling the tip as a simple linear array of dipoles cannot suffice to reproduce a realistic tip-coupling scenario. However, it may be compensated for by making the α^{scat} coefficients complex and forcing the concept of phase dependence in the discrete-dipoles model.

In the scenario where radiation couples to the STM, more scatterers are introduced,
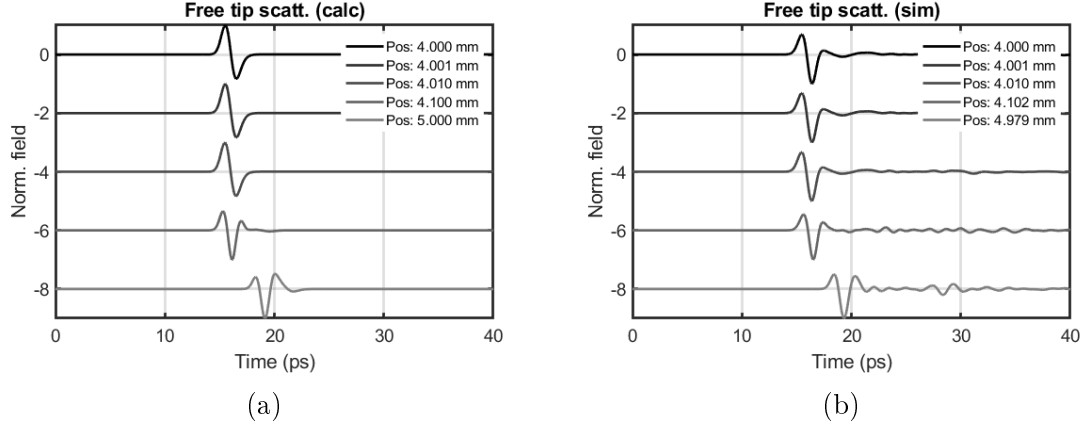
Figure 5.20: Waveforms obtained at various distances away from the tip apex along the tip axis (-z direction) using (a) the discrete dipoles model and (b) COMSOL simulations. Distances are 0, 1 μm, 10 μm, 0.1 mm, and 1 mm from the tip apex. Waveforms are normalized to the peak amplitude with peak values displayed in the legend. The background incident field is subtracted out to obtain the tip-scattering waveforms.

thus increasing the geometry complexity. For the discrete-dipoles modeling, it is reasonable to use the tip scatterer as simulated previously and the disk scatterer for the sample. The tip floats above the sample surface where the tip-sample distance is d_{t-s}. The disk dipole source is positioned at the port window location where the incident propagation axis crosses the sample surface plane at an inclination angle of α, in particular $\alpha = 35°$ for the current THz-STM experimental setup. The geometry is depicted in Fig. 5.21(a). Note that in the discrete-dipoles modeling, the tip-holder is absent, however it was kept for the COMSOL simulation.

Simulations of incident, near-field, and scattered waveforms are plotted at 6 probing locations in Fig. 5.21(b), (c) for the STM geometry. The Incident and scattered waveforms are well-matched between the two simulations. A weakness of the model is that it does not simulate secondary effects such as surface-wave boundary reflections due to the tip-holder as seen on pulse 3. It will later be shown in the next chapter that surface-wave propagation effects can be modeled using transmission line modeling.
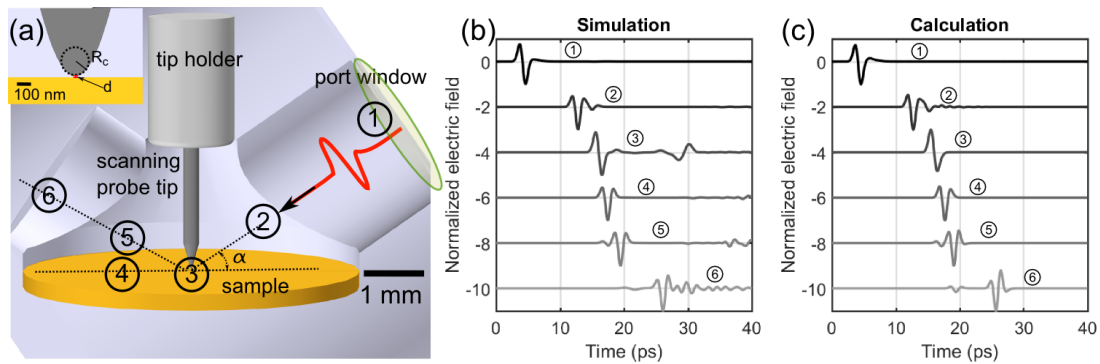
Figure 5.21: Scattered field calculations vs simulations. Here a disk source (Figure 5.7b) was used for the port window while the STM was represented by a linear array of point dipoles (Figure 5.7a). The calculations produced similar results as the COMSOL simulations. (a) Shows the probing regions in the Dipoles model to match the locations in COMSOL. (b) Pulses obtained at the probing regions for COMSOL and (c) for the Dipoles model. Note that the Dipoles model does not calculate the reflection pulse due to traveling waves along the tip shaft as simulated in plots 3 and 5 in (b). A single cycle Gaussian pulse is excited at the port with a Gaussian beam amplitude profile.

5.4 Chapter Summary

Derivations of the near-field have been presented using approximate models of electromagnetism coupling to the tip wire. A discrete dipoles model is used to break up a source emitter and target scatterers into unit dipoles that contribute time-dependent electric field radiation proportional to the dipole transient term summed with its first and second derivatives. At different distances away from the dipole emitter, certain terms dominate.

The waveforms measured from a source or scattering configuration show good agreement when comparing the simulations using the discrete dipoles model and COMSOL. The model presents a faster way to get the near-field waveform in a STM setup by using a wire and disk as simple scatterers. These computations generate approximations for the near-field within seconds to minutes as compared to several hours for COMSOL. However, it fails to reproduce realistic coupling effects such as secondary reflection transients, which would appear in the COMSOL simulations. Complicated source and scatterer shapes can be studied using the discrete dipoles modeling, however it is a future pursuit and would require more time investment in terms of computational development and run-time.

Chapter 6

Circuit modeling of THz-STM

6.1 Lumped-Element circuit model

The link between field theory and circuit theory has been exploited to numerically solve certain EM problems consisting of partial differential equations by constructing equivalent electrical circuit models for them [177, 204, 205]. The size of the junction is much smaller than the incident THz wavelengths, so applying a lumped-element equivalent circuit model is a reasonable approach.

The equation to solve for a simple tip circuit represented by only resistive, inductive and capacitive elements (RLC), is given by the differential expression in the time domain,

$$V_{in}(t) = L_t \frac{d^2Q(t)}{dt^2} + R_t \frac{dQ(t)}{dt} + C_t Q(t) \tag{6.1}$$

where $V_{in}(t)$ is the input source voltage, Q is the charge transient at the tip apex, R_t is the tip resistor value, L_t is the tip inductance parameter, and C_t is the tip's self-capacitance. The current equivalent form of Eq. 6.1 is

$$V_{in}(t) = L_t \frac{dI(t)}{dt} + R_t I + C_t \int^t I(t')dt', \tag{6.2}$$

where $I(t)$ is the current at the tip apex. The expression above can be translated to the point dipole radiation equation in Eq. 2.17 where the RLC parameters encode information about the constitutive properties, $\epsilon, \mu, \sigma, c_0$. Fig. 6.1 shows the circuit diagram where the R and L represent the tip and the tip-sample gap is a capacitor,

166

C. The tip current is equivalent to the derivative of the tip dipole moment.
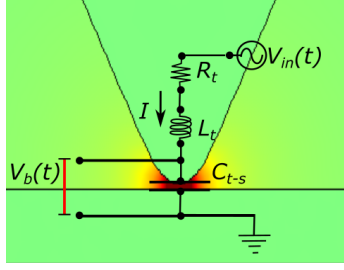
Figure 6.1: Simplifed RLC circuit model which only considers the tip contribution and the gap region between the tip and sample.

The Finite-difference time-domain (FDTD) method can be used to numerically solve Eq. 6.1 and obtain an approximate solution for the charge at the tip-apex. This differential equation in FDTD form is also known as the lumped element circuit model. All terms of the differential equation are approximated by first or second order backward difference or sum expressions where the present value at a time step utilizes present and past values in the computation. The first term to approximate the second derivative using a backward difference formula is given by:

$$L_t \frac{d^2Q(t)}{dt^2} = L_t \frac{Q_n - 2Q_{n-1} + Q_{n-2}}{\Delta t^2}, \tag{6.3}$$

where n is the iteration number and Δt is the time-step increment. If the iteration value goes beyond the 0th time-step, the history values of $n - k$ is assumed to be zero. The second term for Ohm's law is given by

$$R_t \frac{dQ(t)}{dt} = R_t \frac{Q_n - Q_{n-1}}{\Delta t}. \tag{6.4}$$

Finally the capacitive term is

$$C_t Q(t) = C_t Q_n. \tag{6.5}$$

Using the current expression, the approximation for the integrated capactive term using the trapezoidal integration rule is

$$C_t \int^t I(t')dt' = \frac{1}{2}C_t\Delta t \sum_k^N (I_k + I_{k-1}). \tag{6.6}$$

167

Eventually solving for all Q_n or I_n values within their local time steppings will build up a the transient in the full time range. Note that the solving algorithm described above is a first-order approximation which will consequently produce some error from the true solution. Advanced solving methods involve multiple order approximations where past and future time step values have to be solved for simultaneously and readjusted after each iteration. For this simple model, built in ODE solvers are employed when the input voltage transient, $V_{in}(t)$, is a smooth and continuous function.

When the charge is known, the electric field profile is simply given by the Coulomb expression for a charge sphere.

$$E(z,t) = \frac{1}{4\pi\epsilon_0}\frac{Q(t)R_a}{z^3} \tag{6.7}$$

where R_a is the tip apex radius of curvature and z is the observation distance from the sphere's center.

The circuit model in Fig. 6.1 is based on antenna model for the THz tip as introduced in Chapter 2. The STM junction is depicted as an equivalent circuit model consisting of lumped circuit elements representing the tip and sample. The charge fluctuations at the junction is modeled by inputting the voltage transient, $V_{in}(t)$, which uses the same waveform as the incident electric field pulse in Fig. 6.2(a). The RLC values used are $R = 220\,\Omega$, $L = 75$ nH and $C = 35$ fF. The outputted charge quantifies the near-field around the tip apex. Fig. 6.2(b) compares the voltage waveform calculated by the RLC circuit model with the incident pulse and the simulated voltage waveform. To get a pure antenna coupling in the THz-STM simulations, we had to extend the tip length to eliminate reflection pulses caused by THz-SPPs. Their corresponding frequency spectra are also calculated in Fig. 6.2(c) and the amplitude ratio versus frequency are shown in Fig. 6.2(d). Both spectra show similar features such as the early amplitude decay after 0 THz and the peak around 0.25 THz. The RLC model (purple dash) demonstrate the same $1/f$ dependence as the simulated trend (black line). The RLC model results show a greater suppression of the higher

168

frequencies between 1 THz and 2 THz. The simulated spectrum for the apex's near-field nearly matches the calculated RLC response. Overall the FEM simulation for the near-field agrees well with the circuit output.
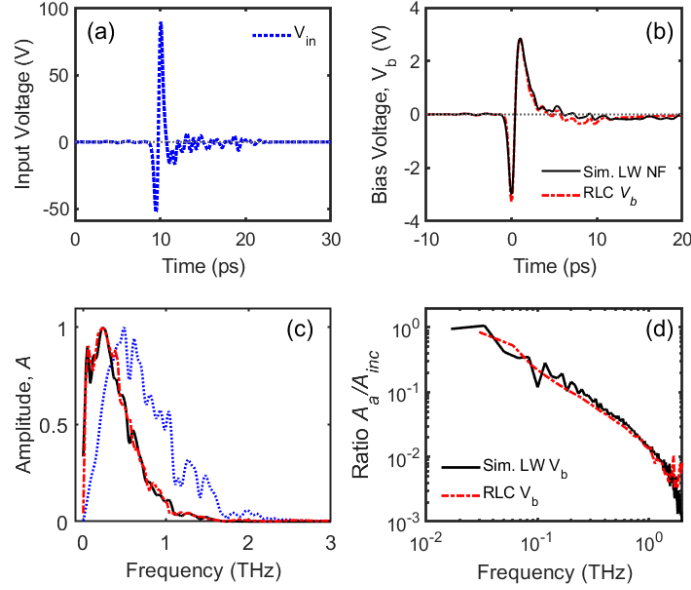
Figure 6.2: V_{in}(t), is proportional the incident field waveform and used as the input voltage into the circuit. The input signal is processed by the R, L, C circuit elements to produce a version the transient bias voltage $V_{b,THz}(t)$ Comparison of the voltage transient calculated by the RLC circuit model (magenta) with the simulated near-field waveform (black) shown in the (b) time and (c) frequency domains. Note that a long-wire (LW) tip was used for the main comparison as it eliminates the SPP contribution observed in the short-wire (SW) tip. The spectra are referenced with the incident spectrum and plotted together. Circuit parameters are: $R_t = 220\,\Omega$, $L_t = 75$ pH, and $C_{t-s} = 35$ fF. (d) Ratio spectra obtained by referencing the incident spectrum.

The spectral dependence of the near-field voltage amplitude is shown in Figs. 6.2(c) and (d), presented in the same manner as it was done in Chapter 4. The RLC results in red dashes are compared with the COMSOL simulations shown by the black solid curves. RLC calculations provide the freedom of using much finer time steps and generate a much quicker calculation compared to COMSOL simulations where decreasing the time step multiplies the simulation time. In Fig. 6.2(c), the spectral amplitude goes to zero at 0 THz. The COMSOL simulations make it appear as if there is a d.c. component in the spectrum. The RLC calculation fits the $1/f$ roll-

off to the near-field enhancement factor as shown in Fig. 6.2(d). Hence, the antenna coupling behaviour is well demonstrated by analyzing the simulated near-field with antenna theory calculations.

6.1.1   Circuit parameters

The values of the constituent circuit parameters used in RLC modeling have implications about the THz coupling mechanism to the experimental setup [56, 69, 206] such as geometry, material dependence and detection schemes. Table 6.1 summarizes parameters used in various reports that employ THz-near-field techniques.

Table 6.1: Summary of R, L and C parameters used in various reports to model the tip as a wire antenna in various experiments. The tip responds to incident THz and converts it into a transient signal that can be fitted as a RLC circuit response. The resonant frequency f_0 is calculated from $1/(2\pi\sqrt{LC})$.

Reference	Technique	R (Ω)	L (pH)	C (fF)	f_0 (THz)
Wang 2004 [56]	THz-SNOM	150	20	100	0.11
Wimmer 2014 [68]	Tip Photoemission	300	100	0.35	0.85
Li and Jones 2016 [69][1]	Tip Photoemission	$0.8 \to 7$	$100 \to 50$	$0.5 \to 0.9$	$0.71 \to 0.75$
Yoshioka 2018 [48]	THz-STM	350	100	0.62	0.64
Müller 2020 [24]	THz-STM	300	320	35	0.048
This work	THz-STM	220	75	35	0.098

The parameters chosen in the literature summarized in Table 6.1 are used to produce good fits to the measurement of their sampled near-field waveforms. The physical interpretation for the RLC values is still not clear since the parameters were merely chosen or optimized to reproduce fitted THz waveforms that agree with experiment. Deriving the values for the specific RLC parameters can be done analytically [206] or computationally in order to obtain a reasonable estimate or range of values for circuit parameters that cater to the experimental configuration. The tip-sample geometry can be simplified as a wire consisting of a cylindrical shaft and conical taper resting

above a sample plane with distance equal to the separation between the tip apex and the detector's planar surface. It is often in near-field waveform sampling experiments that the sample is used as the detector. The RLC values for a conical structure above a plane will be summarized to strive for a better intuition for selecting tip-sample parameters.

The RLC values account for the taper geometry, tip and sample material and since THz frequencies are considered, the skin depth of the material also matters. The resistance of a tip wire with a conical taper is given by [69, 207]

$$R = \frac{\rho\ell}{2\pi r_t \delta(f)} + \frac{\rho}{2\pi\delta(f)\sin\theta/2}\ln\frac{r_t}{r_a}, \tag{6.8}$$

where ρ is the material d.c. resistivity, ℓ is the tip length, r_t is half the tip shaft diameter, r_a is the tip apex radius, θ is the full cone taper angle and δ is the skin depth as a function of frequency. the first term is the shaft portion and the second term is the taper contribution to the tip's total resistance. Calculations inputting the metallic skin depth of tungsten, the tip dimensions in Table 4.1 and skin depth at 1 THz (around 100 nm), Eq. 6.8 yields R values of a few Ω's.

The inductance for the conical tip geometry can be derived using a series of equations that represent different sections of the tip [207]:

$$L_a = 0.5 \cdot \mu_0 \cot\left(\frac{\theta}{2} \cdot \left[r_t - r_a - \ln\frac{r_t}{r_a}\right]\right) \tag{6.9}$$

$$L_b = 0.5 \cdot \delta(f)\mu_r\mu_0 \ln\frac{r_t}{r_a}/\sin(\theta/2) \tag{6.10}$$

$$L_c = 0.5 \cdot \delta(f)\mu_r\mu_0 \left(\frac{r_a}{r_b} - 1\right)\cot(\theta/2) \tag{6.11}$$

$$L = L_a + L_b - L_c, \tag{6.12}$$

where μ_0 is the magnetic permeability of vacuum and μ_r is the relative permeability of the tip material. The inductance is the sum of the components listed above. The capacitance is given by an approximation using a hemisphere above a plane [196, 208]

---

[1]Tip radius values ranging from 20 nm to 800 nm, respectively, in the presented range for the RLC parameters.

is

$$C(z) = 2\pi\epsilon_0 r_a \int_0^\pi \frac{\sin^2\theta}{\theta\left[z/r_a + 1 - \cos\theta\right]} d\theta. \tag{6.13}$$

However a detailed calculation for a tip consisting of a cylindrical tip shaft and conical taper above a plane is given by a set of partial nested formulae [207]:

$$C_{\text{taper}} = 2\pi\epsilon_0 \sqrt{B^2 - A^2} \Big/ \ln\left|\frac{\sqrt{B^2 - A^2}\tan\phi + (A + B)}{\sqrt{B^2 - A^2}\tan\phi - (A + B)}\right| \ , B > A, \textbf{ or} \tag{6.14}$$

$$C_{\text{taper}} = \pi\epsilon_0 \sqrt{A^2 - B^2} \Big/ \arctan\left(\frac{\sqrt{A^2 - B^2}}{A + B}\tan\phi\right) \ , A > B, \text{ where} \tag{6.15}$$

$$A = r_0 \ln\left(\frac{r_1 - r_a}{r_d - r_a}\right), \tag{6.16}$$

$$B = r_1 - r_d, \tag{6.17}$$

$$\phi = (\pi - \theta)/4. \tag{6.18}$$

$$C_{\text{shaft}} = 2\pi\epsilon_0 \sqrt{E^2 - D^2} \Big/ \ln\left|\frac{\sqrt{E^2 - D^2} + (D + E)}{\sqrt{E^2 - D^2} - (D + E)}\right| \ , E > D, \textbf{ or} \tag{6.19}$$

$$C_{\text{shaft}} = \pi\epsilon_0 \sqrt{D^2 - E^2} \Big/ \arctan\left(\frac{\sqrt{D^2 - E^2}}{D + E}\right) \ , D > E, \text{ where} \tag{6.20}$$

$$D = r_t \ln\left(\frac{h_t \tan(\theta/2)}{r_t - r_a}\right), \tag{6.21}$$

$$E = h_t - (r_t - r_a)\cot(\theta/2). \tag{6.22}$$

$$C_{\text{tip}} = C_{\text{taper}} + C_{\text{shaft}}, \tag{6.23}$$

where r_d is the radius where the spherical tip apex is tangential with the cone angle.

Although eq. (6.8) produces resistance of a few Ohm's, it should also be combined with a propagation impedance of at least 150Ω. The propagation impedance of free-space would add 177Ω in series with the tip resistance [56] or alternatively, a transmission line impedance. The L parameter can give values of 0.1 pH up to the order of 100 pH depending on the input frequency. The values of C will yield large capacitance values of 10 to 100 fF when the sample plane is present. The C values plotted using COMSOL simulations in Fig. 4.36 for the tip-sample capacitance already fits this range. Otherwise, if the expression for the nano-capacitance of the tip apex in Eq. 6.13 is used instead, it would yield C values on the order of 0.1 fF.

Running the RLC computation with $C \sim 0.1$ fF and $C \sim 100$ fF produces drastic results for the outputted waveform varying from one shaped like the inputted incident THz pulse to its integral, respectively. Variations of RLC are investigated by running the models for a given set of values according to the literature in Table 6.1. The RLC model using $R = 150$ Ω, $L = 20$ pH and $C = 0.1$ pF from Wang, Mittleman et al., 2004 [56] in Fig. 6.3. The calculated near-field resembles the integral of the incident THz pulse shown in Fig. 6.3(a). The comparison with the COMSOL simulation of the near-field matches reasonably well as shown in Fig. 6.3(b). Note that the long-wire simulation geometry in COMSOL was used for comparison since the lumped-element RLC model does not account for any trailing reflection pulses.
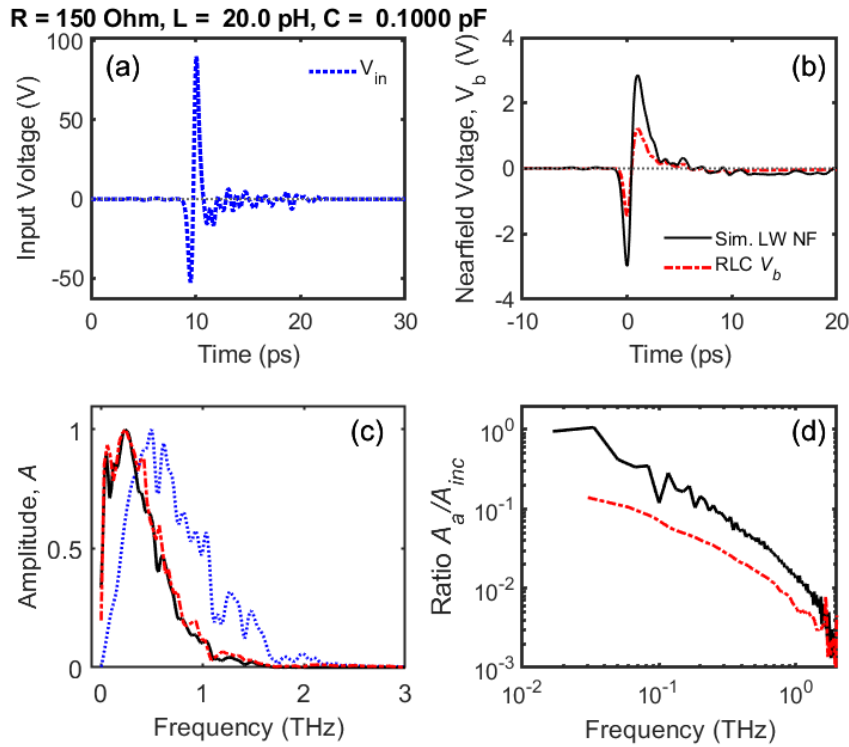
Figure 6.3: RLC model using $R = 150\Omega$, $L = 20$ pH and $C = 0.1$ pF from Wang, Mittleman et al., 2004 [56]. The model is compared against COMSOL simulations. Frequency spectrum is only shown for the circuit model vs the long wire case.

The model output for using $R = 300$ Ω, $L = 100$ pH and $C = 0.35$ fF from Wimmer, Ropers et al., 2014 [68] is shown in Fig. 6.4. In this scenario, the detection

scheme assumes that the detector measuring the THz field at the tip apex is far-field, hence the drastic decrease for the capacitance compared to the values used in [56]. The detected THz waveform in Fig. 6.4(b) resembles the THz pulse in Fig. 6.4(a), except with a different phase of the waveform. In COMSOL, the waveform is obtained in a geometry where the tip-sample distance is several 100 μm's, which is similar to the simulations where the THz pulse couples to a free tip.
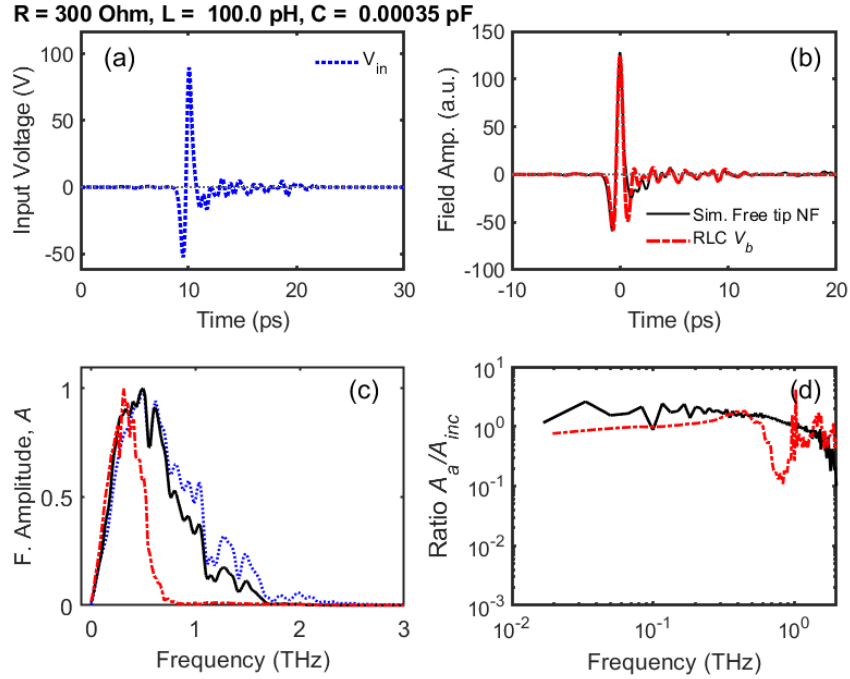
Figure 6.4: RLC model using $R = 300\Omega$, $L = 100$ pH and $C = 0.35$ fF from Wimmer, Ropers et al., 2014 [68]. The model is compared against COMSOL simulations.

A similar result where the near-field is the integral of the incident THz pulse like in 6.3(b) can be obtained using Muller's, Wolf et al., 2020 circuit values of $R = 300\ \Omega$, $L = 320$ pH and $C = 35$ fF. The calculated waveform is quite broad as shown in Fig. 6.5(b) compared to the COMSOL simulation. The high frequency components are well-suppressed as shown in Fig. 6.5(d).

Finally, the RLC model using $R = 7.0\ \Omega$, $L = 50$ pH and $C = 0.9$ fF from Li and Jones, 2016 [69] is shown in Fig. 6.6. The calculated waveform in (b) resembles a damped oscillation corresponding to the spectrum in (c), which depicts a narrower
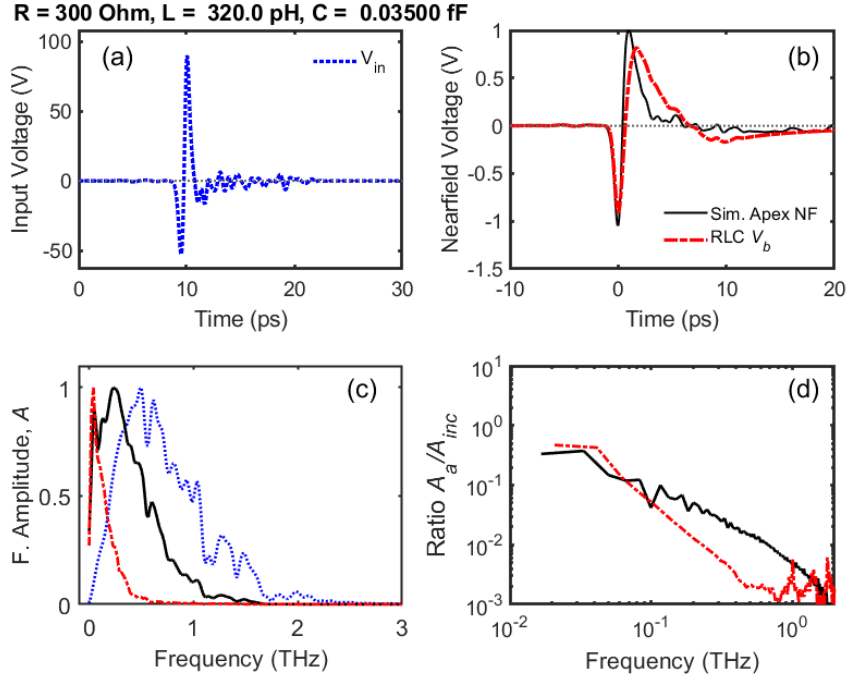
Figure 6.5: RLC model using $R = 300\Omega$, $L = 320$ pH and $C = 35$ fF from Muller, 2020 [24]. The model is compared against COMSOL simulations.

peak. The resonance frequency calculated using $f_0 = 1/2\pi\sqrt{LC}$ yields 0.75 THz, which is where the peak is exactly centered at.

Based on the selected RLC parameters, one can see how the waveform can drastically change from the integral of the input to nearly proportional to the input, and then a waveform with lots of ringing. After including Fig. 6.2 into the series, the striking differences are the variation in C values going from 100 fF down to 0.5 fF. Dropping the resistance down to $1\,\Omega$ as shown in Fig. 6.6 creates an entirely different scenario where the model outputs the result for an LC circuit. The resonance peak can be seen in Fig. 6.6(c) which should correspond with the ringing features of the waveform.

The reason for the discrepancy in the values chosen even though the same model was used is due to the nature of the experimental setup. It matters whether the driving field is observed from a far distance like in the tip emission experiments versus up close as in THz-STM experiments. The capacitance becomes a significant parameter
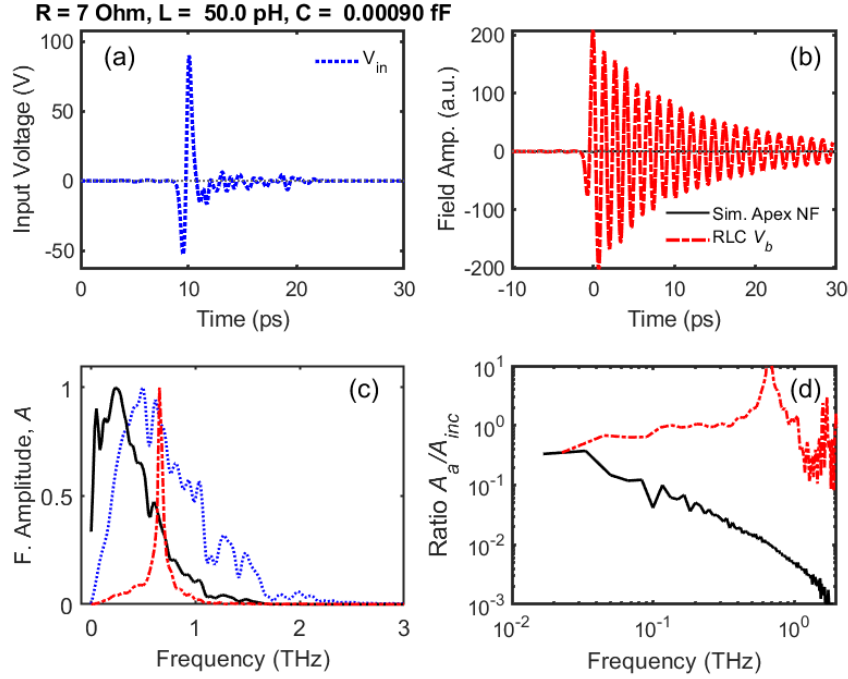
Figure 6.6: RLC model using $R = 7\Omega$, $L = 50$ pH and $C = 0.9$ fF from Li and Jones, 2016 [69]. The model is compared against COMSOL simulations.

when the detector (i.e. the sample) is close to the tip. Such is why fitting parameters for C varies between 10 fF to 100 fF in the experiments where the sample is used as the detector. The observed THz waveforms in these cases look like the integral of the input THz waveform. The capacitance selected for far-field observations was rather chosen to be in the 0.1 fF range, which produces an observed THz waveform that rather looks like the original input waveform. In Table 6.1, all the major variations occur drastically in the selection of C.

6.1.2 Expanded circuit model

A circuit model to add in the sample contributions and the non-linear element that represents tunneling ts shown in Figure 6.7. For simplicity, the sample was assumed to be a perfect conductor in d.c. conditions (i.e. $R = 0\ \Omega$), and which no electric field was allowed to exist inside the material, thus giving skin depth value of zero and overall inductance of zero according to Eq. 6.9. The excitation voltage is generally

176

a.c. since THz response is being modeled, thus the sample will have non-zero values. If the sample contributes a resistance, R_S, and inductance, L_S, it is added to the circuit in series with the tip parameters and the tip-sample capacitance.
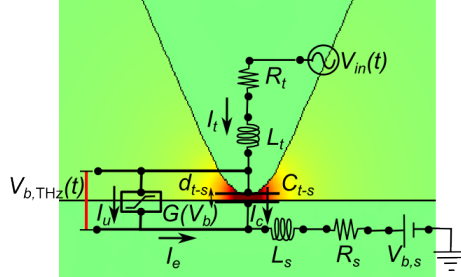
Figure 6.7: An expanded equivalent circuit model of the tunneling junction. Here sample contributions are added as well as a non-linear element that represents the I-V relation of the tunneling interface.

RLC model waveforms are produced for special cases in Fig. 6.8 where the tip dominates in R and L (see Fig. 6.8(b)) or when the sample dominates in R and L, (see Fig. 6.8(c)). Note that the sample mostly consists of R since a cylindrical disk structure cannot generate comparable L values to a wire. The junction bias can be produced based on the voltage drop from either side of the circuit. The waveform shape for $V_b(t)$ changes from the integral shape of $V_{in}(t)$ to the same shape as the $V_{in}(t)$.
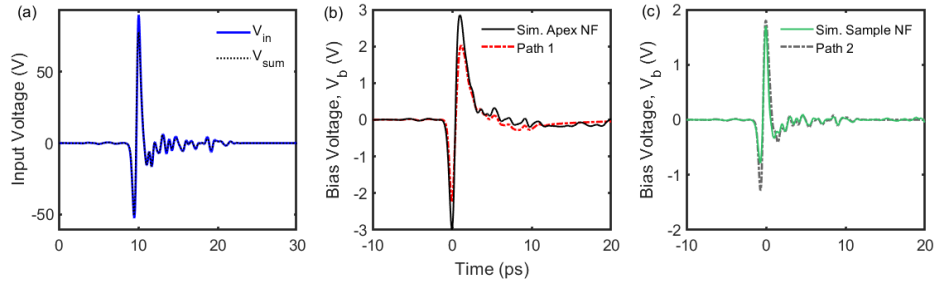
Figure 6.8: Voltage waveforms for V_b generating using the full circuit model. (a) Input waveform V_{in}. (b) V_b for a tip dominant case. (c) V_b for a sample dominant case.

Lastly, the tunneling junction is an additional circuit element that is in parallel with the tip-sample capacitor. The same bias voltage feeds the capacitor and the

tunneling junction. The tunneling junction is to be modeled in detail in the next chapter.

Expanded circuit model for a full tip

An expanded circuit is used to model the complexity of the tip shape. It was noticeable in Fig. 4.42 how the shortest taper (250 μm) produces a near-field waveform that is narrower than the integral waveforms and peaks at 0.300 THz. Fig. 6.9 only intends to model the resulting junction bias by accounting for a detailed tip structure consisting of a shaft and a taper section.
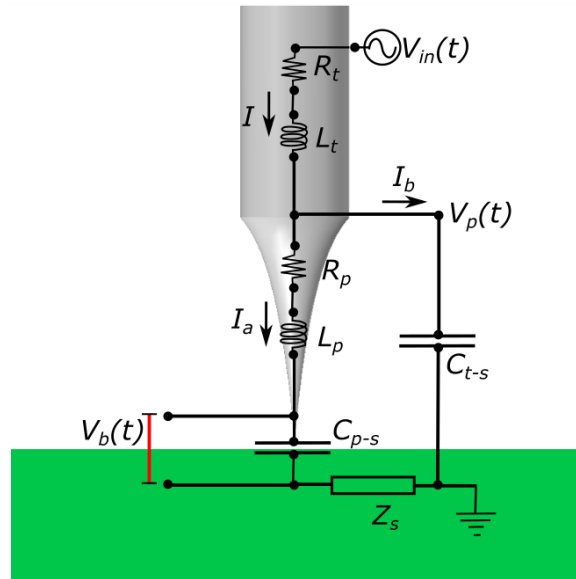
Figure 6.9: An expanded equivalent circuit model of a more detailed tip geometry. The tip circuit parameters are split as the tip shaft and tip taper contributions.

The impedance for the equivalent circuit is shown in Fig. 6.10. The waveforms produced by the simulation of the tip expanded circuit is shown in Fig. 6.11. The modified waveform actually illustrates tip dependence on shaping the near-field. The shaft and taper geometry was simply modified as two branches in parallel with their own capacitance values relative to the sample plane. Unique tip structures such as the cusped and multi-cusped tapers would introduce additional circuit parameters to fully produce a reasonable RLC simulation.
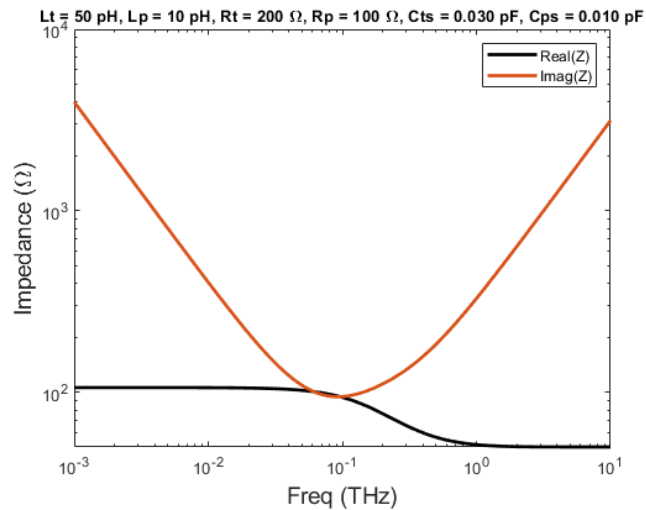
Figure 6.10: Impedance for the equivalent circuit of a divided tip model as a function of frequency.
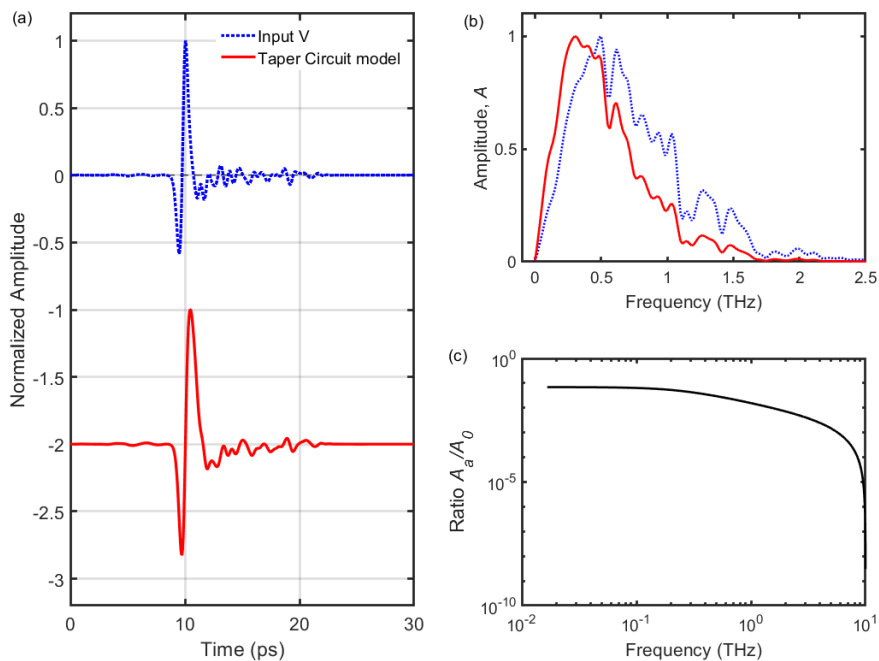
Figure 6.11: Waveform calculated using the lumped RLC model for the split tip circuit in comparison to the input waveform.

The pulse broadening shown in Fig. 6.11(a) implies that both the tip shaft and tip taper contributes to the overall capacitance. The influence of the geometric capacitance on the near-field formation cannot be neglected in modeling for the THz-STM. The COMSOL simulations demonstrate that the tip shape broadens the pulse by creating a delayed propagating pulse along the tip shaft which eventually meets up with the enhanced field to create a superposition waveform. Hence there is usually a delayed pulse feature that creates a shelf after the main peak. An expanded circuit model is one way to approximate tip shape effects to the generation of the THz nearfield.

6.1.3 Transfer function method

A general representation of the full circuit from Fig. 6.7 can be redrawn by collecting all the tip and sample impedances into single parameters, represented by Z, and shown in Fig. fig. 6.13. The capacitor and the junction are the loads that receive the gap bias voltage input V_b, which is assumed to be equal for both components.
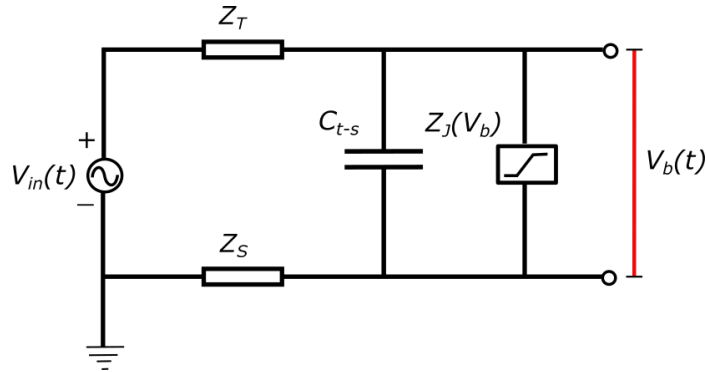
Figure 6.12: Representing the full circuit in a simplified manner by condensing the tip and sample components into a single impedance parameter, Z_T and Z_S respectively.

The transfer function relates the output to the input in the frequency domain. Kirchoff's laws can be used to determine $V_b(t)$ by creating a system of equation of voltage drops in a loop and currents merging and leaving a junction node. In general,

the Kirchoff's Voltage law (KVL) states that

$$V_{in}(t) = Z_T I(t) + V_C(t) + Z_S I(t) \tag{6.24}$$

$$I(t) = I_C(t) + I_J(t) \tag{6.25}$$

$$V_C(t) = V_b(t) = Z_J I_J(t), \tag{6.26}$$

where I_C is the current charging the capacitor and I_J is the current in the tunneling junction branch. Using $V_C = V_b$, and transforming the set of equations above in the frequency domain using a Laplace transformation, it is possible to obtain a transfer function, $H(\omega)$ to relate the output voltage $V_b(\omega)$ to the input voltage $V_{in}(\omega)$, given by

$$V_b(\omega) = H(Z_T(\omega), Z_S(\omega), C(\omega), Z_J(\omega)) \cdot V_{in}(\omega). \tag{6.27}$$

Isolating for the transfer function yields the simple relation

$$H(\omega) = \frac{V_b(\omega)}{V_{in}(\omega)}. \tag{6.28}$$

The transfer function for the circuit shown in diagram Fig. 6.13 is given by

$$H(\omega) = \frac{1}{(Z_T + Z_S)\left(-i\omega C + \frac{1}{Z_J}\right) + 1}. \tag{6.29}$$
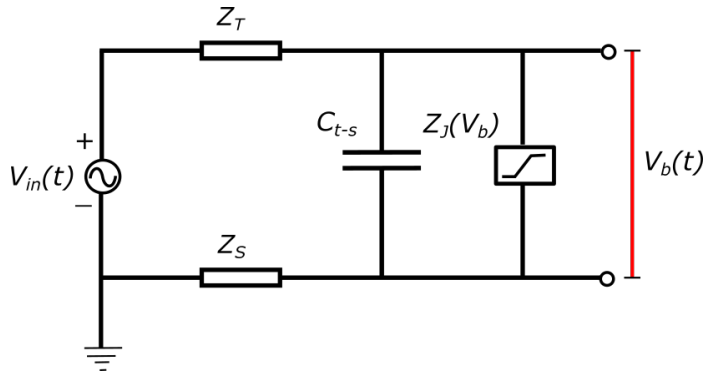
Figure 6.13: Representing the full circuit in a simplified manner by condensing the tip and sample components into a single impedance parameter, Z_T and Z_S respectively.

Fig. 6.14 shows an example of the transfer function produced for the modeled result in Fig. 6.2 using parameters $R = 220\Omega$, $L = 75$ pH and $C = 35$ fF. Fig. 6.15

181

shows how an arbitrary input waveform like the THz pulse can be transformed in the frequency domain and modified by the transfer function. The product amplitude can be inverted back to the time domain, as shown in Fig. 6.16, to get the waveform generated by the RLC model.
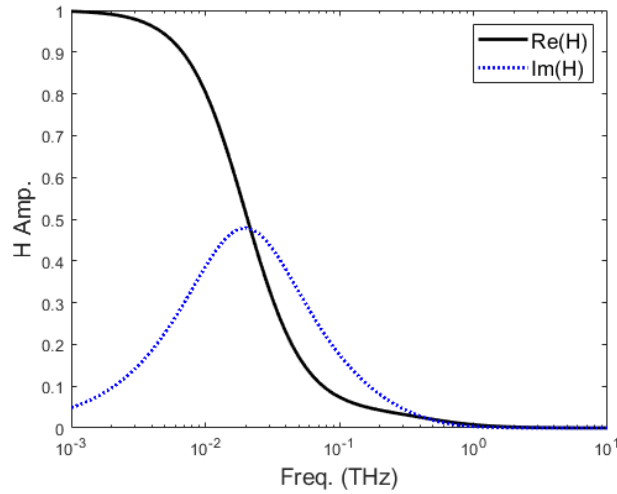
Figure 6.14: Real and imaginary components of the transfer function for the equivalent RLC circuit as a function of frequency. The parameters used were $R = 220\Omega$, $L = 75$ pH and $C = 35$ fF.

The imaginary component of the transfer function plotted in Fig. 6.14 demonstrates the amplitude dependence around the resonance frequency, f_0. The amplitude increases to f_0 and drops afterwards. The near-field amplitude plots versus frequency shown previously in the RLC circuit model in Chapter 4 resemble the latter portion of the transfer function at THz frequencies greater than f_0.

Transfer functions are calculated using different values of RLC from Table 6.1. Fig. 6.17 shows how the transfer function can be used to produce an integral response with the drop off at high frequencies. Fig. 6.18 shows how the transfer function yields back the same waveform as the input, holding the value of 1 for most frequencies.

The advantage of performance analysis using transfer functions is that the Z parameters can be analyzed as a function of frequency. The lumped element circuit model requires the user to input a single value of R, L and C which are assumed to
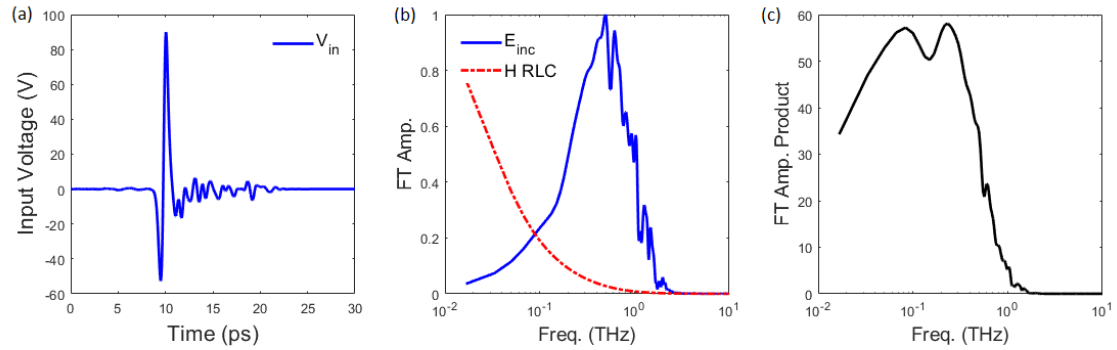
Figure 6.15: (a) Input waveform. (b) Normalized input waveform spectrum with transfer function. (c) Product of the input spectrum with transfer function.
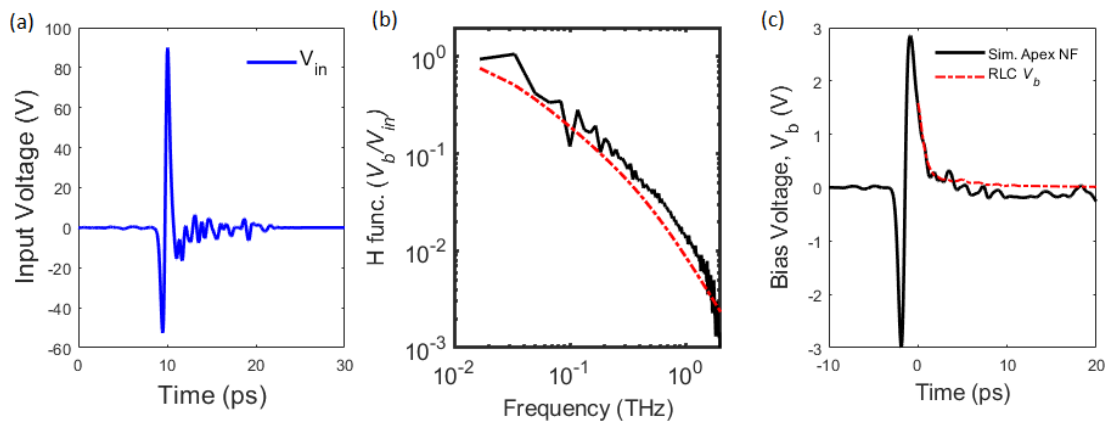
Figure 6.16: (a) Input waveform. (b) Simulated transfer function from COMSOL compared with calculated transfer function from RLC model. (c) Calculated the waveform using inverse FFT compared to the COMSOL simulation.
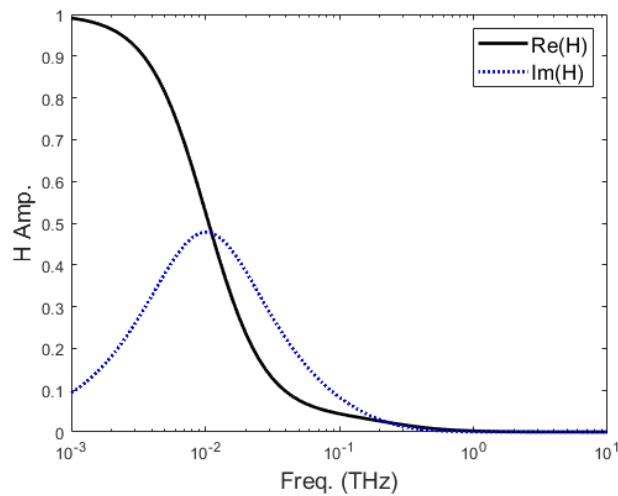
Figure 6.17: Real and imaginary components of the transfer function for the equivalent RLC circuit as a function of frequency. The parameters used were $R = 150\Omega$, $L = 20$ pH and $C = 100$ fF from Wang, Mittleman et al., 2004 [56]
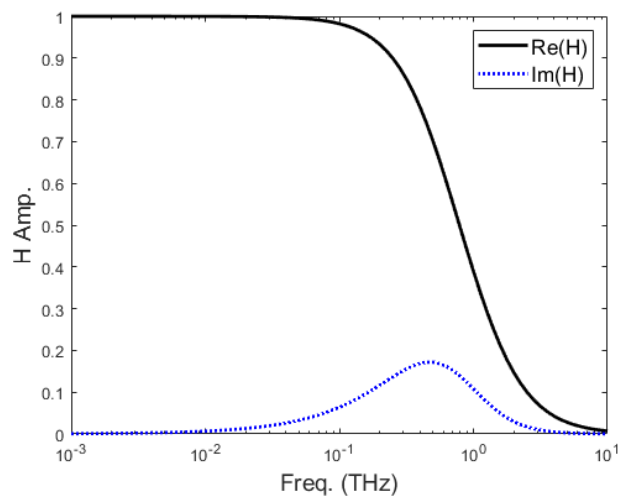
Figure 6.18: Real and imaginary components of the transfer function for the equivalent RLC circuit as a function of frequency. The parameters used were $R = 300\Omega$, $L = 100$ pH and $C = 0.35$ fF from Wimmer, Ropers et al., 2014 [68].

be constants in the frequency range of interest.

6.1.4 Analysis of RLC parameters

The sensitivity of RLC analysis using transfer function method described previously is performed by varying either one or more of the RLC parameters. The real part generally yields the main part of the transfer function that determines the resulting amplitude of each frequency component. The imaginary component represents resistive losses. Fig. 6.19 shows how increasing the resistance from 10Ω to 1000Ω makes the real component drop quicker and as well as increase the proportionality of the imaginary component. The high frequency amplitudes drop as R increases while the low frequencies get preserved as depicted by the plateau at unity amplitude in Figs. 6.19(a) and (b). The resistance must be considerably high to dissipate energy in the infrared regime between 10^{-3} to 10^{-1} THz range. The plots cut off at 10^{-3} THz since we are only interested in the circuit behaviour within the THz regime. The unity plateau in the real part would appear and the low frequency tail of the imaginary part goes to zero if the frequency axis includes microwave frequencies.

(a) $R = 10\,\Omega$ (b) $R = 100\,\Omega$ (c) $R = 1000\,\Omega$
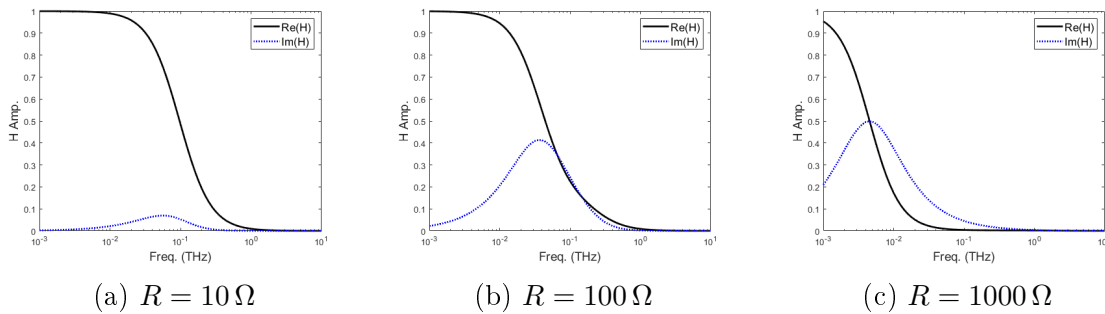
Figure 6.19: Transfer functions for various resistances while fixing $L = 75$ pH and $C = 35$ pF.

Fig. 6.20 shows the variation of the transfer function as L is varied from 10 pH to 1000 pH. The spectra does not vary much in the real component. Increasing L moves the peak of the imaginary component to lower frequencies.

Fig. 6.21 shows the variation of the transfer function as C is dropped from 100

(a) $L = 10$ pH   (b) $L = 100$ pH   (c) $L = 1000$ pH
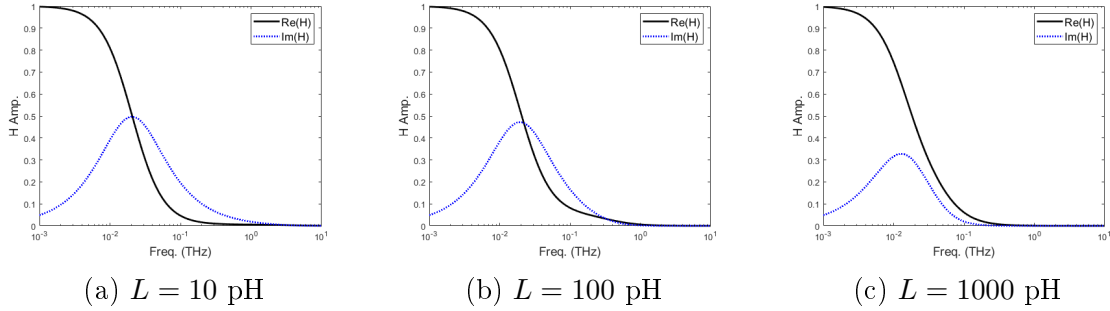
Figure 6.20: Transfer functions for varying inductance while fixing $R = 220\,\Omega$ pH and $C = 35$ fF.

fF to 0.1 fF. The unity shelf is extended to higher frequencies as C decreases. One can see how the spectra of the near-field in the case where the tip and sample are in close proximity (See Figs. 6.2(c,d) or 6.14, 6.3(c,d) or 6.17 and 6.5(c,d)) resemble the plots shown in Fig. 6.21(a) and (b). The spectra in Fig. 6.4(c,d) (or Fig. 6.18) is consistent with the transfer functions plotted in Fig. 6.21(c) and (d).

In the next demonstration, we add a finite tunneling resistance to create an active junction or a conductance channel, as shown by the circuit in Fig. 6.13. The Z_J channel draws some voltage from the source to feed the tunneling branch, thus generating a tunneling current. The current draw due to quantum tunneling typically stays within pA to nA and may get as high as μA via a non-linear process where high density of states of available carriers are accessed. Fig. 6.22 demonstrates how a current generation in the junction branch modifies the transfer function around zero frequency when the junction is switched active from infinite resistance to 10 kΩ. The minor perturbation of the transfer function shown in Fig. 6.22(b) due to inserting an exaggerated tunneling resistance, $R_J = 10$ kΩ, implies that introducing a tunneling conductance channel in parallel to C does not affect the macroscopic circuit, which consists only of the tip, sample and the capacitance gap.

(a) $C = 100$ pF

(b) $C = 10$ pF

(c) $C = 1$ pF

(d) $C = 0.1$ pF
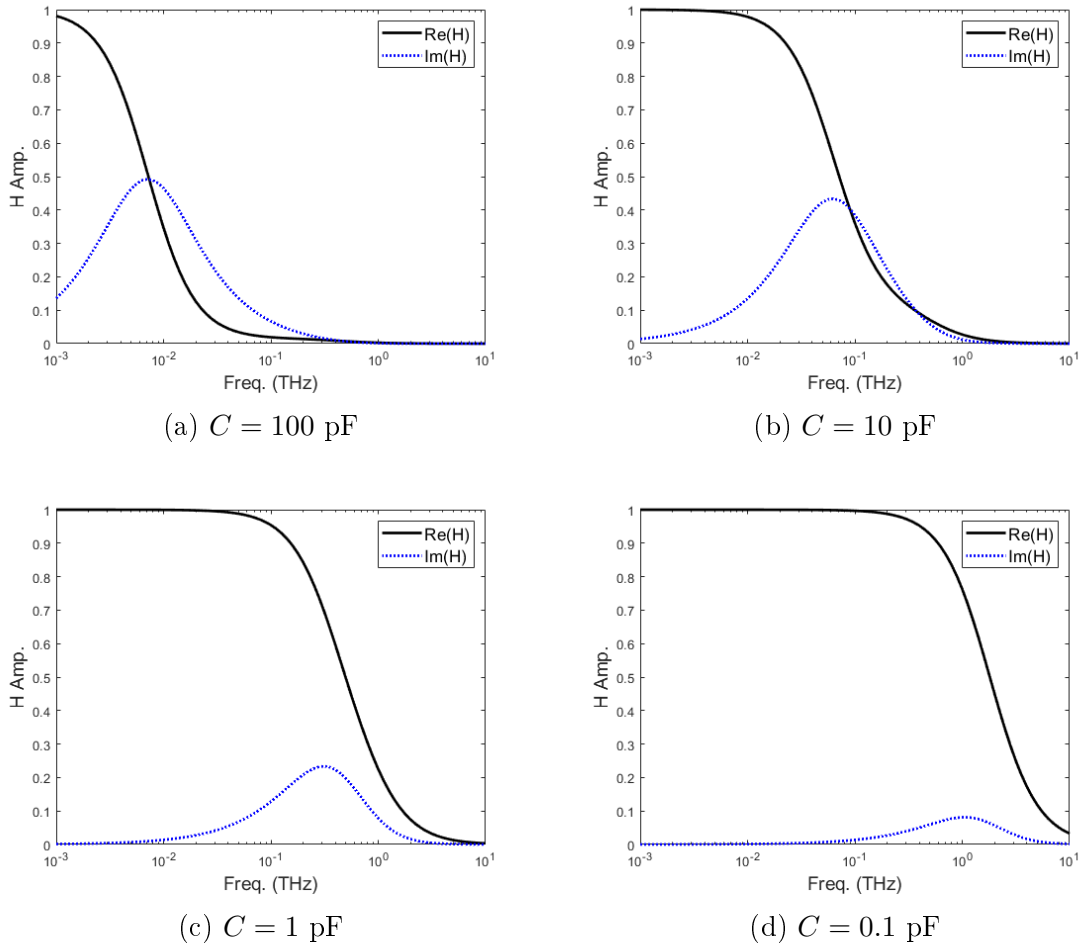
Figure 6.21: Transfer functions for varying capacitance while fixing $R = 220\,\Omega$ pH and $L = 75$ pH.

(a)

(b) $R_J = 10^4\,\Omega$
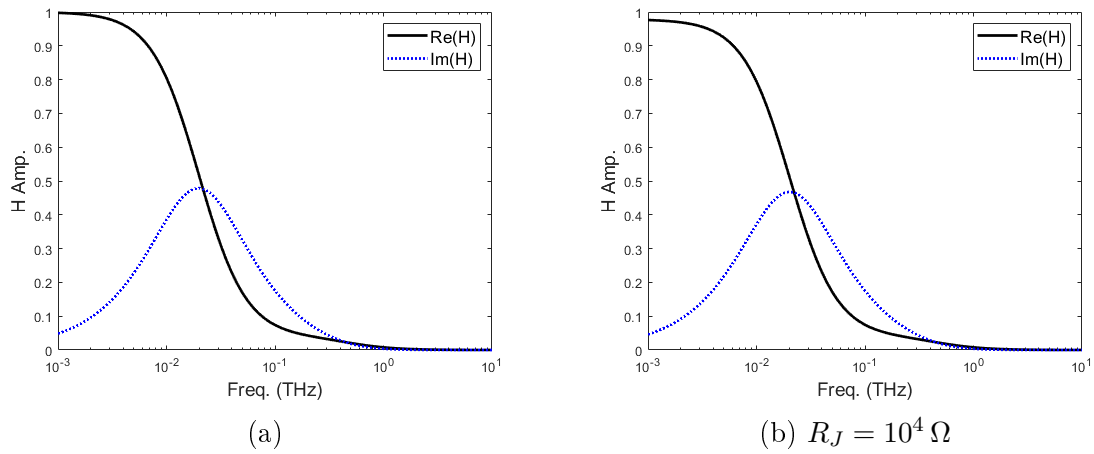
Figure 6.22: Transfer function where the parallel conductance channel at the junction has (a) infinite resistance (i.e. 1 GΩ) and (b) finite resistance (i.e. 10 kΩ) where current can pass through.

6.2 Transmission Line modeling

The lumped-element circuit model described previously only focuses on the NF region and compresses the entire system to a single point. The model can only output the time dependence of the near-field signal as a voltage or current. In order to model the spatial dependence or to simulate time-elapsed propagation, transmission line (TL) theory should be introduced.
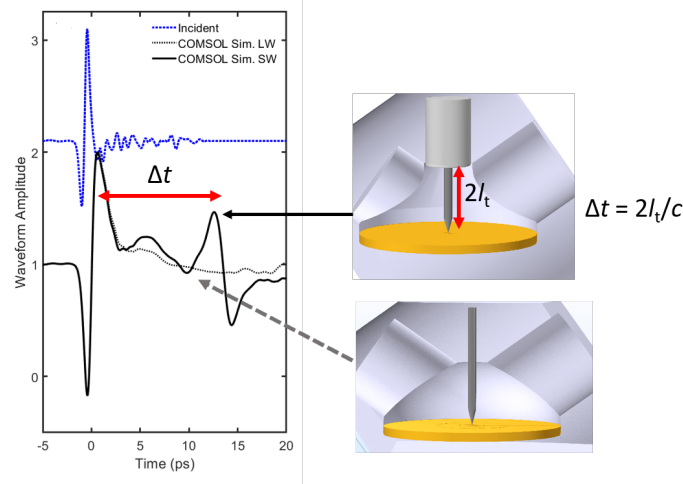
Figure 6.23: Time delay of reflection pulse is equal to the time taken for the pulse to travel twice the tip shaft length. The tip holder acts as a reflecting boundary.

Therefore, it is now possible to simulate a full scenario where the incident field has to propagate to the junction and the circuit for the tip and sample can be defined with a spatial dependence.

6.2.1 Transmission line model

Transmission-line modeling (TLM) is also known as the *transmission-line matrix method*, which is numerical technique for solving field problems based on the equivalence between Maxwell's equations and the equations for voltages and currents on a mesh of continuous two-wire transmission lines [177]. TLM is a physical discretization process where the field having some spatial distribution is replaced by a network or array of lumped elements. Junctions are formed where circuit lines cross forming

impedance discontinuities. The equivalent network is solved by iterative methods. For example, a conducting wire in Fig. 6.24(a) can be replaced by a series of lumped resistors, as shown in Fig. 6.24(b). A comparison between the TL equations and Maxwell's equations allows equivalences to be drawn between voltages and currents of the lines and the EM fields in the solution region.
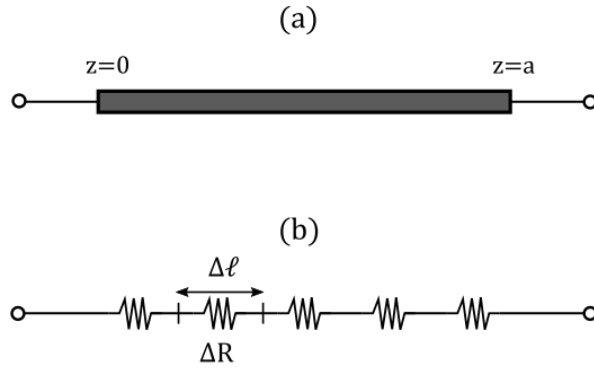
Figure 6.24: (a) 1D conductor. (b) Conductor represented by a series of resistor elements.

Consider an elemental portion of length $\Delta\ell$ of a two-wire TL. An equivalent circuit portion of the line is shown in Fig. 6.25, where the parameters, R, L, G, and C are resistance, inductance, conductance, and capacitance, *all per unit length*, respectively. The wave propagates in the $+z$ direction, from the generator to the load.
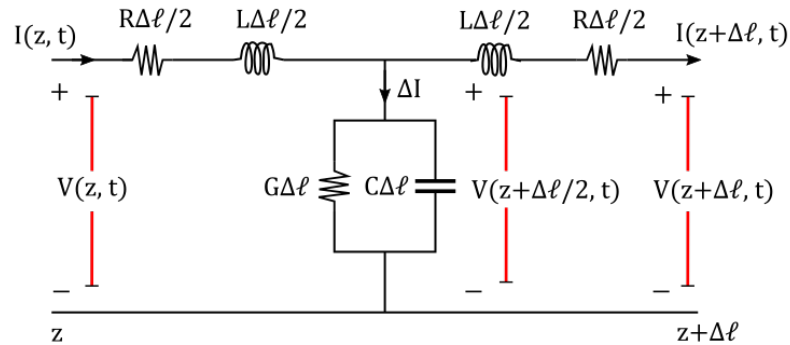
Figure 6.25: Equivalent circuit model for a differential length of a TL.

Kirchoff's voltage law on the left loop of the circuit in Fig. 6.25 yields,

$$V(z,t) = R\frac{\Delta\ell}{2}I(z,t) + L\frac{\Delta\ell}{2}\frac{\partial I}{\partial t}(z,t) + V(z + \Delta\ell/2, t), \qquad (6.30)$$

which leads to the finite-difference equation of

$$-\frac{V(z + \Delta\ell/2, t) - V(z,t)}{\Delta\ell/2} = RI(z,t) + L\frac{\partial I}{\partial t}(z,t). \qquad (6.31)$$

Taking the limit as $\Delta\ell \to 0$ leads to the PDE

$$-\frac{\partial V(z,t)}{\partial z} = RI(z,t) + L\frac{\partial I(z,t)}{\partial t}. \qquad (6.32)$$

Using Kirchoff's current law at the main node at $z = \Delta\ell/2$, the current branches off at the junction, which gives

$$I(z,t) = I(z + \Delta\ell, t) + \Delta I \qquad (6.33)$$

$$= I(z + \Delta\ell, t) + G\Delta\ell V(z + \Delta\ell/2, t) + C\Delta\ell\frac{\partial V}{\partial t}(z + \Delta\ell/2, t), \qquad (6.34)$$

which leads to the finite-difference equation of

$$-\frac{I(z + \Delta\ell, t) - I(z,t)}{\Delta\ell} = GV(z + \Delta\ell/2, t) + C\frac{\partial V}{\partial t}(z + \Delta\ell/2, t). \qquad (6.35)$$

Taking the limit as $\Delta\ell \to 0$ leads to the PDE

$$-\frac{\partial I(z,t)}{\partial z} = GV(z,t) + C\frac{\partial V(z,t)}{\partial t}. \qquad (6.36)$$

Differentiating eq. (6.32) and eq. (6.36) to obtain mixed partial second derivatives give

$$-\frac{\partial^2 V}{\partial z^2} = R\frac{\partial I}{\partial z} + L\frac{\partial^2 I}{\partial z \partial t} \qquad (6.37)$$

$$-\frac{\partial^2 I}{\partial t \partial z} = G\frac{\partial V}{\partial t} + C\frac{\partial^2 V}{\partial t^2}. \qquad (6.38)$$

Substituting Eq. 6.36 and Eq. 6.38 into Eq. 6.37 yields the equations for voltage and current, respectively, as

$$\frac{\partial^2 V}{\partial z^2} = LC\frac{\partial^2 V}{\partial t^2} + (RC + GL)\frac{\partial V}{\partial t} + RGV \qquad (6.39)$$

$$\frac{\partial^2 I}{\partial z^2} = LC\frac{\partial^2 I}{\partial t^2} + (RC + GL)\frac{\partial I}{\partial t} + RGI. \qquad (6.40)$$

The mathematical form for both V and I is written in the general form of a propagating equation along z.

The frequency domain form using Eqs. 6.32 and 6.36 is given by

$$-\frac{\partial V(z,\omega)}{\partial z} = (R + i\omega L)I(z,\omega) \tag{6.41}$$

$$-\frac{\partial I(z,\omega)}{\partial z} = (G + i\omega C)V(z,\omega). \tag{6.42}$$

By taking derivative of the first equation in Eq. 6.41, and replacing the derivative of current with the second equation, the 1D voltage wave equation is obtained.

$$\frac{\partial^2 V(z,\omega)}{\partial z^2} - (R + i\omega L)(G + i\omega C)V(z,\omega) = 0 \tag{6.43}$$

$$\frac{\partial^2 V(z,\omega)}{\partial z^2} - \gamma^2 V(z,\omega) = 0, \tag{6.44}$$

where γ is the complex propagation constant,

$$\gamma = \sqrt{(R + i\omega L)(G + i\omega C)}, \tag{6.45}$$

which can be expanded into real and imaginary parts as

$$\gamma = \alpha_{\text{prop}} + i\beta_{\text{prop}}. \tag{6.46}$$

The general solutions of the wave equations involve a pair of exponentials made up of forward and backward traveling components given by

$$V(z) = V_0^+ e^{-\gamma z} + V_0^- e^{\gamma z} \tag{6.47}$$

$$I(z) = I_0^+ e^{-\gamma z} + I_0^- e^{\gamma z}. \tag{6.48}$$

The first term is a wave propagating in the $+z$ direction and the second term is a wave propagating in the $-z$ direction. Plugging in these equations into the wave equation in Eq. 6.43, solving for current yields

$$I(z) = \frac{\gamma}{(R + i\omega L)}[V_0^+ e^{-\gamma z} + V_0^- e^{\gamma z}] = \frac{\gamma}{(R + i\omega L)}V(z). \tag{6.49}$$

This expression is similar to Ohm's law where the transmission line impedance is then derived as

$$Z_0 = \frac{(R + i\omega L)}{\gamma} = \sqrt{\frac{R + i\omega L}{G + i\omega C}}. \tag{6.50}$$

191
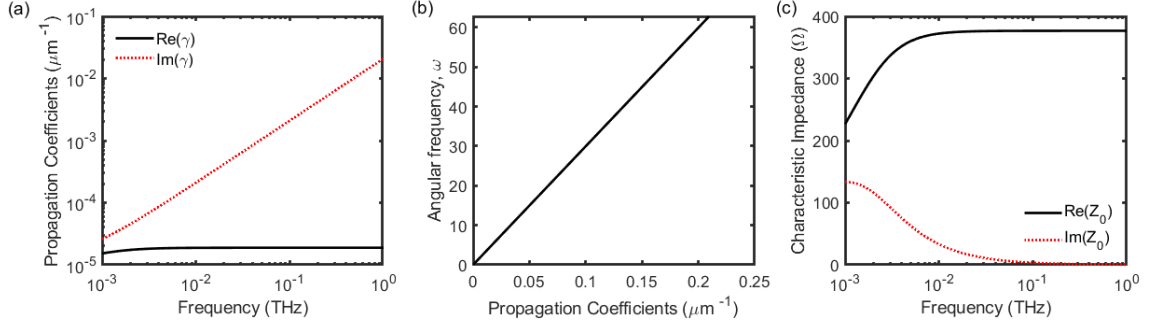
Figure 6.26: (a) Real and imaginary components of the propagation coefficient $\gamma = \alpha + i\beta$ for a free-space-like transmission line. (b) The corresponding linear dispersion relation $\omega(\beta)$. (c) Real and imaginary components for the impedance of free space.

6.2.2 Lossless Transmission Line

In a loss-less transmission line, assume no attenuation losses as the pulse goes along line. This section describes a 1D FDTD simulation on a lossless transmission line wire. In Fig. 6.26(a), the α component is very small and barely attenuates the wave as it is propagating. The β_{prop} component introduces a phase dependence of the wave amplitude as a function of propagation frequency. In Fig. 6.26(b), the dispersion relation is plotted. The slope gives the group velocity which is found to be equal to the speed of light, $v_0 = c_0$. Fig. 6.26(c) shows the characteristic impedance of the line which saturates to $377\,\Omega$.

Even for the simple pulse propagation in air, the case can be modeled with a transmission line with distance ℓ and free-space impedance characteristic $Z_0 = \sqrt{\mu_0/\epsilon_0} = 377\,\Omega$ and velocity $v_0 = 1/\sqrt{\mu_0\epsilon_0}$. The μ parameter is a form for the line inductance, L', with units of $\text{H} \cdot \text{m}^{-1}$, and ϵ corresponds to the line capacitance per unit length, C', with units of $\text{F} \cdot \text{m}^{-1}$. For an transmission line with arbitrary material properties, the characteristic resistance is $Z_c = \sqrt{L'/C'}$ and wave velocity is $v = 1/\sqrt{L'C'}$.

Fig. 6.27 shows a simple TL simulation for a box pulse traveling along the line where the end boundary is an open circuit and a short circuit, respectively. There are no losses in the amplitude as z increases.

A THz pulse is used in Fig. 6.28. When a reflection coefficient at the end of the

192

(a)   (b)
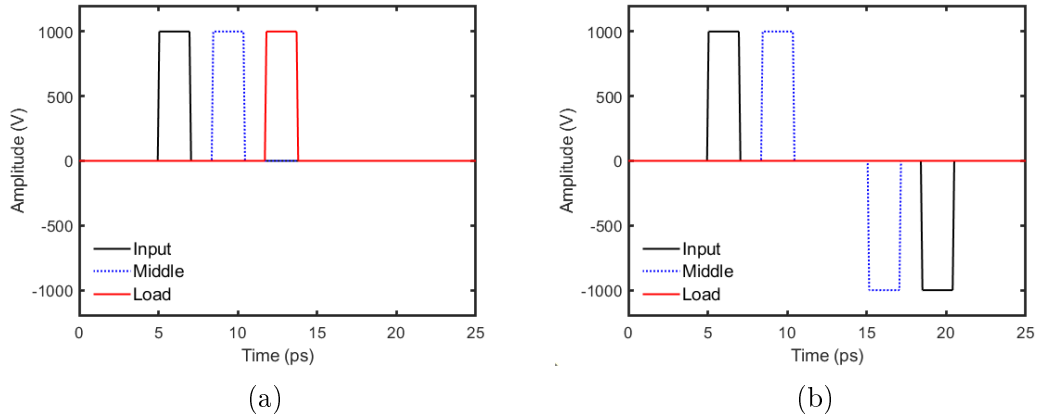
Figure 6.27: Simulation of the propagation of a box pulse along the lossless TL line. (a) Waveforms collected along the input, middle and end of the line without a reflective boundary. (b) Waveforms collected with a reflective boundary. The end of the line reads a net zero amplitude due to the cancellation of the forward and backward traveling waves.

wire is -1, the voltage measured at the end of the line is zero due to the reflection canceling out the incident pulse.

(a)   (b)
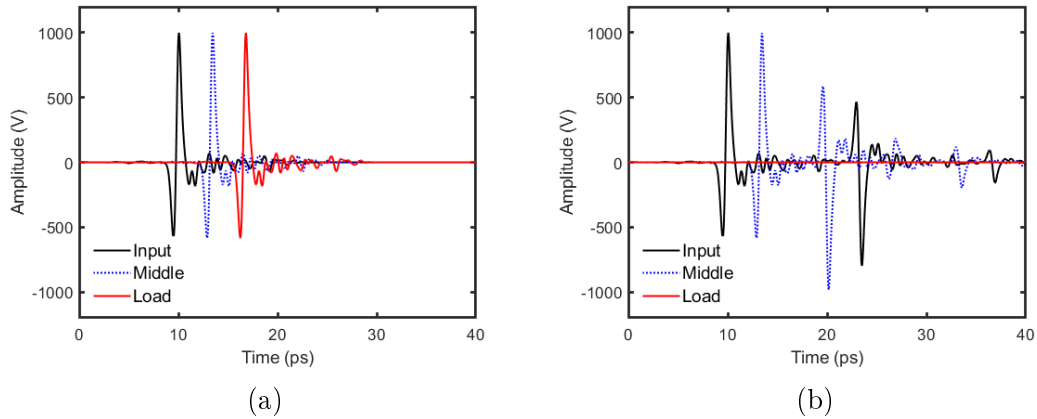
Figure 6.28: Simulation of the propagation of a THz pulse along the lossless TL line. (a) Waveforms collected along the input, middle and end of the line without a reflective boundary. (b) Waveforms collected with a reflective boundary. The end of the line reads a net zero amplitude due to the cancellation of the forward and backward traveling waves.

6.2.3 Propagation losses

The loss parameter is generally encoded in the value R which describes the resistive dissipation as the wave propagates on the line. The real part of the propagation coefficient α is increased by inputting a larger value for R to cause the amplitude to attenuate as shown in Fig. 6.29a. In Fig. 6.29b, the reflected pulse going back towards and into the input port is of smaller amplitude with the opposite sign.

(a)   (b)
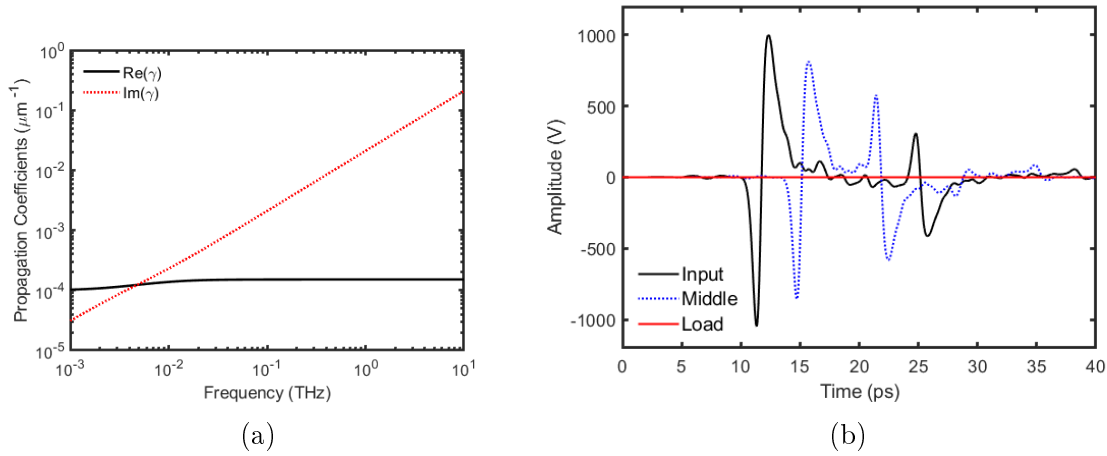
Figure 6.29: (a) Propagation coefficient versus frequency. (b) Simulation of the propagation of a THz pulse along a TL line with resistive losses. The inputs of the TL simulation match that of the circuit model of the previous section, except that the circuit parameters are inputted as linear densities by dividing the parameter values: $R = 220 \ \Omega$, $L = 75$ pH and $C = 35$ fF, over the 2 mm wire length.

The measured transient at the port is compared with the FEM simulation in Fig. 6.30. The peak of the reflection pulse matches exactly in time corresponding to twice the tip shaft distance for a SPP that travels at about the speed of light. The discrepancy between the two simulations where the COMSOL result yields a wider pulse is due to the fact that the TL simulation does not account for the change in tip shape at the taper. The TL only uses a single geometry with one set of propagation parameters. The impedance mismatch due to the tapering and other dispersion effects would already be accounted for in the COMSOL simulation.
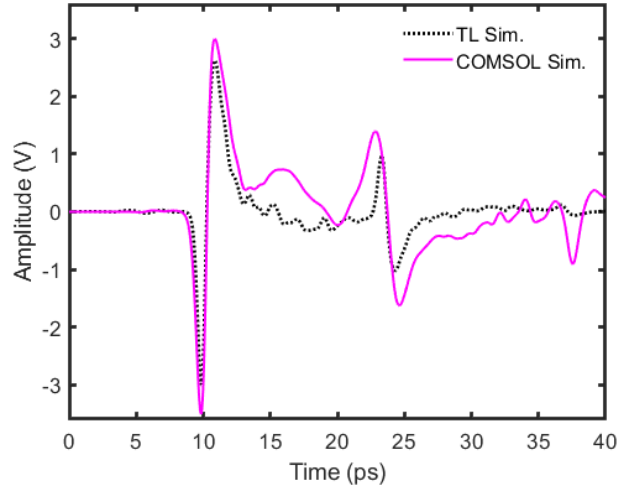
Figure 6.30: Comparing the TL simulation with propagation losses with COMSOL. The reflective boundary at the end of the TL is implemented to reproduce a similar reflection pulse due to the tip holder. Due to propagation losses along the wire, the reflection pulse returns with a smaller amplitude.

6.2.4 Two-Port Model

Transmission line model can be described using the two port model [209]. Instead of running a 1D FDTD simulation, this model can provide a cleaner transfer function analysis. The relation between input voltage and current and output voltage and current of a two port model can be represented as:

$$\begin{pmatrix} V_1 \\ I_1 \end{pmatrix} = \begin{pmatrix} A & B \\ C & D \end{pmatrix} \begin{pmatrix} V_2 \\ I_2 \end{pmatrix} \tag{6.51}$$

where A, B, C and D are frequency dependent coefficients. V_1 is the input voltage of the line and V_2 is the voltage at the load. The circuit diagram is shown in Fig. 6.31 where the transmission line connects the source voltage to the load. The transfer function of the two-port network while factoring in the impedance of the source, Z_S, is given by

$$H = \frac{V_L}{V_{in}} = \frac{Z_C}{AZ_C + B + CZ_CZ_S + DZ_S} \tag{6.52}$$

where Z_C is the characteristic TL impedance.

The ABCD matrix for a TL with characteristic impedance Z_C and propagation
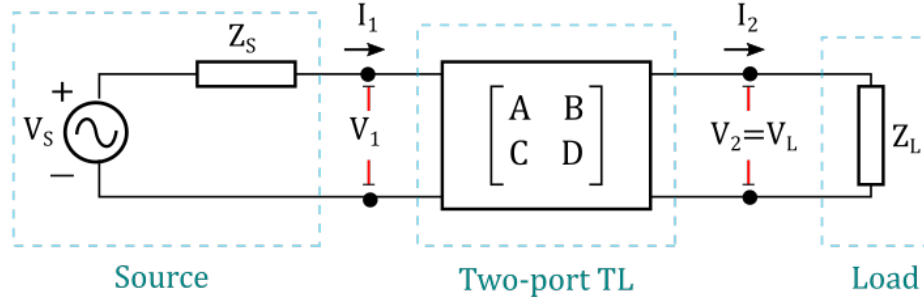
Figure 6.31: Two-port transmission line connected to an input voltage and a load.

constant γ and length l is given as [209]:

$$\begin{pmatrix} V_1 \\ I_1 \end{pmatrix} = \begin{pmatrix} \cosh(\gamma l) & Z_C\sinh(\gamma l) \\ \frac{1}{Z_C}\sinh(\gamma l) & \cosh(\gamma l) \end{pmatrix} \begin{pmatrix} V_2 \\ I_2 \end{pmatrix}. \tag{6.53}$$

The complex transfer function is computed for a large range of THz frequencies in Fig. 6.32. Zooming into the transfer function shows the fundamental frequency of $f_1 = 0.077$ THz for the first reflection pulse and 0.149 THz for the second reflection pulse. Repetition of the troughs occur at multiples of f_1, which corresponds to a period of about 13 ps, the time it takes for a pulse to travel up and back down the tip shaft. This complex transfer function will be used in the next step to transform an arbitrary voltage input waveform such as a THz pulse.

The full 2 Port transmission line analysis is demonstrated in Fig. 6.33 where a known input voltage waveform can be transformed to finally obtain the voltage waveform at the load. The analysis yields both real and imaginary components, however the highlight is that the same reflection pulse produced 13 ps after the main peak as done in the previous simulations, has also been achieved. The comparison with COMSOL simulation is shown in Fig. 6.34. The reflection pulse is slightly broadened compared with the previous TL line with losses in Fig. 6.30.

From these results, it is possible to compute a full transfer function matrix that performs the near-field transformation of the incident THz pulse combined with delayed reflection contributions of a transmission line.

(a)   (b)
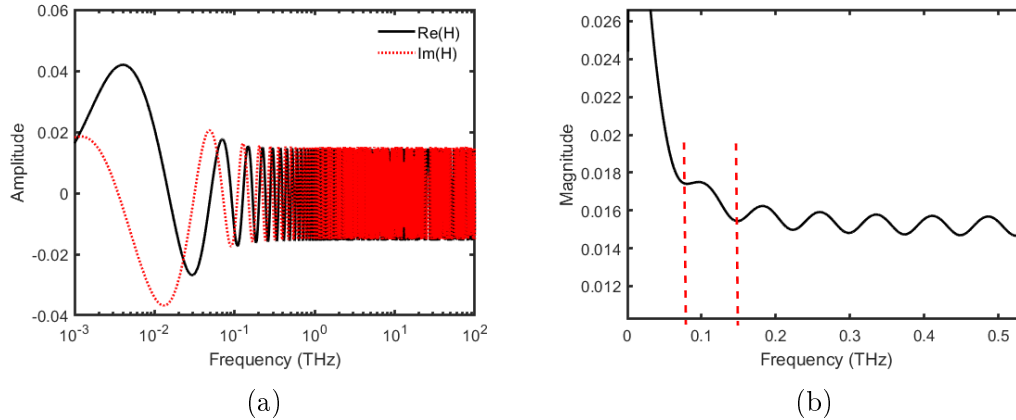
Figure 6.32: (a) The complex transfer function using the two port model for a line of length 2 mm and reflection boundary at the end. (b) Zooming into the transfer function shows the fundamental frequency of 0.077 THz for the first reflection pulse and 0.149 THz for the second reflection pulse. Repetition of the troughs occur at multiples of 0.077 THz. The inputs of the TL simulation match that of the circuit model of the previous section, except that the circuit parameters are inputted as linear densities by dividing the parameter values: $R = 220\ \Omega$, $L = 75$ pH and $C = 35$ fF, over the 2 mm wire length.

6.2.5   Loaded Transmission Line

A simplified circuit model should be perceived as an input source connected to a series of impedance elements connected to a load, as illustrated in Fig. 6.13 and 6.35. In this case, the tip acts as an initial impedance for the source which consumes a fraction of the input voltage. The sample acts as an extra impedance for the signal read-out, whether it is a voltage or current. The load element receives the remainder of the voltage represented by the output bias at the end of the circuit, which can be computed using the voltage divider method. The tip, sample and load impedance elements can consist of real and complex factors since they can be combinations of R, L, C, G, such that the voltage and current through each element are processed as phasors. Thus, the bias voltage connected to the load can have a completely different form compared to the input voltage. In the RLC circuit calculations, the combination of circuit elements produce a load bias that is proportional to the integral of the input voltage. In the TL calculations, the load bias is the sum of the result from the RLC

197

(a)

(b)
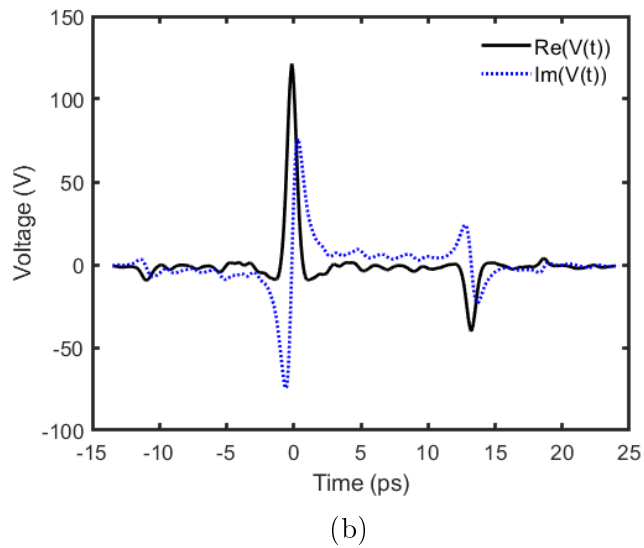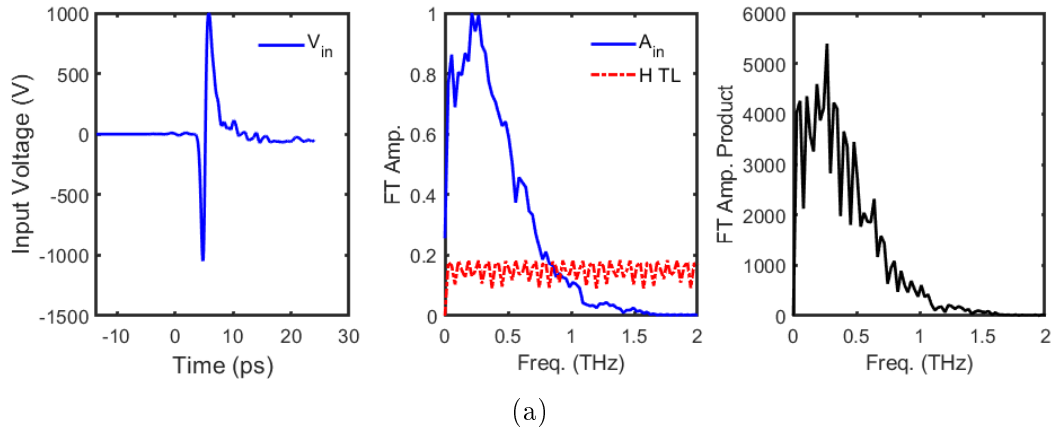
Figure 6.33: (a) Starting with the input pulse (panel 1), the transfer function from the 2 Port model multiplies with the Fourier transform of the input (panel 2) to get the product spectrum (panel 3). (b) The real and imaginary components of the inverse Fourier transform to obtain the voltage waveform observed at the load.
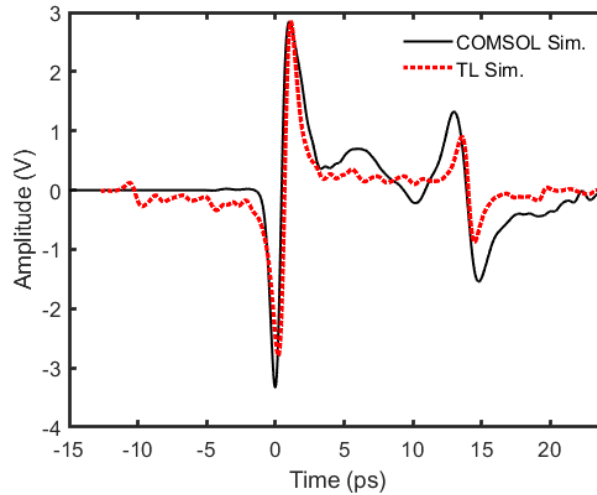
Figure 6.34: Comparing the 2 Port transmission line simulation of a THz pulse propagating along a wire with the results of COMSOL. The inputs of the TL simulation match that of the circuit model of the previous section, except that the circuit parameters are inputted as linear densities by dividing the parameter values: $R = 220\ \Omega$, $L = 75$ pH and $C = 35$ fF, over the 2 mm wire length.

calculation with a time-delayed reflection pulse.

Separate program blocks can be written for circuit sections and then combined together to compute the overall simulation showing all the contributions by the tip wire, tip apex, tip-sample gap and the sample as illustrated in Fig. 6.35. A complex tip model as done for a cusped tip where parallel branches of R, L and C are made for the shaft and taper can be a single module, which accomplishes the voltage pulse shaping due to the wire geometry before moving on to the module for the junction. Furthermore, the signal collection circuit located in the sample branch may consist of a group of other circuit elements for data-acquisition such as amplifiers, integrators, etc, which do not affect the near-field generation at the junction, but may distort the amplitude and phase of the output current.

A transmission line model coupled to the RLC circuit as depicted in Fig. 6.36 allows for contributions by traveling and reflecting pulses due to SPPs. One end of the transmission line is the RLC circuit which is also where the voltage source (i.e. incident THz pulse) excites the entire circuit. The other end is a reflective boundary
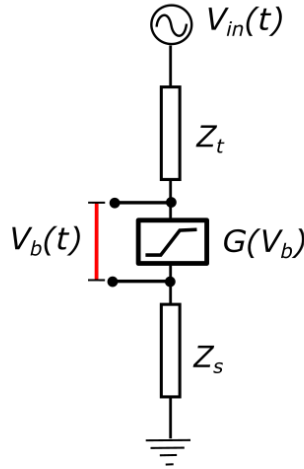
Figure 6.35: Representing major parts or interfaces of the circuit with modules. The tip, junction and sample consist of their own internal circuits. The modules are all coupled together to solve for all electrical quantities. The tunneling junction is represented by a non-linear conductance element G whose I-V characteristic is driven by the near-field bias voltage V_b.

representing the tip holder of the STM. The incident voltage becomes an input to both the RLC circuit and the transmission line. Due to pulse propagation and reflection at the tip holder boundary, there will be a secondary reflection pulse calculated at a time delay equal to twice the tip shaft length. The reflection pulse is then fed back into the RLC circuit.

The THz pulse traveling down the tip shaft is shown in Fig. 6.23. THz radiation may couple well with the mm wire lengths used to form tip modes that exhibit resonance effects [37]. The entire geometry is comparable with THz wavelengths, so it is necessary to expand the circuit model to a transmission line, which is only concerned with the tip shaft part. The transmission line model follows a similar formalism for wave-guides discussed in Chapter 2. At the end of the wire, the output electric field becomes the input for the junction circuit.
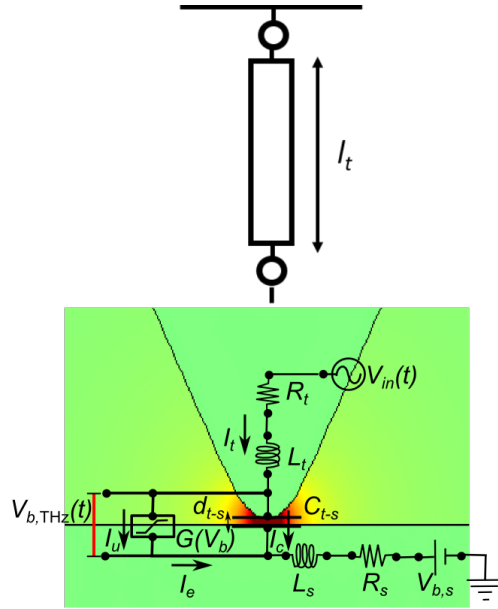
Figure 6.36: Full circuit diagram showing a transmission line coupled to the RLC circuit. The individual circuit elements for the tip, sample and tunneling junction are shown in full. Calculations for the transmission line component and RLC component can be computed and then combined to achieve the final result for the junction's input bias, V_b.

6.3 Circuit model for photo-conductivity

The interaction of light and semiconductors presents an interesting case for understanding transport behaviour. Fundamentally, the light wave provides the electric field for accelerating charge carriers inside the material. However, the carriers are bounded by the macroscopic material properties and also influenced by their local environment within the material, as the properties may vary. Due to this, carriers inside semiconductors exhibit different transport behaviours depending on the frequency of the incident light. THz radiation is suitable for driving and probing transport activity inside typical semiconductors since the frequency range caters to carrier timescales inside the semiconductor. Photo-excited carriers are free charge particles created when energetic photons are absorbed, which cause electron and hole pairs to separate, producing charged populations that can be driven by electric fields. Photocurrent due to photo-excited carriers is a transport phenomenon often stud-

ied with THz spectroscopy as several of the material's electronic properties can be measured and derived. This section presents a circuit model that can be used to determine THz transport and emission in photo-excited semiconductors.

6.3.1 Photocarrier transport

Models can be prescribed to predict the shape of the THz waveform emitted by a simple THz emitter. The simple Drude-Lorentz model is modified to account for ultrafast changes in the bias field owing to screening effects. From the calculations and the experiments, it is evident that the screening process is the key factor in determining the properties of the radiated THz pulses [99]. The lifetime of the carrier is mainly determined by its trapping time, which is the amount of time for the carrier to transition to mid-gap states. The free-carrier trapping time in mid-gap states is much shorter than the recombination time between the electron and hole. The screening of the electric field is contributed by free carriers as well as trapped carriers. The electric field recovers after the recombination of the electron and hole, which occurs at a duration much longer than the time scale of the THz pulse. Overall, the recombination process has minor effects on the carrier dynamics and THz radiation. The carrier scattering time determines the transport behaviour such as the saturation velocity of the photocurrent, which affects the amplitude of the THz emission.

To model the carrier transport, parts of the 1D Drude–Lorentz model, as already presented in Chapter 2, will be paraphrased here. The current density is related to the velocity of the free carriers in the THz antenna as:

$$j(t) = en_h v_h(t) - en_e v_e(t), \qquad (6.54)$$

where n_f is the density of free carriers and v is the carrier velocity averaged over the carrier distribution. Holes contribute a minor current as they are much slower, thus the first term can be dropped. The time dependence of the carrier density where τ_c is the trapping time and $G(t)$ describes the generation of free carriers by the laser pulse

is given by:

$$\frac{dn_f(t)}{dt} = -\frac{n_f(t)}{\tau_c} + G(t) \qquad (6.55)$$

The time dependence of the average velocity is in the Drude–Lorentz picture, given as

$$\frac{dv(t)}{dt} = -\frac{v}{\tau_c} + \frac{e}{m^*}E_{loc}, \qquad (6.56)$$

where τ_g is the momentum relaxation time. The local electric field at position of the carriers, E_{mol} is given by:

$$E_{loc} = E_{bias} - \frac{P_{sc}}{\eta\epsilon}. \qquad (6.57)$$

The time dependence of the space-charge polarization, P_{sc}, can be represented by

$$\frac{dP_{sc}}{dt} = -\frac{P_{sc}}{\tau_r} + j(t) = -\frac{P_{sc}}{\tau_r} + n_f ev, \qquad (6.58)$$

where τ_r is the recombination lifetime. Using the equations above, a second order differential equation can be obtained for the carrier velocity:

$$\frac{d^2v2}{dt^2} + \frac{1}{\tau_s}\frac{dv}{dt} + \frac{\omega_p^2 v}{\eta} = -\frac{eP_{sc}}{m^*\eta\epsilon\tau_r}, \qquad (6.59)$$

where $\omega_p^2 = n_f e^2/m^*\epsilon$ is the plasma frequency. The radiated electric field is proportional to the carrier acceleration, dv/dt, so solving the coupled equations together gives full information about the radiated THz pulse and the dynamics of the local field. Typical densities are 10^{16} to 10^{18} cm^{-3} where scattering works efficiently to restore thermal equilibrium.

The waveform features of a THz pulse originate from carrier acceleration in the emitter. At a relatively high carrier generation density, the local electric field will oscillate. The attraction between the electron and hole and the screening of the electric field produce this effect. The opposing charges cause the electrons and the holes to be initially accelerated in opposite directions in the local electric field. This will induce a polarization, which acts as a restoring force for the motions of the electron and hole. When the carrier density is high enough, the electric field may be

screened to a comparable magnitude of the restoring force between the electron and hole. In this case, the electron and hole form an oscillator, and the oscillation of the electron and hole induces an oscillating electric field at high carrier densities [92].

6.3.2 Screening fields

Photoexcitation is a dynamic process as presented in the previous subsection. It is possible to implement time-dependent lumped elements, as shown in Fig. 6.37. The bias source is connected to a time-dependent conductance which is in parallel with a time-dependent capacitor, which influences the voltage and current activity across the antenna load when activated by laser pulse illumination. The circuit [210–213] predicts the microscopic behaviour of the antenna, thus the local fields.
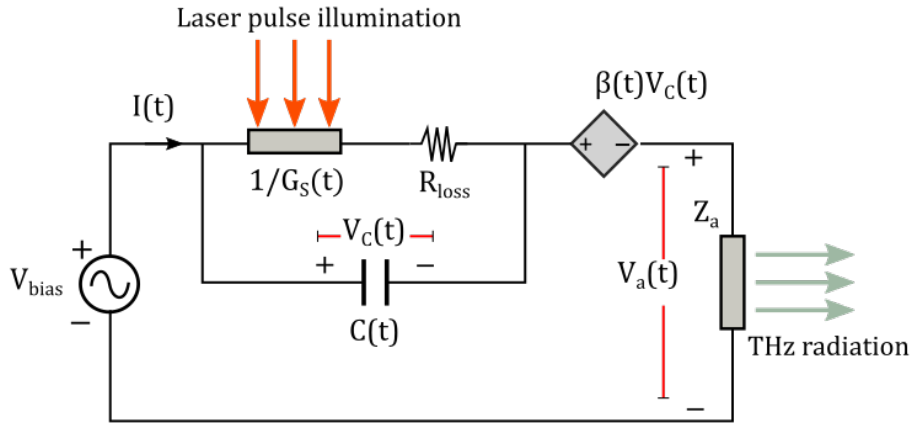
Figure 6.37: Equivalent circuit for the photoconducting THz antenna which consists of time varying source resistance, time varying capacitance, time varying voltage source due to space-charge screening and the antenna impedance at the load.

Space-charge pairs cannot find the opposite sign pair for recombination, they remain in the proximity of the antenna electrodes. This phenomenon can be interpreted as the formation of a time-dependent capacitance influenced by the generated carrier density in the gap and recombination time of the photoconductive material. They also produce a voltage in the reverse direction of the externally applied bias voltage.

204

In Fig. 6.37, the screening voltage due to electron and hole excitation is represented by the time-dependent voltage source $\beta(t)V_C(t)$ which acts against the source bias. The screening voltage is transient which vanishes after the recombination time.

The dynamics of the screening field from the accelerated charge carriers become a crucial factor to account for the characteristics of the THz pulses from a PC emitter when the carrier density is high enough to satisfy $\omega_p\tau_s > 0$. The screening of the electric field is contributed by free carriers as well as trapped carriers. The electric field recovers after the recombination of the electron and hole, which occurs at a duration much longer than the time scale of the THz pulse.

There is a reduction in the effective local bias field as a result of THz radiation due to the separation of charges and the creation of the radiated field that counteracts the external bias.

The mechanism of THz generation, known as the photocurrent surge effect, is observed in semiconductors where strong band bending occurs. The photoexcited semiconductor surface can emit THz radiation either by a fast-changing photocurrent or by a nonlinear optical polarization in the material. In the far field region, the THz field which combines the two effects can be expressed as [91]

$$E_{THz} = -\frac{S}{c^2 R} \int_0^\infty \left(\frac{dj}{dt} + \frac{d^2P}{dt^2} \right) dz \qquad (6.60)$$

Where S is the area of the laser excitation spot on the semiconductor surface.

Therefore the overall photo-current arising from the dynamic processing of the photo-conducting and photo-screening elements makes its way to the antenna load and radiation is generated according to the antenna impedance.

6.3.3 Model for the local electric field

The local electric field that drives the photoexcited carriers is determined by the voltage across the photo-conductance element, G in Fig. 6.37. The photocurrent

density by electrons as the main carriers is given as

$$J(t) = en(t)v(t) \tag{6.61}$$

where the velocity is calculated from the electron mobility μ_e and electric field,

$$v(t) = \mu_e \cdot E_C(t). \tag{6.62}$$

Thus in the $J = \sigma E$ form, the conductivity is

$$\sigma(t) = en(t)\mu_e, \tag{6.63}$$

which has units of $\Omega^{-1}\text{cm}^{-1}$. The photocurrent that flows into the antenna load is

$$I_{PC}(t) = en(t)\mu_e V_C(t)\frac{A}{L}, \tag{6.64}$$

where A is the photoexcited area and L is the antenna gap length (i.e. distance between the electrodes). The voltage across the antenna load is given by

$$V_a(t) = Z_a en(t)\mu_e \cdot V_C(t) \cdot \frac{A}{L}. \tag{6.65}$$

The unknown variable to solve for is $V_C(t)$ or equivalently $E_C(t)$. Using the voltage sum rule,

$$V_a(t) = V_b - V_C(t) - \beta V_C(t) = Z_a I(t). \tag{6.66}$$

The current sum rule at the G and C branches is given by

$$I(t) = V_C(t) \cdot G_s(t) + \frac{d}{dt}\left(C(t) \cdot V_C(t)\right) \tag{6.67}$$

$$= V_C(t) \cdot G_s(t) + C(t)\frac{dV_C(t)}{dt} + \frac{dC(t)}{dt}V_C(t) \tag{6.68}$$

Isolating for $I(t)$ in Eq. 6.66 and for $dV_C(t)/dt$ in Eq. 6.67 gives an integrable differential equation,

$$\frac{dV_C(t)}{dt} = \frac{1}{Z_a C(t)}V_b - \frac{1}{Z_a C(t)}V_C(t) - \frac{\beta(t)}{Z_a C(t)}V_C(t) - \frac{G_s(t)}{C(t)}V_C(t) - \frac{1}{C(t)}\frac{dC(t)}{dt}V_C(t) \tag{6.69}$$

The polarization field inside the material is related to the screening field by

$$P_{sc} = \epsilon_s \xi E_{sc} \tag{6.70}$$

where ϵ_s is the dielectric constant of the material and ξ is a screening factor. Using Eq. 2.10 for polarization field and the expressions for photoconductivity current, the unknown electric field can be solved for with the integrable differential equation,

$$\left(1 + \sigma(t)Z_a \frac{A}{L}\right) \frac{dE_C(t)}{dt} = \frac{1}{\tau_r} E_b - \frac{1}{\tau_r} E_C(t) - \frac{\sigma(t)}{\xi} E_C(t)$$
$$- \frac{\sigma(t)Z_a A}{L\tau_r} E_C(t) - \frac{Z_a A}{L} \frac{d\sigma(t)}{dt} E_C(t), \tag{6.71}$$

where τ_r is the carrier recombination lifetime. Comparing Eqs. 6.69 and 6.71, the capacitance term is

$$C(t) = \frac{\tau_r}{Z_a}\left(1 + \sigma Z_a \frac{A}{L}\right), \tag{6.72}$$

and the $\beta(t)$ term is

$$\beta(t) = \frac{\tau_r \sigma(t)}{\xi} = \frac{en(t)\mu_e \tau_r}{\xi}. \tag{6.73}$$

Using Eq. 6.66 to convert the voltage components to electric field, the screening field can be isolated for. All the field components should all sum up to the bias field.

6.4   Chapter Summary

A lumped element circuit model consisting of resistors, inductors and capacitors can be used to model the nearfield at the tip junction where the input into the circuit model is a THz voltage transient. The fitted parameters to reproduce the nearfield waveform created by the COMSOL simulation are $R = 220$ Ω, $L = 75$ pH and $C = 35$ fF. The parameters can also be approximated using physical models for the resistance, inductance and capacitance of a tip-sample geometry at THz frequencies. COMSOL was also used to verify the geometric capacitance for a partially biased tip over a sample to resemble the case for a partially illuminated tip by a THz beam. For example, the simulated tip-sample capacitance was expected to be around 10 to

50 fF when illuminated by a 1 mm radius THz beam, which allowed the RLC fitting parameter for C to be optimized within that range. The nearfield waveform produced by the RLC model using appropriate fitting parameters resemble the integral of the incident THz waveform, which is also simulated by COMSOL. The nearfield can also be calculated in the frequency domain where RLC transfer function is determined for the range of THz frequencies of the incident THz broadband.

A transmission line model can also be coupled to the RLC circuit model. The tip shaft and tip holder provides a path for the incident pulse to reflect and travel back to the junction at a time delay equal to twice the tip shaft length. The reflection pulse appears in the nearfield at the time delay duration. The transmission line model assumes an attenuation loss as the pulse travels along the wire and reflective loss from the boundary reflection. However there is additional dispersion that appears in the COMSOL simulations, which is not reproduced by the transmission line model.

The circuit model can be expanded to account for tip-shape dependence where the nearfield can vary. Using a cusp tip circuit model where the capacitance is split between the tip taper and tip shaft, the circuit model calculated nearfield has a better match with the simulated nearfield for a cusped tip taper.

Lastly, the photoconductive emitter circuit is presented. Photoconductive currents are modeled as transients influenced by screening effects in the semiconductor. These concepts will be relevant in Chapters 7 and 8 for THz-STM on photo-excited semiconductors.

Chapter 7

The THz-driven STM tunneling junction

The tunneling junction is an intriguing topic of condensed matter physics. Electrons in an interface which may partake in tunneling can be manipulated by external applied fields, the selection of material, optical excitation and interactions with other tunneling electrons. Quantum mechanics model the interface as a potential energy landscape to predict electron wavefunctions and tunneling probabilities in space and time, then finally the tunneling current. When perturbations such as external fields or excitations are applied, we can use approximations to calculate the tunneling currents as a function of the perturbation. Circuit analysis and simulations for the nearfield of the STM presented in the previous chapter segues to presenting equivalent circuits for the STM tunneling junction. It will be used for determining the transient behaviour of voltages and currents when THz pulses bias the junction.

The overview of Chapter 7 for tunneling junction shows the transient bias as presented in the simulated bias and the voltage amplitude. Figure 7.1 calls towards tip separation, electric fields and voltage bias. In the presentation of 7.2, STM junction demonstrates as a circuit load, which influences the tunneling process. In presenting for 7.2 metal to metal tunneling portrays the emission of electrons through photoemission and thermionic, allowing a greater energy input. Therefore in the 7.7 summary, COMSOL simulations were consolidated as a criterion, to transform THz electron

fields into near field bias voltage. This highlights the direct tunneling components of the component and the mesoscopic capacitive respectively, when analyzing the metal to metal junction. In observing metal to semiconductor junction, this demonstrates the method of tunneling between the tip, the sample, the surface, in tandem with the bulk and the surface.

7.1   Tunneling in the Schottky barrier

Before discussing the phenomenon that occurs in the transient case, we need to understand the basic mechanisms for tunneling where a constant bias is applied. Important terminology for the STM junction interface has to be clearly understood before diving deeper into the non-equilibrium scenarios.

The schematic of a basic STM junction is shown in Fig. 3.1 where the Fermi level, work functions and tunneling barrier function are presented. One must have a clear understanding of Chapter 3 as a prerequisite before proceeding to this chapter. The Schottky barrier for carriers to tunnel from the bulk to the surface is depicted in 7.1.

The tunneling interface between two or more materials can make up for a long historical review. They have been studied since the 1930s and still ongoing to this day. A metal-semiconductor interface, known as a Schottky barrier, is the rectifying junction formed by the intimate contact of a metal and semiconductor having different work functions (or electronegativities). The majority carrier current is considered the measurable current for the device in an experiment. Electrons are the majority charge carriers for n-type and holes are for p-type semiconductors. The current flow mechanism through a Schottky barrier can be either thermionic or field emission. Thermionic emission models were developed early by Mott [151] and Schottky [214, 215] to successfully explain the behaviour of metal-semiconductor junctions in early experiments. Mead was able to present an approach to model the Schottky barrier under the illumination of light [154]. The Simmons tunneling model utilizes the foundations presented by Mott and Schottky to develop a robust equation that calculates

the tunneling between two metallic planes separated by an insulating gap layer [145, 146].

A device is under forward bias when the conduction electrons tunnel from the material (Conduction band of n-type) into the metal tip. Reverse biasing is where the tunneling goes from the metal tip to the material. When interface is under a bias voltage, an electric field forms within the junction regions. The depletion region, also known as the space charge layer, is an insulating region in the interface where the mobile charge carriers have been diffused away by an electric field. The field induces a band bending in the subsurface depletion layer to enable the transport between the surface and the bulk. Usually in the steady state, the Fermi level of the surface remains pinned to the bulk Fermi level and band bending through the depletion region. When the device is under forward bias, the tunneling occurs from the edge of the depletion region at the conduction band through the barrier and into the metal. Under reverse bias, the tunneling occurs from the metal to the conduction band in the semiconductor. The two cases must be treated separately since in the forward bias case, both the forbidden gap where tunneling occurs and the tunneling distance are functions of voltage whereas in the reverse bias case, only the distance matters.
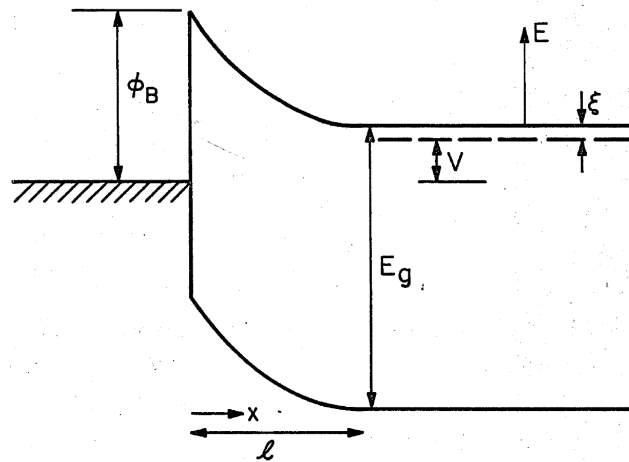
Figure 7.1: Energy band diagram of the Schottky barrier interface. (Adapted from [216].)

From Fig. 7.1, the potential energy, E, of the barrier in the bulk of the material where the conduction band edge is set to zero, is given by

$$E = Nq(\ell - x)^2/2\epsilon_s \tag{7.1}$$

where N is the dopant concentration in the semiconductor, q is the electron charge, x is the distance measured from the metal, and ϵ_s is the permittivity of the semiconductor sample. The width of the space charge layer ℓ is given by

$$\ell = \sqrt{\frac{2\epsilon_s\left(\phi_B - V - \xi\right)}{Nq}}, \tag{7.2}$$

which is a function of the Schottky barrier ϕ_B, the bias V, and the energy difference between the Fermi energy and the CB band edge, ξ.

The room temperature current-voltage characteristics follow the usual diode equation:

$$J = J_0 \left[\exp\left(\frac{qV}{nk_BT}\right) - 1\right] \tag{7.3}$$

where q is usually $-e$ for electron carriers, T is the temperature, and the parameter n is the ideality factor, usually equal or close to unity.

In the reverse bias tunneling case, the electrons tunnel from around the Fermi energy in the metal to the conduction band of the semiconductor. For the forward bias, there are no electrons available below the CB energy, since it is in the forbidden energy gap region. In the reverse bias, there are electrons in states below the Fermi energy of the metal that can contribute to the current. The conduction electrons are energetically distributed according to the Fermi-Dirac equation:

$$f(E) = \frac{1}{1 + \exp\left(\frac{E - E_F}{k_BT}\right)}. \tag{7.4}$$

As a simplifying assumption, within the space-charge region, the electric field is nearly constant. Taking the energy as zero at the CB edge, the energy as a function of distance from the metal is given by

$$\varepsilon(x) = \phi_B - E_{\mathrm{pk}}x \tag{7.5}$$

212

where E_{pk} is the maximum electric field in the space-charge region.

The general case for Schottky tunneling is presented below. The Schottky barrier determines the tunneling from the bulk to the surface of the semiconductor. The tunneling current density through a biased Schottky diode junction is given by

$$J = \frac{emk_BT}{2\pi h^3} \int_0^\infty \exp\left(-\frac{E}{k_BT}\right) P(E,\varepsilon)dE, \tag{7.6}$$

where $P(E,\varepsilon)$ is the transmission probability for an electron with energy E. In order to produce the J-V characteristic relation for either the forward or reverse bias, the functional relation for the energy distribution must be known. The electric field can be converted to the bias to get the integration range.

In Eq. 7.6, the J-V characteristics should display a linear Ohmic behaviour for low applied bias. Under the appropriate bias conditions, the Schottky tunneling dominates over the standard tunneling due to the majority current flow from the bulk carriers. At high voltages, the current increases superlinearly. High field effects (beyond 10 V bias) have to also be accounted for [147, 217] where the current flow is mainly from electron emission.

Thermionic emission describes the process where thermally energetic electrons acquire sufficient kinetic energy perpendicular to the surface of the emitter to overcome its work function. This process is described as the Richardson's law,

$$J_R = A_R T^2 \exp\left(-\Phi/k_BT\right) \tag{7.7}$$

where the Richardson constant is $A_R = 4\pi emk_B^2/h^3 \simeq 1.2 \times 10^6 \text{A}/(\text{m}^2\text{K}^2)$. Thermionic emission is usually characterized by a broadened spectrum of the electron energy due to the range of kinetic energy of thermal electrons. It is difficult to control on a fast time scale, however when the temperature is high, thermionic emission generates extremely large currents.

7.2 STM junction in a circuit model

In the transient case for modeling the junction, one way to look at transient behaviour of a system to use a circuit analogy. Modifications to the standard RLC circuit can be done by introducing new circuit elements that would have an effect on the tunneling interface [218–221]. The expanded circuit model now includes the tunneling junction element as shown in the right branch of Fig. 7.2.

The circuit model relies on multiple processes to influence tunneling process. That is the gap voltage, as simulated from the near-field, and a voltage to access the bulk region [222, 223], thus the revised circuit shows dependence on the sample.
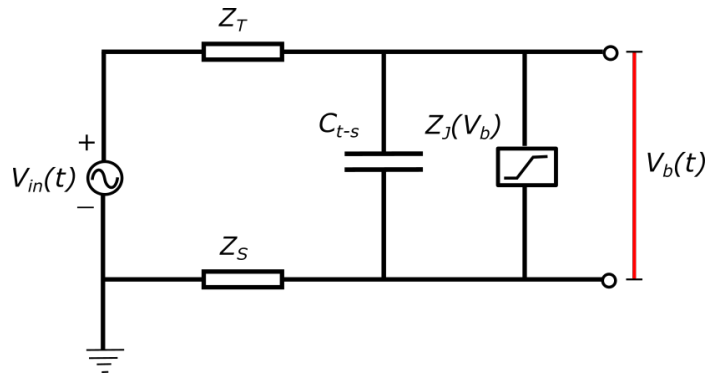
Figure 7.2: Representing the full circuit in a simplified manner by condensing the tip and sample components into a single impedance parameter, Z_T and Z_S respectively.

The circuit elements impede and modify the phase of the voltage and current response at each junction of the circuit. A preferred analysis to simulate the voltage and current transients is in the frequency domain via the transfer function method as described in the previous chapter. When the real and imaginary components for the tip and sample impedances are known, the voltage biasing the gap can be solved for.

The simplification of the circuit model from Fig. 7.2 to Fig. 7.3 requires knowledge of behaviour of the tip and the sample on the input bias to produce the parameter of interest, V_b, without the load being present. Here we can just use the voltage divider method to get the voltage response between the tip and sample. If the tunneling junction load is modeled as a simple resistor, the voltage divider method in a 3
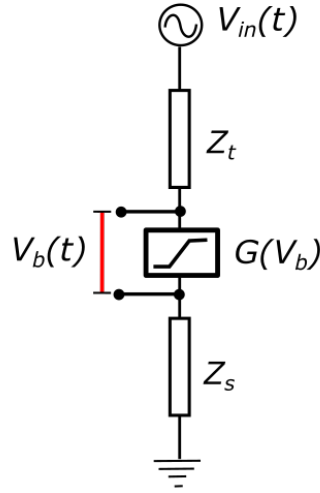
Figure 7.3: General circuit model for the junction interfaces. The tip and sample have their own set of lumped circuit elements which affects the resulting bias going into the junction element.

lumped element circuit can be used to get the bias voltage V_b using the transfer function method described in Chapter 6.

7.3 THz Transient Bias

In a circuit, one can determine the voltage and current across each element when a d.c. voltage is applied through elementary circuit analysis methods. In the time-dependent case where the voltage source is transient, each circuit element implements their treatment to the voltage and current via differential equations. The response of the circuit is determined by transforming the set of differential equations in the frequency domain.

The key variable to solve for is the voltage transient that biases the STM junction. Everything else around it such as the tip and sample will modify the voltage before biasing the junction. However, when the junction exhibits non-linearities or functional transformations of the input voltage to generate current, the voltage and current behaviour throughout the entire circuit also gets affected.

The STM junction is influenced not only by the presence of coupling THz radiation, but also the fact that several tunneling electrons will have an influence on each other. This creates a quantum mechanical system of the many body problem under the potential of an external field. The transient field E_{THz} must be strong enough to cause a voltage drop comparable to the potential barrier height ϕ of interest over typical tunneling distances (< 1 nm). The field enhancement must be strong enough to allow the THz near-field to produce a voltage drop across the junction in the V/nm range.

Fig. 7.4 shows how to use the THz near-field to obtain the THz bias to the junction. The tip-sample separation for the THz-STM experiment is typically held at 0.7 nm. From Fig. 7.4(b) and the approximation in Eq. 4.7, the gap voltage stays constant at scanning distances, which yields a field enhancement factor of $F = 220000$ for an incident pulse with a 200 V/cm peak. The peak bias voltage and peak incident electric field scale as 3.2 V per 200 V/cm which is done by integrating the electric field in the gap as shown in fig. 7.4(c). The voltage is constant after crossing the interface. For the lower doped sample, the electric field in the gap is lower leading to a lower gap voltage. fig. 7.4(d) shows the electric field magnitude in the gap when the sample varies from Au to dielectric the bias. fig. 7.4(e) shows that even though the field enhancement factor drops as the tip-sample distance increase, the integrated field equating the gap voltage is constant. Lastly the peak incident electric field is mapped out to the field magnitude in the gap with the corresponding gap voltage in fig. 7.4(f).

The simulated calibration in Fig. 7.4 allows an approximate mapping for input electric field to a nearfield bias voltage at a fixed tip-sample distance. The remainder of this section uses the simulated nearfield bias voltage to drive the tunneling junction and simulate tunneling currents. Then the number of rectified electrons per THz pulse can be determined.
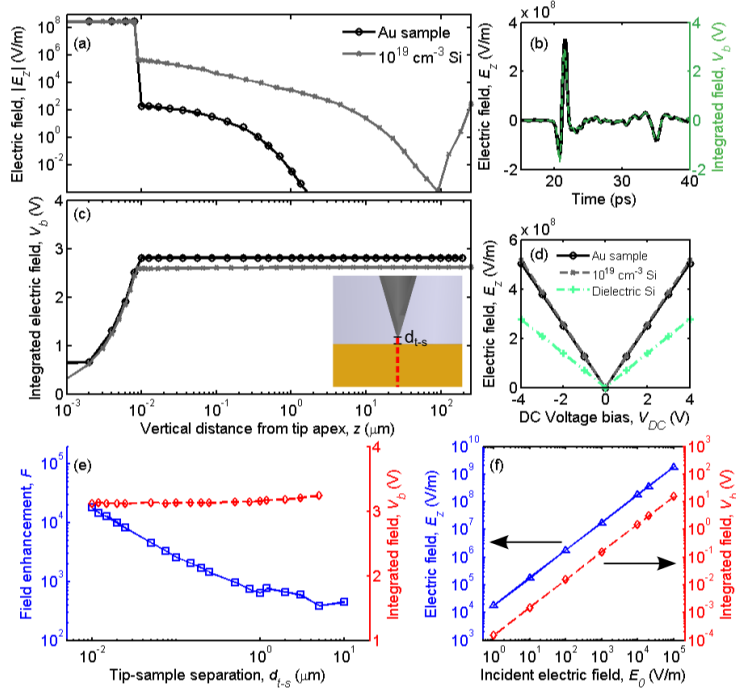
Figure 7.4: (a) The vertical profile of E_z along the center $x = 0\mu$m at $t = t_p$ for Au sample and for the 1E19 cm^{-3} n-doped Si sample. (c) Integration of E_z along the z direction determines the potential of the sample relative to the unbiased tip as a function of the sample depth. The running integral along z shows that the voltage bias is mainly the integration of the field inside the gap region to result in a uniformly biased sample. The electric field drops by a few orders of magnitude when it crosses the interface. (b) The voltage bias calculated using integration has the same shape as the measured electric field, E_z, at the tip apex. (d) Electrostatics simulations were carried out in the same simulation geometry where the tip is biased between -4 V to 4 V while the sample is grounded. Similar electric field magnitudes were measured. The integrated electric field of 2.5 to 3.0 V from a 3.5×10^8 V/m peak field measured at the tip apex corresponds to 2.0 to 2.5 V in the DC case. (e) The field enhancement factors and integrated voltage are plotted as a function of tip-sample separation. Although the field is enhanced as the gap decreases, the voltage stays nearly constant. (f) Peak electric field and voltage bias measured when the peak of the incident electric field is varied.

7.4 Metal-to-Metal tunneling

7.4.1 Electron emission processes

Photoemission and thermionic emission are both effects that allow electrons to be emitted by overcoming the metallic work function Φ via an energy input greater than Φ. In metals, the work function is the energy distance from the Fermi level to the vacuum level. In the case of photoemission, an electron requires the assistance of a single or several photons to be absorbed in order to overcome the work function barrier. Fig. 7.5(a) shows how an electron can absorb at least one photon to overcome the work function. The photoemitted electron density N follows a power law, $N \propto I^n$ where I is the intensity of the incident light and n is the number of photons involved in the absorption process. The electron is emitted with excess kinetic energy of

$$K_e = nh\nu - \Phi. \tag{7.8}$$

Therefore, higher photon energies are more efficient in photoemisson. Low energy photons are inefficient since they require many photons to be absorbed to overcome the work function.
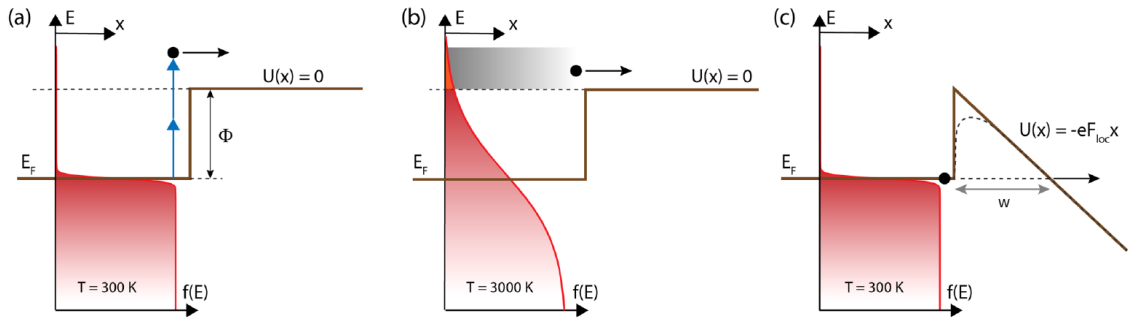
Figure 7.5: Diagrams for three main electron emission mechanisms from a metal-vacuum interface. E_F is the Fermi level, Φ is the work function, $f(E)$ is the Fermi-Dirac distribution, and F is the external electric field. (a) Two-photon photoemission, (b) thermionic emission at 3000 K, and (c) field-emission where the externally applied field tilts the triangular profile of the vacuum potential. The image potential is illustrated by the dashed rounded profile. w is the tunnel barrier width. Adpated from [71].

Thermionic emission, which is already discussed in the previous section and shown

in Fig. 7.5(b) where high energy electrons that exceed the work function is emitted from the metal and contributes to the measurable current.

Instead of lifting the electron energy over the work function to be ejected into vacuum, field emission is a process in which an externally applied electric field modifies the potential energy landscape so that at a given distance from the surface, the effective vacuum potential energy equals the Fermi level of the emitter. The external field tilts the barrier enough so that electrons near the Fermi level can tunnel over the barrier and generate a tunneling current when the field is switched on. The process can occur at room temperature where the smearing of the Fermi-Dirac distribution can lead to a small tunneling contribution. The process is usually derived for $T = 0$K, which coins the process as cold field emission in order to distinguish this process from any other thermal process.

The simplest barrier takes on a linear triangular form:

$$U_{\mathrm{FN}}(x) = -eE_{\mathrm{loc}}x, \tag{7.9}$$

where $U_{\mathrm{FN}}(x)$ is the electric potential at distance x from the emitter's surface and $E_{\mathrm{loc}} = FE$ is the local electric field enhanced by factor F. The field enhancement factor can be determined from FEM simulations as described in Chapter 4. The distance where the effective vacuum potential aligns with the Fermi level of the metal is

$$w = \frac{\Phi}{eE_{\mathrm{loc}}}. \tag{7.10}$$

This physical barrier is known as the Fowler-Nordheim barrier. The Schottky-Nordheim barrier which takes into account the image potential is equal to

$$U_{\mathrm{SN}} = -eE_{\mathrm{loc}}x - \frac{e^2}{16\pi\varepsilon_0 x}. \tag{7.11}$$

Although electric fields and photons are analogous, in photoemission, the energy supplied by the photon is used to overcome the work function. In field-driven emission, energy is spent to actually move the electron from the metal to the physical distance

of the barrier. The work applied by the field in the process of moving the electron is

$$W = eE_{\text{loc}}w = e\Phi, \tag{7.12}$$

which happens to be the same energy as a single photon required for photoemission. The Fowler-Nordheim current density for a Schottky-Nordheim barrier is

$$J_{\text{FN}} = \frac{a_{\text{FN}}}{t_F^2} \frac{(FE)^2}{\Phi} \exp\left(-\frac{v_F b_{\text{FN}} \Phi^{3/2}}{FE}\right), \tag{7.13}$$

where $a_{FN} \simeq 1.54 \times 10^{-6}\text{AeV}/\text{V}^2$ and $b_{FN} \simeq 6.83 \times 10^9 VeV^{3/2}/m$ are Fowler-Nordheim constants. v_F and t_F are constants approximately equal to 1 for the weak field case and for simplicity, however they are usually evaluated as series expansions when the fields get stronger [71].

Next, a semi-classical viewpoint is used to estimate the transit time for escaping electrons to traverse the barrier. The electron velocity in a material with work function Φ is of the order of

$$v_F = \sqrt{2\Phi/m}. \tag{7.14}$$

For the Fowler-Nordheim barrier subject to a sinusoidal field with oscillation frequency f, the RMS value tunnel time is equal to

$$t_{\text{tun}} = \frac{w}{v_F} = \frac{\sqrt{m\Phi}}{eE}. \tag{7.15}$$

Note that half the oscillation period of the electric field is used for one direction of the tunneling current. The Keldysh parameter [217] is a dimensionless quantity obtained by multiplying the tunnel time by frequency to yield

$$\gamma_K = f \times t_{\text{tun}} = \frac{f\sqrt{m\Phi}}{eE}. \tag{7.16}$$

$\gamma_K \ll 1$ is known as the field emission or electrostatic regime where electrons have sufficient time to tunnel through the barrier within the oscillation period of the field. $\gamma_K \gg 1$ means the barrier is too wide for the electron to pass the barrier within the available time, thus multiphoton excitation is required to assist the electron over the

barrier. The Keldysh parameter can be interpreted as a scale between multiphoton excitation and field emission probabilities. A low γ_K can be achieved either by using low energy excitations or highly enhanced fields which is the case for THz incident fields on the STM junction where both factors are at play.

7.4.2 Tunneling gap conductance

Next we attempt to model the junction interface in hopes of utilizing it in a circuit. The tunneling barrier is often seen as a mega resistor where the current output is extremely small compared to the voltage input applied. With the help of preamplifiers in the electronics of STM instruments, they allow micro-, nano- and even pico-scale currents to be measured since they are required for the piezo-electric controller's sensitivity of the tip scan head over atomic-scale topographies of the sample. Thus it is reasonable to think of the tunneling gap as a resistive pathway with resistance R, or inversely conductance G. However, the proper way to map out tunneling currents with respect to applied biases is to calculate tunneling probabilities by using quantum mechanical or semi-classical approaches.

The metal-to-metal tunneling model should only consist of the density of states of the tip and sample and their barrier heights. Electrons can overcome the barrier height with an applied bias to either side of the junction or in the presence of an external background field. The equivalent circuit of the junction traditionally consists of a variable resistor (or conductance element) that depends on the tunneling parameters. Assuming the barrier heights are known quantities and the distance is constant, then the tunneling junction is a lumped element that functionalizes current with the applied bias. Sweeping the voltage across this element produces the I-V curve which is typically non-linear. It is possible to approximate the I-V curve with odd ordered polynomial expansion or by fitting the I-V curve measured experimentally with a series of functions. The variable tunneling resistance is given as

$$R_T = k_R V_b^{-p},\tag{7.17}$$

where p is a power obtained from a power-law fitting a section of the I-V curve, k_R is a calibration constant that would give the tunneling current at a particular set-point value at a particular value of V_b. The transient tunneling current as a function of the bias is an Ohmic expression given by

$$I_T(t) = \frac{V_b(t)}{R_T(V_b(t))}. \tag{7.18}$$

The I-V relation is symmetric from this expression. Actual I-V's for metal-metal tunneling takes into account fuller forms for the density of states of actual metals [224–226].

Metal-to-metal tunneling in a THz near-field environment adds more variables such as the skin depth or local THz conductivity [227–230] and high near-field effects like electron emission occur [71, 74, 202, 231, 232].

7.4.3 Junction Capacitance

The tunneling junction I-V is traditionally viewed as a non-linear conductance that maps voltage to current. The tunneling signal is thought to be measured as a consequence of direct tunneling. However, when electrons transfer from tip to sample or vice versa, the presence of charge on one side of the interface influences the tunneling of the next electrons, which leads to the discussion of space-charge effects [233–237]. Traditionally in a simple junction circuit model, the tunneling current is in phase with the applied field. However the buildup of charges and currents on the tip and sample during live tunneling generates inductive and capacitive effects that makes the tunneling junction more complicated.

Space charge layer can be interpreted as the Helmholtz Capacitance given by [223]

$$C = \frac{\epsilon_t \epsilon_0}{d} = \frac{q}{\Delta \phi_H}, \tag{7.19}$$

where $\Delta \phi_H$ is the potential difference across the junction. The tunneling capacitance is not to be equated to the geometric capacitance between the tip and sample [238,

239]. The tunneling junction is a mesoscopic system, so the capacitance is orders of magnitudes smaller than the geometric capacitance (in the range aF compared to fF). Detailed formalism for the mesoscopic capacitance is presented in various reports [234, 240–247].

Due to the discrete description in quantum mechanics, current through a tunnel junction is the accumulation of events where exactly one electron tunnels through the tunnel barrier. The tunnel junction capacitor is charged with one elementary charge by the tunneling electron, producing a unit voltage $V = e/C$. A large accumulation of voltage can be accomplished by many tunneling electrons or if C is small, which consequently prevents the next electron from tunneling. The electric current becomes suppressed, causing the Coulomb blockade effect.

Eq. 7.19 is equivalent to the conventional $Q = CV$, however in here, we are dealing with time-dependent quantities. The circuit components gets charged or discharged and the bias changes throughout. Just as the tip can have inductive, resistive and capacitive components, the same applies to the sample. The overall circuit is shown in Fig. 7.6. The tip and sample still share the same geometric capacitance while the tunneling junction element is shown in parallel with the capacitance.
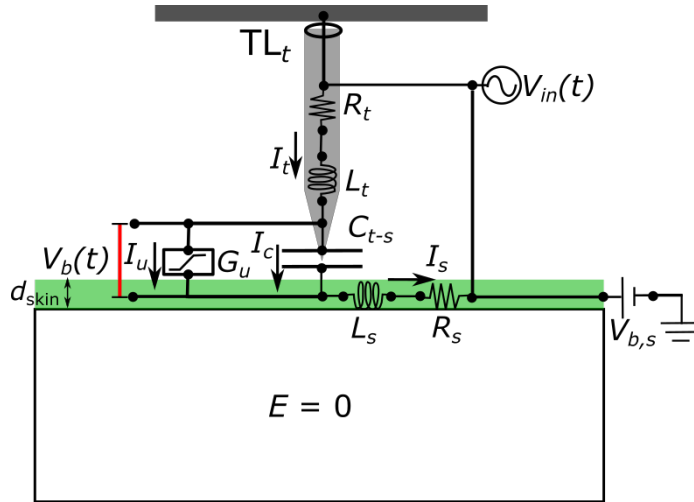
Figure 7.6: Circuit diagram and schematics for a metal-to-metal interface.

Lumping the tip and sample elements simplifies the circuit as shown in Fig. 7.7.

This circuit representation allows the transfer function method outlined in Chapter 6 to be applied to obtain all the voltage and current values versus time at circuit element.
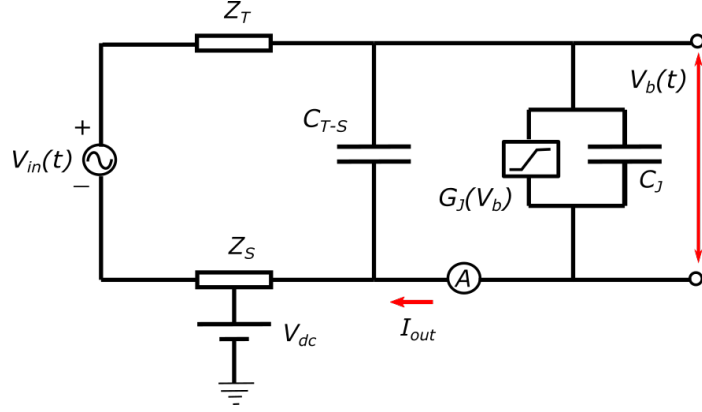
Figure 7.7: Full circuit diagram where the tip and sample elements are lumped impedance elements and the tunneling junction is a conductance and capacitor.

The tunneling junction is modeled as conductance element which gives the direct tunneling current in parallel with a tunneling capacitance. The junction is simplified to an admittance element as shown in Fig. 7.8. The inputted bias voltage transient, $V_{NF}(t)$, is obtained from calculating the near-field voltage, without the influence of the junction where only the tip and sample impedances are taken into consideration. Note that the effects of the junction is extremely small to perturb the calculation of V_b, so it can be assumed that the gap voltage transient, $V_{NF}(t)$, that results from the macro circuit consisting of the tip, sample and gap capacitance is used to bias the tunneling junction in addition to the external d.c. bias.

Tunneling currents can have a direct and out-of-phase component with respect to the voltage biasing the junction. Figs. 7.9 and 7.12 show the resulting tunneling current when the capacitance grows beyond the magnitude of the conductance.

Now we allow the tunneling conductance (real part of admittance) to vary as a function of the voltage bias transient and combine it with the capacitance term (imaginary part) to produce I-V curves as shown in Figs. 7.10 and 7.11. The transient conductance in Fig. 7.10 (or inversely, its corresponding resistance) is produced using

224

(a)   (b)
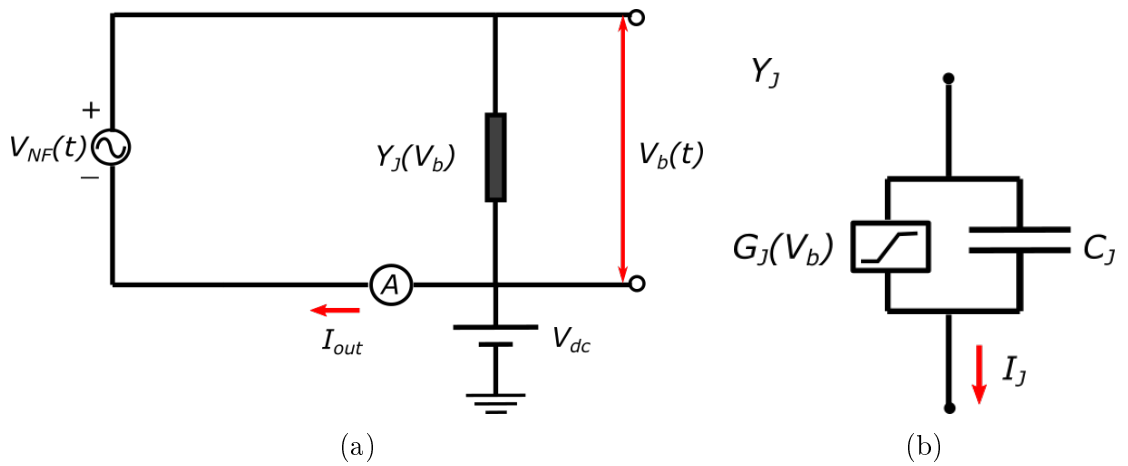
Figure 7.8: (a) A simplified circuit where the junction is compressed into a single admittance lumped element and is biased by the near-field voltage. (b) The lumped admittance where the junction is a conductance element in parallel with a capacitor.
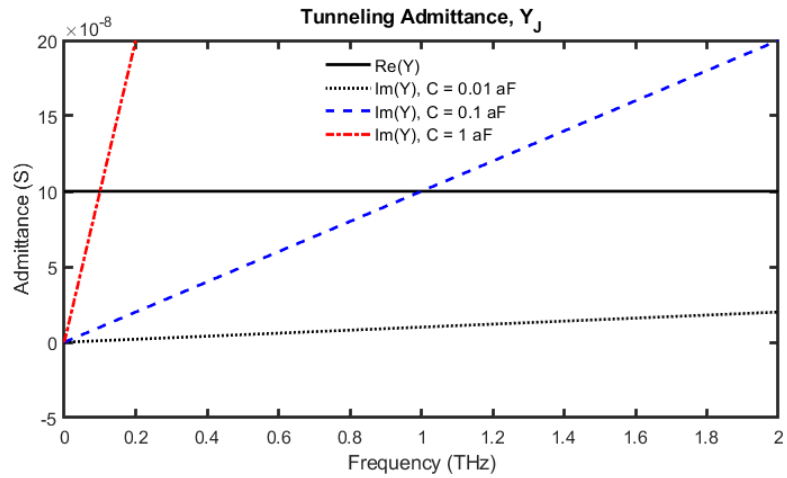
Figure 7.9: Plots of the real and imaginary components of the tunneling admittance where $G = 1\,\mu S$, and varying tunnel capacitance at $C = 0.01$ aF $C = 0.1$ aF and $C = 1$ aF.

the variable non-linear resistor in Eq. 7.17. The times where the bias peaks due to the applied field is where the conductance rise or where the resistance drops, hence allowing for a conduction pathway that produces a measurable current transient.
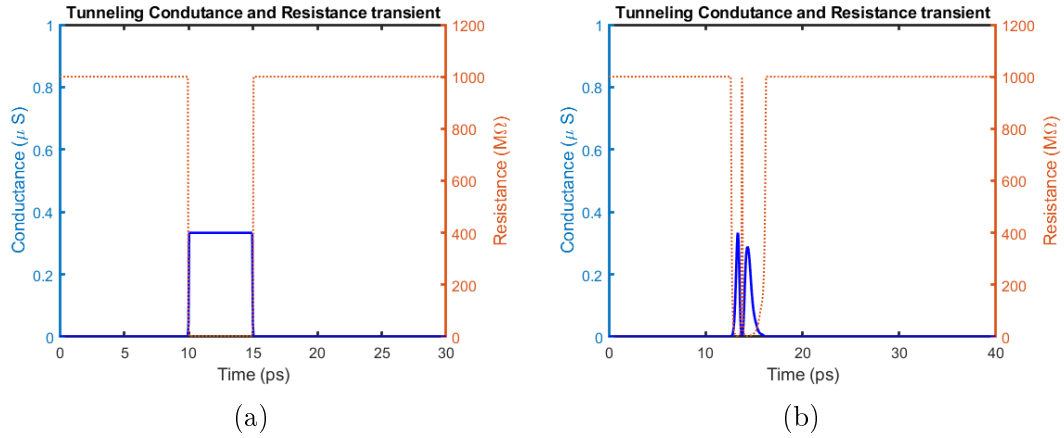
Figure 7.10: Conductance transient produced by sweeping the tunneling junction with a (a) box pulse and (b) THz pulse.

The I-V becomes non-linear beyond 1 V bias in either direction and the voltage amplitude from the NF THz pulses are usually large due to field enhancement. The combination of these two leads to the generation of rectified tunneling current which is orders of magnitude larger than the standard STM tunneling current as shown in Fig. 7.11(b), which can be factors of 100 and beyond.

All of this can be combined to produce tunneling current transients as shown in Fig. 7.12 where the junction admittance is varied using capacitances ranging over a few orders of magnitude. In general, when there is no d.c. bias, the V_b waveform usually follows that of the simulated near-field V_{NF}, and is used as an input to generate the current transient in the tunneling branch.

In 7.12(c), the current waveforms are normalized for shape comparison. As the junction capacitance increase, the out-of-phase current component which resembles the derivative of the junction near-field becomes more prominent.

(a)　　　　　　　　　　　　　　　　　　(b)
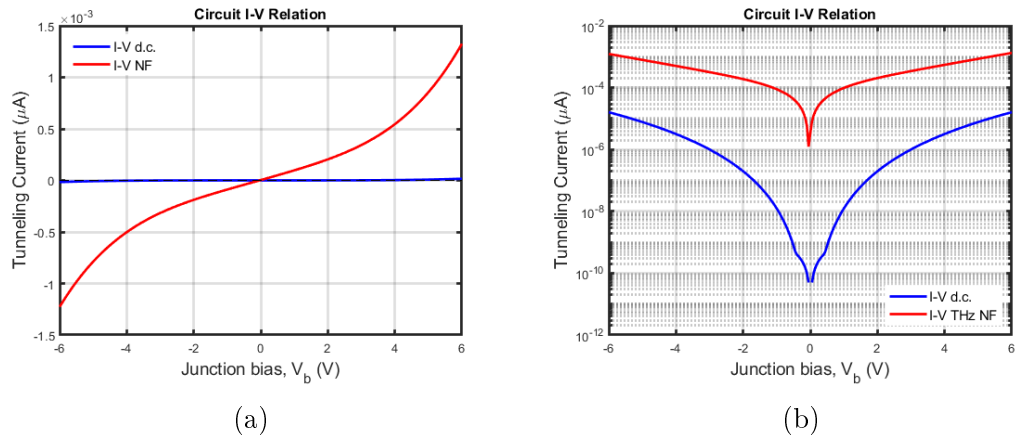
Figure 7.11: (a) Tunneling IV curve produced on a tunneling junction using a variable conductance function and $C = 0.1$ aF (blue). The x-axis is the d.c. bias on the junction. The IV is plotted where a THz pulse of 3 V peak amplitude is added to the constant bias $V_{d.c.}$. (b) Plots the absolute value of current in log scale to show the THz pulse rectification of the IV curve by a few orders of magnitude.
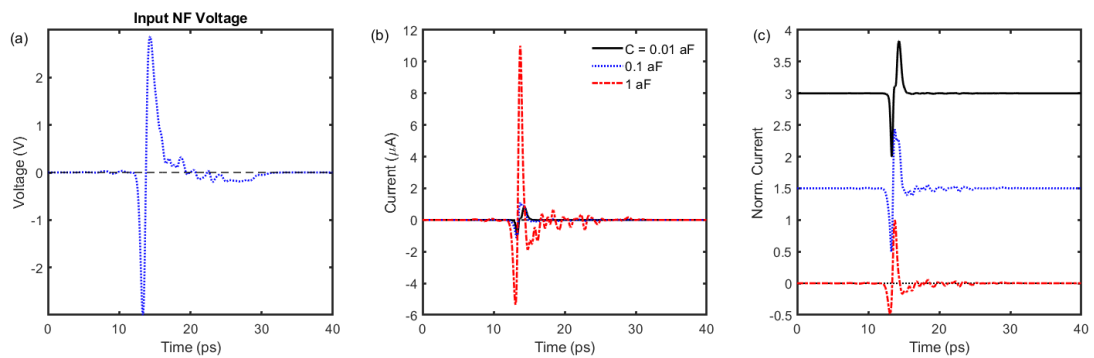
Figure 7.12: Tunneling current waveforms for (a) $C = 0.01$ aF, (b) $C = 0.1$ aF and (c) $C = 1$ aF, which illustrates how the transient tunneling waveform can evolve as the junction capacitance increases. Conductance $G = 1\,\mu S$.

7.5   Internal Fields

STM studies on semiconductors have measured tunneling current that must come from below the surface of the sample [248–251]. The driving electric field continues beyond the sample surface nanometers deep into the bulk of the sample to be able to cause band bending and modify the apparent barrier height so that bulk electrons are contributing to the overall tunneling [252–254].

Simulations show that part of the near-field extends into the sample region. The internal field is penetrated near-field below the sample surface. A voltage-divider method is used to obtain the residual voltage in the sample part of the junction circuit. The sample is assigned an impedance based on the volume of the conducting region. The residual voltage is the product of the resulting tunneling current and impedance. It is possible to get the derivative of the input NF waveform when the junction capacitance dominates in the tunneling signal generation. In Fig. 7.13, even when the input to the junction resembles the near-field form (i.e. integral of the incident THz pulse), the output voltage waveform calculated using the divider method waveform ends up resembling the derivative of the near-field waveform.

A measurable d.c. current of 1 nA corresponds to about 1 tunneling electron for every 160 ps, thus the timescale for non-equilibrium charging of the semiconductor is on the order of 100 ps. The THz-STM is able to probe extremely fast non-equilibrium tunneling currents at high charging and discharging rates over sub-picosecond timescales, which is faster than the rate of electron transport between surface and bulk states.

Fig. 7.14 show the sample voltage transients as the tunneling capacitance varies using the full nearfield waveform from COMSOL simulations to bias the non-linear tunneling junction modeled as varying admittance. The waveform evolves to the derivative form as the capacitance increases.

It will later be shown that the internal field is the one that influences the majority
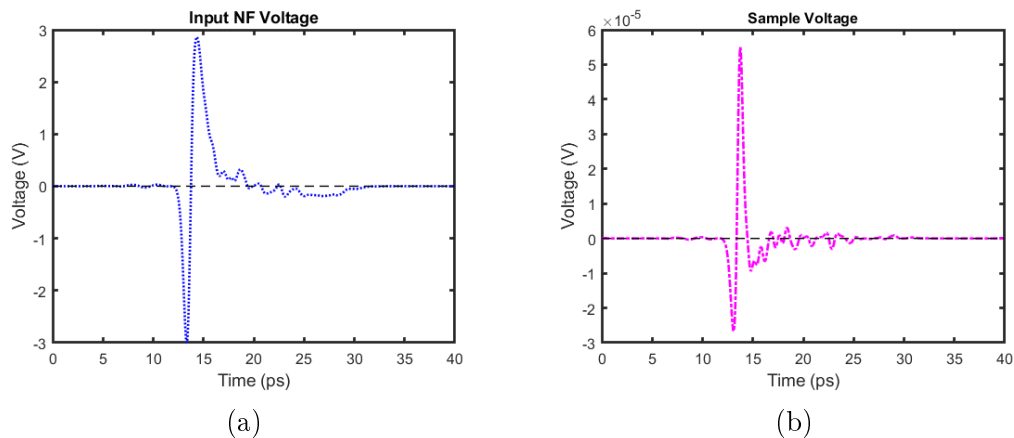
Figure 7.13: (a) Input nearfield voltage corresponding to the near-field around the tip apex. (b) Sample driving voltage corresponding to the penetration field in the sample. The variable conductance is used for the tunneling junction and $C_J = 1$ fF.
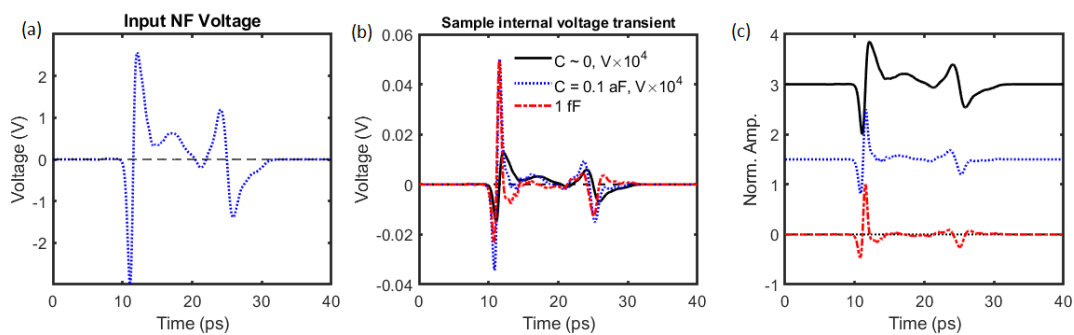
Figure 7.14: Using the full nearfield voltage waveform from simulations as the input, the calculated voltage at the sample node when (a) $(C \to 0)$, (b) $C = 0.1$ aF and (c) $C = 1$ fF.

carriers. If the system was one electron tunneling in the junction, then the field influencing the lone electron would be the enhanced near-field. When other electrons are present, there is a Coulomb blockade effect. If the tunneling electron senses the presence of other electrons, then there would be a Coulomb potential that could hinder the tunneling process. Thus when near-fields with a.c. components are present, electrons slosh around within the junction rather than undergo direct tunneling. The tunneling current would actually have a phase dependence due to contribution by the tunneling capacitance. In the STM, the tip and sample are grounded to the chassis of the chamber. Eventually the STM circuit would discharge any remnant charges within the milliscond STM operating time scales. Within a THz pulse cycle, which is much quicker in the grand scheme, tunneling currents and charge build-up occur before the junction can be discharged long after.

7.6 Metal to semiconductor tunneling

Early models postulated for the metal-semiconductor rectifying junction [151, 154, 155, 214, 215] are useful for developing the theory for THz-STM. The metal to semiconductor junction is complex because electrons can tunnel via multiple avenues.

In normal STM of semiconductors, bulk states are usually excluded from directly contributing to the tunnel current due to the subsurface depletion region and their metallic surfaces that screens external electric fields. However, the screening occurs for external d.c. and low frequency fields. For semiconductors like Si(111)-(7×7), the conductivity is lower at higher frequencies such as in the THz regime. Lower conductivity results in a poorer screen for external electric fields. The poor conductivity of the semiconductor surface in the THz regime cause external THz fields to penetrate through into the bulk, leading to THz-pulse-induced banding banding in the subsurface depletion layer. The penetrated field induces transport between the surface and the bulk, hence providing a pathway for the bulk contributions to tunneling in the junction.

In addition to the standard metal-metal tunneling barrier, the Schottky barrier is a parameter to be factored into THz-STM. Tunneling is contributed by carriers in both the surface and bulk [147, 222, 255, 256]. Tip-induced band bending occurs where the Fermi level of the semiconductor attempts to be pinned to the metal by bending the band energy levels towards the metal [257]. The band bending is illustrated in Fig. 7.15(a) for n-type semiconductors and Fig. 7.15(b) for p-type semiconductors. The transfer of charge or movement of electrons and holes in the junction interface creates a depletion layer quantified by the band bending voltage V_{bb}.
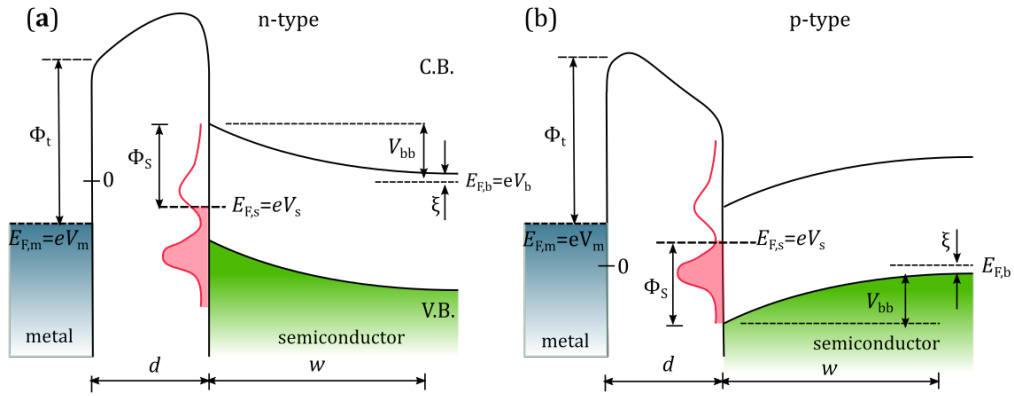
Figure 7.15: Metal-semiconductor energy band diagrams shown for (a) n-type and (b) p-type semiconductor.

STM experiments on semiconductors to collect I-V relations help determine the components of the semiconductor band structure that contribute the tunneling current. The Schottky barrier, band-bending, depletion width can be quantified. The temporal dependence of tunneling currents are measured in light-wave STM on semiconductors [258–275]. Such experiments motivate further modeling for interpreting the time-dependence of the tunnel currents [165, 213, 276–281]. Equivalent circuit models were also developed to fit the tunneling current signals.

7.6.1 Circuit model for the Schottky barrier junction

The circuit model is further expanded to deal with the metal tip and semiconductor junction case. According to the diagram in Fig. 7.15, the junction consists of the

interacting regions between the metal tip and the sample surface states, and the sample surface states with the sample bulk. There are multiple Fermi levels for each entity which do not necessarily have to be equal to each other, especially if the applied bias is non-steady. The equivalent circuit for a Schottky barrier junction is shown in Fig. 7.16 and simplified in Fig. 7.17. The tunnel barrier capacitance between the surface and the tip is simplified as a 1D parameter determined by the tip-sample separation d:

$$C_t = \frac{\epsilon_0 \epsilon_t}{d}, \tag{7.20}$$

where ϵ_t is the relative permittivity of the tip.
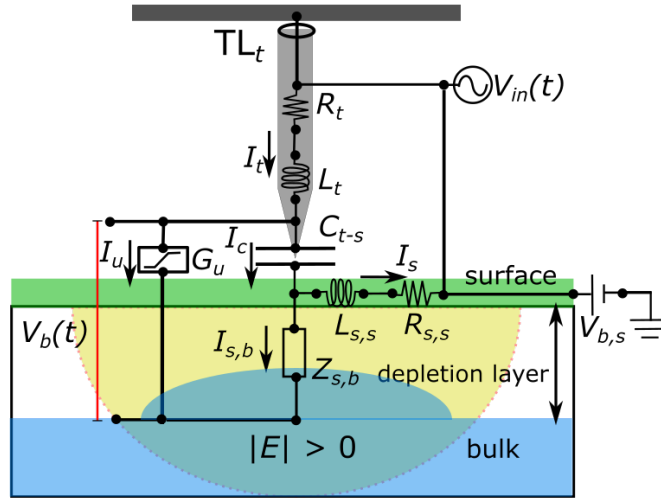
Figure 7.16: Circuit diagram and schematics for a metal-to-semiconductor interface.

Capacitance of a Schottky barrier is associated with the modification of the depth of the space charge region upon change of band bending. For a density of space charge N, the space charge capacitance is given by

$$C_{\text{S.C.}} = \frac{\epsilon_0 \epsilon_s}{\ell} \tag{7.21}$$

where ϵ_s is the relative permittivity of the sample and the space charge width is $\ell = \sqrt{2\epsilon_0 \epsilon_s V_b / eN}$. The space-charge capacitance is contained within the bulk of the sample, thus we can reassign the sample capacitance to the same parameter, $C_s = C_{\text{S.C.}}$.
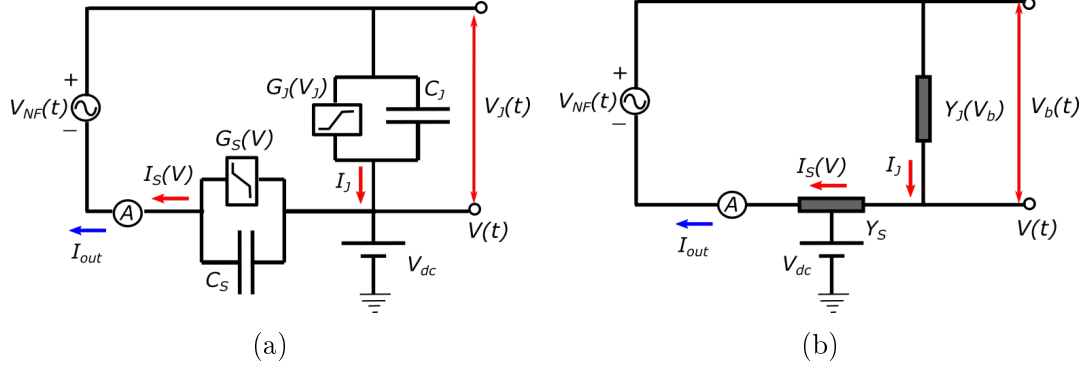
Figure 7.17: (a) Full equivalent circuit diagrams for the metal-semiconductor interface. (b) Simplified circuit diagram using admittance elements. The readout current is influenced by the lumped elements of the tip and sample junctions.

Overall, the circuit elements can be combined to create a set of differential equations that has to be solved in order to map out the voltage and current transients across each element. The junction contains two interfaces to deal with: the region between the tip and the sample surface and the depletion region consisting of the sample bulk connected to the sample surface. The tunneling junction circuit model adds in admittance parameters for the sample, G_S and C_S. The following differential equation must be solved for the intermediate voltage $V(t)$ between the tip and sample bulk interfaces.

$$(C_S + C_T)\frac{dV}{dt} + [G_S(t) + G_J]V = C_T\frac{dV_{in}}{dt} + G_J V_{in} \qquad (7.22)$$

The equation above can be rewritten as

$$\frac{dV}{dt} + a(t)V = b(t) \qquad (7.23)$$

where the solution has an integrable form given as

$$V(t) = e^{-A(t)}H(t). \qquad (7.24)$$

The integrable factors are

$$A(t) = \int_0^t a(t')dt' \qquad (7.25)$$

$$H(t) = \int_0^t b(t')e^{A(t')}dt'. \qquad (7.26)$$

233

The measured signal is the correlation current given as

$$I_{out} = \frac{1}{T} \int_0^T G_S(t')V(t',\tau)dt'. \tag{7.27}$$

where T is the period of the sampling repetition rate and τ is a delay time between the peak of the junction excitation and the peak of the probing pulse.

Fig. 7.18 utilizes Eq. 7.6 to generate the plot of the I-V profiles for the steady-state biasing. One can see that Schottky tunneling is orders of magnitude larger than standard tunneling. The pool of carriers that can contribute to the overall current mainly comes from the bulk of the semiconductor.
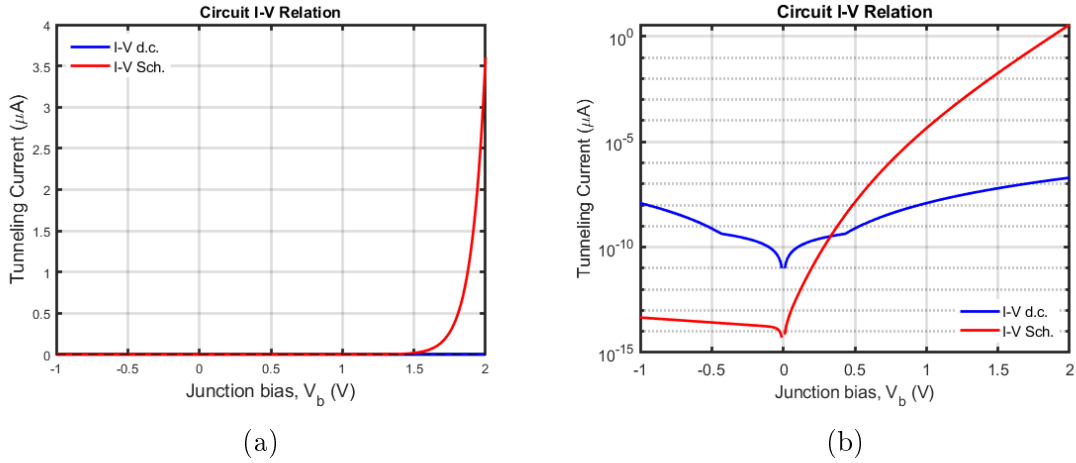
Figure 7.18: Calculated Schottky IV curve vs normal tunneling (b) Compares magnitude in log scale.

In the transient case where the applied bias is a THz pulse with peak incident electric field amplitude E_{pk} calibrated to V_{pk}, the rectified current is shown in Fig. 7.19 with the corresponding electron count. Note that the steady state STM I-V is subtracted out to get the rectified response in the calculation. The electron count or current contribution scales up to 10^4 electrons per THz pulse and produces extreme current measurements in the μA at strong THz fields.

Non-equilibrium tunneling must be considered to model transport on semiconductors. Bulk electrons scatter on the surface and rapidly thermalize to a Fermi-Dirac distribution within 10s of femtoseconds before tunneling to the tip via surface states
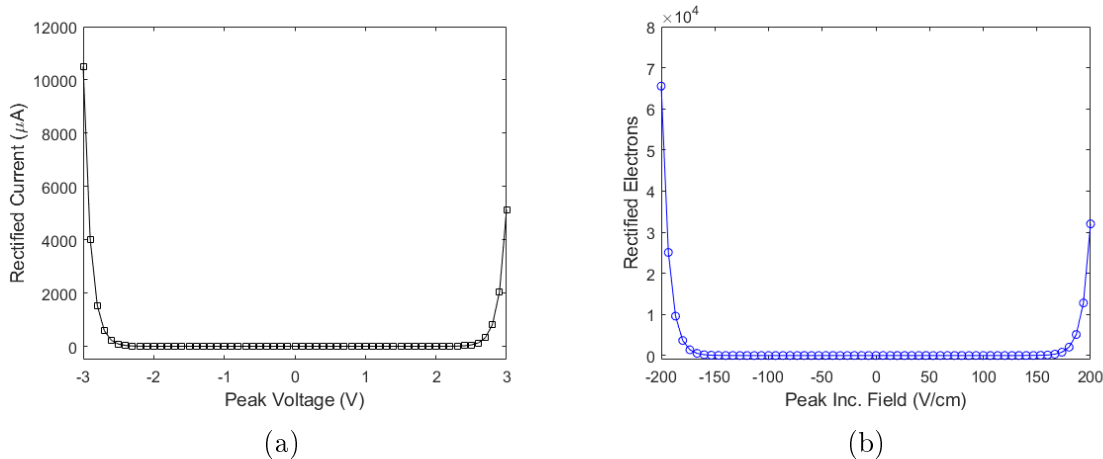
Figure 7.19: (a) Rectified current per THz pulse versus the peak of the nearfield THz voltage in a Schottky junction. (b) Corresponding rectified tunneling electrons versus the peak incident electric field.

around the Fermi level. In the reverse direction where electrons flow from tip to the sample, the subsurface layer is in depletion, allowing charge to build up on the surface until the formation of an inversion layer and until the electric field becomes strong enough to tunnel electrons directly into the sample's conduction band states. The THz-STM I-V characteristics is much different from the standard STM I-V due to the THz-pulse-induced band bending and ultrafast charging of the surface.

7.6.2 THz-STM currents on semiconductors

The step-by-step methodology for calculating the THz-STM signal consists of obtaining a THz voltage transient, sweeping the THz Tunneling I-V curve (or alternatively, convoluting with the conductance curve) to get the tunneling current transient and then integrating the current transient to obtain charge per THz pulse cycle. Lastly, the tunneling current vs peak THz voltage amplitude is a curve of interest and depends greatly on the shape of the THz voltage waveform as well as the I-V curve.

The THz induced tunneling current can be processed by inputting the near-field voltage waveforms generated by simulations. In this case, the sample driving voltage waveform is used as shown in Fig. 7.13(b), which corresponds to the simulated

near-field pulse in the penetration region of the sample bulk. The waveform has a peak amplitude of 3.2 V. The appropriate pulse for tunneling calculations must be carefully selected. A few options are to use the incident field (see Fig. 7.20(a)), the near-field around the tip apex generated by near-field simulations (see Fig. 7.21(a)), or penetration near-field in the bulk of the sample from simulations (see Fig. 7.22(a)).

The tip-sample separation of 0.7 nm and the bias voltages are inputted into Bardeen tunneling equations to calculate the current-voltage (IV) behavior of the STM junction. Fig. 7.22(b) shows the normal STM IV curve (blue) and the THz IV curve (red). The THz-IV shows orders of magnitude increase in the tunneling current due to the additional input bias provided by the THz voltage waveform. A constant d.c. bias sweep where $V_b = V_{d.c.}$ forms the STM IV. A THz driven STM junction where the total bias is the sum of the $V_{d.c.}$ and VTHz, yields current several orders of magnitude higher than a normal STM. The THz-induced conductance in Fig. 7.22(c), $G(V_b)$, is obtained by differentiation of the THz IV curve. G is the non-linear conductance element placed in parallel with the RLC components as it uses the same tip voltage to produce the tunneling current.

In Fig. 7.20(f), one can see that the incident THz pulse similar to the one measured by electro-optic sampling in the far-field of the THz source is a reasonable candidate to obtain a global fit of the THz current versus peak THz electric field curve.

Fig. 7.21(f) shows that the near-field transient around the tip apex determined by COMSOL and RLC simulations cannot succeed in producing tunneling transients that would yield the global THz I-E fit. In fact the THz current versus peak amplitude relation failed to change signs and only remained in the negative current region. Note that the peak of the pulse is at negative polarity, so the overall tunnel current waveform settles mostly in the negative. Fig. 7.19 shows a similar behaviour where the THz rectified current fails to change sign. Therefore, utilizing the THz waveform in the vicinity of the tip is not appropriate for generating a sequence of I-V, THz current transient and THz I-E plots due to the fact that semiconductors are not
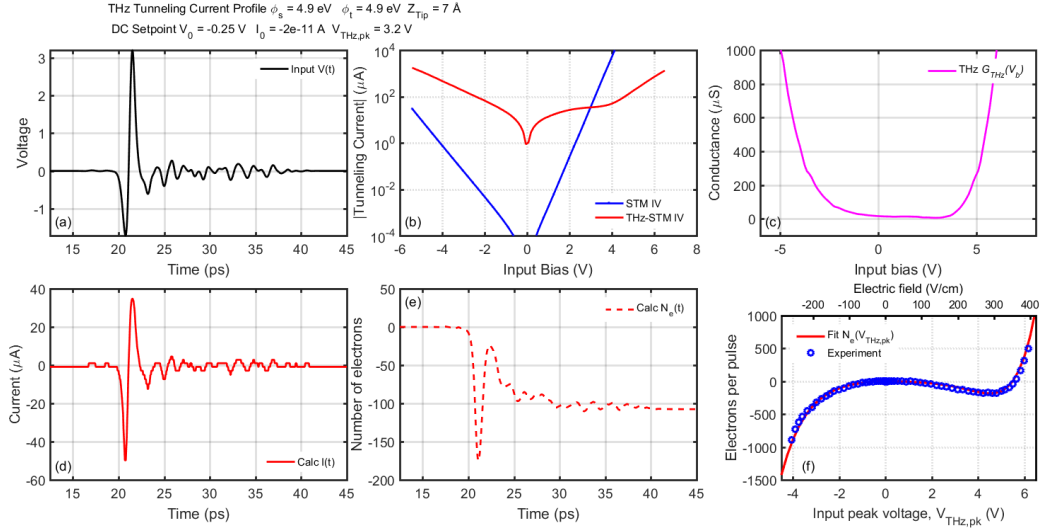
Figure 7.20: Tunneling profile calculation using the THz incident field waveform (a). (b) Simulated STM-I-V and THz I-V curves (adapted from [2]) where the tip-sample separation is 0.7 nm. The THz I-V curve is calculated by inputting the voltage waveform (a). The addition of the THz pulse provides orders of magnitude increase to the tunneling current. (c) The non-linear THz-driven conductance, $G(V_b)$, at the STM junction is obtained from differentiating the THz I-V curve in (b). (d) The calculated tunneling current waveform obtained by integrating the voltage waveform in (a) with conductance $G(V_b)$ in (c). (e) Integration of the tunneling current transients yields the net current at the end of the pulse cycle that is proportional to the number of rectified electrons per pulse. (f) The electron yield per pulse cycle versus the incident electric field, is the global THz I-E relation. Using the simulated waveform where the THz pulse propagates away from the port window produces a reasonable fit to the I-E curve in (g).

237
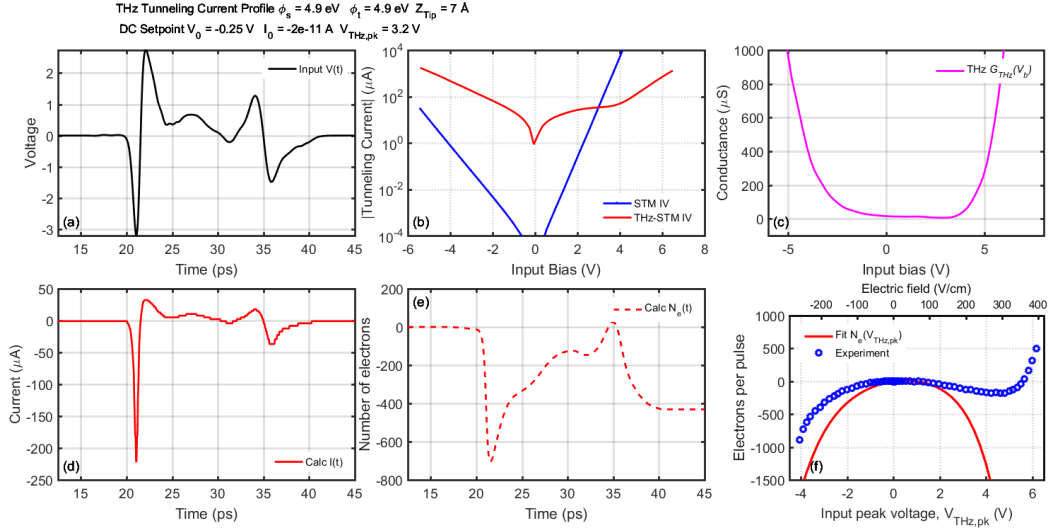
Figure 7.21: Tunneling profile calculation using the near-field waveform around the tip apex (a). (b) Simulated STM-I-V and THz I-V curves (adapted from [2]) where the tip-sample separation is 0.7 nm. The THz I-V curve is calculated by inputting the voltage waveform (a). The addition of the THz pulse provides orders of magnitude increase to the tunneling current. (c) The non-linear THz-driven conductance, $G(V_b)$, at the STM junction is obtained from differentiating the THz I-V curve in (b). (d) The calculated tunneling current waveform obtained by integrating the voltage waveform in (a) with conductance $G(V_b)$ in (c). (e) Integration of the tunneling current transients yields the net current at the end of the pulse cycle that is proportional to the number of rectified electrons per pulse. (f) The electron yield per pulse cycle versus the incident electric field, is the global THz I-E relation. The process shows how using the incorrect near-field waveform does not produce a reasonable I-E fit in (g).

sensitive to external fields outside of the material.

The figures show that fitting to the data requires a particular THz waveform that resembles the incident pulse. The bulk of the semiconductor does not sense any external electric field, not even the near-field in the gap between the tip and sample. Thus only penetrated electric fields can only drive bulk carriers. It turns out that the simulated nearfield waveform within the sample bulk coincidentally resembles the incident THz electric field instead of the field around the tip apex. The penetration field drives bulk electrons in the sample to produce the additional THz induced tunneling current. The THz voltage must be proportional to the driving electric field, which is indeed the pulse simulated below the sample surface. Hence, the tunneling current profile should be generated by using the gap voltage amplitude modulated by the penetration field waveform.

7.7 Metal and photoexcited semiconductor tunneling junction

For a photoconductor sample that is optically excitated and probed with a tip, the tunneling channels consist of surface to tip, the semiconductor bulk, and a population of photo-electrons created by the optical pulse as shown in Figs. 7.25. A circuit model for the photo-conductor tunneling interface such as GaAs or InAs systems in a pump-probe experiment is introduced in Fig. 7.25(b). The total current is a sum of the regular tunneling current and a photocurrent [282].

The model is a 3 electrode model consisting of metallic states for the tip, surface states and bulk bands for the sample. The tip-sample connection is a series circuit where the tunneling and Schottky interfaces are joined. The model takes into account both an incomplete screening of the electrostatic potential by the surface states as well as a current-induced voltage drop (i.e. drop of electrochemical potential) across the Schottky barrier, emulating a dynamic charging effect.

Photo-excited minority carriers are swept to the surface by the depletion field,
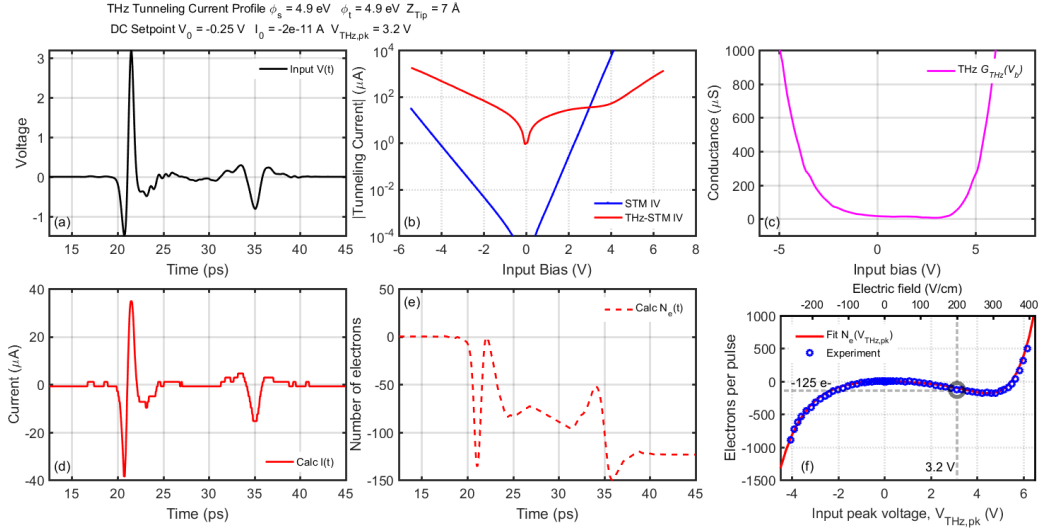
Figure 7.22: Tunneling profile calculation using the near-field waveform below the sample surface. THz tunneling current profile (STM set points: bias voltage $V_0 = -0.25V$; tunnel current $I_0 = -20pA$): (a) The simulated near-field waveform probed below the sample surface is converted to a voltage waveform peaking at $+3.2V$. (b) Simulated STM-I-V and THz I-V curves (adapted from [2]) where the tip-sample separation is 0.7 nm. The THz I-V curve is calculated by inputting the voltage waveform (a). The addition of the THz pulse provides orders of magnitude increase to the tunneling current. (c) The non-linear THz-driven conductance, $G(V_b)$, at the STM junction is obtained from differentiating the THz I-V curve in (b). (d) The calculated tunneling current waveform obtained by integrating the voltage waveform in (a) with conductance $G(V_b)$ in (c). (e) Integration of the tunneling current transients yields the net current at the end of the pulse cycle that is proportional to the number of rectified electrons per pulse. (f) The electron yield per pulse cycle versus the incident electric field, is the global THz I-E relation. Experimentally measured THz I-E data (circles) is fitted with the calculated THz I-E (red line). Dashed lines mark the single data point corresponding to plots (a) – (e). -125 electrons are yielded at the end of the pulse cycle when the reflection pulse is included in the near-field waveform.

240
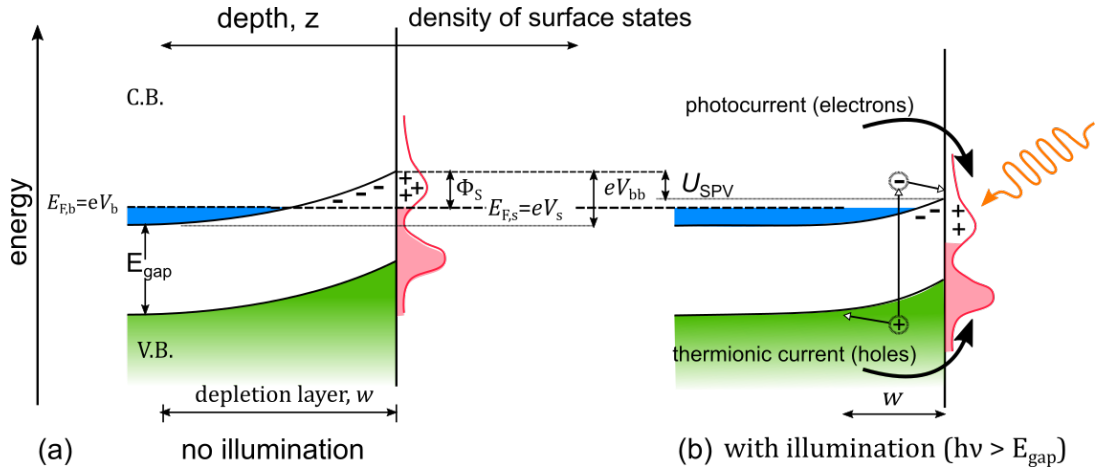
Figure 7.23: Band energy diagram for a photoconducting semiconductor (a) without illumination and (b) with photoexcitation. After photoexcitation, the depletion width decreases and the net change in the conduction band edge energy levels corresponds to the surface photovoltage.

constituting a subsurface photocurrent, I_p, and accumulate in the surface states. The change of the surface potential gives rise to a change in the Schottky current, I_S, which compensates for I_p, and thus change the tunneling current simultaneously. The surface photovoltage, V_{SPV}, is an additional voltage across the tunnel gap independent of the gap width.

If the Schottky barrier is strongly reversed biased, the tunneling conductance dominates and the surface potential adjusts itself so that I_t balances out with I_p. The system is driven away from thermal equilibrium and the subsurface potential is shifted by V_{SPV}. If a surface charge carries charge Q_{ss}, it is balanced by an opposite space charge in the depletion layer. Upon illumination where electron-hole pairs are created, the field inside the space charge layer separates the carrier pairs, which results in a minority carrier current flowing towards the surface. The surface charge gets reduced and so does the band-banding.

The photo-amperic regime is indepedent of gap width. Increasing the reverse bias leads to a slow increase of I_p. At higher voltages, there is a more efficient collection of photo-excited carriers. If the layer in which electron-hole pairs are created is thicker than the space charge region due to a weaker light absorption, a higher reverse bias

will cause the band banding to reach deeper into the semiconductor.

The full circuit for a metal and photoexcited semiconductor junction is the same as the before with the bare semiconductor, except we introduce optical excitation to create electron-hole pairs resulting in a SPV and photocurrent as shown in Fig. 7.24.
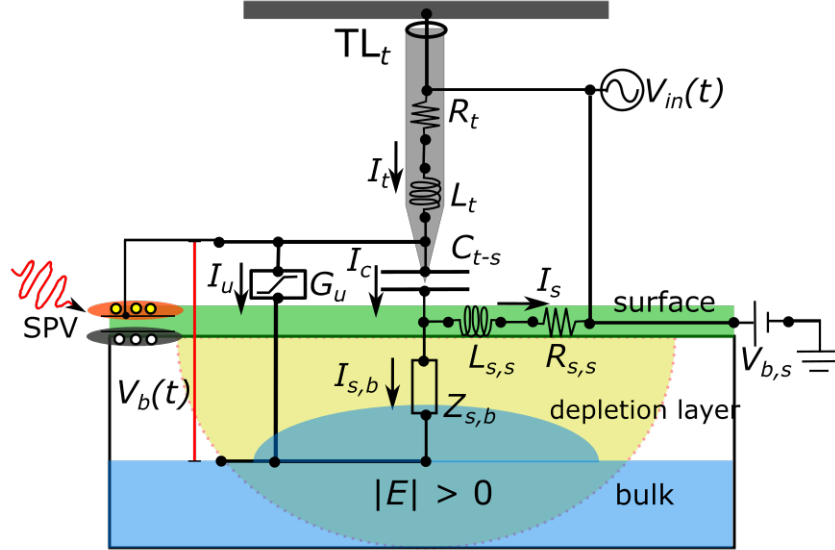
Figure 7.24: A metal-photoconducting semiconductor interface where the metal tip is situated above a photoconducting semiconducting sample such as GaAs.

The simplified circuit is shown in Fig. 7.25. The currents must balance out according to Kirchoff's Rule: $I_S = I_t + I_P$. The SPV is used to generate the photocurrent term I_P. The plot in Fig. 7.26 shows that the SPV is bias dependent.

The model introduces another branch for the surface photo voltage (SPV) to contribute to the current generation. There is a reduced barrier height due to the SPV [282–284]. Fig. 7.27 shows the modified Schottky IV curve when a photovoltage is present. At the low junction bias, the current shows a linear dependence. At the higher bias, the SPV influenced current converges with the Schottky curve.

In the next chapter, this model will be applied to fit sampled near-field waveforms using OPP-THz-STM on GaAs and other photo-conducting samples. IV curves are calculated and the tunneling signal is determined using lumped elements.

(a)   (b)
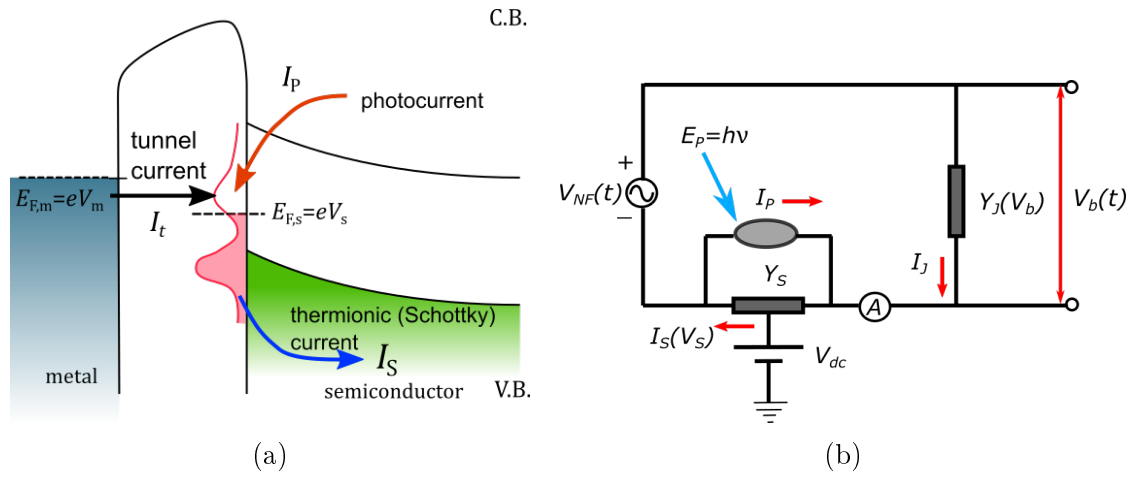
Figure 7.25: ((a) Band diagram of a metal and semiconductor interface showing the current flow in the junction. (b) Corresponding circuit diagram and schematics for a metal-to-photo-conducting semiconductor interface.
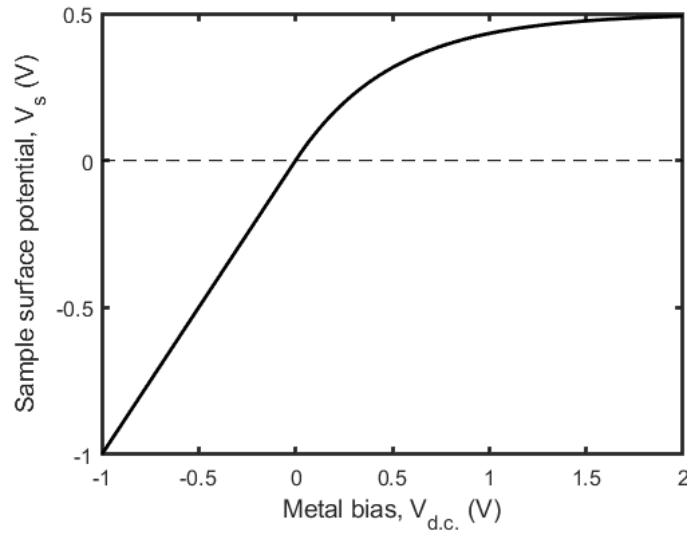
Figure 7.26: Calculated surface photo-voltage as a function of bias on the metal-photoconducting semiconductor interface.
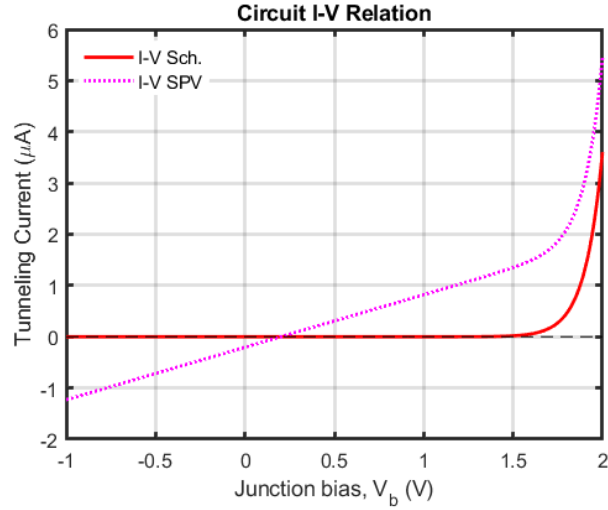
Figure 7.27: Calculated IV curve with Schottky current and photocurrent contributions. The negative bias regime, the current is linear due to the photocurrent. In the positive bias, at larger biases, the curve converges towards the Schottky current curve.

7.8 Chapter Summary

The process of using the the input bias voltage transient to calculate the tunneling current signal in THz-STM has been demonstrated. COMSOL simulations were used as a benchmark to convert THz electric field to a nearfield bias voltage. The internal penetration nearfield below the sample surface has been modeled using an expanded circuit model for the tunneling junction.

In a metal-to-metal junction, space charge effects is demonstrated using a tunneling admittance model. There is a both direct tunneling component and mesoscopic capacitive component.

In a metal-to-semiconductor junction, the circuit model for the junction is further expanded to consist of current contributions by tunneling between the tip and the sample surface and current between the bulk and surface.

Chapter 8

Sampling Near-field Transients with THz-STM

The THz-STM is a platform capable of controlling, characterizing and imaging ultra-fast non-equilibrium carrier transport on the atomic scale. Time-resolved mapping of the nearfield of the STM junction was accomplished recently using the THz-STM [23, 24, 39, 50, 51]. Here, time-resolved THz-STM imaging and spectroscopy of optically photoexcited semiconductors is demonstrated. The semiconductor samples presented here are GaAs(110) and InAs, however analysis is only performed for GaAs(110) which had a bigger data-set due to more experimental time spent and more emphasis to investigate the mechanisms of THz-STM on photoexcited semiconductors. The THz-induced tunnel current is locally enhanced by the optically induced surface photovoltage (SPV) occuring at charged defects. The SPV gets suppressed when the tip is positioned within a screening-length distance of the defect. When the THz field is perturbative, the tunneling of optically-excited carriers is linearly proportional with the field, which allows the THz pulse near-field to be photoconductively sampled. At strong THz field strengths, the field penetrates deeply into the sample and the resulting transient tunnel current response waveform have interesting transient structures which will be presented and analyzed in this chapter.

The circuit model for the photoconducting junction presented in the previous chapter is used to simulate and analyze THz near-fields measured by the THz-STM. Anal-

ysis and simulations will be performed on the results of unreported OPP-THz-STM experiments on GaAs(110) samples [133].

8.1 THz-STM to measure the near-field

THz-STM measurements were performed on optically excited n-type GaAs(110) surface. The relative time delay of the optical pulse with respect to the main peak of the THz pulse is scanned as the THz-pulse-induced tunnel current is measured. This technique is known as Optical pump THz-STM probe (OPP-THz-STM) as shown in Fig. 8.1.
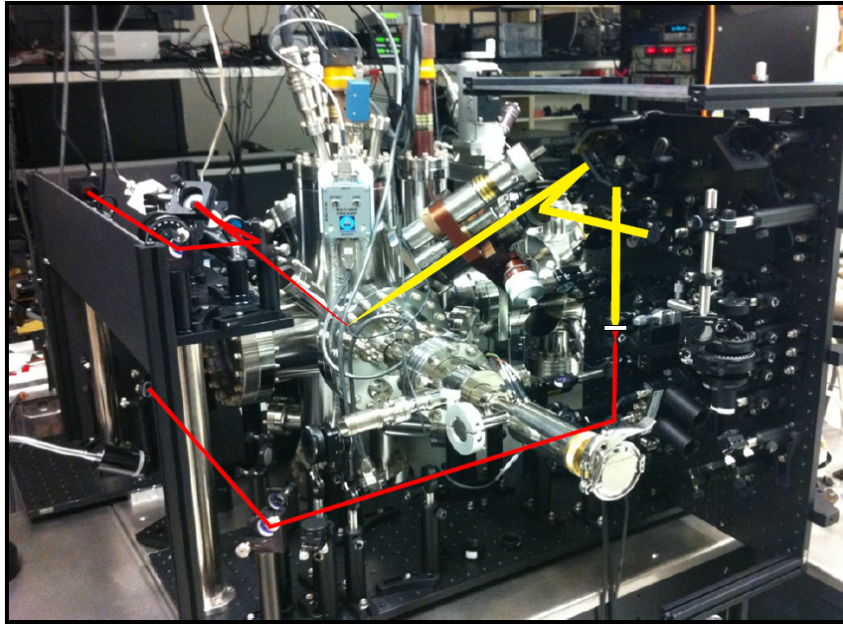
Figure 8.1: Photo and diagram of the OPP-THz-STM experiment. The yellow lines outline the directions of travel of the THz pulse through the optical bench setup into the STM window. The redlines outline the directions of travel of the optical pump pulse through the optical bench setup into another STM window. (Adapted from [133].)

Fig. 8.2 shows an example of an experimentally acquired THz-STM signal transient by optically exciting a GaAs sample and probing the photo-electrons with a THz pulse. Some features consist of near-field waveform shaping on the main pulse and a reflection pulse. The OPP-THz-STM waveform in Fig. 8.2 was acquired using a

sharp W tip on GaAs(110) surface. Its temporal profile was found to be quite similar to the waveforms from simulations presented in previous chapters where the main pulse of the waveform is broadened compared to the incident THz pulse followed by a series of reflection pulses. There are shifts in the carrier-envelope-phase (CEP) in the sampled pulse compared to the incident pulse measured by EO sampling due to propagation effects towards the STM junction and tip shape distortions [34].
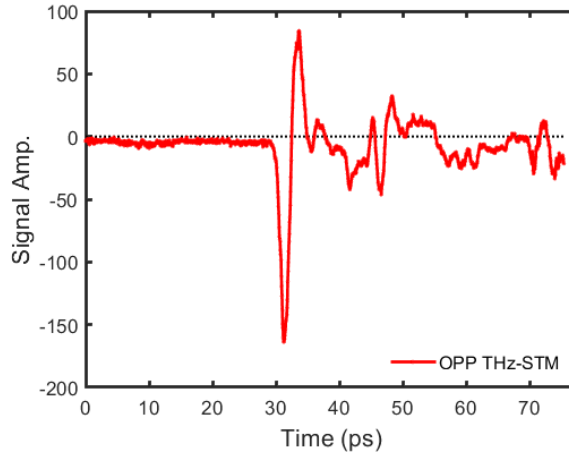
Figure 8.2: Near-field waveform sampling using the THz-STM showing features outputted by simulations. The broadened main peak from antenna coupling and reflection pulses from traveling SPPs. (Credit V. Jelic)

Fig. 8.3 compares the incident pulse, simulated near-field waveform to the experimentally sampled waveform via OPP-THz-STM. The temporal profile of the THz near-field closely resembles the time-integrated far-field THz waveform. The COMSOL electromagnetic simulations presented in Chapter 4 and summarized in Fig. 8.3(b) and (c) show that the THz near-field waveform around the tip apex is much different from the waveform inside the sample. The macroscopic tip shape modifies the CEP of the THz pulse near-field with respect to the far-field which is evident when comparing the phase of the reflection pulses (13 ps after the main pulse) in the simulation versus the experimentally sampled waveform using OPP-THz-STM on GaAs(110). CEP shifts can range from 0 to $\pi/2$ for typical STM tip shapes, which vary throughout day-to-day experiments. The amplitude spectrum shown in Fig.

8.3(c) shows significant differences between the sampled near-field and incident THz pulse. Spectral and phase shifts are caused by the dispersion of the THz pulse upon coupling to the metal-wire-antenna and then propagating to the tip apex.
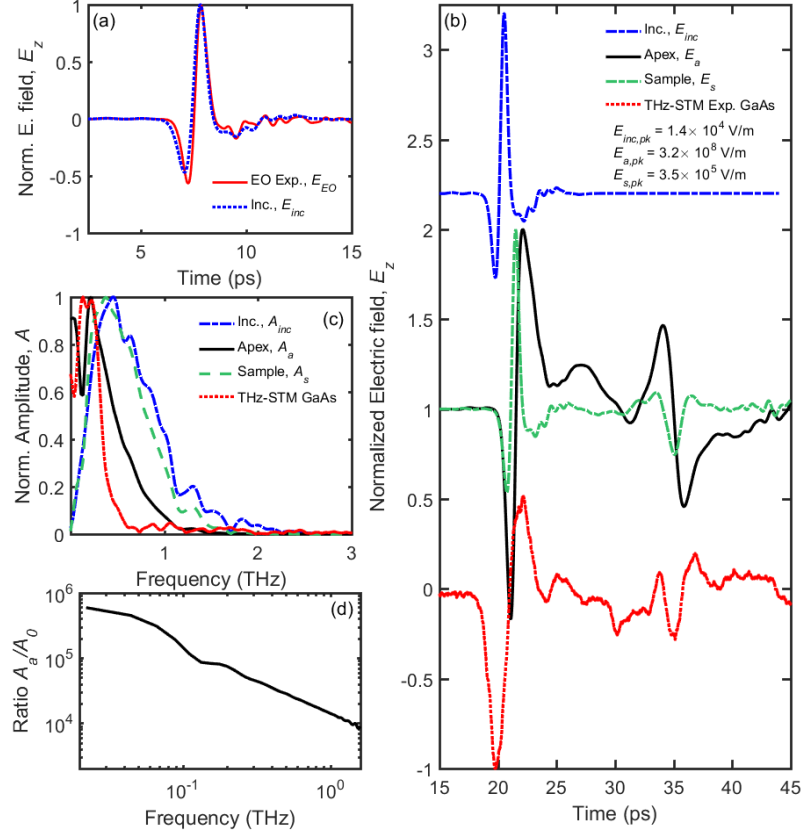
Figure 8.3: (a) The simulated incident pulse in the far-field propagating 4 mm from the port window compared with an experimentally measured pulse using electro-optic (EO) sampling. (b) The THz near-field pulse probed at the tip apex (black), and 2 nm below the sample surface (green) plotted with the simulated incident pulse (blue dash). The pulses are normalized to their peak amplitude. Their actual peak amplitudes of the apex pulse and the incident pulse are annotated. Experimentally sampled waveform corresponding to the near-field in the gap (red) from Fig. 8.2. (c) Corresponding frequency spectra for the near-field pulses with normalized amplitudes. The experimental EO spectrum (blue) is shown for reference. (d) The amplitude of the apex near-field spectrum divided by the amplitude of the incident spectrum which gives the field enhancement factor as a function of frequency.

Fig. 8.3 shows the simulated nearfield in the junction in comparison to the experimental data in Fig. 8.2. Remarkably, both waveforms show the same features such as the shelf after the main pulse and the reflection pulse at the same waveform peak

times, as shown in Fig. 8.3. The simulation and experimental waveforms are not an exact match when overlapped. Especially with the different phases traced out by the reflection pulse where the simulation follows a sine curve while the experimental trace follows a cosine curve.

In Fig. 8.3(b), the comparison of the simulated near-field waveform (black solid) and experimental data (red) highlights that the transient near-field actually resemble these waveforms. Pulse broadening due to the THz-antenna coupling, tip shape distortions and propagation/reflection of SPPs are actual contributors to the near-field formation, which is remarkably predicted by the full-scale THz-STM FEM simulations. The waveform features shown for the experimentally sampled near-field waveform in Fig. 8.2 validates all the time-dependent features predicted by simulations.

8.2   The photoexcited metal-semiconductor interface

Now we revisit the junction consisting of metal and the photoexcited semiconductor interface. Fig. 8.4 presents the band bending and carrier dynamics under a transient bias supplied by the enhanced THz field that couples to the junction. In this scenario, the surface photovoltage V_{SPV} contributes to the transport dynamics in the metal and photoexcited semiconductor interface. In the non-equilibrium transport scenario, we consider the Fermi levels of the tip, sample surface and sample bulk given by $\epsilon_{\mathrm{F,tip}}$, $\epsilon_{\mathrm{F,S}}$, and $\epsilon_{\mathrm{F,B}}$, respectively. The relationship between the biases and Fermi levels are given by

$$eV_{\mathrm{d.c.}} + eV_{\mathrm{THz}}(t) = \epsilon_{\mathrm{F,tip}} - \epsilon_{\mathrm{F,B}} \tag{8.1}$$

$$\epsilon_{\mathrm{F,S}} = \epsilon_{\mathrm{F,B}} - eV_{\mathrm{SPV}}(t - \tau, I_{\mathrm{THz}}). \tag{8.2}$$

We revisit the band diagram in Fig. 7.23, circuit in Fig. 7.24 and circuit in Fig. 7.25a(b). The discussion here attempts to describe the transport effects in the metal and photoexcited semiconductor interface. We will make an attempt to simplify the
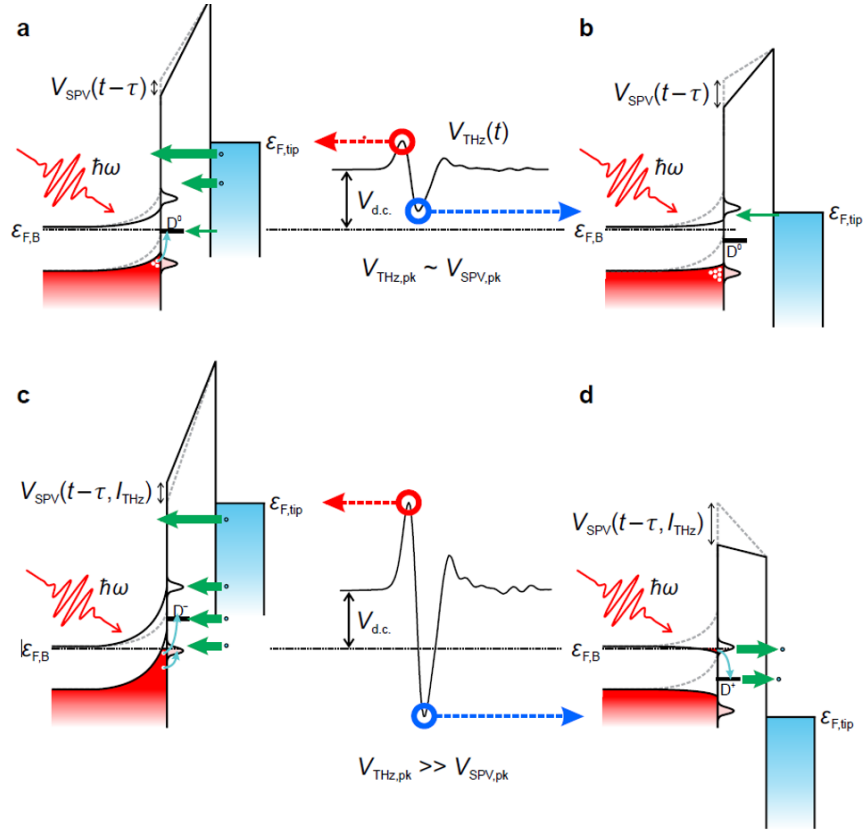
Figure 8.4: Tunneling and band bending diagram for the semiconducting tunneling interface with the THz electric field combined with the bias. (a) and (b) shows the case of the weak-field regime for small THz fields under reverse and forward bias conditions, respectively. In the same bias conditions as before, (c) and (d) shows the case for the strong-field regime using large amplitude THz fields. The two small Gaussians represent the intrinsic surface states for the GaAs(110) sample, while a solid black bar represents the extrinsic in-gap surface state also known as defect centers. The dashed grey lines show the change in the band-bending due to the transient THz-current-modified surface photovoltage. Green arrows indicate the direction of electron tunneling, while teal arrows indicate the non-equilibrium transport of electrons and holes through the surface states. (Credit V. Jelic [133])

carrier transport in the junction under steady-state and transient biases towards a circuit model. The metallic-like surface screens the external field, which also applies to THz frequencies. The bulk is unaffected by the external field when there is effective screening.

The model is a 3 electrode model consisting of metallic states for the tip, surface states and bulk bands for the sample. The tip-sample connection is a series circuit where the tunneling and Schottky interfaces are joined. The model takes into account both an incomplete screening of the electrostatic potential by the surface states as well as a current-induced voltage drop (i.e. drop of electrochemical potential) across the Schottky barrier, emulating a dynamic charging effect.

Photo-excited minority carriers are swept to the surface by the depletion field, constituting a subsurface photocurrent, I_p, and accumulate in the surface states. The change of the surface potential gives rise to a change in the Schottky current, I_S, which compensates for I_p, and thus changes the tunneling current simultaneously. The surface photovoltage, V_{SPV}, is an additional voltage across the tunnel gap independent of the gap width.

If the Schottky barrier is strongly reversed biased, the tunneling conductance dominates and the surface potential adjusts itself so that I_t balances out with I_p. The system is driven away from thermal equilibrium and the subsurface potential is shifted by V_{SPV}. If a surface charge carries charge Q_{ss}, it is balanced by an opposite space charge in the depletion layer. Upon illumination where electron-hole pairs are created, the field inside the space charge layer separates the carrier pairs, which results in a minority carrier current flowing towards the surface. The surface charge gets reduced and so does the band-banding.

The photo-amperic regime is indepedent of gap width. Increasing the reverse bias leads to a slow increase of I_p. At higher voltages, there is a more efficient collection of photo-excited carriers. If the layer in which electron-hole pairs are created is thicker than the space charge region due to a weaker light absorption, a higher reverse bias

will cause the band banding to reach deeper into the semiconductor.

8.3   Optical Pump THz-STM Probe on Semiconductors

This section presents a collection of THz-STM near-field waveforms for photoexcited semiconductor samples. Analysis and simulations are presented on the results of unreported OPP-THz-STM experiments on GaAs(110) samples [133]. A near-field waveform on InAs will be shown, however, it exhibits complex features that could not be analyzed using the same analysis method.

8.3.1   GaAs sampling

Fig. 8.5 show some waveforms obtained on GaAs at different THz field amplitudes. Fig. 8.6 shows an extended sampling where the polarity is switched. Switching the polarity of the input THz bias drastically changes the sampled THz-STM current waveform as if the dynamical behaviour of carriers in the sample is different when the THz field is positive or negative.

When the field is weak, the sampled current waveforms are nearly symmetric as seen in Fig. 8.6(a) and (c) where the input THz field strength is ± 60 V/cm and ± 25 V/cm. In Fig. 8.5(a), the waveforms are measured when the THz input has a negative polarity and (b) positive polarity with increasing strength. The waveform shapes are clearly defined with higher field strengths where the main pulse takes on the sine shape in Fig. 8.5(a) and cosine shape in (b).

8.3.2   Modeling pump-probe THz-STM

After photoexcitation, there is a temporal evolution of the free carrier population in the semiconductor. For simplicity, the transient carrier density is a free parameter approximated by a Gaussian centered around the Fermi level. Dynamic processes determine the evolution of the carrier energy distribution presented below in Eq. 8.3.
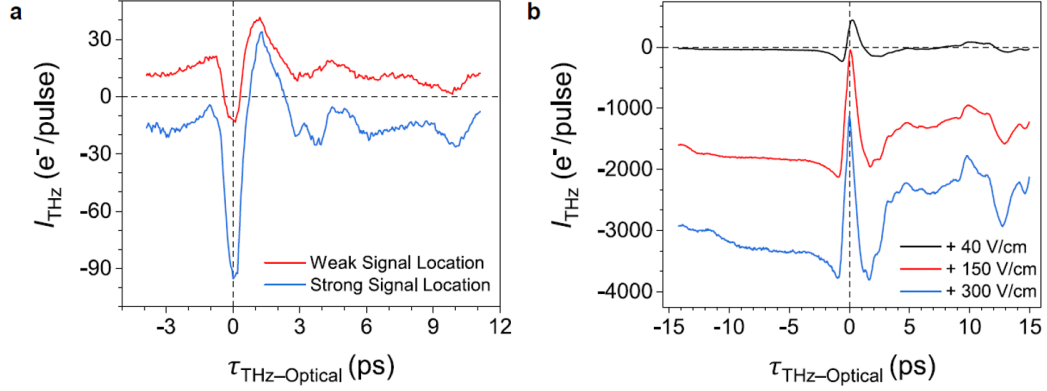
Figure 8.5: Sampled THz waveforms using OPP-THz-STM on GaAs (110). (a) The measurements were acquired at two different locations of the sample surface exhibiting a weak and strong signal. The sample bias is +2 V, total current setpoint is at +50 pA, optical pulse energy is 2.6 nJ and the peak THz pulse amplitude is $-120\,\mathrm{V/cm}$. (b) Waveforms are shown at a fixed location using various THz pulse field amplitudes. The sample bias is set to 0 V and optical pulse energy is 100 nJ. The STM feedback loop was disengaged after the tip-sample separation established equilibrium due to thermal expansion from the optical pulse. (Adapted from [133].)

The functional behaviour of the carrier population usually follows a rise and then a decay that can be fitted with decay constant, θ. The photoexcited free carrier population is quantified with the transient carrier density, $n(\epsilon, t)$.

The Bardeen model including the image potential effects presented in Chapter 3 is used to develop a model for transient photoconductivity due to the photoexcitation in the STM junction. There are several dynamic processes that determine the evolution of the transient carrier density. Waveforms generated by simulating THz-STM tunnel current transients using the model presented in Chapter 3 are generally characterized by an exponential decay curve with decay parameter, θ. The time and energy dependence of the photoexcited carriers is embedded in a transient function, $n(\epsilon, t)$. For a starting basis, the LDOS of the sample, $\rho_s(\epsilon)$, is assumed to be steady-state (i.e. has no time dependence). Thus the transient optical-pulse-induced term is the difference between $n(\epsilon, t)$ and $\rho_s(\epsilon)$.

The energy dependence is modeled to a first approximation as a Gaussian with amplitude, A_0, and standard deviation width σ, centered at ϵ_c with respect to ϵ_F of

253
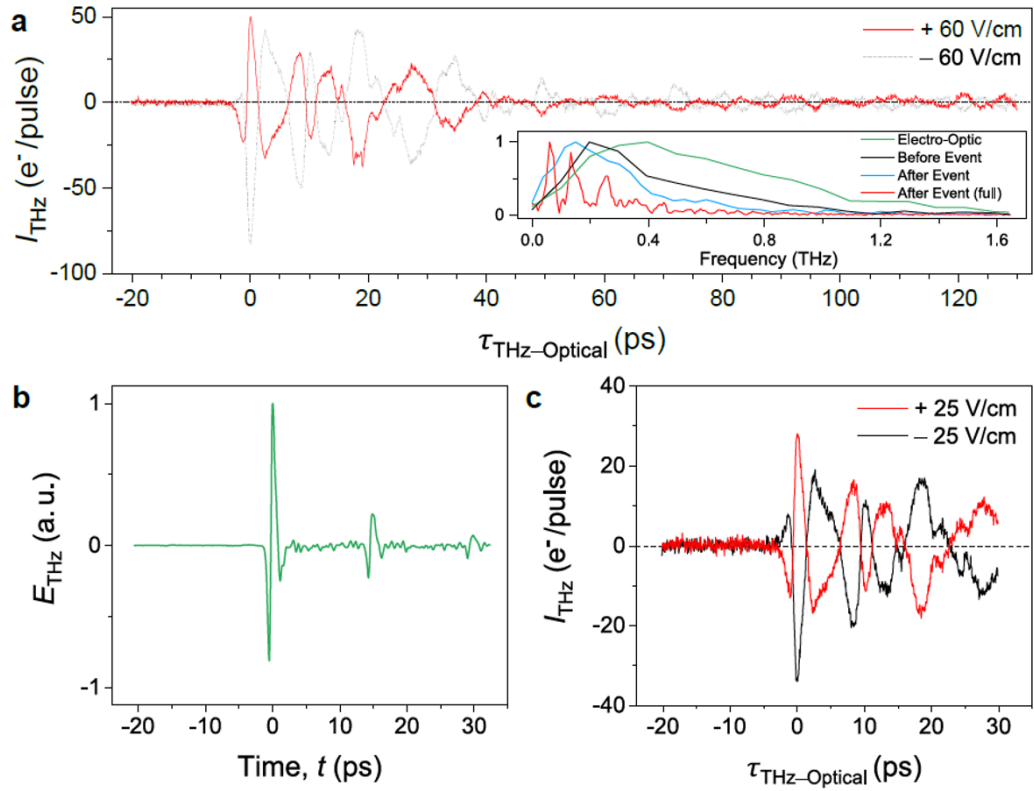
Figure 8.6: Near-field waveform sampling using the THz-STM on optically excited GaAs (110) sample. (a) OPP-THz-STM waveforms acquired using weak amplitude THz pulses of opposite polarities. The sample was biased at +2 V, total current setpoint is at +50 pA, optical pulse energy is 2.6 nJ and the peak THz amplitudes are ±60 V/cm for the solid and dashed waveforms, respectively. (b) The THz pulse used to probe the near-field. (c) Same settings as (a) were used to acquire OPP-THz-STM waveforms, but using weaker THz pulse amplitudes of ±25 V/cm for the red and black waveforms, respectively. (Adapted from [133])

the sample. The full expression is given by

$$n(\epsilon, t) = \rho_s(\epsilon) + A_0 \exp\left(-\frac{t}{\theta}\right) \cdot \exp\left(-\frac{(\epsilon - \epsilon_c)^2}{2\sigma^2}\right) \cdot \frac{1}{2}\left[\text{erf}\frac{t}{\gamma_{rt}} + 1\right] \quad (8.3)$$

where θ is the temporal decay constant and γ_{rt} is a parameter that sets the rise-time of the transient carrier density.

In pump-probe analysis, the signal is analyzed at times $t - \tau$, where t represents the time axis of the THz pulse and τ represents the time delay of the THz pulse with respect to the optical pulse. The full evaluation of the transient tunneling current is given by

$$I_{\text{THz}}(t, \tau) = \frac{\pm 1}{\Sigma_0}\int_0^{e|V_{\text{d.c.}} + V_{\text{THz}}(t)|} n(\epsilon, t - \tau)T\left(\phi_t, \phi_s, \epsilon, V_{\text{d.c.}} + V_{\text{THz}}(t), z\right) d\epsilon \dots$$

$$\dots \mp \frac{1}{\Sigma_0}\int_0^{e|V_{\text{d.c.}}|} n(\epsilon, t - \tau)T\left(\phi_t, \phi_s, \epsilon, V_{\text{d.c.}}, z\right) d\epsilon \quad (8.4)$$

where the tip density of states, $\rho_t(\epsilon)$ has been set to unity, T is the transmission factor defined in Chapter 3 and Σ_0 is a scaling factor determined by the operating current and voltage set points during STM measurements. Σ_0 can be determined experimentally by measuring I-V or I-z curves. The fine print at the top of Figs. 7.20 to 7.22 exemplify scaling values for the d.c. current set point, I_0, to be used in STM current calculations.

Equation 8.4 consists of a transient term containing the time-dependence of the THz pulse and a steady-state component for the I-V sweep over the sample. We will later see that this assumption is not true when the THz field penetrates deeply into the sample and generate carriers in the bulk that become readily available to contribute to the tunneling current. The model is expanded in the next section where the time dependence of the sample must be considered.

GaAs has a weak dispersion in the THz range where the absorption increases monotonically with frequency [90], which should be factored into the sample impedance. If $n(t) = \delta(t)$ for PC materials with ultra-short carrier lifetimes, then the detected current will be proportional to the original incoming THz pulse. On the other

end, if the carrier has a long life-time where $n(t)$ behaves like a step function, then $j(\omega) = E_{\text{THz}}(\omega)/\omega$.

Pump-probe THz-STM does not necessarily require the use of optical pulses to excite the system. There are variations of pump-probe THz-STM such as THz pump THz probe STM.[2] The high fields from the enhancement of the THz field is sufficient to induce the emission of cold electrons which can be measured in experiment [26]. The combination of optical and THz pulses produce both hot and cold electrons [2, 26, 133] where the tunneling current signal analysis shows both fast decay and slow decay components for photoelectrons and thermal electrons respectively.

8.3.3 InAs sampling

Fig. 8.7 shows a waveform of OPP-THz-STM on InAs, which is much different compared to GaAs. A Similar waveform seen in [49], which is explained by the convolution of the THz near-field with a long life-time decay function. Pairs of near-field waveform signals are acquired at horizontal and vertical optical-pump polarizations. When the optical pump polarization is horizontal, the waveform appears like a step function. An excitation peak of several ps lifetime is shown when the optical pump polarization is vertical.

The horizontal optical pump polarization case is actually a rise of signal followed by a slow decay of that last several nanoseconds. The signal is expected to diminish when the carrier population recombine. The vertical polarization waveforms show the transport of thermally excited photo-excited carrier populations that last several picoseconds before they scatter or recombine. The remarkable observation to take note of is the trailing reflection pulse 10 to 15 ps after the main peak for either polarizations. The probing THz waveform is convoluted with the carrier population. In other words, the THz electric field is driving the transport of the existing carriers to produce the observed signals.

---

[2]Discussion with colleagues and also with research fellow Hüseyin Azozoglu from the University of Duisburg-Essen in Germany who is working on a THz-THz pump probe STM system.
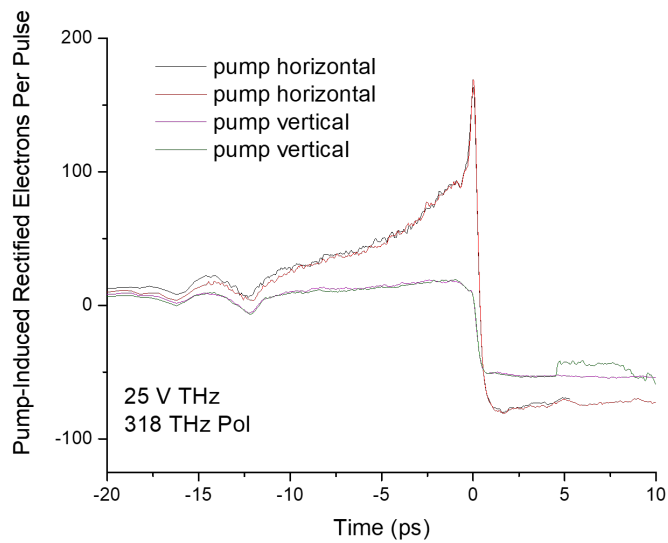
Figure 8.7: Near-field waveform sampling using the THz-STM on optically excited InAs sample showing long-lived effects that can be probed in the next THz pulse cycle. Two waveforms were acquired where the optical pump polarization is varied between horizontal and vertical. The THz peak pulse amplitude is fixed at $-25\,\text{V/cm}$. Note that the time axis is flipped where the excitation relative to the pump time. The peak of the excitation is at zero while the decay is traced out in the negative time direction. (Credit V. Jelic and T.W. Wang)

8.4   Systematic fitting of the THz-STM signals

The process to fit the sampled waveforms with THz-STM is presented here. The circuit shown in Fig. 8.8 is used to attempt fits on sampled waveforms.

The measured signal is the correlation current given as

$$I_{out} = \frac{1}{T} \int_0^T G_S(t')V(t',\tau)dt'. \tag{8.5}$$

where T is the period of the sampling repetition rate, G_S is the photoexcitation conductivity of the sample, and τ is a delay time between the peak of the junction excitation and the peak of the probing pulse.
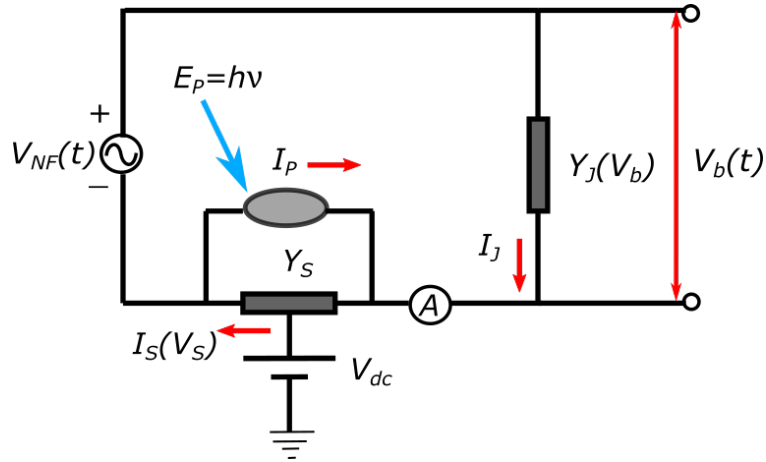
Figure 8.8: Equivalent circuit for a metal-photoconductor interface. The near-field bias from the THz electric field activates the tunneling junction and photo-excited sample. Photons excite the sample with energy E_P. Admittance elements for the junction, Y_J and sample, Y_S, are driven by near-field biases, V_b and V_S, respectively. The photo-current is quantified by I_P.

The transient conductance function is determined from the tunneling conductance of the junction. Fig. 8.9 shows the transient conductance where the photoexcitation timescale is varied. Even though the laser pulse train that excites a semiconductor may be about 50-100 femtoseconds, the signal show features that vary from femtoseconds all the way to nanoseconds or longer. The recombination between electrons and holes depend on many factors according to the bulk material properties and microscopic details in the probing region of the material (i.e. sample defects, structural

258

features, recombination times).

(a)   (b)
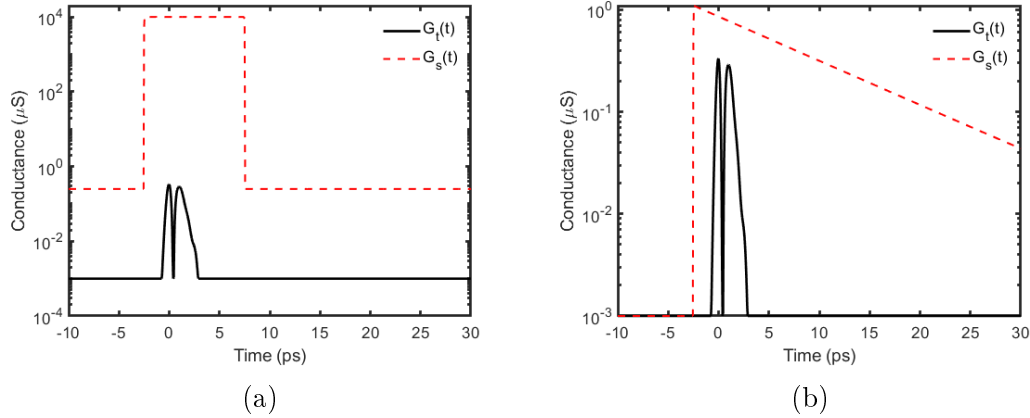
Figure 8.9: (a) Transient conductances where the near-field THz pulse biases the tunneling junction and a box pulse for the sample's conductance. (b) Transient conductances with the same THz pulse biasing the tunneling junction and sample conductance consisting of a 10 ps recombination lifetime.

In Fig. 8.10, when a THz bias waveform is swept with a box pulse conductance, the tunneling current transient develops a large negative lobe.
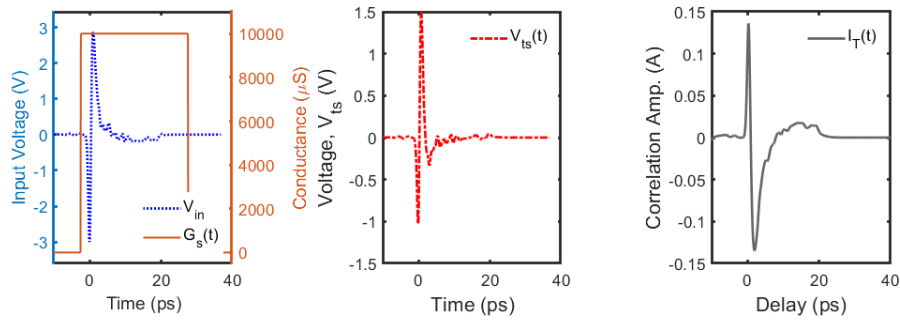
Figure 8.10: Tunneling signal calculation using the near-field THz pulse as the input and the sample conductance as a box pulse. (a) The near-field THz pulse biasing the junction and the sample's conductance represented by a box pulse function. (b) The calculated near-field bias driving the sample, V_{ts}. (c) The convoluted signal as a result of the THz pulse probing the photo-excited tunneling junction.

The convolution process shows that the shape of the outputted waveform depends on the life-time of the carrier decay function. The photo-carriers are shown to live quite shortly (under 10 ps) as probed with THz-STM. Figures 8.11 show the convolution of the THz bias waveform with conductance transients that have a (a) 0.1 ps, (b)

1 ps and (c) 10 ps decay lifetimes. The conductance transient amplitudes are directly proportional to the carrier population after the photoexcitation. The 0.1 ps lifetime convolution returns the same signal waveform as the bias THz voltage transient. The longer the lifetime, the tunneling waveform eventually develops the large negative lobe like the non-decaying conductance in Fig. 8.10.

(a)

(b)

(c)
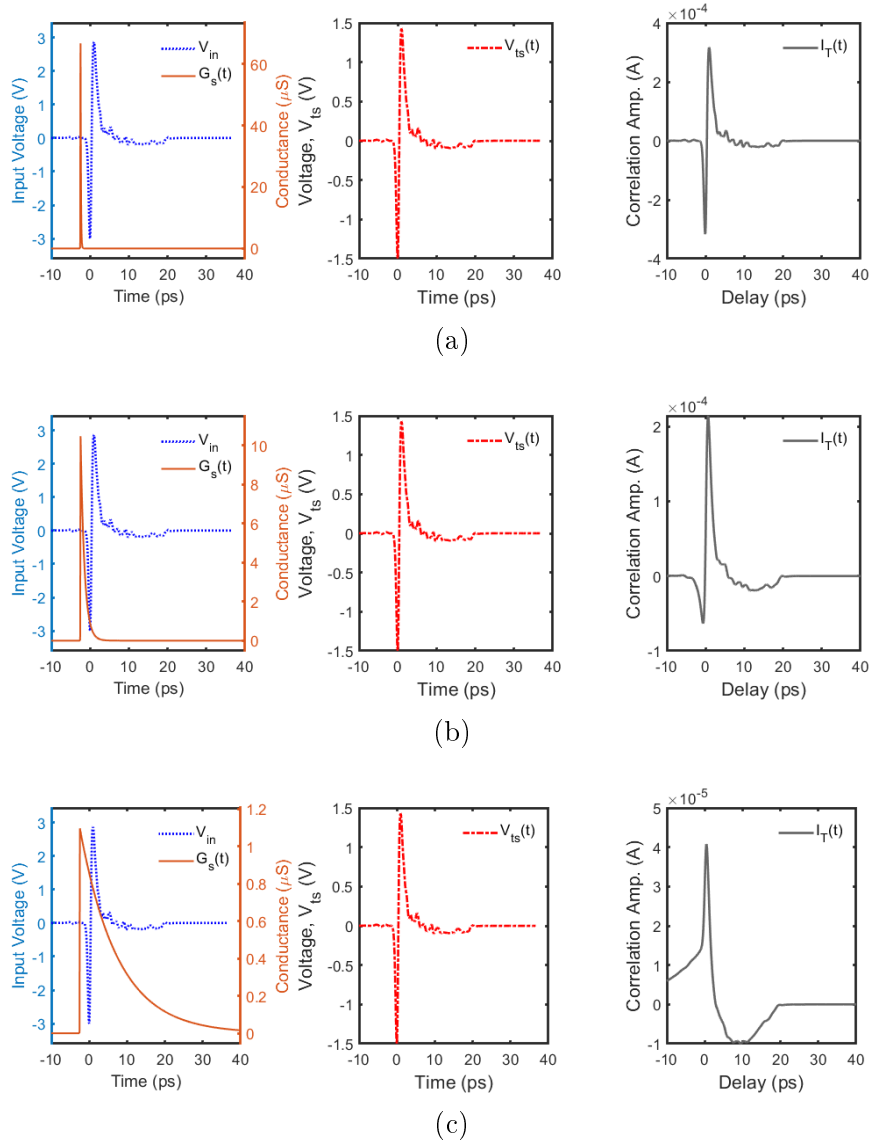
Figure 8.11: Current signal waveforms using different values of decay time constant: (a) 0.1 ps, (b) 1 ps, (c) 10 ps.

The sample's conductance is proportional to the carrier population density. Fig. 8.11(b) showed the case where a simulated near-field THz pulse from the long-wire

geometry COMSOL simulations is convoluted with a sample conductance that has a 1 ps life-time decay. In Fig. 8.12, the full THz near-field voltage waveform with reflection pulses from the full geometry COMSOL simulations is used to convolute with the conductance transient with 1 ps lifetime. The calculated signal shows additional features after the main peak due to the reflection pulse. The additional features due to the reflection pulse as shown in the signal waveform of Fig. 8.12 resemble the waveform features observed on the long complex waveforms acquired using OPP-THz-STM on GaAs(110) from Fig. 8.6
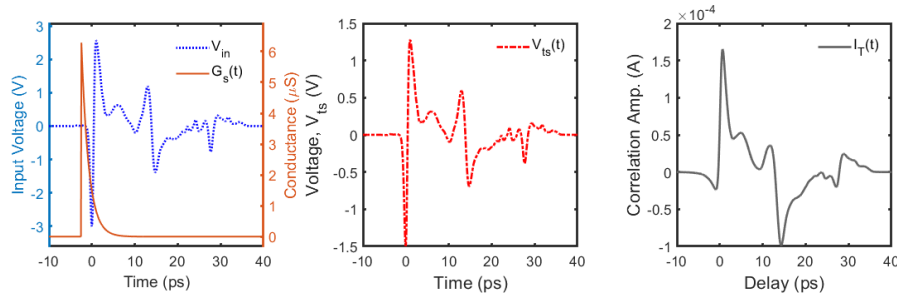
Figure 8.12: Sampling signal calculation using the full nearfield voltage input with the reflection pulse.

In Fig. 8.13, the incident THz pulse is used to convolute with the conductance transients with 0.1 ps, 1 ps, 1.7 ps lifetimes. The current waveforms develop the large negative lobe for the longer lifetimes.
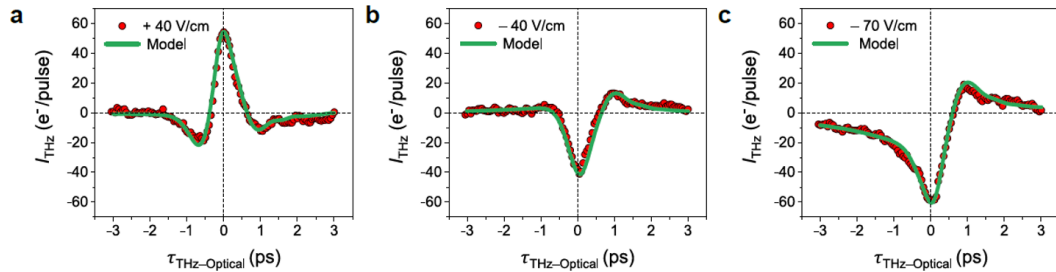
Figure 8.13: Sampling signal calculations on sampled pulses using lifetimes of (a) 0.1 ps, (b) 1 ps, and (c) 1.7 ps using OPP-THz-STM data on GaAs (110). The sample bias is $+2$ V, total current setpoint is at $+50$ pA, optical pulse energy is 1 nJ and the peak THz pulse amplitude varies as stated in the legend. (Adapted from [133].)

It is possible to extract the photoexcitation transient from the experimentally sam-

pled current waveforms. Using the measured current signal transient in Fig. 8.14(b) and using the transfer function method, the waveform in Fig. 8.14(a) is extracted. In this case, the photoexcitation has a decay constant of 1.32 ps which is consistent to carrier dynamical behaviour measured on GaAs on the order of 1 ps. The fitted exponential decay and a THz bias transient are convoluted to produce the calculated THz-STM current signal in 8.14(b) in attempt to reproduce the measurement.
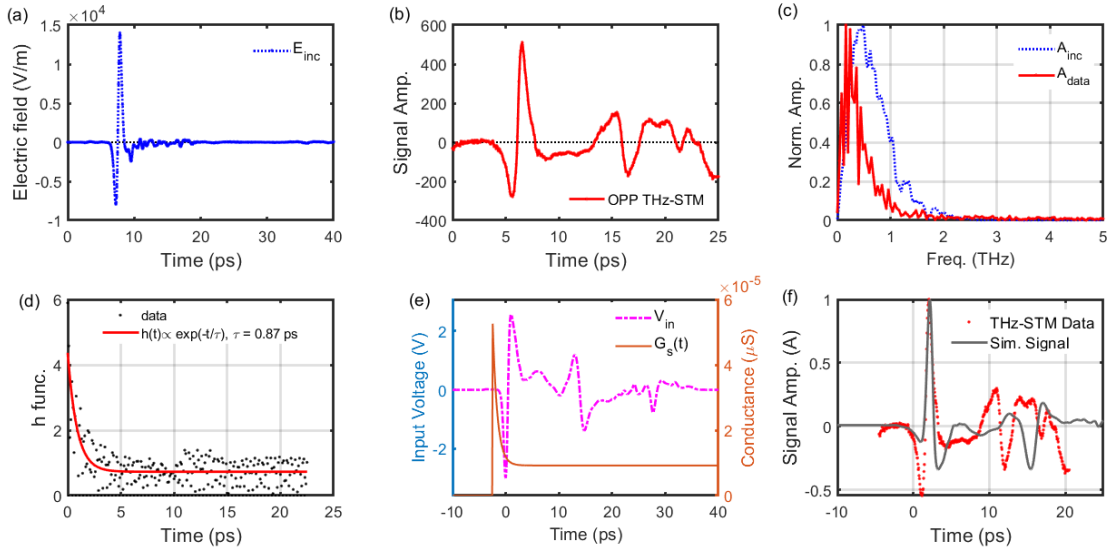
Figure 8.14: OPP-THz-STM signal fitting starting with the incident THz pulse. (a) Incident THz pulse measured by EO sampling. (b) Target experimental OPP-THz-STM signal waveform to fit. (c) THz spectra of the incident THz pulse and signal waveform. (d) Approximate photoexcitation decay is fitted with a single exponential with a 0.87 ps lifetime. (e) The sampling conductance is convoluted with the input THz near-field bias voltage. (f) Signal fitting result using the model in comparison with the experimental waveform in (b).

The sampled near-field waveforms can vary in GaAs. The waveform in Fig. 8.15 matches almost exact to the penetrated near-field waveform simulated below the sample surface. The close agreement between the fitting and the data is mostly coincidental, as the region at that particular location where the STM tip is held at on the GaAs sample exhibited simple carrier population dynamics that can be modeled by a decay function of 0.1 ps lifetime. Nearly the exact waveform as the sample driving field gets outputted from calculations when the sample carrier dynamics resemble a

delta function. Experimental measurements of waveforms like the one shown in Fig. 8.15 are quite rare while the waveforms shown in Figs. 8.5 and 8.6 are more common. Some experimental preconditions to obtain near-field waveforms where the fitting works out nicely are ideal STM tips, clean flat sample surface, uniform doping levels in the scanning area of the sample and good alignment with the OPP-THz optics.
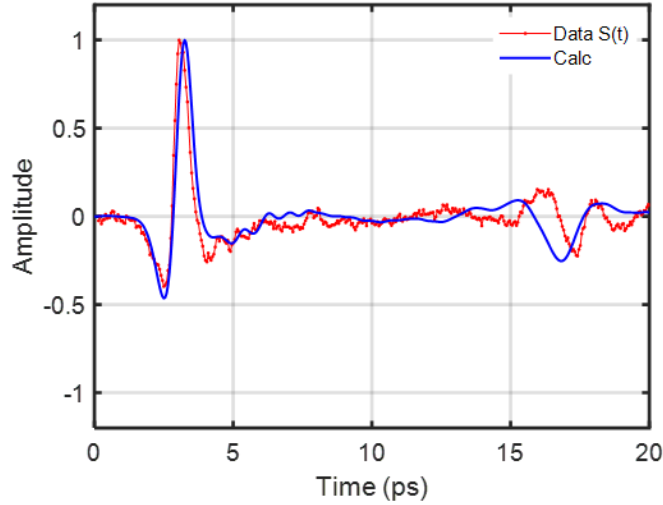
Figure 8.15: Near-field waveform sampling on a GaAs region exhibiting a very short decay life-time that the tunneling signal resembles the coupling THz near-field inside the sample. The calculation was performed using a sampling photoexcitation with 0.1 ps lifetime.

The fits have not been attempted on the InAs since there was not a sizeable data set to work with. In Fig. 8.7, one can see that a photoexciation with a very long decay and a THz voltage bias transient with a long series of reflection pulses should be used to reproduce the sampled current waveform with a widened negative lobe and stretched reflection pulse features. Here we only assumed that the carrier excitation follows a simple rise and decay function. There are deeper dynamical processes that have to be considered in order to properly model the wide range of carrier behaviour that occur in photo-excited semiconductor materials.

Finally, we revisit the sampled waveform in Fig. 8.2 and perform the systematic fitting shown in Fig. 8.16. In part (f) of the plot, the fitted signal nearly matches

in the main pulse of the transient and the time at which the reflection pulse occurs. The tip used during the sampling must have had close dimensions with that of the simulation unlike in Fig. 8.14 where the trailing reflection pulse is a few ps closer to the main pulse indicating that the tip used during that OPP THz-STM measurement was shorter than 2 mm used in the simulation.
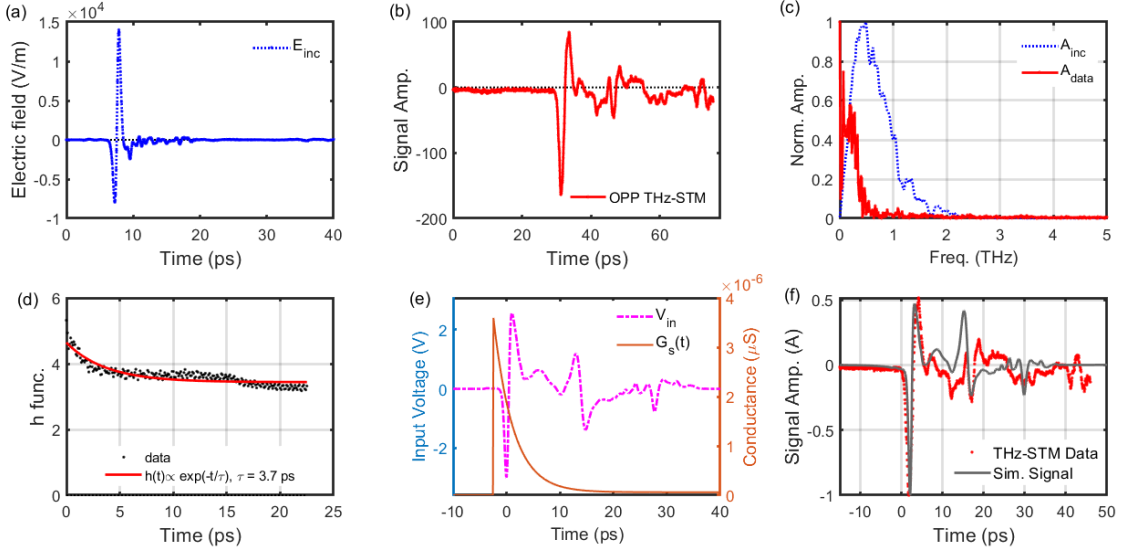
Figure 8.16: Near-field waveform sampling on a GaAs region exhibiting a longer decay life-time that the tunneling signal resembles the coupling THz near-field. (a) Incident THz pulse measured by EO sampling. (b) Target experimental OPP-THz-STM signal waveform to fit. (c) THz spectra of the incident THz pulse and signal waveform. (d) Approximate photoexcitation decay is fitted with a single exponential with a 3.7ps lifetime. (e) The sampling conductance is convoluted with the input THz near-field bias voltage. (f) Signal fitting result using the model in comparison with the experimental waveform in (b).

Good fittings shown in Figs. 8.15 and 8.16 are merely coincidental where the probed region of the sample exhibit simple carrier dynamical behaviour. In most experimental OPP-THz-STM near-field THz waveform acquisitions, the model and the fitting process does not generally produce close fits. It is more common to obtain waveforms shown in Figs. 8.14, 8.6 and the InAs waveforms in Fig. 8.7, where the model struggles. Much needs to be understood about the carrier dynamics of the sample in order to refine the model. Furthermore, THz interaction with the sample

must also be factored in to reproduce full fits of sampled waveforms acquired by THz-STM experiments.

8.5 Chapter Summary

THz waveforms were sampled using OPP-THz-STM. Most of them reveal waveform structures not like the incident THz pulse measured by EO sampling. The reflection pulse is present. The detected main pulse is usually followed up with long-lived shelf feature that correlate with carrier excitations that live out longer than a THz pulse cycle.

Using the waveform construction method where the voltage transient biasing the junction is convoluted with the conductance of the junction, tunneling current waveforms are produced. They show features seen in the sampled tunneling waveforms such as the shelf at the end of the main pulse that has a long duration.

Tip and sample photo-emission experiments using THz-STM on metals and other semiconductors is an alternative method to acquire near-field waveforms. In this scenario, the tip is out of range for tunneling, however the tip-sample distance, which can go up to a few microns, still satisfies the criteria to be in the near-field regime. Similar waveform features are shown as presented for OPP-THz-STM on GaAs(110). Future work is needed to design simulations and analyses for interpreting near-field signals.

Chapter 9

Conclusions

THz-STM has been around for about a decade and its potential to unravel phenomena in the nano-to-atomic size scale and ultrafast time scales is not perceived to have limitations due to the vast array of materials and physical systems that can be studied with the technique. The coupling of THz spectroscopy and STM into a broad regime of interesting phenomena that can be probed. However, lots of work still needs to be done to address how THz-STM fundamentally works and to build theoretical foundations for progressing the technique to study advanced materials. This thesis demonstrated that both computational electromagnetic simulations and analytical modeling were needed to illustrate various aspects of THz-STM. A bench-marking simulation/model that can incorporate as much of the relevant physical concepts in electrodynamics and condensed matter physics that are applicable for THz-STM was used to generate results that can observed in THz-STM experiments. The amount of extensive modeling and analysis needed to explain complexities observed in experiment made a remark that THz-STM is unique from standard microscopic techniques and present peculiar challenges to build theoretical foundations for, especially as new experimental results continue to be reported.

9.1 Summary

Foundations of THz science and near-field microscopy necessary for understanding THz-STM from THz generation all the way to coupling THz with the STM are discussed. The mechanisms and formalism for generating a photo-current, free-space and wave-guide propagation of THz radiation, generation of plasmons in materials, and the focusing of fields in near-field microscopy are all useful for understanding the variables that constitute a measurement in a THz-STM experiment. As THz-STM is proven to be a multidisciplinary field, these concepts should help with the design of future experiments and applications. These principles are used to guide the design of THz-STM simulations and modeling, as presented later on.

STM spectroscopy formalism is used to quantify quantum mechanical tunneling through a potential barrier that exists between the tip and sample. The equations of tunneling is used to support a transient bias that takes on the form of a THz pulse, which sets up the basis for modeling THz-STM tunneling currents. Furthermore, an areal tunneling model is used to calculate additonal tunneling from the entire tip apex.

We established a simulation using COMSOL Multiphysics software for the THz-STM experiment. Preliminary results such as the dependence of the electric field enhancement at the tip-sample junction by varying a few geometric parameters were performed to help benchmark the simulation. The results show that the tip and sample act as a THz antenna, which is seen in the electromagnetic near-field waveform profile at the tip apex. The near-field is enhanced by several orders of magnitude and is the integration of the excitation field incident to the tip. Simulations were conducted to investigate the optimization of THz-pulse-to-tip-coupling, where the tip shape is varied at the apex, taper and shaft as parameter sweep studies. A multi-probe simulation consisting of a geometry with two tips was carried out, this introduces a unique selectivity process where the angles between the tips' orientation relative

to the incident THz polarization determines which tip the dominant near-field is generated at. Electromagnetic computations were performed using a discrete dipoles model. A source emitter and target scatterers are an assembly of unit dipoles that contribute time-dependent electric field radiation proportional to the dipole transient term summed with its first and second derivatives. At different distances away from the dipole emitter, certain terms dominate. The waveforms measured from a source or scattering configuration show good agreement when comparing the simulations using the discrete dipoles model and COMSOL simulations for THz-STM.

Circuit modeling have been a traditional way to analyze transients produced in near-field microscopy experiments. A lumped element circuit model consisting of resistors, inductors and capacitors can be used to model the nearfield at the tip junction where the input into the circuit model is a THz voltage transient. The fitted parameters to reproduce the integral near-field waveform created by the COMSOL simulation are $R = 220\Omega$, $L = 75$ pH and $C = 35$ fF.

A transmission line model is coupled to the RLC circuit model. The tip shaft and tip holder provides a path for the incident pulse to reflect and travel back to the junction at a time delay equal to twice the tip shaft length. The reflection pulse appears in the nearfield at the time delay duration. Variations of the circuit model was presented to model tip-shape dependence. In a photoconductive circuit, the field screening can be emulated by introducing a time-dependent capacitance which causes the net bias at the load to be filtered like an RC circuit.

The process of using the the input bias voltage transient to calculate the tunneling current signal in THz-STM has been demonstrated. The COMSOL simulations were used as a benchmark to quantitatively convert THz electric field to a nearfield bias voltage. The internal penetration nearfield below the sample surface has been modeled using an expanded circuit model for the tunneling junction.

Circuit models were introduced to calculate current and voltage transients for a few junction interfaces. In a metal-to-metal junction, space charge effects is demonstrated

using a tunneling admittance model. There is a both direct tunneling component and mesoscopic capacitive component. In a metal-to-semiconductor junction, the circuit model for the junction is further expanded to consist of current contributions by tunneling between the tip and the sample surface and current between the bulk and surface.

THz tunneling current transients were sampled using OPP-THz-STM. They reveal interesting waveform structures such as a long-lived shelf feature tailing the end of the main pulse and reflection pulses. Fits to the sampled waveforms have been attempted by calculating the THz voltage transient biasing the junction and then convoluting the waveform with the junction conductance. The calculated waveforms show a reasonable fit with the sampled waveforms on GaAs using OPP-THz-STM where the carrier transport can be modeled by a single component of rising and decaying photo-excited carrier population. However, in regions of GaAs and other semiconductors such as InAs where the carrier dynamics is more complex, the model in incapable of reproducing the fits of the sampled near-field waveforms. Near-field waveforms obtained in photo-emission THz-STM experiments still have to be examined and modeled.

9.2   Future Outlook

There are many routes that can be taken to help refine the theoretical foundations for interpreting and analyzing THz-STM experiments. A few topics which have been worked through to some degree in this Thesis are rementioned here to emphasize how they may be explored further.

9.2.1   Expanded circuit modeling

Advanced numerical electromagnetic formalism can be used to create detailed circuit models to simulate electromagnetic field variables for devices at THz and optical frequencies [177, 219]. A lumped element model fails to produce a full-scale calculation, hence transmission line aspects had to be introduced for the purpose of propagat-

ing electromagnetic fields in the simulation geometry. A larger scale circuit model incorporating traveling wave mechanisms between junction points can be created to integrate THz propagation and dispersion effects in various geometries and materials.

9.2.2 THz-STM on the Schottky Junction

One of the key highlights of THz-STM was the measurements and analysis on THz-driven tunneling on semiconductors [2, 33]. The metal-to-semiconductor interface has further complexities not explored in the recent publications nor in this Thesis. The tunneling profile accessible by THz fields has origins that goes beyond the standard tunneling model. Tunneling cannot be viewed as tunneling between the tip and the surface of the sample when the semiconductor has a bulk region of available electrons that can contribute to the overall tunneling.

In this work, the circuit representation for the Schottky junction assumes values for parameters such as the Schottky barrier. A deeper solid-state approach has to be implemented to be able to model the band structure, surface states, tip-induced band-bending, etc. for the interface. Better versions of I-V characteristics can be used for understanding THz-STM measurements on semiconductor samples (or tips).

9.2.3 Zooming in further

Fundamentally we are dealing with simulations at the atomic scale. Density functional theory (DFT) simulations has been conducted for THz-STM [22, 23, 28, 47] to zoom into the atomic scale processes when the tip is perturbed by an electromagnetic field excitation. DFT simulation packages [285, 286] are powerful tools for simulating/visualizing the wavefunctions and density of states for molecular-to-atomic scaled systems. Transient fields affect the position of atoms and also drive molecular vibrations. The molecular dynamics caused by transient fields can be simulated for both the tip and sample using other simulation packages and software.

Currently, the workstation used to carry out all the COMSOL simulations and

analytical calculations in this thesis work does not have enough computing capacity to carry out such simulations. Access to a computational grid will enable multi-scale modeling and further detailed studies of THz-STM at the molecular-to-atomic and ultrafast time scale.

References

[1]   P. H. Nguyen, C. Rathje, G. J. Hornig, V. Jelic, C. Ropers, and F. A. Hegmann, "Coupling terahertz pulses to a scanning tunneling microscope", *Physics in Canada*, vol. 71, no. 3, pp. 157–160, 2015.

[2]   V. Jelic *et al.*, "Ultrafast terahertz control of extreme tunnel currents through single atoms on a silicon surface", *Nature Physics*, vol. 13, no. 6, pp. 591–598, 2017.

[3]   Y. Luo *et al.*, "Nanoscale terahertz stm imaging of a metal surface", *Phys. Rev. B*, vol. 102, p. 205 417, 20 2020.

[4]   T. L. Cocker *et al.*, "Imaging ultrafast dynamics on the nanoscale with a THz-STM", in *Ultrafast Phenomena and Nanophotonics XVIII*, M. Betz, A. Y. Elezzabi, J.-J. Song, and K.-T. Tsen, Eds., International Society for Optics and Photonics, vol. 8984, SPIE, 2014, pp. 137–149.

[5]   A. J. Huber, F. Keilmann, J. Wittborn, J. Aizpurua, and R. Hillenbrand, "Terahertz near-field nanoscopy of mobile carriers in single semiconductor nanodevices", *Nano Letters*, vol. 8, no. 11, pp. 3766–3770, 2008, PMID: 18837565.

[6]   M. Eisele *et al.*, "Ultrafast multi-terahertz nano-spectroscopy with sub-cycle temporal resolution", *Nature Photonics*, vol. 8, no. 11, pp. 841–845, 2014.

[7]   M. A. Huber *et al.*, "Femtosecond photo-switching of interface polaritons in black phosphorus heterostructures", *Nature Nanotechnology*, vol. 12, no. 3, pp. 207–211, 2017.

[8]   E. Sakat *et al.*, "Near-field imaging of free carriers in zno nanowires with a scanning probe tip made of heavily doped germanium", *Phys. Rev. Applied*, vol. 8, p. 054 042, 5 2017.

[9]   M. Wagner *et al.*, "Ultrafast and nanoscale plasmonic phenomena in exfoliated graphene revealed by infrared pump–probe nanoscopy", *Nano Letters*, vol. 14, no. 2, pp. 894–900, 2014, PMID: 24479682.

[10] L. Zhang *et al.*, "Electrically driven single-photon emission from an isolated single molecule", *Nature Communications*, vol. 8, no. 1, p. 580, 2017.

[11] C. Guo *et al.*, "Probing nonequilibrium dynamics of photoexcited polarons on a metal-oxide surface with atomic precision", *Phys. Rev. Lett.*, vol. 124, p. 206 801, 20 2020.

[12] T. L. Cocker, V. Jelic, R. Hillenbrand, and F. A. Hegmann, "Nanoscale tera-hertz scanning probe microscopy", *Nature Photonics*, vol. 15, no. 8, pp. 558–569, 2021.

[13] K. Liang, L. Bi, Q. Zhu, H. Zhou, and S. Li, "Ultrafast dynamics revealed with time-resolved scanning tunneling microscopy: A review", *ACS Applied Optical Materials*, vol. 1, no. 5, pp. 924–938, 2023.

[14] S. Loth, M. Etzkorn, C. P. Lutz, D. M. Eigler, and A. J. Heinrich, "Measurement of fast electron spin relaxation times with atomic resolution", *Science*, vol. 329, no. 5999, pp. 1628–1630, 2010.

[15] Y. Terada, S. Yoshida, O. Takeuchi, and H. Shigekawa, "Real-space imaging of transient carrier dynamics by nanoscale pump-probe microscopy", *Nature Photonics*, vol. 4, no. 12, pp. 869–874, 2010.

[16] P. Kloth and M. Wenderoth, "From time-resolved atomic-scale imaging of individual donors to their cooperative dynamics", *Science Advances*, vol. 3, no. 3, 2017.

[17] J. Lee, S. M. Perdue, A. Rodriguez Perez, and V. A. Apkarian, "Vibronic motion with joint angstrom–femtosecond resolution observed through fano progressions recorded within one molecule", *ACS Nano*, vol. 8, no. 1, pp. 54–63, 2014, PMID: 24261832.

[18] K. Kuhnke, C. Große, P. Merino, and K. Kern, "Atomic-scale imaging and spectroscopy of electroluminescence at molecular interfaces", *Chemical Reviews*, vol. 117, no. 7, pp. 5174–5222, 2017, PMID: 28294599.

[19] S. Yoshida, Y. Terada, M. Yokota, O. Takeuchi, H. Oigawa, and H. Shigekawa, "Optical pump-probe scanning tunneling microscopy for probing ultrafast dynamics on the nanoscale", *The European Physical Journal Special Topics*, vol. 222, no. 5, pp. 1161–1175, 2013.

[20] S. Yoshida *et al.*, "Probing ultrafast spin dynamics with optical pump–probe scanning tunnelling microscopy", *Nature Nanotechnology*, vol. 9, no. 8, pp. 588–593, 2014.

[21] Z. Schumacher, A. Spielhofer, Y. Miyahara, and P. Grutter, "The limit of time resolution in frequency modulation atomic force microscopy by a pump-probe approach", *Applied Physics Letters*, vol. 110, no. 5, p. 053 111, 2017.

[22] D. Peller *et al.*, "Sub-cycle atomic-scale forces coherently control a single-molecule switch", *Nature*, vol. 585, no. 7823, pp. 58–62, 2020.

[23] D. Peller *et al.*, "Quantitative sampling of atomic-scale electromagnetic waveforms", *Nature Photonics*, vol. 15, no. 2, pp. 143–147, 2021.

[24] M. Müller, N. Martín Sabanés, T. Kampfrath, and M. Wolf, "Phase-resolved detection of ultrabroadband thz pulses inside a scanning tunneling microscope junction", *ACS Photonics*, vol. 7, no. 8, pp. 2046–2055, 2020.

[25] M. Abdo *et al.*, "Variable repetition rate thz source for ultrafast scanning tunneling microscopy", *ACS Photonics*, vol. 8, no. 3, pp. 702–708, 2021, PMID: 33763504.

[26] N. Martín Sabanés, F. Krecinic, T. Kumagai, F. Schulz, M. Wolf, and M. Müller, "Femtosecond thermal and nonthermal hot electron tunneling inside a photoexcited tunnel junction", *ACS Nano*, vol. 16, no. 9, pp. 14 479–14 489, 2022, PMID: 36027581.

[27] S. Yoshida *et al.*, "Terahertz scanning tunneling microscopy for visualizing ultrafast electron motion in nanoscale potential variations", *ACS Photonics*, vol. 8, no. 1, pp. 315–323, 2021.

[28] S. E. Ammerman *et al.*, "Lightwave-driven scanning tunnelling spectroscopy of atomically precise graphene nanoribbons", *Nature Communications*, vol. 12, no. 1, p. 6794, 2021.

[29] J. Lloyd-Hughes *et al.*, "The 2021 ultrafast spectroscopic probes of condensed matter roadmap", *Journal of Physics: Condensed Matter*, vol. 33, no. 35, p. 353 001, 2021.

[30] M. Rashidi *et al.*, "Time-resolved imaging of negative differential resistance on the atomic scale", *Phys. Rev. Lett.*, vol. 117, p. 276 805, 27 2016.

[31] M. Garg, A. Martin-Jimenez, M. Pisarra, Y. Luo, F. Martín, and K. Kern, "Real-space subfemtosecond imaging of quantum electronic coherences in molecules", *Nature Photonics*, vol. 16, no. 3, pp. 196–202, 2022.

[32] S. Chen, W. Shi, and W. Ho, "Single-molecule continuous-wave terahertz rectification spectroscopy and microscopy", *Nano Letters*, vol. 23, no. 7, pp. 2915–2920, 2023, PMID: 36999877.

[33] T. L. Cocker *et al.*, "An ultrafast terahertz scanning tunnelling microscope", *Nature Photonics*, vol. 7, no. 8, pp. 620–625, 2013.

[34] K. Yoshioka *et al.*, "Real-space coherent manipulation of electrons in a single tunnel junction by single-cycle terahertz electric fields", *Nature Photonics*, vol. 10, no. 12, pp. 762–765, 2016.

[35] P. Klarskov, H. Kim, V. L. Colvin, and D. M. Mittleman, "Nanoscale laser terahertz emission microscopy", *ACS Photonics*, vol. 4, no. 11, pp. 2676–2680, 2017.

[36] F. Mooshammer *et al.*, "Nanoscale near-field tomography of surface states on (bi0.5sb0.5)2te3", *Nano Letters*, vol. 18, no. 12, pp. 7515–7523, 2018, PMID: 30419748.

[37] F. Mooshammer, M. A. Huber, F. Sandner, M. Plankl, M. Zizlsperger, and R. Huber, "Quantifying nanoscale electromagnetic fields in near-field microscopy by fourier demodulation analysis", *ACS Photonics*, vol. 7, no. 2, pp. 344–351, 2020.

[38] A. Rosławska *et al.*, "Single charge and exciton dynamics probed by molecular-scale-induced electroluminescence", *Nano Letters*, vol. 18, no. 6, pp. 4001–4007, 2018, PMID: 29799760.

[39] Y. Arashida *et al.*, "Subcycle mid-infrared electric-field-driven scanning tunneling microscopy with a time resolution higher than 30 fs", *ACS Photonics*, vol. 9, no. 9, pp. 3156–3164, 2022.

[40] P. Jepsen, D. Cooke, and M. Koch, "Terahertz spectroscopy and imaging – modern techniques and applications", *Laser & Photonics Reviews*, vol. 5, no. 1, pp. 124–166, 2011.

[41] N. C. J. van der Valk and P. C. M. Planken, "Electro-optic detection of sub-wavelength terahertz spot sizes in the near field of a metal tip", *Applied Physics Letters*, vol. 81, no. 9, pp. 1558–1560, 2002.

[42] N. C. J. van der Valk and P. C. M. Planken, "Electro-optic detection of sub-wavelength terahertz spot sizes in the near field of a metal tip", *Applied Physics Letters*, vol. 81, no. 9, pp. 1558–1560, 2002.

[43] P. C. M. Planken and N. C. J. van der Valk, "Spot-size reduction in terahertz apertureless near-field imaging", *Opt. Lett.*, vol. 29, no. 19, pp. 2306–2308, 2004.

[44] H.-T. Chen, S. Kraatz, G. C. Cho, and R. Kersting, "Identification of a resonant imaging process in apertureless near-field microscopy", *Phys. Rev. Lett.*, vol. 93, p. 267 401, 26 2004.

[45] R. Kersting, H.-T. Chen, N. Karpowicz, and G. C. Cho, "Terahertz microscopy with submicrometre resolution", *Journal of Optics A: Pure and Applied Optics*, vol. 7, no. 2, S184–S189, 2005.

[46] K. Kimura *et al.*, "Terahertz-field-driven scanning tunneling luminescence spectroscopy", *ACS Photonics*, vol. 8, no. 4, pp. 982–987, 2021.

[47] T. L. Cocker, D. Peller, P. Yu, J. Repp, and R. Huber, "Tracking the ultrafast motion of a single molecule by femtosecond orbital imaging", *Nature*, vol. 539, no. 7628, pp. 263–267, 2016.

[48] K. Yoshioka *et al.*, "Tailoring single-cycle near field in a tunnel junction with carrier-envelope phase-controlled terahertz electric fields", *Nano Letters*, vol. 18, no. 8, pp. 5198–5204, 2018, PMID: 30028952.

[49] S. Yoshida *et al.*, "Subcycle transient scanning tunneling spectroscopy with visualization of enhanced terahertz near field", *ACS Photonics*, vol. 6, no. 6, pp. 1356–1364, 2019.

[50] M. B. Heindl *et al.*, "Ultrafast imaging of terahertz electric waveforms using quantum dots", *Light: Science & Applications*, vol. 11, no. 1, p. 5, 2022.

[51] K. Iwaya *et al.*, "Externally-triggerable optical pump-probe scanning tunneling microscopy with a time resolution of tens-picosecond", *Scientific Reports*, vol. 13, no. 1, p. 818, 2023.

[52] K. Wang and D. M. Mittleman, "Metal wires for terahertz wave guiding", *Nature*, vol. 432, no. 7015, pp. 376–379, 2004.

[53] G. Gallot, S. P. Jamison, R. W. McGowan, and D. Grischkowsky, "Terahertz waveguides", *J. Opt. Soc. Am. B*, vol. 17, no. 5, pp. 851–863, 2000.

[54] J. A. Deibel, K. Wang, M. Escarra, N. Berndsen, and D. M. Mittleman, "The excitation and emission of terahertz surface plasmon polaritons on metal wire waveguides", *Comptes Rendus Physique*, vol. 9, no. 2, pp. 215–231, 2008, Recent developments in terahertz optoelectronics.

[55] S. A. Maier, S. R. Andrews, L. Martín-Moreno, and F. J. García-Vidal, "Terahertz surface plasmon-polariton propagation and focusing on periodically corrugated metal wires", *Phys. Rev. Lett.*, vol. 97, p. 176 805, 17 2006.

[56] K. Wang, D. M. Mittleman, N. C. J. van der Valk, and P. C. M. Planken, "Antenna effects in terahertz apertureless near-field optical microscopy", *Applied Physics Letters*, vol. 85, no. 14, pp. 2715–2717, 2004.

[57] G. C. Cho, H.-T. Chen, S. Kraatz, N. Karpowicz, and R. Kersting, "Apertureless terahertz near-field microscopy", *Semiconductor Science and Technology*, vol. 20, no. 7, S286–S292, 2005.

[58] N. Behr and M. B. Raschke, "Optical antenna properties of scanning probe tips: Plasmonic light scattering, tip-sample coupling, and near-field enhancement", *The Journal of Physical Chemistry C*, vol. 112, no. 10, pp. 3766–3773, 2008.

[59] S. Berweger, J. M. Atkin, R. L. Olmon, and M. B. Raschke, "Light on the tip of a needle: Plasmonic nanofocusing for spectroscopy on the nanoscale", *The Journal of Physical Chemistry Letters*, vol. 3, no. 7, pp. 945–952, 2012, PMID: 26286425.

[60] D. Richards, A. Zayats, F. Keilmann, and R. Hillenbrand, "Near-field microscopy by elastic light scattering from a tip", *Philosophical Transactions of the Royal Society of London. Series A: Mathematical, Physical and Engineering Sciences*, vol. 362, no. 1817, pp. 787–805, 2004.

[61] L. Novotny and B. Hecht, *Principles of nano-optics*. Cambridge university press, 2012.

[62] M. B. Raschke and C. Lienau, "Apertureless near-field optical microscopy: Tip–sample coupling in elastic light scattering", *Applied Physics Letters*, vol. 83, no. 24, pp. 5089–5091, 2003.

[63] P. Vasa, C. Ropers, R. Pomraenke, and C. Lienau, "Ultra-fast nano-optics", *Laser & Photonics Reviews*, vol. 3, no. 6, pp. 483–507, 2009.

[64] C. Ropers, D. R. Solli, C. P. Schulz, C. Lienau, and T. Elsaesser, "Localized multiphoton emission of femtosecond electron pulses from metal nanotips", *Phys. Rev. Lett.*, vol. 98, p. 043 907, 4 2007.

[65] R. Bormann, M. Gulde, A. Weismann, S. V. Yalunin, and C. Ropers, "Tip-enhanced strong-field photoemission", *Phys. Rev. Lett.*, vol. 105, p. 147 601, 14 2010.

[66] G. Herink, D. R. Solli, M. Gulde, and C. Ropers, "Field-driven photoemission from nanostructures quenches the quiver motion", *Nature*, vol. 483, no. 7388, pp. 190–193, 2012.

[67] G. Herink, L. Wimmer, and C. Ropers, "Field emission at terahertz frequencies: AC-tunneling and ultrafast carrier dynamics", *New Journal of Physics*, vol. 16, no. 12, p. 123 005, 2014.

[68] L. Wimmer, G. Herink, D. R. Solli, S. V. Yalunin, K. E. Echternkamp, and C. Ropers, "Terahertz control of nanotip photoemission", *Nature Physics*, vol. 10, no. 6, pp. 432–436, 2014.

[69] S. Li and R. R. Jones, "High-energy electron emission from metallic nanotips driven by intense single-cycle terahertz pulses", *Nature Communications*, vol. 7, no. 1, p. 13 405, 2016.

[70] J. Vogelsang *et al.*, "Ultrafast electron emission from a sharp metal nanotaper driven by adiabatic nanofocusing of surface plasmons", *Nano Letters*, vol. 15, no. 7, pp. 4685–4691, 2015, PMID: 26061633.

[71] S. L. Lange, N. K. Noori, T. M. B. Kristensen, K. Steenberg, and P. U. Jepsen, "Ultrafast THz-driven electron emission from metal metasurfaces", *Journal of Applied Physics*, vol. 128, no. 7, p. 070 901, 2020.

[72] J.-Y. Kim *et al.*, "Terahertz quantum plasmonics of nanoslot antennas in nonlinear regime", *Nano Letters*, vol. 15, no. 10, pp. 6683–6688, 2015, PMID: 26372787.

[73] V. E. Babicheva, S. Gamage, M. I. Stockman, and Y. Abate, "Near-field edge fringes at sharp material boundaries", *Opt. Express*, vol. 25, no. 20, pp. 23 935–23 944, 2017.

[74] K. Iwaszczuk, M. Zalkovskij, A. C. Strikwerda, and P. U. Jepsen, "Nitrogen plasma formation through terahertz-induced ultrafast electron field emission", *Optica*, vol. 2, no. 2, pp. 116–123, 2015.

[75] B. M. Ross and L. P. Lee, "Plasmon tuning and local field enhancement maximization of the nanocrescent", *Nanotechnology*, vol. 19, no. 27, p. 275 201, 2008.

[76] M. Sukharev and T. Seideman, "Optical properties of metal tips for tip-enhanced spectroscopies", *The Journal of Physical Chemistry A*, vol. 113, no. 26, pp. 7508–7513, 2009.

[77] M. Lenner, P. Rácz, P. Dombi, G. Farkas, and N. Kroó, "Field enhancement and rectification of surface plasmons detected by scanning tunneling microscopy", *Phys. Rev. B*, vol. 83, p. 205 428, 20 2011.

[78] S. F. Becker *et al.*, "Gap-plasmon-enhanced nanofocusing near-field microscopy", *ACS Photonics*, vol. 3, no. 2, pp. 223–232, 2016.

[79] M. Müller, V. Kravtsov, A. Paarmann, M. B. Raschke, and R. Ernstorfer, "Nanofocused plasmon-driven sub-10 fs electron point source", *ACS Photonics*, vol. 3, no. 4, pp. 611–619, 2016.

[80] S. E. Ammerman, Y. Wei, N. Everett, V. Jelic, and T. L. Cocker, "Algorithm for subcycle terahertz scanning tunneling spectroscopy", *Phys. Rev. B*, vol. 105, p. 115 427, 11 2022.

[81] S. Banerjee and P. Zhang, "Scaling of time-dependent tunneling current in terahertz scanning tunneling microscopes", *Phys. Rev. Applied*, vol. 18, p. 024 011, 2 2022.

[82] W. L. Chan, J. Deibel, and D. M. Mittleman, "Imaging with terahertz radiation", *Reports on Progress in Physics*, vol. 70, no. 8, pp. 1325–1379, 2007.

[83] J. Lloyd-Hughes and T.-I. Jeon, "A review of the terahertz conductivity of bulk and nano-materials", *Journal of Infrared, Millimeter, and Terahertz Waves*, vol. 33, no. 9, pp. 871–925, 2012.

[84] D. H. Auston, K. P. Cheung, and P. R. Smith, "Picosecond photoconducting hertzian dipoles", *Applied Physics Letters*, vol. 45, no. 3, pp. 284–286, 1984.

[85] C. Fattinger and D. Grischkowsky, "Point source terahertz optics", *Applied Physics Letters*, vol. 53, no. 16, pp. 1480–1482, 1988.

[86] M. Tani, K. Sakai, and H. Mimura, "Ultrafast photoconductive detectors based on semi-insulating GaAs and InP", *Japanese Journal of Applied Physics*, vol. 36, no. Part 2, No. 9A/B, pp. L1175–L1178, 1997.

[87] M. van Exter, C. Fattinger, and D. Grischkowsky, "High-brightness terahertz beams characterized with an ultrafast detector", *Applied Physics Letters*, vol. 55, no. 4, pp. 337–339, 1989.

[88] J. Darrow, X.-C. Zhang, D. Auston, and J. Morse, "Saturation properties of large-aperture photoconducting antennas", *IEEE Journal of Quantum Electronics*, vol. 28, no. 6, pp. 1607–1616, 1992.

[89] A. J. Taylor, P. K. Benicewicz, and S. M. Young, "Modeling of femtosecond electromagnetic pulses from large-aperture photoconductors", *Opt. Lett.*, vol. 18, no. 16, pp. 1340–1342, 1993.

[90] D. Grischkowsky, S. Keiding, M. van Exter, and C. Fattinger, "Far-infrared time-domain spectroscopy with terahertz beams of dielectrics and semiconductors", *J. Opt. Soc. Am. B*, vol. 7, no. 10, pp. 2006–2015, 1990.

[91] A. Krotkus, "Semiconductors for terahertz photonics applications", *Journal of Physics D: Applied Physics*, vol. 43, no. 27, p. 273 001, 2010.

[92] Z.-S. Piao, M. Tani, and K. Sakai, "Carrier dynamics and THz radiation in biased semiconductor structures", in *Terahertz Spectroscopy and Applications*, M. S. Sherwin, Ed., International Society for Optics and Photonics, vol. 3617, SPIE, 1999, pp. 49–56.

[93] B. Kolner and D. Bloom, "Electrooptic sampling in gaas integrated circuits", *IEEE Journal of Quantum Electronics*, vol. 22, no. 1, pp. 79–93, 1986.

[94] Y.-S. Lee, *Principles of terahertz science and technology.* Springer Science & Business Media, 2009, vol. 170.

[95] T. K. Nguyen *et al.*, "Photoconductive dipole antennas for efficient terahertz receiver", *Optics Communications*, vol. 383, pp. 50–56, 2017.

[96] D. R. Dykaar, B. I. Greene, J. F. Federici, A. F. J. Levi, L. N. Pfeiffer, and R. F. Kopf, "Log-periodic antennas for pulsed terahertz radiation", *Applied Physics Letters*, vol. 59, no. 3, pp. 262–264, 1991.

[97] L. Duvillaret, F. Garet, J.-F. Roux, and J.-L. Coutaz, "Analytical modeling and optimization of terahertz time-domain spectroscopy experiments, using photoswitches as antennas", *IEEE Journal of Selected Topics in Quantum Electronics*, vol. 7, no. 4, pp. 615–623, 2001.

[98] R. W. Boyd, A. L. Gaeta, and E. Giese, *Nonlinear Optics*, G. W. F. Drake, Ed. Cham: Springer International Publishing, 2023.

[99] P. U. Jepsen, R. H. Jacobsen, and S. R. Keiding, "Generation and detection of terahertz pulses from biased semiconductor antennas", *J. Opt. Soc. Am. B*, vol. 13, no. 11, pp. 2424–2436, 1996.

[100] D. W. Pohl, "Near-field optics and the surface plasmon polariton", in *Near-Field Optics and Surface Plasmon Polaritons*, S. Kawata, Ed. Berlin, Heidelberg: Springer Berlin Heidelberg, 2001, pp. 1–13.

[101] P. U. Jepsen and S. R. Keiding, "Radiation patterns from lens-coupled terahertz antennas", *Opt. Lett.*, vol. 20, no. 8, pp. 807–809, 1995.

[102] H. Kogelnik and T. Li, "Laser beams and resonators", *Appl. Opt.*, vol. 5, no. 10, pp. 1550–1567, 1966.

[103] J. V. Rudd and D. M. Mittleman, "Influence of substrate-lens design in terahertz time-domain spectroscopy", *J. Opt. Soc. Am. B*, vol. 19, no. 2, pp. 319–329, 2002.

[104] D. You and P. H. Bucksbaum, "Propagation of half-cycle far infrared pulses", *J. Opt. Soc. Am. B*, vol. 14, no. 7, pp. 1651–1655, 1997.

[105] M. Walther, M. R. Freeman, and F. A. Hegmann, "Metal-wire terahertz time-domain spectroscopy", *Applied Physics Letters*, vol. 87, no. 26, p. 261 107, 2005.

[106] M. Walther, G. S. Chambers, Z. Liu, M. R. Freeman, and F. A. Hegmann, "Emission and detection of terahertz pulses from a metal-tip antenna", *J. Opt. Soc. Am. B*, vol. 22, no. 11, pp. 2357–2365, 2005.

[107] G. Goubau, "Surface waves and their application to transmission lines", *Journal of Applied Physics*, vol. 21, no. 11, pp. 1119–1128, 1950.

[108] T.-I. Jeon, J. Zhang, and D. Grischkowsky, "THz Sommerfeld wave propagation on a single metal wire", *Applied Physics Letters*, vol. 86, no. 16, p. 161904, 2005.

[109] R. Mendis and D. Grischkowsky, "Plastic ribbon THz waveguides", *Journal of Applied Physics*, vol. 88, no. 7, pp. 4449–4451, 2000.

[110] R. W. McGowan, G. Gallot, and D. Grischkowsky, "Propagation of ultraw-ideband short pulses of terahertz radiation through submillimeter-diameter circular waveguides", *Opt. Lett.*, vol. 24, no. 20, pp. 1431–1433, 1999.

[111] H. Bao, K. Nielsen, O. Bang, and P. U. Jepsen, "Dielectric tube waveguides with absorptive cladding for broadband, low-dispersion and low loss thz guiding", *Scientific Reports*, vol. 5, no. 1, p. 7620, 2015.

[112] R. Mendis and D. Grischkowsky, "Undistorted guided-wave propagation of subpicosecond terahertz pulses", *Opt. Lett.*, vol. 26, no. 11, pp. 846–848, 2001.

[113] R. Mendis and D. Grischkowsky, "THz interconnect with low-loss and low-group velocity dispersion", *IEEE Microwave and Wireless Components Letters*, vol. 11, no. 11, pp. 444–446, 2001.

[114] G. Balistreri *et al.*, "Time-domain integration of broadband terahertz pulses in a tapered two-wire waveguide", *Laser & Photonics Reviews*, vol. 15, no. 8, p. 2 100 051, 2021.

[115] M. Awad, M. Nagel, and H. Kurz, "Tapered sommerfeld wire terahertz near-field imaging", *Applied Physics Letters*, vol. 94, no. 5, p. 051 107, 2009.

[116] M. Schnell *et al.*, "Nanofocusing of mid-infrared energy with tapered transmission lines", *Nature Photonics*, vol. 5, no. 5, pp. 283–287, 2011.

[117] S. Kawata, M. Ohtsu, and M. Irie, *Near-field optics and surface plasmon polaritons*. Springer Science & Business Media, 2001, vol. 81.

[118] S. A. Maier, *Plasmonics: fundamentals and applications*. Springer Science & Business Media, 2007.

[119] J.-J. Greffet and R. Carminati, "Image formation in near-field optics", *Progress in Surface Science*, vol. 56, no. 3, pp. 133–237, 1997.

[120] J. A. Porto, R. Carminati, and J.-J. Greffet, "Theory of electromagnetic field imaging and spectroscopy in scanning near-field optical microscopy", *Journal of Applied Physics*, vol. 88, no. 8, pp. 4845–4850, 2000.

[121] B. Hecht *et al.*, "Scanning near-field optical microscopy with aperture probes: Fundamentals and applications", *The Journal of Chemical Physics*, vol. 112, no. 18, pp. 7761–7774, 2000.

[122] Z. Zheng, N. Kanda, K. Konishi, and M. Kuwata-Gonokami, "Efficient coupling of propagating broadband terahertz radial beams to metal wires", *Opt. Express*, vol. 21, no. 9, pp. 10 642–10 650, 2013.

[123] O. Mitrofanov, C. C. Renaud, and A. J. Seeds, "Terahertz probe for spectroscopy of sub-wavelength objects", *Opt. Express*, vol. 20, no. 6, pp. 6197–6202, 2012.

[124] O. Mitrofanov *et al.*, "Terahertz pulse propagation through small apertures", *Applied Physics Letters*, vol. 79, no. 7, pp. 907–909, 2001.

[125]   O. Mitrofanov *et al.*, "Near-field probing of mie resonances in single tio2 microspheres at terahertz frequencies", *Opt. Express*, vol. 22, no. 19, pp. 23 034–23 042, 2014.

[126]   A. Novitsky, A. M. Ivinskaya, M. Zalkovskij, R. Malureanu, P. Uhd Jepsen, and A. V. Lavrinenko, "Non-resonant terahertz field enhancement in periodically arranged nanoslits", *Journal of Applied Physics*, vol. 112, no. 7, p. 074 318, 2012.

[127]   A. Cvitkovic, N. Ocelic, and R. Hillenbrand, "Analytical model for quantitative prediction of material contrasts in scattering-type near-field optical microscopy", *Opt. Express*, vol. 15, no. 14, pp. 8550–8565, 2007.

[128]   C. Maissen, S. Chen, E. Nikulina, A. Govyadinov, and R. Hillenbrand, "Probes for ultrasensitive thz nanoscopy", *ACS Photonics*, vol. 6, no. 5, pp. 1279–1288, 2019.

[129]   R. Berndt, J. K. Gimzewski, and P. Johansson, "Inelastic tunneling excitation of tip-induced plasmon modes on noble-metal surfaces", *Phys. Rev. Lett.*, vol. 67, pp. 3796–3799, 27 1991.

[130]   R. Berndt, J. K. Gimzewski, and P. Johansson, "Electromagnetic interactions of metallic objects in nanometer proximity", *Phys. Rev. Lett.*, vol. 71, pp. 3493–3496, 21 1993.

[131]   A. J. Adam, N. C. van der Valk, and P. C. Planken, "Measurement and calculation of the near field of a terahertz apertureless scanning optical microscope", *J. Opt. Soc. Am. B*, vol. 24, no. 5, pp. 1080–1090, 2007.

[132]   V. Jelic *et al.*, "Ultrafast THz-pulse-induced tunneling dynamics in an STM", in *Ultrafast Phenomena and Nanophotonics XVIII*, M. Betz, A. Y. Elezzabi, J.-J. Song, and K.-T. Tsen, Eds., International Society for Optics and Photonics, vol. 8984, SPIE, 2014, pp. 150–159.

[133]   V. Jelic, *Thesis: Imaging Ultrafast Dynamics on the Atomic Scale with a Terahertz Scanning Tunneling Microscope.* 2019.

[134]   A. van Houselt and H. J. W. Zandvliet, "Colloquium: Time-resolved scanning tunneling microscopy", *Rev. Mod. Phys.*, vol. 82, pp. 1593–1605, 2 2010.

[135]   C. Saunus, J. Raphael Bindel, M. Pratzer, and M. Morgenstern, "Versatile scanning tunneling microscopy with 120 ps time resolution", *Applied Physics Letters*, vol. 102, no. 5, p. 051 601, 2013.

[136]   M. J. Feldstein, P. Vöhringer, W. Wang, and N. F. Scherer, "Femtosecond optical spectroscopy and scanning probe microscopy", *The Journal of Physical Chemistry*, vol. 100, no. 12, pp. 4739–4748, 1996.

[137]   M. Garg and K. Kern, "Attosecond coherent manipulation of electrons in tunneling microscopy", *Science*, vol. 367, no. 6476, pp. 411–415, 2020.

[138]   C. Sammet, M. Völcker, W. Krieger, and H. Walther, "Optical mixing of CO_2-laser radiation in a scanning tunneling microscope", *Journal of Applied Physics*, vol. 78, no. 11, pp. 6477–6480, 1995.

[139] M. J. Hagmann, "Simulations of the generation of broadband signals from dc to 100thz by photomixing in laser-assisted field emission", *Ultramicroscopy*, vol. 73, no. 1, pp. 89–97, 1998.

[140] R. Huber, M. Koch, and J. Feldmann, "Laser-induced thermal expansion of a scanning tunneling microscope tip measured with an atomic force microscope cantilever", *Applied Physics Letters*, vol. 73, no. 17, pp. 2521–2523, 1998.

[141] T. L. Cocker, *Thesis: Exploring conductivity in nanomaterials with terahertz pulses*. 2012.

[142] C. J. Chen, *Introduction to scanning tunneling microscopy*. Oxford University Press on Demand, 1993, vol. 4.

[143] B. Voigtländer, *Scanning probe microscopy: Atomic force microscopy and scanning tunneling microscopy*. Springer, 2015.

[144] Ø. Fischer, M. Kugler, I. Maggio-Aprile, C. Berthod, and C. Renner, "Scanning tunneling spectroscopy of high-temperature superconductors", *Rev. Mod. Phys.*, vol. 79, pp. 353–419, 1 2007.

[145] J. G. Simmons, "Generalized formula for the electric tunnel effect between similar electrodes separated by a thin insulating film", *Journal of Applied Physics*, vol. 34, no. 6, pp. 1793–1803, 1963.

[146] J. G. Simmons, "Electric tunnel effect between dissimilar electrodes separated by a thin insulating film", *Journal of Applied Physics*, vol. 34, no. 9, pp. 2581–2590, 1963.

[147] R. Stratton, "Tunneling in schottky barrier rectifiers", in *Tunneling Phenomena in Solids: Lectures presented at the 1967/NATO Advanced Study Institute at Risö, Denmark*, E. Burstein and S. Lundqvist, Eds. Boston, MA: Springer US, 1969, pp. 105–125.

[148] I. Bâldea, "Transition voltage spectroscopy in vacuum break junction: Possible role of surface states", *EPL (Europhysics Letters)*, vol. 98, no. 1, p. 17 010, 2012.

[149] W. S. Koh and L. K. Ang, "Quantum model of space–charge-limited field emission in a nanogap", *Nanotechnology*, vol. 19, no. 23, p. 235 402, 2008.

[150] C. B. Duke, "Theory of metal-barrier-metal tunneling", in *Tunneling Phenomena in Solids: Lectures presented at the 1967/NATO Advanced Study Institute at Risö, Denmark*, E. Burstein and S. Lundqvist, Eds. Boston, MA: Springer US, 1969, pp. 31–46.

[151] N. F. Mott, "Note on copper-cuprous oxide photocells", *Proceedings of the Royal Society of London. Series A. Mathematical and Physical Sciences*, vol. 171, no. 946, pp. 281–285, 1939.

[152] R. Feenstra, "A prospective: Quantitative scanning tunneling spectroscopy of semiconductor surfaces", *Surface Science*, vol. 603, no. 18, pp. 2841–2844, 2009.

[153] R. T. Shuey, "Interband tunneling-theory", in *Tunneling Phenomena in Solids: Lectures presented at the 1967/NATO Advanced Study Institute at Risö, Denmark*, E. Burstein and S. Lundqvist, Eds. Boston, MA: Springer US, 1969, pp. 93–103.

[154] C. Mead, "Metal-semiconductor surface barriers", *Solid-State Electronics*, vol. 9, no. 11, pp. 1023–1033, 1966.

[155] P. V. Gray, "Tunneling from metal to semiconductors", *Phys. Rev.*, vol. 140, A179–A186, 1A 1965.

[156] H. Neddermeyer, "Scanning tunnelling microscopy of semiconductor surfaces", *Reports on Progress in Physics*, vol. 59, no. 6, pp. 701–769, 1996.

[157] M. Dürr and U. Höfer, "Dissociative adsorption of molecular hydrogen on silicon surfaces", *Surface Science Reports*, vol. 61, no. 12, pp. 465–526, 2006.

[158] D. J. Scalapino, "The theory of josephson tunneling", in *Tunneling Phenomena in Solids: Lectures presented at the 1967/NATO Advanced Study Institute at Risö, Denmark*, E. Burstein and S. Lundqvist, Eds. Boston, MA: Springer US, 1969, pp. 477–518.

[159] L. K. Ang, T. J. T. Kwan, and Y. Y. Lau, "New scaling of child-langmuir law in the quantum regime", *Phys. Rev. Lett.*, vol. 91, p. 208 303, 20 2003.

[160] Y. Zhu and L. K. Ang, "Child–langmuir law in the coulomb blockade regime", *Applied Physics Letters*, vol. 98, no. 5, p. 051 502, 2011.

[161] Y. B. Zhu and L. K. Ang, "Space charge limited current emission for a sharp tip", *Physics of Plasmas*, vol. 22, no. 5, p. 052 106, 2015.

[162] W. S. Koh, L. K. Ang, and T. J. T. Kwan, "Three-dimensional child–langmuir law for uniform hot electron emission", *Physics of Plasmas*, vol. 12, no. 5, p. 053 107, 2005.

[163] P. Zhang, "Scaling for quantum tunneling current in nano- and subnano-scale plasmonic junctions", *Scientific Reports*, vol. 5, no. 1, p. 9826, 2015.

[164] W. S. Koh and L. K. Ang, "Transition of field emission to space-charge-limited emission in a nanogap", *Applied Physics Letters*, vol. 89, no. 18, p. 183 107, 2006.

[165] M. W. J. Prins, R. Jansen, R. H. M. Groeneveld, A. P. van Gelder, and H. van Kempen, "Photoelectrical properties of semiconductor tips in scanning tunneling microscopy", *Phys. Rev. B*, vol. 53, pp. 8090–8104, 12 1996.

[166] J. T. Krug, E. J. Sánchez, and X. S. Xie, "Design of near-field optical probes with optimal field enhancement by finite difference time domain electromagnetic simulation", *The Journal of Chemical Physics*, vol. 116, no. 24, pp. 10 895–10 901, 2002.

[167] W. Zhang, X. Cui, and O. J. F. Martin, "Local field enhancement of an infinite conical metal tip illuminated by a focused beam", *Journal of Raman Spectroscopy*, vol. 40, no. 10, pp. 1338–1342, 2009.

[168] R. M. Roth, N. C. Panoiu, M. M. Adams, R. M. Osgood, C. C. Neacsu, and M. B. Raschke, "Resonant-plasmon field enhancement from asymmetrically illuminated conical metallic-probe tips", *Opt. Express*, vol. 14, no. 7, pp. 2921–2931, 2006.

[169] W. Chen and Q. Zhan, "Numerical study of an apertureless near field scanning optical microscope probe under radial polarization illumination", *Opt. Express*, vol. 15, no. 7, pp. 4106–4111, 2007.

[170] A. Downes, D. Salter, and A. Elfick, "Finite element simulations of tip-enhanced raman and fluorescence spectroscopy", *The Journal of Physical Chemistry B*, vol. 110, no. 13, pp. 6692–6698, 2006, PMID: 16570974.

[171] A. Downes, D. Salter, and A. Elfick, "Heating effects in tip-enhanced optical microscopy", *Opt. Express*, vol. 14, no. 12, pp. 5216–5222, 2006.

[172] A. Downes, D. Salter, and A. Elfick, "Simulations of tip-enhanced optical microscopy reveal atomic resolution", *Journal of Microscopy*, vol. 229, no. 2, pp. 184–188, 2008.

[173] M. Micic, N. Klymyshyn, Y. D. Suh, and H. P. Lu, "Finite element method simulation of the field distribution for afm tip-enhanced surface-enhanced raman scanning microscopy", *The Journal of Physical Chemistry B*, vol. 107, no. 7, pp. 1574–1584, 2003.

[174] A. Mustonen, P. Beaud, E. Kirk, T. Feurer, and S. Tsujino, "Efficient light coupling for optically excited high-density metallic nanotip arrays", *Scientific Reports*, vol. 2, no. 1, p. 915, 2012.

[175] W. Iida, S. Katano, and Y. Uehara, "Finite-difference time-domain analysis of scanning tunneling microscope light emission spectra", *Japanese Journal of Applied Physics*, vol. 49, no. 9, p. 095 202, 2010.

[176] Y. Uehara, S. Katano, M. Kuwahara, and T. Suzuki, "Electromagnetic properties of scanning tunneling microscope tip–sample gap in the terahertz frequency range", *Japanese Journal of Applied Physics*, vol. 54, no. 8S2, 08LB06, 2015.

[177] M. N. Sadiku, *Numerical techniques in electromagnetics*. CRC press, 2000.

[178] K.-J. Bathe, "Finite element procedures for solids and structures linear analysis", *Finite Element Procedures*, pp. 148–214, 1982.

[179] J. A. Deibel, K. Wang, M. D. Escarra, and D. M. Mittleman, "Enhanced coupling of terahertz radiation to cylindrical wire waveguides", *Opt. Express*, vol. 14, no. 1, pp. 279–290, 2006.

[180] J. A. Deibel, M. Escarra, N. Berndsen, K. Wang, and D. M. Mittleman, "Finite-element method simulations of guided wave phenomena at terahertz frequencies", *Proceedings of the IEEE*, vol. 95, no. 8, pp. 1624–1640, 2007.

[181] J. L. Bohn, D. J. Nesbitt, and A. Gallagher, "Field enhancement in apertureless near-field scanning optical microscopy", *J. Opt. Soc. Am. A*, vol. 18, no. 12, pp. 2998–3006, 2001.

[182] C. Multiphysics®, "Introduction to comsol multiphysics®", *COMSOL Multiphysics*, 2015.

[183] C. Multiphysics®, "Introduction to the wave optics module®", *COMSOL Documentation*, 2015.

[184] R. Courant, K. Friedrichs, and H. Lewy, "Über die partiellen differenzengleichungen der mathematischen physik", *Mathematische Annalen*, vol. 100, no. 1, pp. 32–74, 1928.

[185] C. A. De Moura and C. S. Kubrusly, "The courant–friedrichs–lewy (cfl) condition", *AMC*, vol. 10, p. 12, 2013.

[186] G. Baccarani and P. Ostoja, "Electron mobility empirically related to the phosphorus concentration in silicon", *Solid State Electronics*, vol. 18, no. 6, pp. 579–580, 1975.

[187] M. Walther, D. G. Cooke, C. Sherstan, M. Hajar, M. R. Freeman, and F. A. Hegmann, "Terahertz conductivity of thin gold films at the metal-insulator percolation transition", *Phys. Rev. B*, vol. 76, p. 125 408, 12 2007.

[188] P. Parkinson *et al.*, "Transient terahertz conductivity of GaAs nanowires", *Nano Letters*, vol. 7, no. 7, pp. 2162–2165, 2007.

[189] J. Lloyd-Hughes, "Generalized conductivity model for polar semiconductors at terahertz frequencies", *Applied Physics Letters*, vol. 100, no. 12, p. 122 103, 2012.

[190] L. Olsson, N. Lin, V. Yakimov, and R. Erlandsson, "A method for in situ characterization of tip shape in ac-mode atomic force microscopy using electrostatic interaction", *Journal of Applied Physics*, vol. 84, no. 8, pp. 4060–4064, 1998.

[191] J. A. Porto, P. Johansson, S. P. Apell, and T. López-Ríos, "Resonance shift effects in apertureless scanning near-field optical microscopy", *Phys. Rev. B*, vol. 67, p. 085 409, 8 2003.

[192] I. Notingher and A. Elfick, "Effect of sample and substrate electric properties on the electric field enhancement at the apex of spm nanotips", *The Journal of Physical Chemistry B*, vol. 109, no. 33, pp. 15 699–15 706, 2005, PMID: 16852992.

[193] T. Wutscher, A. J. Weymouth, and F. J. Giessibl, "Localization of the phantom force induced by the tunneling current", *Phys. Rev. B*, vol. 85, p. 195 426, 19 2012.

[194] S. Neppl *et al.*, "Direct observation of electron propagation and dielectric screening on the atomic length scale", *Nature*, vol. 517, no. 7534, pp. 342–346, 2015.

[195] C. K. Moy, G. Ranzi, T. C. Petersen, and S. P. Ringer, "Macroscopic electrical field distribution and field-induced surface stresses of needle-shaped field emitters", *Ultramicroscopy*, vol. 111, no. 6, pp. 397–404, 2011, Special Issue: 52nd International Field Emission Symposium.

[196] S. Hudlet, M. Saint Jean, C. Guthmann, and J. Berger, "Evaluation of the capacitive force between an atomic force microscopy tip and a metallic surface", *The European Physical Journal B - Condensed Matter and Complex Systems*, vol. 2, no. 1, pp. 5–10, 1998.

[197] D. Biswas, "A universal formula for the field enhancement factor", *Physics of Plasmas*, vol. 25, no. 4, p. 043 113, 2018.

[198] K. Wang and D. M. Mittleman, "Guided propagation of terahertz pulses on metal wires", *J. Opt. Soc. Am. B*, vol. 22, no. 9, pp. 2001–2008, 2005.

[199] O. Marti, H. Bielefeldt, B. Hecht, S. Herminghaus, P. Leiderer, and J. Mlynek, "Near-field optical measurement of the surface plasmon field", *Optics Communications*, vol. 96, no. 4, pp. 225–228, 1993.

[200] C. Girard and A. Dereux, "Near-field optics theories", *Reports on Progress in Physics*, vol. 59, no. 5, pp. 657–699, 1996.

[201] W. Denk and D. W. Pohl, "Near-field optics: Microscopy with nanometer-size fields", *Journal of Vacuum Science & Technology B: Microelectronics and Nanometer Structures Processing, Measurement, and Phenomena*, vol. 9, no. 2, pp. 510–513, 1991.

[202] P. Hommelhoff, Y. Sortais, A. Aghajani-Talesh, and M. A. Kasevich, "Field emission tip as a nanometer source of free electron femtosecond pulses", *Phys. Rev. Lett.*, vol. 96, p. 077 401, 7 2006.

[203] M. Krüger, M. Schenk, and P. Hommelhoff, "Attosecond control of electrons emitted from a nanoscale metal tip", *Nature*, vol. 475, no. 7354, pp. 78–81, 2011.

[204] G. Kron, "Equivalent circuit of the field equations of maxwell-i", *Proceedings of the IRE*, vol. 32, no. 5, pp. 289–299, 1944.

[205] G. Kron, "Numerical solution of ordinary and partial differential equations by means of equivalent circuits", *Journal of Applied Physics*, vol. 16, no. 3, pp. 172–186, 1945.

[206] J. Houard, L. Arnoldi, A. Ayoub, A. Hideur, and A. Vella, "Nanotip response to monocycle terahertz pulses", *Applied Physics Letters*, vol. 117, no. 15, p. 151 105, 2020.

[207] A. R. Kerr, J. A. Grange, and J. A. Lichtenberger, *Contact whiskers for millimeter wave diodes*, NASA STI/Recon Technical Report N, 1978.

[208] T. Sandu, G. Boldeiu, and V. Moagar-Poladian, "Applications of electrostatic capacitance and charging", *Journal of Applied Physics*, vol. 114, no. 22, p. 224 904, 2013.

[209] P. Mlynek, J. Misurec, M. Koutny, and P. Silhavy, "Two-port network transfer function for power line topology modeling.", *Radioengineering*, vol. 21, no. 1, 2012.

[210] N. Khiabani, Y. Huang, Y.-C. Shen, and S. Boyes, "Theoretical modeling of a photoconductive antenna in a terahertz pulsed system", *IEEE Transactions on Antennas and Propagation*, vol. 61, no. 4, pp. 1538–1546, 2013.

[211] N. Khiabani, *Modelling, design and characterisation of terahertz photoconductive antennas*. The University of Liverpool (United Kingdom), 2013.

[212] C. L. Von Gabriel, "Investigation of low-temperature-grown gaas photoconductive antennae for continous-wave and pulsed terahertz generation", *Uni-Frankfurt. De*, vol. 2007, 2007.

[213] G. C. Loata, T. Löffler, and H. G. Roskos, "Evidence for long-living charge carriers in electrically biased low-temperature-grown GaAs photoconductive switches", *Applied Physics Letters*, vol. 90, no. 5, p. 052 101, 2007.

[214] W. Schottky, "Zur halbleitertheorie der sperrschicht- und spitzengleichrichter", *Zeitschrift für Physik*, vol. 113, no. 5, pp. 367–414, 1939.

[215] W. Schottky, "Vereinfachte und erweiterte theorie der randschicht-gleichrichter", *Zeitschrift für Physik*, vol. 118, no. 9, pp. 539–592, 1942.

[216] G. H. Parker, *Tunneling in Schottky barriers*. California Institute of Technology, 1970.

[217] L. Keldysh *et al.*, "Ionization in the field of a strong electromagnetic wave", *Sov. Phys. JETP*, vol. 20, no. 5, pp. 1307–1314, 1965.

[218] M. Staffaroni, J. Conway, S. Vedantam, J. Tang, and E. Yablonovitch, "Circuit analysis in metal-optics", *Photonics and Nanostructures - Fundamentals and Applications*, vol. 10, no. 1, pp. 166–176, 2012.

[219] N. Engheta, A. Salandrino, and A. Alù, "Circuit elements at optical frequencies: Nanoinductors, nanocapacitors, and nanoresistors", *Phys. Rev. Lett.*, vol. 95, p. 095 504, 9 2005.

[220] N. Engheta, "Circuits with light at nanoscales: Optical nanocircuits inspired by metamaterials", *Science*, vol. 317, no. 5845, pp. 1698–1702, 2007.

[221] A. M. Moore and P. S. Weiss, "Functional and spectroscopic measurements with scanning tunneling microscopy", *Annual Review of Analytical Chemistry*, vol. 1, no. 1, pp. 857–882, 2008, PMID: 20636100.

[222] Y. C. Liao, C. K. Yang, T. L. Wu, I. S. Hwang, M. K. Wu, and C. C. Chi, "Evolution of surface to bulk tunneling spectrum by scanning tunneling microscopy", *Phys. Rev. B*, vol. 81, p. 195 435, 19 2010.

[223] A. J. Bard, A. B. Bocarsly, F. R. F. Fan, E. G. Walton, and M. S. Wrighton, "The concept of fermi level pinning at semiconductor/liquid junctions. consequences for energy conversion efficiency and selection of useful solution redox couples in solar devices", *Journal of the American Chemical Society*, vol. 102, no. 11, pp. 3671–3677, 1980.

[224] C. B. Duke, "Theory of metal-barrier-metal tunneling", in *Tunneling Phenomena in Solids: Lectures presented at the 1967/NATO Advanced Study Institute at Risö, Denmark*, E. Burstein and S. Lundqvist, Eds. Boston, MA: Springer US, 1969, pp. 31–46.

[225] J. Bardeen, "Tunneling into superconductors", *Phys. Rev. Lett.*, vol. 9, pp. 147–149, 4 1962.

[226] J. Bardeen, "Tunneling theory of charge-density-wave depinning", *Phys. Rev. Lett.*, vol. 45, pp. 1978–1980, 24 1980.

[227] M. A. Seo *et al.*, "Terahertz field enhancement by a metallic nano slit operating beyond the skin-depth limit", *Nature Photonics*, vol. 3, no. 3, pp. 152–156, 2009.

[228] J. R. Knab, A. J. L. Adam, E. Shaner, H. J. A. J. Starmans, and P. C. M. Planken, "Terahertz near-field spectroscopy of filled subwavelength sized apertures in thin metal films", *Opt. Express*, vol. 21, no. 1, pp. 1101–1112, 2013.

[229] P. Kužel and H. Němec, "Terahertz conductivity in nanoscaled systems: Effective medium theory aspects", *Journal of Physics D: Applied Physics*, vol. 47, no. 37, p. 374 005, 2014.

[230] Y. Kwok, G. Chen, and S. Mukamel, "Stm imaging of electron migration in real space and time: A simulation study", *Nano Letters*, vol. 19, no. 10, pp. 7006–7012, 2019, PMID: 31509425.

[231] S. L. Lange, N. K. Noori, T. M. B. Kristensen, K. Steenberg, and P. U. Jepsen, "Ultrafast thz-driven electron emission from metal metasurfaces", *Journal of Applied Physics*, vol. 128, no. 7, p. 070 901, 2020.

[232] D. Matte *et al.*, "Extreme lightwave electron field emission from a nanotip", *Phys. Rev. Research*, vol. 3, p. 013 137, 1 2021.

[233] D. J. BenDaniel and C. B. Duke, "Space-charge effects on electron tunneling", *Phys. Rev.*, vol. 152, pp. 683–692, 2 1966.

[234] T. Christen and M. Büttiker, "Low frequency admittance of a quantum point contact", *Phys. Rev. Lett.*, vol. 77, pp. 143–146, 1 1996.

[235] V. A. Gopar, P. A. Mello, and M. Büttiker, "Mesoscopic capacitors: A statistical analysis", *Phys. Rev. Lett.*, vol. 77, pp. 3005–3008, 14 1996.

[236] N. D. Lang and W. Kohn, "Theory of metal surfaces: Induced surface charge and image potential", *Phys. Rev. B*, vol. 7, pp. 3541–3550, 8 1973.

[237] L. K. Ang, W. S. Koh, Y. Y. Lau, and T. J. T. Kwan, "Space-charge-limited flows in the quantum regime", *Physics of Plasmas*, vol. 13, no. 5, p. 056 701, 2006.

[238] S. Kurokawa and A. Sakai, "Gap dependence of the tip-sample capacitance", *Journal of Applied Physics*, vol. 83, no. 12, pp. 7416–7423, 1998.

[239] A. Sakai, S. Kurokawa, and Y. Hasegawa, "Geometrical capacitance of the tip–semiconductor junction", *Journal of Vacuum Science & Technology A*, vol. 14, no. 3, pp. 1219–1222, 1996.

[240] M. Büttiker, H. Thomas, and A. Prêtre, "Mesoscopic capacitors", *Physics Letters A*, vol. 180, no. 4, pp. 364–369, 1993.

[241] M. Büttiker and C. A. Stafford, "Charge transfer induced persistent current and capacitance oscillations", *Phys. Rev. Lett.*, vol. 76, pp. 495–498, 3 1996.

[242] K. Flensberg, "Capacitance and conductance of mesoscopic systems connected by quantum point contacts", *Phys. Rev. B*, vol. 48, pp. 11 156–11 166, 15 1993.

[243] U. Meirav and E. B. Foxman, "Single-electron phenomena in semiconductors", *Semiconductor Science and Technology*, vol. 11, no. 3, pp. 255–284, 1996.

[244] Q. Hu, C. A. Mears, P. L. Richards, and F. L. Lloyd, "Observation of nondissipative quasiparticle tunnel currents in superconducting tunnel junctions", *Phys. Rev. Lett.*, vol. 64, pp. 2945–2948, 24 1990.

[245] B. J. van Wees *et al.*, "Quantized conductance of point contacts in a two-dimensional electron gas", *Phys. Rev. Lett.*, vol. 60, pp. 848–850, 9 1988.

[246] N. R. Werthamer, "Nonlinear self-coupling of Josephson radiation in superconducting tunnel junctions", *Phys. Rev.*, vol. 147, pp. 255–263, 1 1966.

[247] A. H. Worsham, N. G. Ugras, D. Winkler, D. E. Prober, N. R. Erickson, and P. F. Goldsmith, "Quantum tunneling currents in a superconducting junction", *Phys. Rev. Lett.*, vol. 67, pp. 3034–3037, 21 1991.

[248] M. McEllistrem, G. Haase, D. Chen, and R. J. Hamers, "Electrostatic sample-tip interactions in the scanning tunneling microscope", *Phys. Rev. Lett.*, vol. 70, pp. 2471–2474, 16 1993.

[249] R. M. Feenstra and J. A. Stroscio, "Tunneling spectroscopy of the GaAs(110) surface", *Journal of Vacuum Science & Technology B: Microelectronics Processing and Phenomena*, vol. 5, no. 4, pp. 923–929, 1987.

[250] D. G. Cahill and R. J. Hamers, "Scanning tunneling microscopy of photoexcited carriers at the si(001) surface", *Journal of Vacuum Science & Technology B: Microelectronics and Nanometer Structures Processing, Measurement, and Phenomena*, vol. 9, no. 2, pp. 564–567, 1991.

[251] D. G. Cahill and R. J. Hamers, "Surface photovoltage of Ag on Si(111)-7×7 by scanning tunneling microscopy", *Phys. Rev. B*, vol. 44, pp. 1387–1390, 3 1991.

[252] M. Weimer, J. Kramar, and J. D. Baldeschwieler, "Band bending and the apparent barrier height in scanning tunneling microscopy", *Phys. Rev. B*, vol. 39, pp. 5572–5575, 8 1989.

[253] W. J. Kaiser, L. D. Bell, M. H. Hecht, and F. J. Grunthaner, "Scanning tunneling microscopy characterization of the geometric and electronic structure of hydrogen-terminated silicon surfaces", *Journal of Vacuum Science & Technology A*, vol. 6, no. 2, pp. 519–523, 1988.

[254] H. C. Card and E. H. Rhoderick, "Studies of tunnel MOS diodes I. Interface effects in silicon Schottky diodes", *Journal of Physics D: Applied Physics*, vol. 4, no. 10, pp. 1589–1601, 1971.

[255] M. N. Feiginov and V. A. Volkov, "Skin effect and response of semiconductor barrier structures", *Journal of Experimental and Theoretical Physics Letters*, vol. 69, no. 4, pp. 336–342, 1999.

[256] S. V. Kalinin and D. A. Bonnell, "Scanning impedance microscopy of an active schottky barrier diode", *Journal of Applied Physics*, vol. 91, no. 2, pp. 832–839, 2002.

[257] R. Dombrowski, C. Steinebach, C. Wittneven, M. Morgenstern, and R. Wiesendanger, "Tip-induced band bending by scanning tunneling spectroscopy of the states of the tip-induced quantum dot on InAs(110)", *Phys. Rev. B*, vol. 59, pp. 8043–8048, 12 1999.

[258] Y. De Wilde *et al.*, "Thermal radiation scanning tunnelling microscopy", *Nature*, vol. 444, no. 7120, pp. 740–743, 2006.

[259] A. van Houselt and H. J. W. Zandvliet, "Colloquium: Time-resolved scanning tunneling microscopy", *Rev. Mod. Phys.*, vol. 82, pp. 1593–1605, 2 2010.

[260] S. D. Brorson, J. Zhang, and S. R. Keiding, "Ultrafast carrier trapping and slow recombination in ion-bombarded silicon on sapphire measured via thz spectroscopy", *Applied Physics Letters*, vol. 64, no. 18, pp. 2385–2387, 1994.

[261] M. W. J. Prins, M. C. M. M. van der Wielen, R. Jansen, D. L. Abraham, and H. van Kempen, "Photoamperic probes in scanning tunneling microscopy", *Applied Physics Letters*, vol. 64, no. 10, pp. 1207–1209, 1994.

[262] H. Nguyen *et al.*, "Mechanisms of current rectification in an STM tunnel junction and the measurement of an operational tunneling time", *IEEE Transactions on Electron Devices*, vol. 36, no. 11, pp. 2671–2678, 1989.

[263] J. R. Jensen, U. D. Keil, and J. M. Hvam, "Spatio-temporal imaging of voltage pulses with an ultrafast scanning tunneling microscope", *Applied Physics Letters*, vol. 70, no. 20, pp. 2762–2764, 1997.

[264] U. D. Keil, J. R. Jensen, and J. M. Hvam, "Fiber coupled ultrafast scanning tunneling microscope", *Journal of Applied Physics*, vol. 81, no. 7, pp. 2929–2934, 1997.

[265] U. D. Keil, J. R. Jensen, and J. M. Hvam, "Transient measurements with an ultrafast scanning tunneling microscope on semiconductor surfaces", *Applied Physics Letters*, vol. 72, no. 13, pp. 1644–1646, 1998.

[266] G. Nunes and N. M. Amer, "Atomic resolution scanning tunneling microscopy with a gallium arsenide tip", *Applied Physics Letters*, vol. 63, no. 13, pp. 1851–1853, 1993.

[267] G. Nunes and M. R. Freeman, "Picosecond resolution in scanning tunneling microscopy", *Science*, vol. 262, no. 5136, pp. 1029–1032, 1993.

[268] G. P. Donati, G. Rodriguez, and A. J. Taylor, "Ultrafast, dynamical imaging of surfaces by use of a scanning tunneling microscope with a photoexcited, low-temperature-grown GaAs tip", *J. Opt. Soc. Am. B*, vol. 17, no. 6, pp. 1077–1083, 2000.

[269] U. Dürig, D. W. Pohl, and F. Rohner, "Near-field optical-scanning microscopy", *Journal of Applied Physics*, vol. 59, no. 10, pp. 3318–3327, 1986.

[270] R. Groeneveld, M. Prins, and H. van Kempen, "Modulated photodetection with semiconductor tips in a scanning tunneling microscope", *Surface Science*, vol. 331-333, pp. 1299–1304, 1995, Proceedings of the 14th European Conference on Surface Science.

[271] R. H. M. Groeneveld and H. van Kempen, "The capacitive origin of the picosecond electrical transients detected by a photoconductively gated scanning tunneling microscope", *Applied Physics Letters*, vol. 69, no. 15, pp. 2294–2296, 1996.

[272] G. M. Steeves, A. Y. Elezzabi, and M. R. Freeman, "Nanometer-scale imaging with an ultrafast scanning tunneling microscope", *Applied Physics Letters*, vol. 72, no. 4, pp. 504–506, 1998.

[273] S. Weiss, D. F. Ogletree, D. Botkin, M. Salmeron, and D. S. Chemla, "Ultrafast scanning probe microscopy", *Applied Physics Letters*, vol. 63, no. 18, pp. 2567–2569, 1993.

[274] S. Weiss, D. Botkin, D. F. Ogletree, M. Salmeron, and D. S. Chemla, "The ultrafast response of a scanning tunneling microscope", *physica status solidi (b)*, vol. 188, no. 1, pp. 343–359, 1995.

[275] R. Yano, H. Gotoh, Y. Hirayama, and S. Miyashita, "Systematic pump-probe terahertz wave emission spectroscopy of a photoconductive antenna fabricated on low-temperature grown GaAs", *Journal of Applied Physics*, vol. 96, no. 7, pp. 3635–3638, 2004.

[276] T. Brandes, D. Weinmann, and B. Kramer, "Frequency-dependent conductance of tunnel junctions", *Europhysics Letters (EPL)*, vol. 22, no. 1, pp. 51–56, 1993.

[277] R. H. Jacobsen, K. Birkelund, T. Holst, P. Uhd Jepsen, and S. R. Keiding, "Interpretation of photocurrent correlation measurements used for ultrafast photoconductive switch characterization", *Journal of Applied Physics*, vol. 79, no. 5, pp. 2649–2657, 1996.

[278] R. Jansen, M. W. J. Prins, and H. van Kempen, "Theory of spin-polarized transport in photoexcited semiconductor/ferromagnet tunnel junctions", *Phys. Rev. B*, vol. 57, pp. 4033–4047, 7 1998.

[279] M. Tonouchi, N. Kawasaki, T. Yoshimura, H. Wald, and P. Seidel, "Pump and probe terahertz generation study of ultrafast carrier dynamics in low-temperature grown-GaAs", *Japanese Journal of Applied Physics*, vol. 41, no. Part 2, No. 6B, pp. L706–L709, 2002.

[280] F. Wang *et al.*, "Silicon-based quantum mechanical tunnel junction for plasmon excitation from low-energy electron tunneling", *ACS Photonics*, vol. 8, no. 7, pp. 1951–1960, 2021.

[281] D. A. Yarotski *et al.*, "Ultrafast carrier-relaxation dynamics in self-assembled InAs/GaAs quantum dots", *J. Opt. Soc. Am. B*, vol. 19, no. 6, pp. 1480–1484, 2002.

[282] B. Schröder *et al.*, "Controlling photocurrent channels in scanning tunneling microscopy", *New Journal of Physics*, vol. 22, no. 3, p. 033 047, 2020.

[283] S. Yoshida, J. Kikuchi, Y. Kanitani, O. Takeuchi, H. Oigawa, and H. Shigekawa, "Tip-induced band bending and its effect on local barrier height measurement studied by light-modulated scanning tunneling spectroscopy", *e-Journal of Surface Science and Nanotechnology*, vol. 4, pp. 192–196, 2006.

[284] M. Schnedler, V. Portz, P. H. Weidlich, R. E. Dunin-Borkowski, and P. Ebert, "Quantitative description of photoexcited scanning tunneling spectroscopy and its application to the GaAs(110) surface", *Phys. Rev. B*, vol. 91, p. 235 305, 23 2015.

[285] X. Andrade *et al.*, "Real-space grids and the octopus code as tools for the development of new simulation approaches for electronic systems", *Physical Chemistry Chemical Physics*, vol. 17, no. 47, 2015.

[286] N. Tancogne-Dejean *et al.*, "Octopus, a computational framework for exploring light-driven phenomena and quantum dynamics in extended and finite systems", *The Journal of Chemical Physics*, vol. 152, no. 12, p. 124 119, 2020.